UNIVERSITY OF SOUTHAMPTON

The genesis of grey monazite

A thesis presented for the degree of doctor of philosophy

Stephen John Windle

Department of Geology
University of Southampton
March 1994

UNIVERSITY OF SOUTHAMPTON

ABSTRACT

FACULTY OF SCIENCE

GEOLOGY

Doctor of Philosophy

The genesis of grey monazite
by Stephen John Windle

Grey monazite occurs as sub-millimetre sized, ellipsoidal, authigenic concretions in Llanvirn-aged shales of the Calymene Formation, Montes de Toledo area, Central Spain. The nodules are similar to those previously described from Palaeozoic shales in Wales, Brittany and Belgium. They are Eu-rich and poor in Th by comparison with igneous monazites. They are concentrically zoned, with La, Ce- rich rims and Nd, Sm- rich cores; all the heavy REE and Y are weakly enriched in the cores. The host rocks are massive shales with thin silty horizons, deposited in a distal shelf environment near the oxic/anoxic boundary. The host shales have been metamorphosed under anchizonal conditions, with a peak temperature of 260 to 275 °C. They have largely recrystallised to the assemblage quartz - chlorite - illite. A crenulation cleavage post-dates the monazite nodules. The nodules contain typically 20% inclusions with similar mineralogy to the host shale, often forming an aligned fabric parallel to the long axis of the nodule, which is interpreted as original bedding.

The monazite nodules grew replacively; phyllosilicates, especially illite, were replaced in preference to quartz. No authigenic illites are present within the nodules, only detrital micas with interlayer charge > 0.85. Chlorites included in nodules, as well as those in the host shale, exhibit a range of tetrahedrally coordinated aluminium contents, suggesting that nodule growth spanned a range of temperature, up to near the maximum temperature experienced by the shale.

Silicified cone-in-cone concretions occur in a zone about 280 m above the base of the Calymene Formation. They formed at about 20 m. depth and originally had a carbonate matrix. The carbonate was replaced by quartz and chlorite under anchizonal conditions; heavy REE were mobile at this stage, and are depleted in the concretion. Monazite nodules post-date, or are syngenetic with, the chlorite + quartz alteration of the cone-in-cone. During late-stage weathering under oxidising conditions, REE were leached from the cores of cone-in-cone concretions and a rare lead mineral, corkite-hidalgoite, was formed.

Two sections in the Navas de Estana syncline were sampled for detailed geochemical study. The presence or absence of monazite could not be ascertained in the field, so bulk samples were collected and the heavy mineral fractions separated in order to estimate monazite abundance, by REE analysis of the separates. Monazite abundance correlates with K, Ba and a suite of elements associated with the coarser grained portion of the sediment, but does not correlate with P or with the REE content of the shales, which is controlled by the sedimentology. This suggests that REE transport was very localised. Greater abundances of monazite nodules are associated with nodule compositions richer in light REE. Sm/Nd isotopic measurements indicate that the source of the REE was isotopically heterogeneous, with a range of ≈ 1.5 ε_{Nd} units. Mass balance suggests that the spacing between nodules may be only 0.5 cm.

It is proposed that REE were derived initially mostly from detrital clay minerals, possibly at temperatures as low as 60 °C. At higher temperature, the major REE source were coarser-grained detrital mafic minerals derived from storm-related silt horizons. It is this second source of REE which controls the overall abundance of monazite in the rock. The fluid composition was initially HREE-rich, because of the greater stability of HREE complexes; later, it switched to LREE-rich because of the greater ease of desorption of light REE from the source minerals. This change in fluid chemistry caused the observed concentric zoning of monazites. Regionally, the distribution of monazite may be linked to the availability of mobile phosphorus during diagenesis.

Table of contents

List of figures

List of tables

Acknowledgements

This work was funded by EEC Raw Materials project number MA2M - 0049, "The assessment of alluvial deposits related to strata-bound Eu-rich grey monazite mineralization: a major future source for specific rare earths used in new technology." It was supervised by Professor R.W.Nesbitt, who is thanked for his unfailing support, prompt and constructive criticism, and willingness to indulge some of my wilder notions. Enrique Ortega and Jose-Manuel Amor of Almaden Mining were generous with their data and with logistic help in Spain; Miguel-Angel Gomez is thanked for his company and for stimulating discussions in the field. Michel Laval of the BRGM was very supportive throughout the project, and is thanked for his generous hospitality in Orléans. André Lacomme helped with freighting of samples from the Pyrenees. Tony Milodowski at BGS was kind enough to show me material from Wales, share his ideas, and talk monazites ad infinitum. Kim Jarvis and John Williams at RHBNC, Egham, were endlessly helpful with ICPMS work and admirably stoical when I broke the instrument. For ICPMS work at Southampton, Takafumi Hirata was a patient and gifted teacher. Microprobe work at Cambridge was possible thanks to the generosity of Dr. S. Reed. Isotope work at Southampton was in collaboration with Dr. Jean-Alix Barrat, who was tolerant of a novice in the field, and generous with his knowledge and experience. Most of the staff here have been pestered by me at one stage or another: Drs. Andy Barker, Rex Taylor, John Marshall, Ian West, Barbara Cressey and Ian Croudace have all given helpful advice when it was sought. Trevor Clayton was especially helpful on all matters pertaining to clays, and remarkably patient when trying to deepen my rather shallow grasp of the subject. Many thanks are due to the technical staff: Shir Akbari for organic reflectance work; Bob Jones and John Ford for thin sections and for surreptitiously fixing sundry items which broke when I abused them; Posy Boella for all things geochemical; Dave Spanner for computer things; and to Barry Marsh for some virtuoso photography. Finally, thankyou to Sarah for her forbearance, and to Eleanor, whose impending arrival spurred the project to completion.

This work is dedicated to Scruffy, who never got the chance to nibble at it.

Chapter 1: Background Information

1.0 Introduction.

Grey monazite was first described in 1936 in Russia (Zemel, 1936), and has since been found frequently in alluvial material and, more rarely, in place. It occurs as concretions in low grade mudrocks of Palaeozoic and older age. Its characteristic features are: grain size about one millimetre or less; typical ellipsoidal form; grey or black in colour; density ≈ 4.4 gcm^{-3}, abundant inclusions of silicate minerals and a relatively high europium tenor, up to ≈ 0.5%, combined with a low thorium content. This is in contrast to yellow monazite of igneous origin (Table 1-1). The high density and resistance to weathering and erosion mean that grey monazites are readily concentrated by alluvial processes to produce economic accumulations of rare earth elements (REE). The most commercially valuable of the REE are Eu, Sm, Nd, Tb and Dy (Mariano, 1989). Typical applications are in high technology materials, e.g: magnets (Sm,Nd); phosphors (Eu); batteries, catalytic converters (Ce); superconductors (Y) and optical fibres (Er) (Murphy, 1993). Production from placer deposits of igneous monazite, for example in Western Australia, produces quantities of potentially hazardous ThO_2 as a by-product. Thorium-poor, europium-rich, grey monazite is therefore an environmentally as well as economically attractive future resource of REE. Figure 1-1 shows the worldwide distribution of grey monazites, after Rosenblum and Mosier (1983). It is interesting to note the age range, from ≈ 2.0 Ga in the Francevillian of Gabon, ≈1.1 Ga in Rwanda, 400 - 500 Ma for the Hercynian occurrences of Europe, to ≈270 Ma for alluvial monazites from Permian rocks of Montana. No grey monazites are known from strata of younger than Palaeozoic age. In localities where monazite has been observed in place, the host rocks are either relatively massive black shales (Spain (this study); Belgium (Burnotte

	Grey Monazite	Yellow Monazite
La_2O_3	11.51	13.25
CeO_2	27.18	26.90
Pr_6O_{11}	3.28	3.11
Nd_2O_3	14.29	11.71
Sm_2O_3	2.36	2.70
Eu_2O_3	0.36	0.05
Gd_2O_3	1.25	1.27
Y_2O_3	0.65	1.58
ThO_2	0.81	7.15
Total REE	61.69	67.74
P_2O_5	22.07	26.00
SiO_2	9.90	1.70
TiO_2	0.69	0.05
Al_2O_3	2.27	0.17
Fe_2O_3	1.89	0.57
CaO	0.33	1.98
MgO	0.23	0.01
H_2O^+	1.16	0.11
Others		0.42
Total	100.23	98.33

Table 1-1: comparison of compositions of grey (31 samples) and yellow (64 samples) monazites. From Rosenblum and Mosier (1983).

et al.,1989); Brittany (Donnot et al.,(1973)) or the shaly horizons of interlaminated shale/sand sequences, probably distal turbidites (Wales (Milodowski and Zalasiewicz, 1991) and Rwanda (M.Laval, pers. comm.)). Some organic carbon is frequently present.

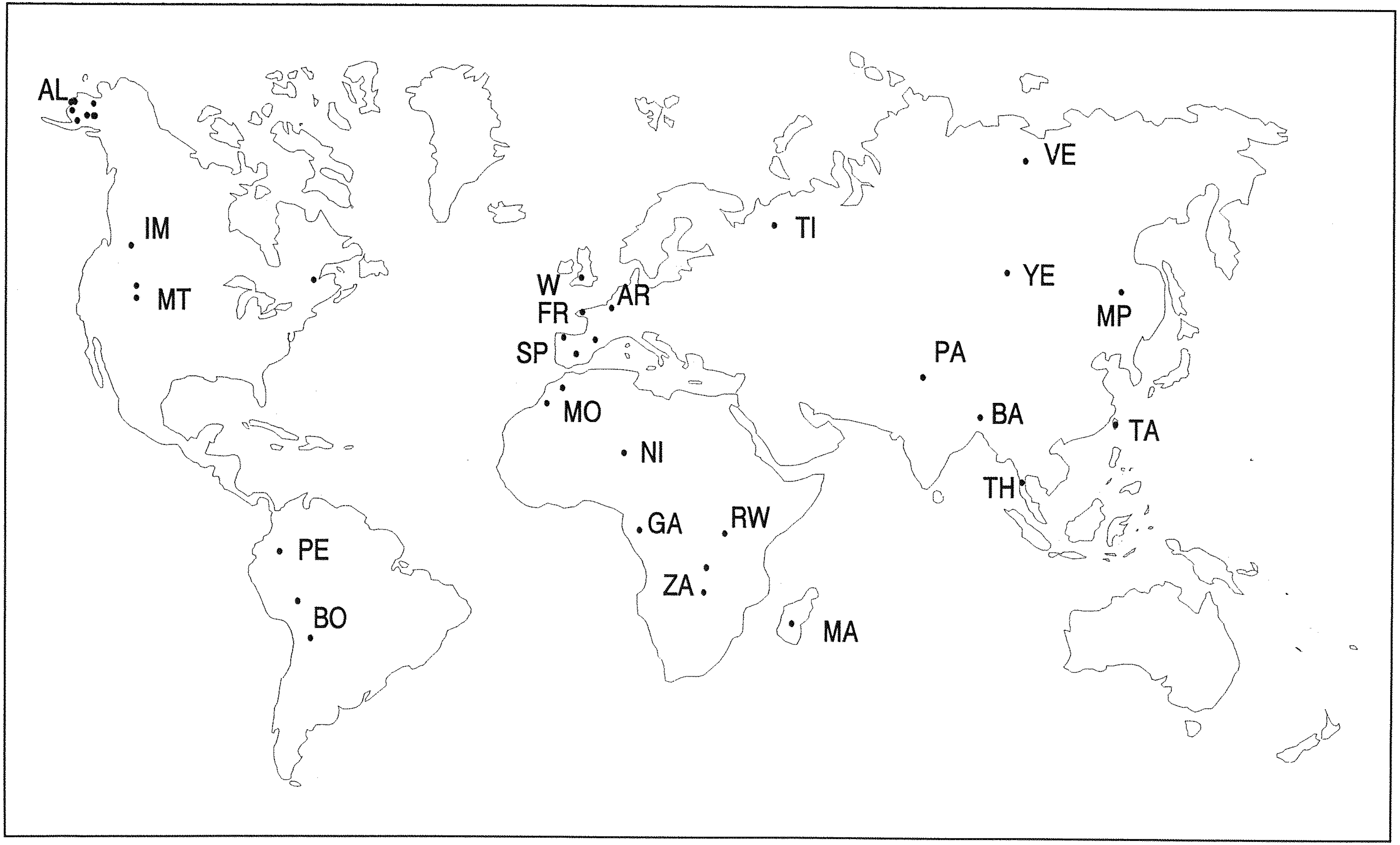

Figure 1-1: Worldwide occurrence of grey monazite(after Rosenblum and Mosier, 1983).AL: Alaska; MT: Montana; IM: Idaho - Montana; PE: Peru; PA: Pakistan; BA: Bangladesh; TH: Thailand; FR: France; W: Wales; AR: Ardennes; SP: Spain; MO: Morocco; NI: Niger; RW: Rwanda; GA: Gabon; ZA: Zaire; MA: Madagascar; TI: Timan; VE: Verkhoyan'e; YE: South Yenesei; MP: Maritime Province; TA: Taiwan; QU: Quebec; BO: Bolivia.

1.1 Previous Studies

Because of its high density and durability in the sedimentary cycle, grey monazite is a common constituent of alluvial panning concentrates. The majority of the early published descriptions refer to alluvial material (reviewed in Rosenblum and Mosier, 1983). Rosenblum and Mosier (1983) studied Alaskan panning concentrates from the USGS collections, and discovered that a high proportion of them contained thitherto unnoticed quantities of monazite. They concluded, on the basis of a spatial association with granites, that the monazites were the product of contact metamorphism.

In the review of Pouit and Laval (1990), only six instances of grey monazite identified *in situ* could be cited: Brittany (Donnot et al., 1973); Belgium (Burnotte et al., 1989); Wales (Read et al., 1987); The Idaho-Montana border (Huebschman, 1973) and two occurrences in Siberia (Isailev and Solovleva, 1974; Serdyuchenko and Kochetkov, 1974). To this list may now be added Rwanda and the French Pyrenees (Laval et al., 1993) and Central Spain (this study). In addition, Milodowski and Zalasiewicz (1991) have made a detailed study of the Welsh monazites.

USA: Idaho - Montana

Huebschman (1973) reports the presence of grey monazite in fine silt layers within massive quartzites of the Precambrian Prichard Formation (IM, figure 1-1). The silt layers are rich in organic carbon and contain pyrrhotite; they can be traced laterally for hundreds of kilometers. The metamorphic grade is greenschist facies. The monazites are incidental to Huebschman's (1973) study and are not described in detail. No phosphate-enriched horizons are described, although it is inferred by Huebschman (1973) that phosphate was derived from the organic material.

Siberia

Israilev and Solovleva (1974) describe grey monazite occurrences in a thick sequence of Permo-Carboniferous sandstones, shales and siltstones from the Verkhoyan'e region of Northern Siberia (VE, figure 1-1). Monazite is present throughout the series, several thousand metres in thickness, but only in the fine-grained shale facies. The nodules are authigenic, with inclusions of the same fine-grained detrital minerals which are found in the host shales. The growth of the monazites predates the cleavage. The levels which contain monazite are rich in organic carbon (up to 2.2%) but relatively poor in phosphorus compared to the monazite-poor levels, suggesting a possible mobilisation of phosphorus to form monazite.

In the Timan Mountains area of the Urals (Ti, figure 1-1), grey monazites are reported *in situ* in Devonian to Silurian rocks and in schists of middle Proterozoic age (Serdyuchenko and Kochetkov, 1974). No details are given.

Brittany

Donnot et al. (1973) studied grey monazites in the Grand Fougeray area, 50km south of Rennes. The host rocks are black shales of Lower Ordovician age, metamorphosed to the upper anchizone. They are the lateral equivalents of the monazite-bearing rocks in Spain, with the greatest amount of monazite in the shales of Llanvirn age overlying the Armorican quartzites. The nodules are apparently authigenic, lie at an oblique angle to bedding and cleavage, and pre-date the cleavage. The host rocks are iron-rich, depleted in calcium and not noticably enriched in phosphate. Donnot et al (1973) suggest that the monazites formed diagenetically via a precursor of rhabdophane (a hydrated REE phosphate) at low temperature which later dehydrated to form monazite.

Ardennes, Belgium

Figure 1-2 shows the distribution of grey monazite localities in Belgium. The only detailed petrographic work that has been published is that of Burnotte et al. (1989) in the Cambro - Ordovician Stavelot massif. Monazites are hosted by black phyllites of turbiditic origin, interbedded with phosphatic microconglomerates. The stratigraphy is not described in detail.

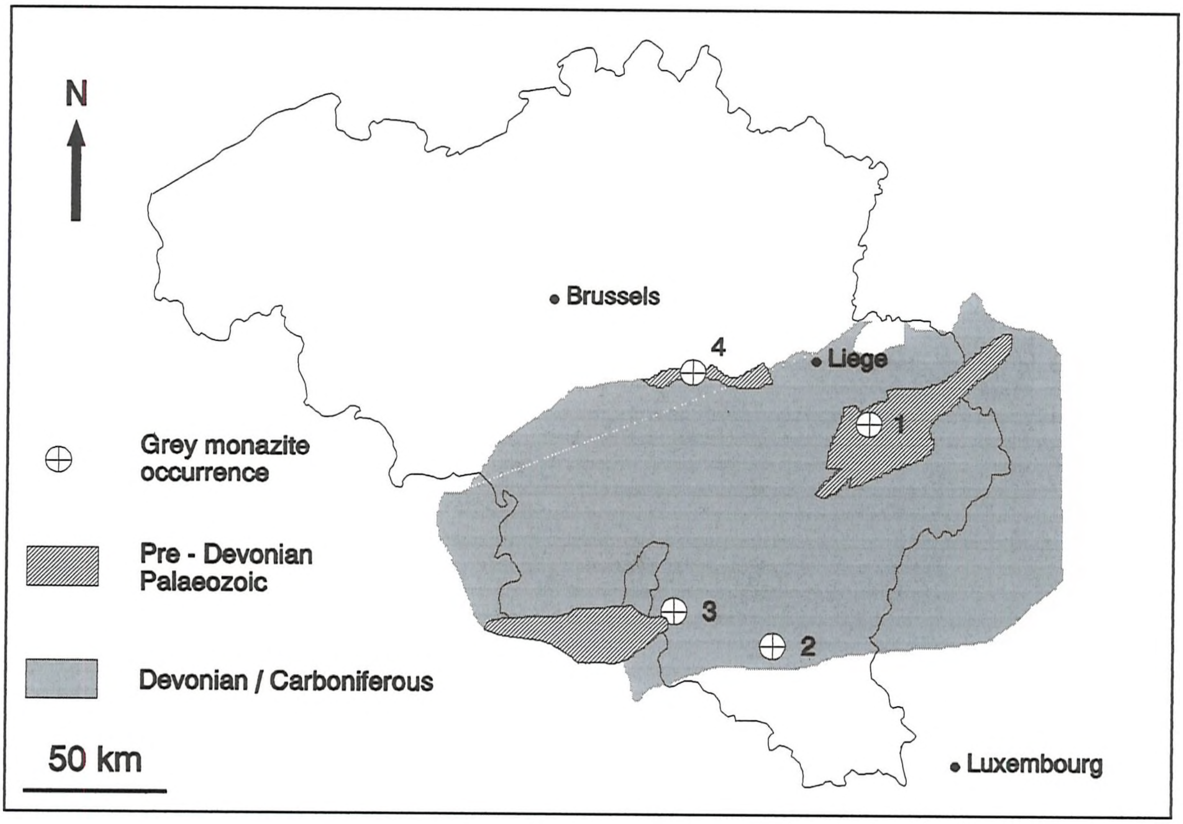

Figure 1-2: Grey monazite occurrences in Belgium (after Burnotte et al, 1989). 1 = Stavelot massif (Burnotte et al, 1989); 2 = Neufchateau (Limbourg, 1986); 3 = Rocroi massif (Nonnon, 1984); 4 = Brabant massif (Nonnon, 1989).

Burnotte et al. (1989) draw the following conclusions:

1. The host rocks are black shales with flat shale-normalised REE patterns, metamorphosed to the anchizone.
2. Monazites are authigenic, pre-cleavage, with aligned fabrics of inclusions parallel to the long axis of the ellipsoidal nodule.
3. Monazites have strongly light-REE enriched patterns with no Eu anomaly relative to the host shales.
4. For monazite formation, an anomalous concentration of phosphate was required in the same lithological sequence. Although monazite only contains 3% of the whole-rock phosphorus, Burnotte et al. (1989) argue that the bulk of this was immobile during diagenesis and so unavailable to form the nodules.
5. Their model envisages fluids originating from the dewatering of mudstones during burial which first scavenge phosphorus from enriched horizons, then

> pass through REE-bearing shales. REE are desorbed from clay minerals as phosphate complexes, transported a short distance, and precipitated as monazite.

It is noteworthy that, of the Belgian locations, only the Stavelot area studied by Burnotte et al. (1989) contains phosphate-enriched horizons.

Nonnon (1989) describes *in situ* monazites from slates of Ordovician age in the Brabant massif. The textures he describes (oriented inclusion fabric, pressure shadows around the nodule, cleavage at a high angle to the inclusion fabric) are identical to those reported by other workers (Burnotte et al.,1989; Milodowski and Zalasiewicz, 1991; Read et al, 1987). However, Nonnon (1989) concludes, on the basis of the aligned fabric of the inclusions, that the Brabant nodules are syn-metamorphic and cannot be diagenetic. It seems likely that he is mistaking the early diagenetic compaction-induced fabric for a higher grade metamorphic cleavage.

French Pyrenees

Lacomme et al. (1993) report on monazites from the Arize catchment in the eastern Pyrenees. Ordovician mudrocks have undergone regional metamorphism from sericite-chlorite grade through to migmatites; grade increases progressively to the south. Alluvial monazites are present in the stream sediments only up to the biotite zone, disappearing at around the andalusite isograd (figure 1-3). Seen in thin section, *in situ* grains are smaller than average, with an embayed morphology suggesting they might be unstable. They exhibit the typical abundant inclusions and pre-cleavage textural relations.

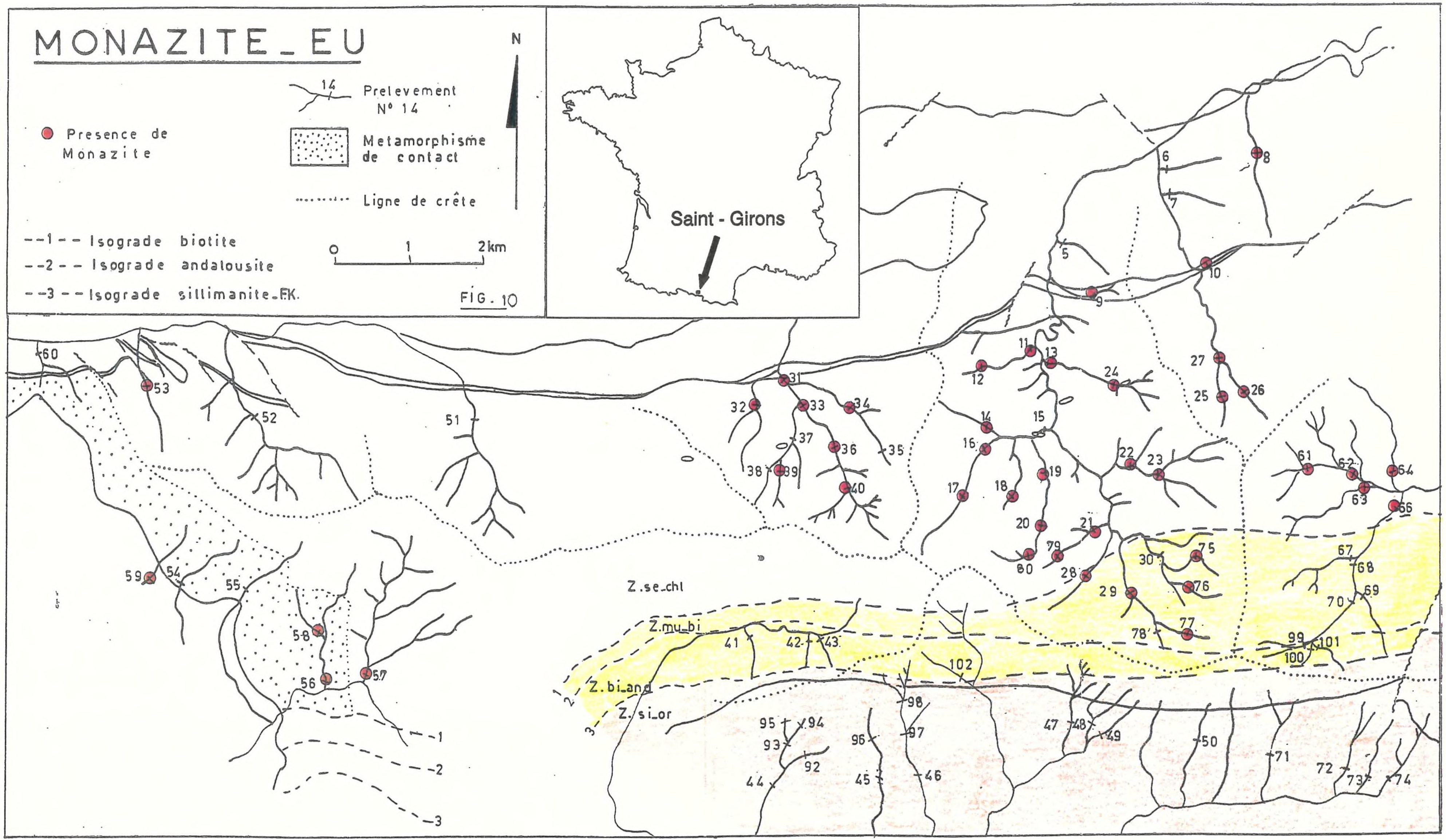

Figure 1-3: Results of an alluvial panning survey in the French Pyrenees, showing the apparent disappearance of grey monazite above the andalusite isograd. Note that monazite appears to be present within the granite contact aureole to the west. From Lacomme et al., (1993).

Wales

Alluvial grey monazite was initially identified in Wales from Ce anomalies in panning concentrates (Cooper et al., 1983). Read et al. (1987) describe concentric zoning in this material, with La, Ce enriched rims and Nd, Sm, Dy enriched cores. They note the lack of a Eu anomaly with respect to the host shale, and describe two distinct sorts of chondrite-normalised REE pattern. The cores of the nodules have light-enriched patterns which peak at samarium, while the rims have light-enriched patterns which show a steady decrease in abundance from La to Lu. The genetic model of Read et al. (1987) is based on *in situ* recrystallization of detrital yellow monazite, although they offer no explanation for the low thorium and high europium content of the grey monazites.

The most detailed study of grey monazite published to date is by Milodowski and Zalasiewicz (1991), who describe monazite nodules forming *in situ* in turbidites of

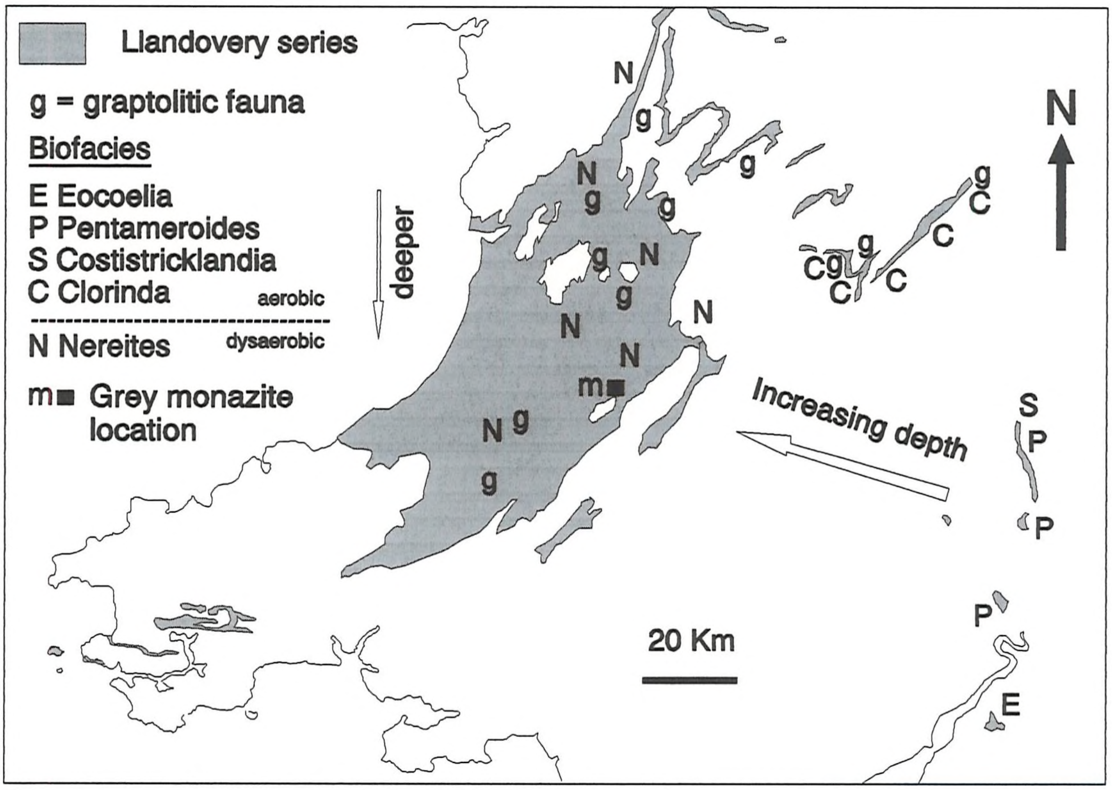

Figure 1-4: Location of grey monazites from Central Wales (Milodowski and Zalasiewicz, 1991), with biofacies zones after Smith (1987).

upper Llandovery age in central Wales (figure 1-4). The rocks were deposited on a continental shelf, deepening to the west, in about 500m to 1000m water depth (Smith, 1987). The area where the monazite-bearing turbidites occur (figure 1-4) corresponds approximately to the oxic/anoxic boundary as deduced from biofacies evidence by Smith (1987).

The typical sequences studied by Milodowski and Zalasiewicz (1991) are cyclic units consisting of distal turbidite sandstone fining upwards into an associated turbidite mudstone, overlain by a thin layer of hemipelagite (figure 1-5). They were able to demonstrate:

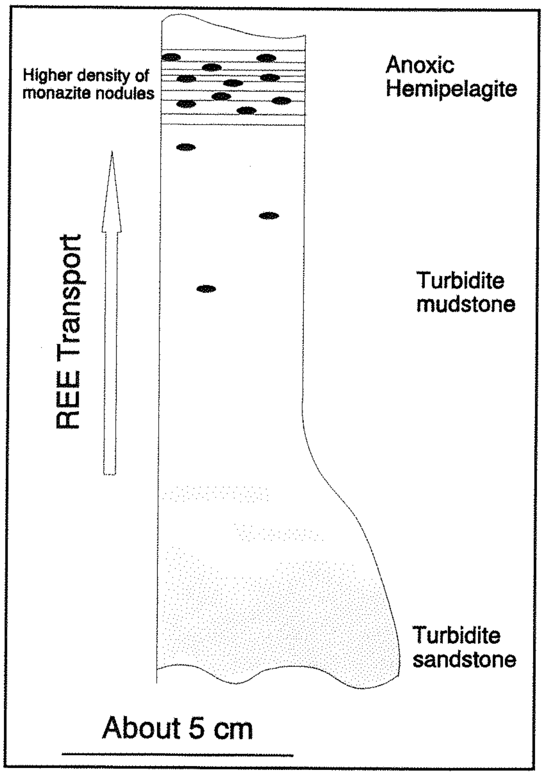

Figure 1-5: Lithofacies of monazite-bearing strata in Wales (after Milodowski and Zalasiewicz, 1991).

1. Monazites are more abundant in the hemipelagite layers than in the turbidites.
2. Monazite abundance in a hemipelagite layer is proportional to the thickness of the underlying turbidite layer.
3. The hemipelagites are light REE-enriched, and the turbidites show a complementary LREE depletion.
4. Textural evidence favours a post-compactional, pre-metamorphic origin for the nodules.

They confirm the concentric zoning reported by Read (1983), demonstrating that the heavy REE enrichment of the cores includes Sm and Gd. The model suggested by Milodowski and Zalasiewicz (1991) (figure 1-6) involves transport of REE as bicarbonate or organic complexes from the turbidite horizons into the hemipelagites, where they are preferentially concentrated as phosphates. This scavenging effect is linked to higher concentrations of organic matter in the hemipelagite horizons which release phosphate during diagenesis. The zoning is attributed to the greater mobility,

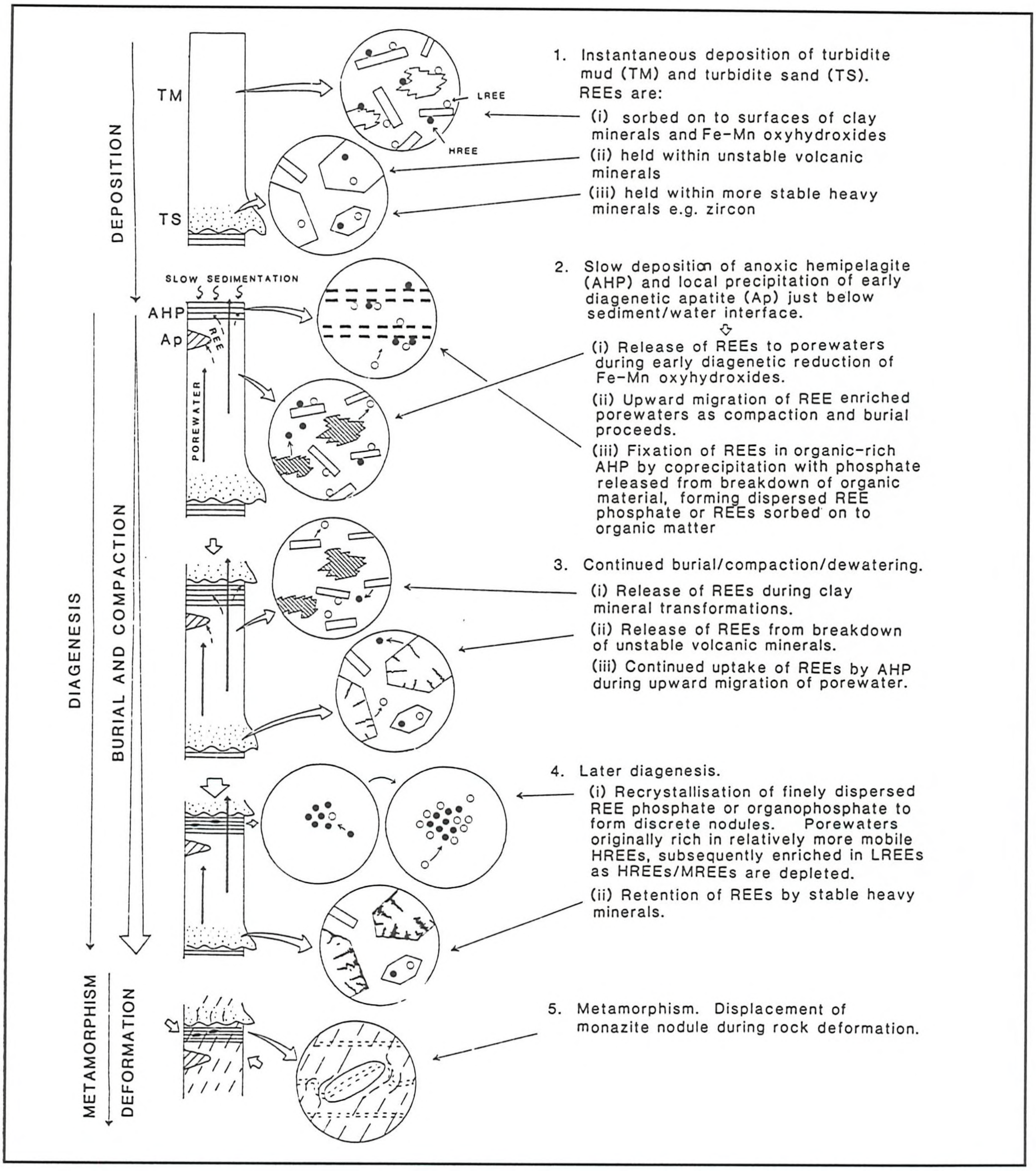

Figure 1-6: Summary model for the origin of Welsh monazite nodules (Milodowski and Zalasiewicz, 1991).

as organic or bicarbonate complexes, of the heavy REE which are therefore enriched in the earlier fluids; subsequently they become depleted in the source area leading to a later light REE enrichment.

1.2 Conclusions from previous work

There is an important degree of uniformity in the previous observations which may place constraints on any susequent model. The main points are:

1. **Size**. The grains range from a few tenths to about one millimetre, with the great majority about 500 μm. The exception is Kivu, Zaire, whence 7mm grains are known (Pouit and Laval, 1990).
2. **Shape**. The concretions are ellipsoidal in shape. There is apparently a crystallographic control (Rosenblum and Mosier, 1983; Milodowski and Zalasiewicz, 1991) with the long axis parallel to [100].
3. **Host rock**. The host rocks are invariably fine-grained sediments, either massive black shales (Spain, Belgium, Brittany) or the finer grained portions of turbidite sequences (Wales, Rwanda). They are often rich in iron and organic matter, and sometimes contain phosphatic horizons. The metamorphic grade is always of greenschist facies or lower. Rosenblum and Mosier (1983), on the basis of their widespread alluvial survey, suggest that grey monazite is not stable at higher grades. This conclusion is borne out by the recent work of the BRGM (Lacomme et al., 1993).
4. **Structural relations**. In all the *in situ* studies, grey monazites are seen to pre-date metamorphic cleavage formation. Observed textures of the silicate inclusions suggest a post-compactional origin.
5. **Inclusions**. The nodules always contain abundant inclusions of silicate minerals similar to those in the host rock.
6. **Chemistry**. The REE are always zoned with the same sense: La and Ce enriched in the rims, Sm and Nd in the cores.
7. **Age.** Monazite has not been found in any sediments younger than Permian in age (Phosphoria formation, Montana).

Possible models of monazite formation, taking into account these conclusions, are considered in chapter 6.

1.3 Aims and methodology of this study

This study was originally associated with an EEC raw materials R & D programme investigating grey monazite occurrences in Belgium, France, Spain and Rwanda (Ortega, 1993). The University of Southampton was in partnership with BRGM (France), ULB (Brussels University), Almaden Mining (Spain) and Idrogeo (Italy). The other partners were concentrating mostly on the identification and evaluation of alluvial deposits in Belgium, Spain and Rwanda. The present study is concerned with the source rocks of such placer deposits; it seeks to identify monazites *in situ*, and to investigate the mechanism by which they are formed.

The Navas de Estena area of South-Central Spain in the Montes de Toledo was chosen for close study because:

1. *In situ* monazites had recently been discovered there by Minas de Almaden.
2. Monazite is relatively abundant in the area.
3. The metamorphic grade is low, with relatively little deformation.
4. It is possible to examine a ≈ 500m thick section of monazite - bearing shales, allowing the study of variations with depth as well as laterally.
5. Detailed sedimentological logs were available for some of the monazite-bearing sections.

A programme of detailed petrographic and geochemical work was planned to characterise the monazites and their host shales. The aim was to integrate these data with the available sedimentological and other information in order to produce a model of monazite genesis.

1.4 Geological setting of the field area

Lower Paleozoic rocks are exposed in the cores of numerous synclines, associated with Hercynian folding, over a wide area of central Spain (figure 1-7. 1-8). The Armorican Quartzite, a thick succession of massive quartzites, Arenig in age, with 1-2m thick bedding, is exposed regionally and marks the culmination of a major regressive cycle. The Llanvirn was marked by a regional transgression leading to the deposition of several hudred metres of marine shales across a broad shelf area covering most of the Central Iberian Zone . Minor regressive cycles were superimposed on this major event, leading to the deposition of thin sandy horizons (Brenchley et al., 1986). The most significant was in Upper Llanvirn/Llandeillan time, the Monte da Sombadeira formation, and corresponds to a regional fall in sea level (Brenchley et al., 1986). In a detailed sedimentological study, Brenchley et al. (1986) deduced that the mid Ordovician shelf dipped very gently (< 0.1°) to the north. The palaeo-shoreline was approximately parallel to the Ossa-Morena shear zone (figure 1-8). The sandstone units are inferred to have derived from storm wave deposition; they thin to the north and are absent or of very reduced extent in the more distal parts of the shelf. The Navas de Estena area is typical of the more distal facies; the coarsest material is silt sized and no wave-derived bedforms are seen after the first few metres of mudstones (Gomez, 1991).

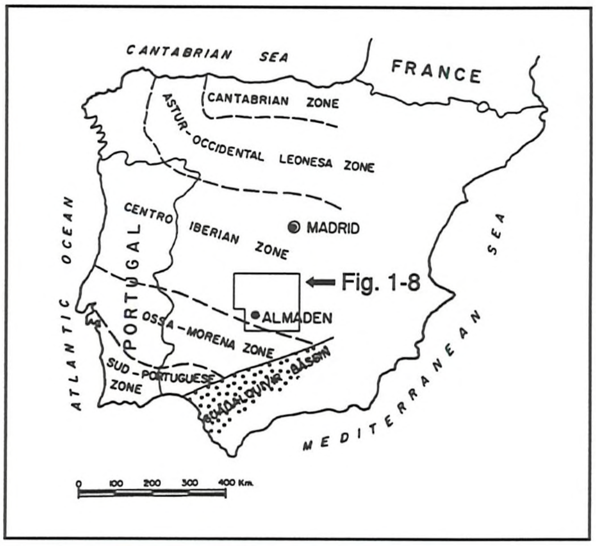

Figure 1-7: Location map showing tectonic overview of the Iberian Peninsula.

Rabano (1989) established regional associations of trilobite fauna which occur in zones complementary to the sedimentological zones of Brenchley et al. (1986). He places the Montes de Toledo area in the most distal part of the shelf, with water depths of sixty metres or more.

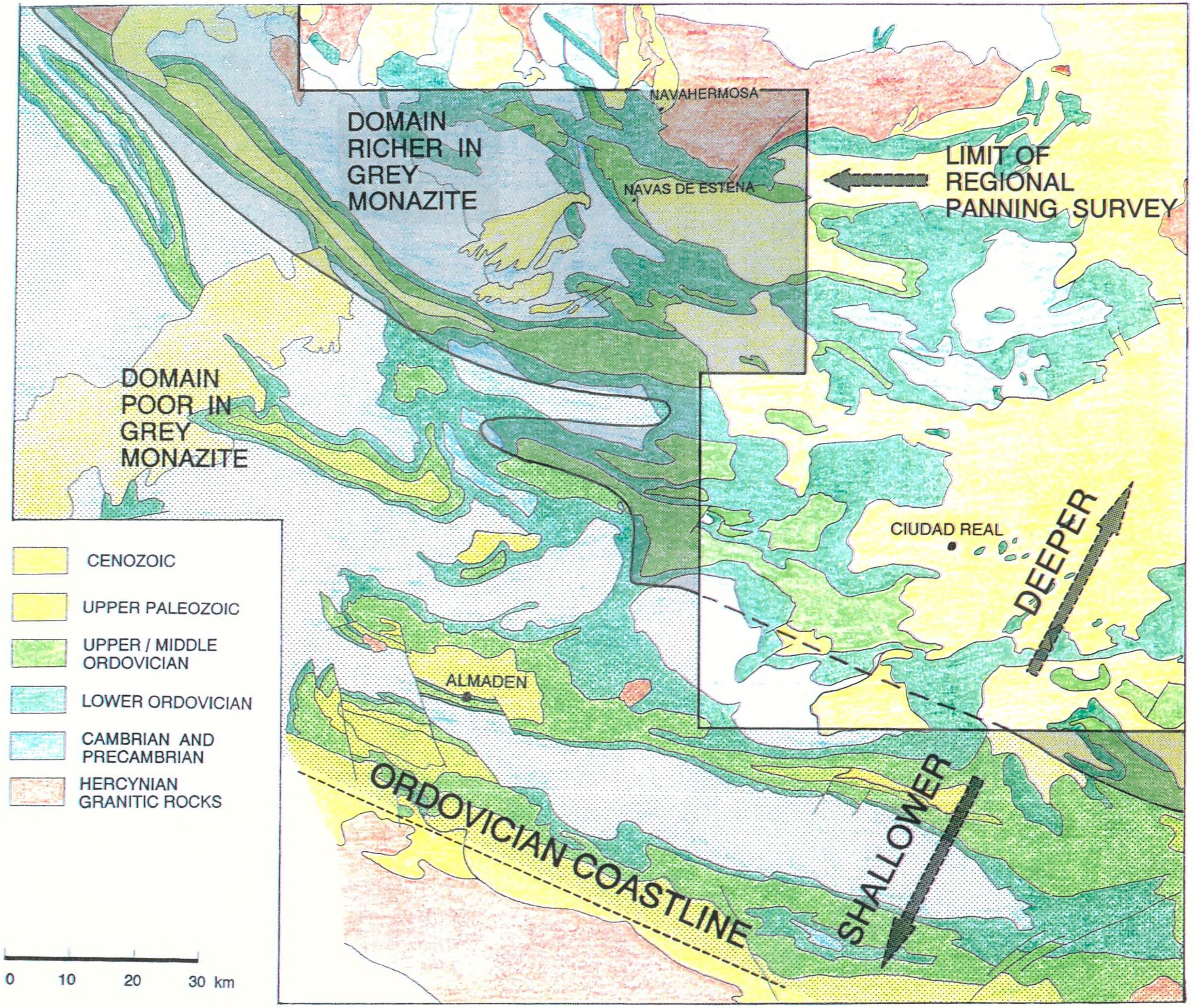

Figure 1-8: Simplified geological map showing the distribution of Lower Palaeozoic rocks in central-southern Spain. Paleogeography is inferred from Brenchley et al. (1986) and Rabano (1989). The shaded areas depict the results of an alluvial panning survey by Almaden Mining (J.M.Amor, Minas de Almaden, personal communication).

Regional exploration by Almaden Mining, using alluvial panning, shows a greater abundance of monazite in pan concentrates in the more northern part of the area (figure 1-8), which suggests that the palaeodepth may be important. This finding is in agreement with the location of monazites in the Welsh basin (figure 1-3). Like the Welsh rocks, the monazite-bearing shales of Lower Llanvirn age in the Navas de Estena area contain graptolites and are close to the oxic / anoxic boundary.

In the Navas de Estena syncline (figure 1-9), the lowest unit exposed is the Armorican Quartzite, which has a thickness of about 400 m. Towards the top, occasional shale laminae are found, and these become more abundant up section. This unit of alternating shales and sands, locally called the Pochico Beds, is also about 400m thick; in turn it grades into more massive shales of the Calymene Formation, representing a rapid change to deeper water facies. In the Navas de Estena syncline, they attain a thickness of some 500m.

A section from the top of the Pochico Beds up through the first 400 m of Calymene shales at Valleleor (Fig. 1-9) was chosen for a detailed geochemical and petrological study. The sedimentary log (figure 1-10a) made by Minas de Almaden (Ortega, 1993; Gomez, 1991), shows little lithological variation, and is dominated by fine grained slates. The first 50 metres of section contain occasional thin silty layers exhibiting swaley-cross-stratification, indicative of deposition by storm waves (Gomez, 1991). Higher in the section, occasional silty layers fine and thin upwards; they are accompanied by an abundant fauna of trilobites and brachiopods. Higher still, there is a thick series of massive, graptolitic, dark grey shales, representing a low-energy, distal shelf environment. About 350 m above the base of the section, a series of silty horizons, 0.5 - 3m in thickness, occurs; they are ferruginized and very rich in shelly fauna. These condensed sections, or "hardgrounds", may represent relatively long periods of very slow sedimentation, probably linked to lower sea levels. They are laterally continuous and mappable; some of the more prominent are shown in figure 1-9. Although in outcrop (figure 1-11) they resemble the calcareous cemented hardgrounds of limestone areas (e.g. Sellwood, 1986), they are in fact siliceous (see chapter 2).

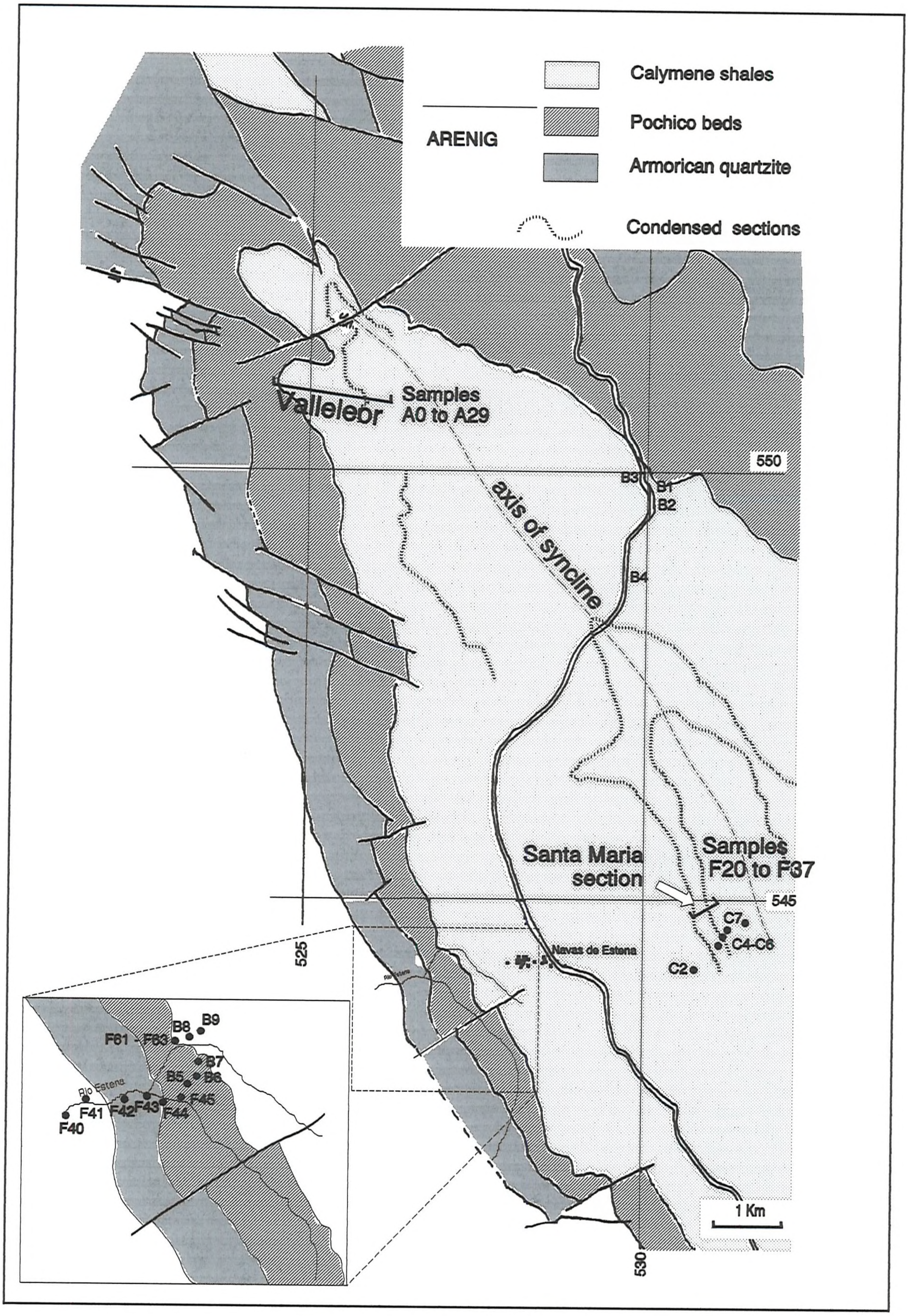

Figure 1-9: Geology of the Navas de Estena syncline, showing locations of samples referred to in the text. Condensed section horizons from Ortega (1993).

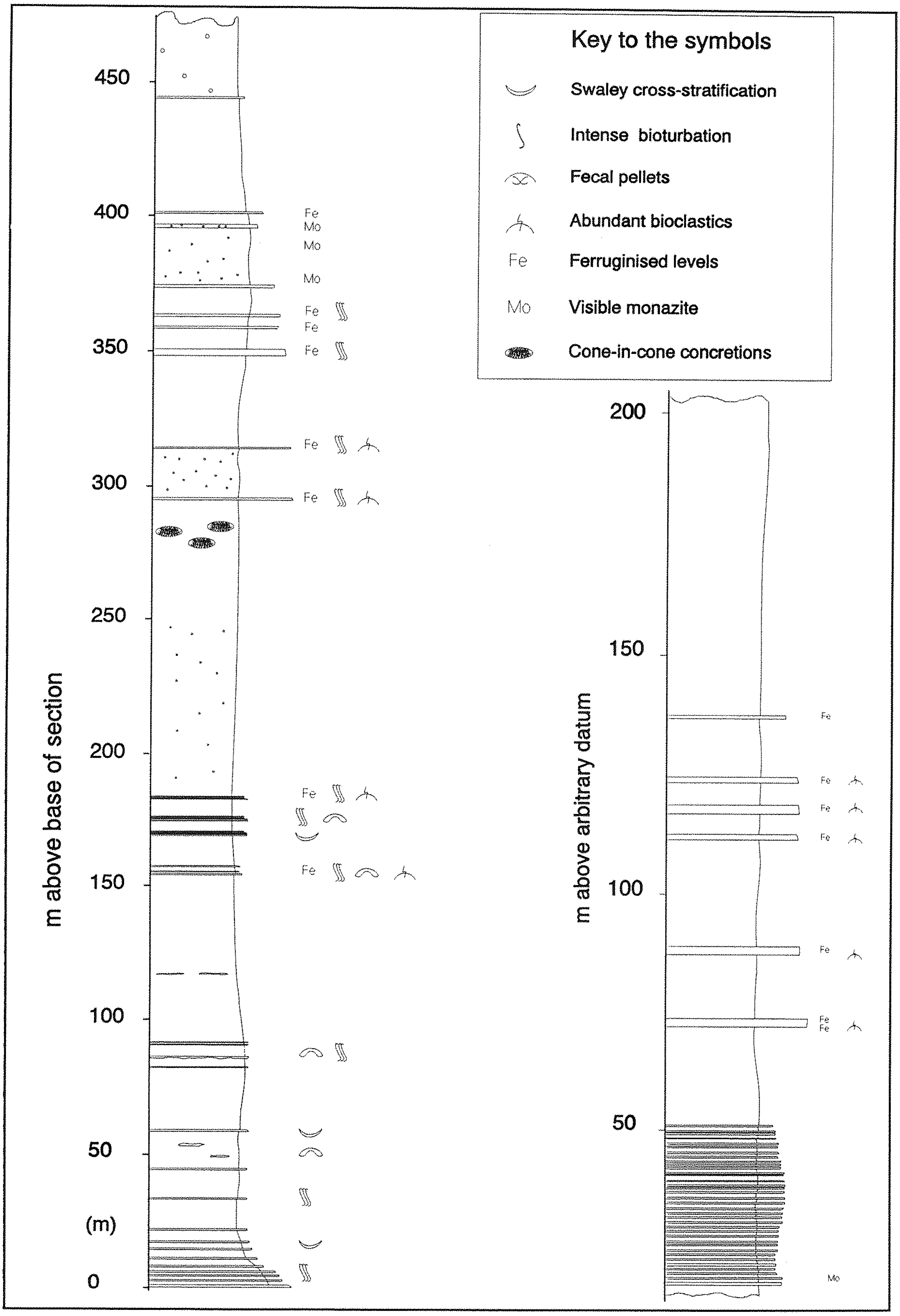

Figure 1-10: Sedimentary logs of the sections at Valleleor (a) and Santa Maria (b). After Gomez (1991).

Figure 1-11: View of the NW edge of the Navas de Estena syncline, looking south. Armorican quartzites (a) are overlain by the Pochico Beds (p) and the Calymene Formation (c).

Figure 1-12: Prominent "hardgrounds" weathering out as ridges in Calymene Formation shales. Santa Maria (figure 1-9).

A second section at Santa Maria (figure 1-10b; location in figure 1-9) was also studied in detail. This section features spectacular development of hardgrounds (figure 1-12). It is stratigraphically higher than Valleleor (see figure 1-9) and represents generally shallower conditions, with more abundant silty horizons. This section was chosen in particular to assess the relationship between monazite mineralization and the hardgrounds.

Chapter 2: Mineralogy and petrographic relationships of shales and monazites

2.0 Objectives

This chapter will describe the mineralogy and petrology of grey monazite concretions and their host shales, and will attempt to use textural and chemical data to place constraints on the timing and style of growth of the concretions.

2.1 Host shales

The monazite-bearing black shales of the Calymene Formation are dark grey and fine grained, with a well-developed cleavage. Iron staining on cleavage surfaces gives a yellow-brown colour in outcrop (figure 2-2(a)). Silicified, ferruginous nodules, frequently containing fossil trilobites or bivalves, are relatively common (figure 2-2(b)). Occasional thin silty horizons (figure 2-2(c)) give an indication of the bedding. Although outcrops may locally display open to tight folding, the larger

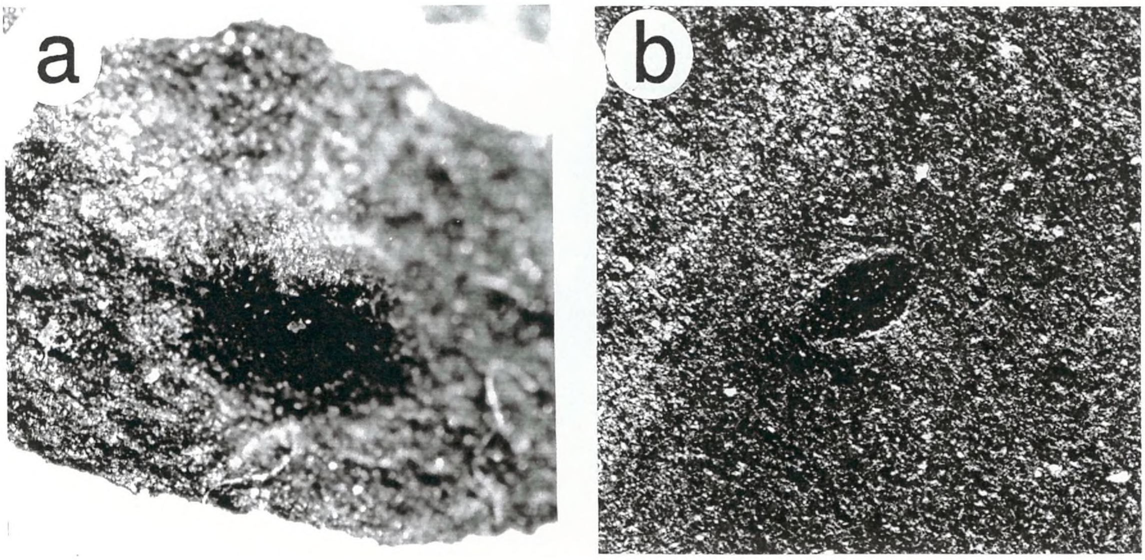

Figure 2-1: Appearance of grey monazite in hand specimen (a) and on a cut surface (b). Field of view = 3.5 mm (a) and 3.0 mm (b).

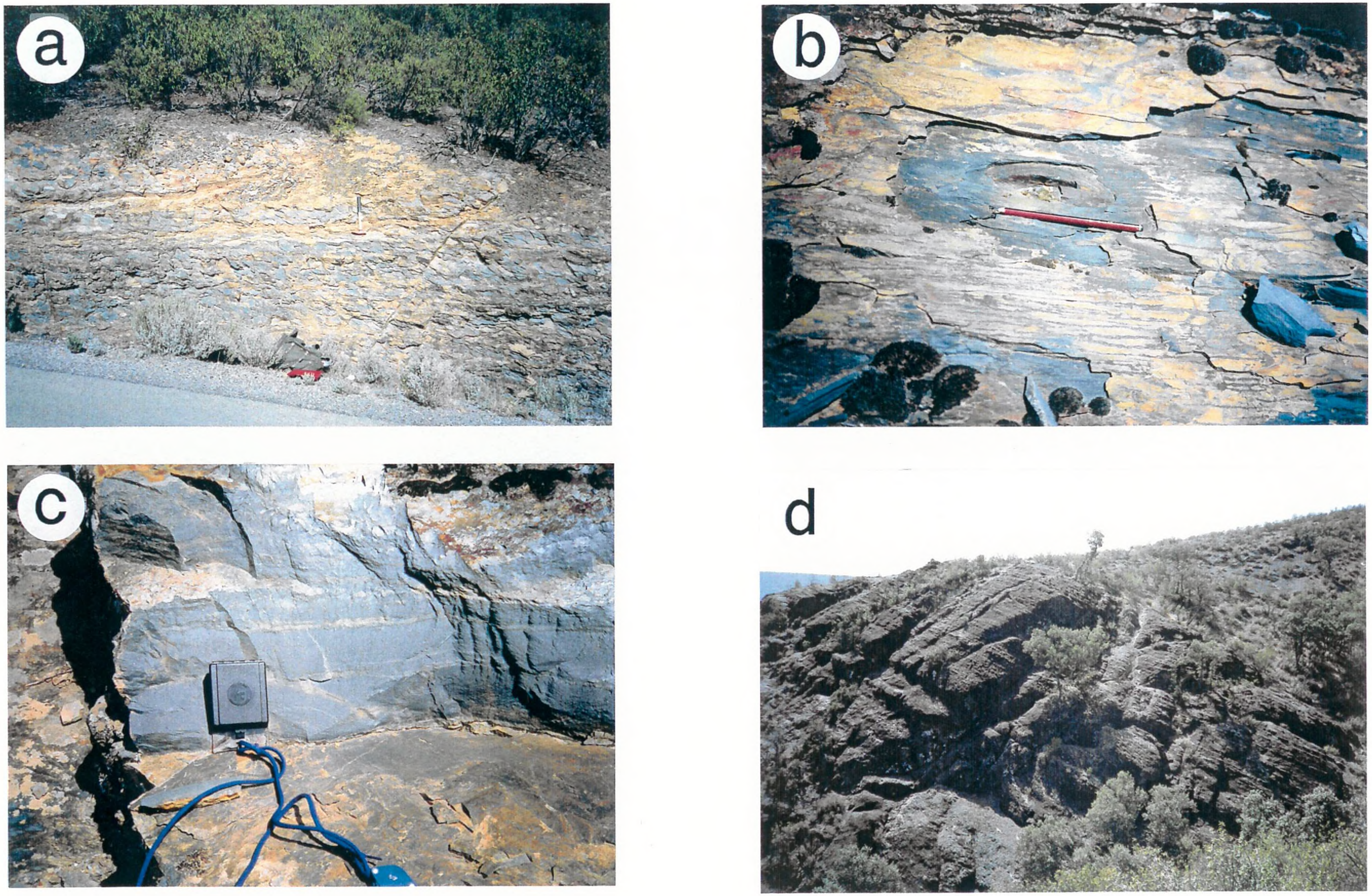

Figure 2-2: Calymene Formation in the field. (a): Typical appearance in outcrop, with ferruginised surfaces, fissile character, and absence of bedding. (b): Silicified nodule, frequently nucleated on bivalve shells. (c): Thin silty horizons in massive black shale, probably very distal storm sand layers. (d): Alternating shales and siltstones dipping towards the core of the syncline, with more typical massive shales above them. Las Cuevas area.

scale structure is relatively coherent, with strata dipping towards the core of the syncline at 30 to 40 degrees (figure 2-2(d)). In hand specimen, little internal structure is visible. Finely dispersed framboidal pyrite is often evident. Grey monazites are occasionally visible on smooth cleavage surfaces, where they weather out as small blebs (figure 2-1); in general, however, they are very difficult to spot in the field.

2.2 Metamorphic grade

Various indices of illite crystallinity have been proposed as indicators of the degree of low temperature metamorphism (reviewed in Kisch, 1987). The sharpening of the basal 001 diffraction peak is associated with the degree of transformation of illite-smectite to mica and is a function primarily of temperature. Other kinetic and chemical factors may influence the reaction, but provided burial is sufficiently prolonged, illite crystallinities potentially record the maximum metamorphic grade to which the rock has been subjected. Kübler (1967) defined the anchimetamorphic zone in terms of the width at half height of the 10 Å basal illite peak; his limits were 2.5 and 4.2 mm for the high and low grade boundaries, respectively. This translates to roughly 0.25° and 0.42° $\Delta 2\Theta$ (Kisch, 1987), although there is some confusion as to sample preparation techniques and scanning speeds.

The reflectance of organic material is another commonly used index of low temperature metamorphism. Organic reflectance is a measure of the degree of transformation of metastable organic matter into graphite. It is highly sensitive to temperature (Kisch, 1987; Suggate, 1982), and so is perhaps a more trustworthy paleothermometer than illite crystallinity. The majority of studies have been on vitrinite and other plant debris (reviewed in Teichmüller, 1987). In Lower Paleozoic rocks, where such material is absent, various microfossils can be substituted. Chitinozoa (Tricker *et al.*, 1992) have been calibrated against the vitrinite scale, and show good correlation and linearity, generally giving R_0 values about 0.5% higher.

Organic concentrates were prepared from six specimens from the Navas de Estena syncline by dissolution of the mineral components using HF and HCl. The residues were mounted and polished as described by Hillier and Marshall (1988). Two

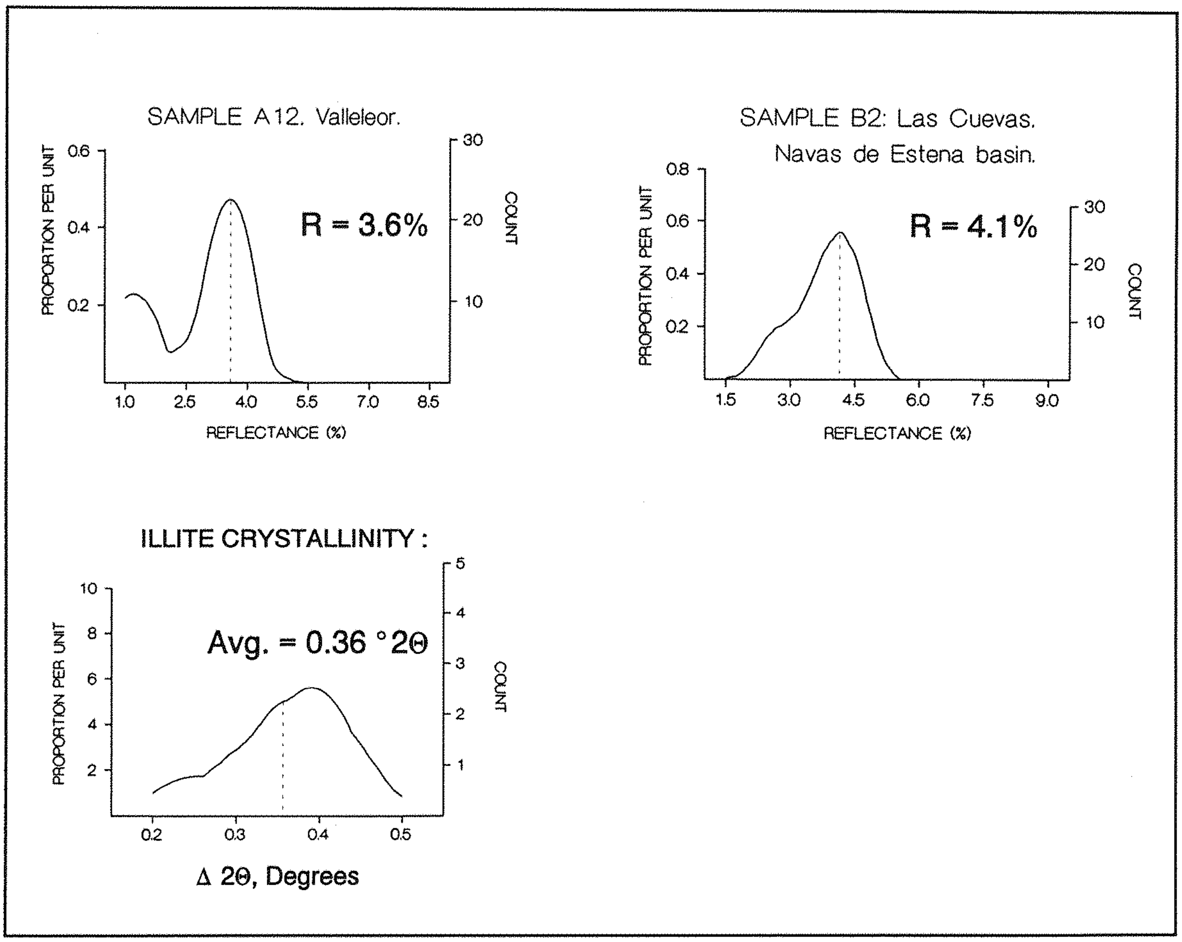

Figure 2-3: Indices of thermal maturation. Chitinozoan reflectance for shales B2 and A12, and illite crystallinity data for nine Navas de Estena shales.

specimens contained chitinozoan fragments; the reflectance was measured using a Zeiss UMSP microscope at 546nm with an oil immersion objective.

Results for the organic reflectance determinations and measurements of illite crystallinity are shown in figure 2-3. The mean value of 0.36° Δ2Θ for nine measurements of clay fractions of Navas de Estena shales places them in the anchizone. This compares with lower grade (diagenesis zone) values for the Calymene Formation found by Saupé *et al.* (1977), working in the Almaden area, 80 km to the south. The reflectance values determined in the present study were 3.6% (sample A12) and 4.1% (sample B2), equivalent to vitrinite values of 3.0% and 3.5%, respectively, according to the calibration of Tricker *et al.* (1992) (the bimodal distribution in sample A12 is caused by the inclusion of some amorphous organic matter in the measurements). The empirical formula of Barker and Pawlewicz (1986):

$$T_{max} = (\ln(R_0) + 1.4) / 0.0096$$

yields temperatures of 260 and 275°C for A12 and B2, respectively. Kisch (1987) places the boundaries of the anchizone at 2.5% and about 5% reflectance, corresponding to temperatures of 200-250 °C and 300°C, respectively. Since both illite crystallinity and organic reflection data indicate mid-anchizonal conditions, it is probable that the maximum temperature attained at Navas de Estena lay within this range.

2.3 Clay mineralogy of Calymene Formation

The clay mineralogy of the shales at Navas de Estena was investigated by X-ray diffraction (XRD) analysis. Sub- 2µm size fractions were prepared using standard techniques of suspension, repeated centrifugation and flocculation in magnesium chloride (Jackson, 1975). The clays were smeared onto glass slides and analysed using Cu-$K\alpha$ radiation after air-drying, glycolation (vapour pressure method), and heating to 375°C and 550°C. The resulting patterns are illustrated in figures 2-5 to 2-8. All the clay concentrates consist principally of mixtures of illite and chlorite. Środoń (1984) describes a methodology for the identification of illite, different

	Glycolated samples: peak positions				$\Delta_{002\text{-}001}$ (Glycolated)	BB1(°2Θ)	$\Delta_{002\text{-}001}$ (Air dried)	I_r	Mineral Identity
A0	-	8.85	17.72	26.70	8.88	1.44	8.90	1.66	I+ISII
A5	-	8.87	17.76	26.74	8.89	2.44	8.94	0.71	I
A8	3.34	8.86	17.74	26.68	8.88	2.80	8.90	1.23	I+ISII
A13	3.32	8.82	17.74	26.68	8.92	2.50	8.90	1.24	I+ISII
A16	3.38	8.84	17.72	26.68	8.88	2.60	8.90	1.01	I
A19	3.28	8.83	17.70	26.68	8.87	2.50	8.90	0.99	I
A23	3.32	8.84	17.70	26.72	8.86	2.70	8.92	1.12	I+ISII
A26	3.42	8.84	17.72	26.72	8.88	2.40	8.92	1.36	I+ISII
B2	-	8.84	17.72	26.72	8.88	2.50	8.96	1.40	I+ISII

Table 2-1: XRD peak data for illites and illite-smectites after Środoń (1984). See text for details.

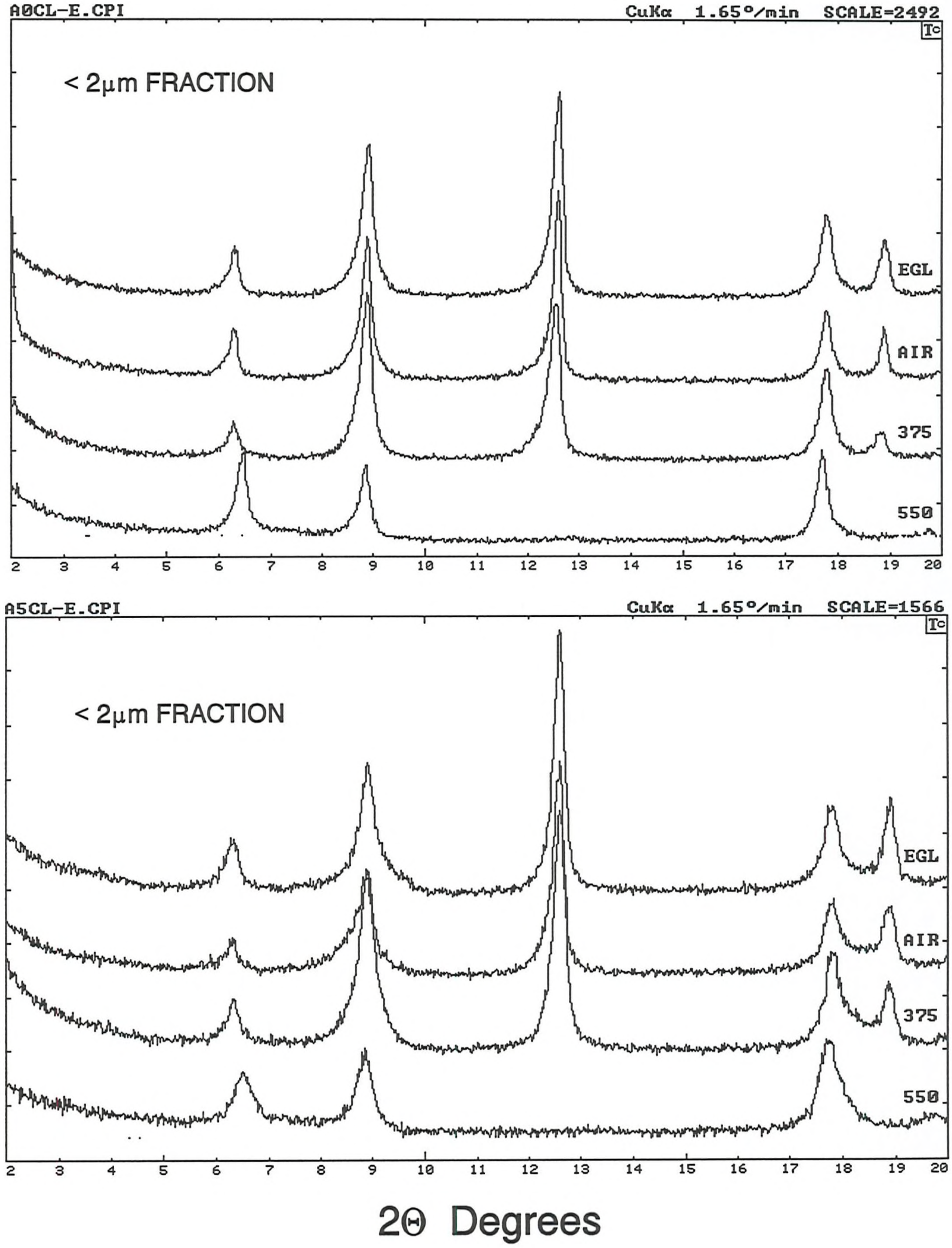

Figure 2-5: X-ray diffraction results for clay fractions of shales A0 and A5. See text for details.

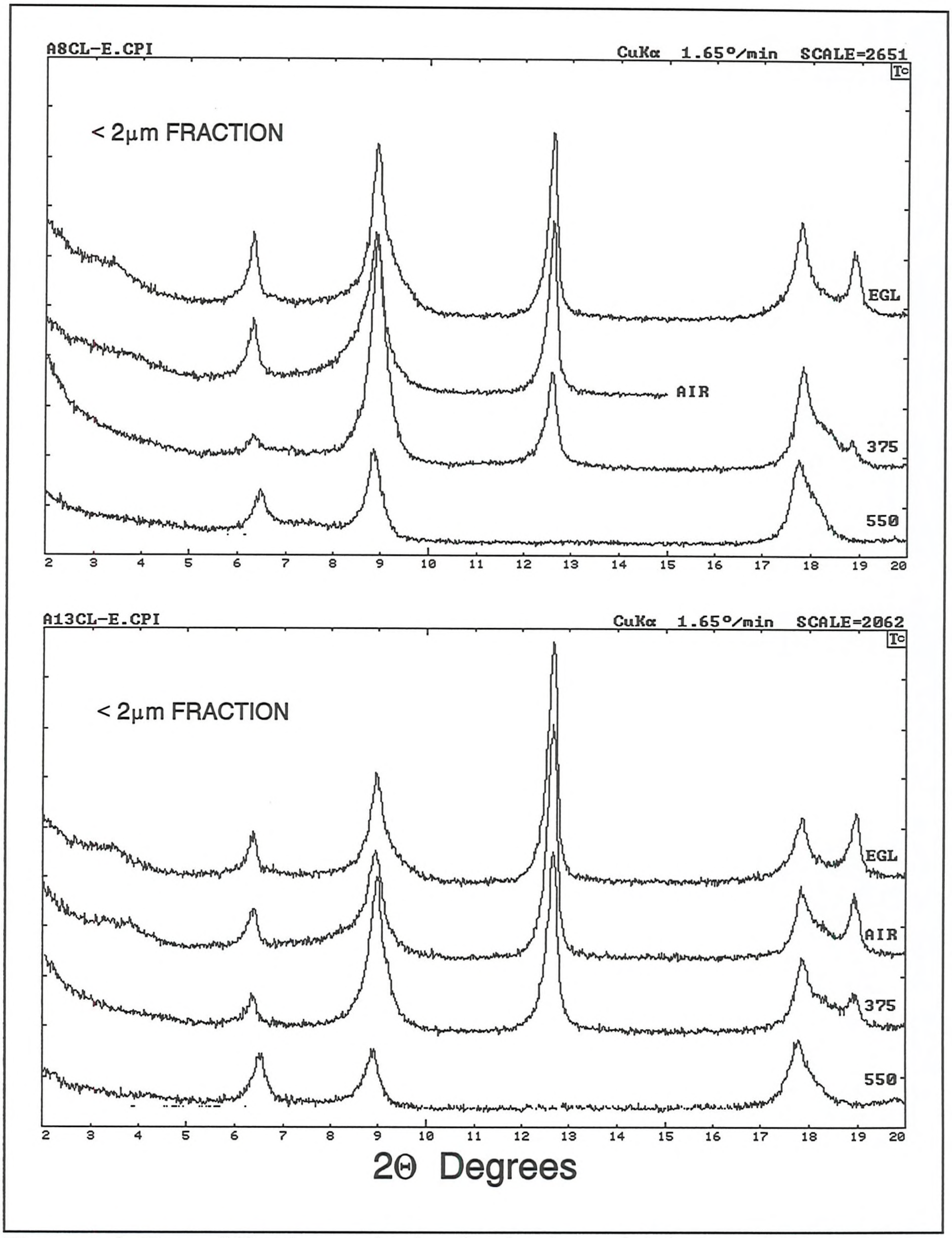

Figure 2-6: X-ray diffraction results for clay fractions of shales A8 and A13. See text for details.

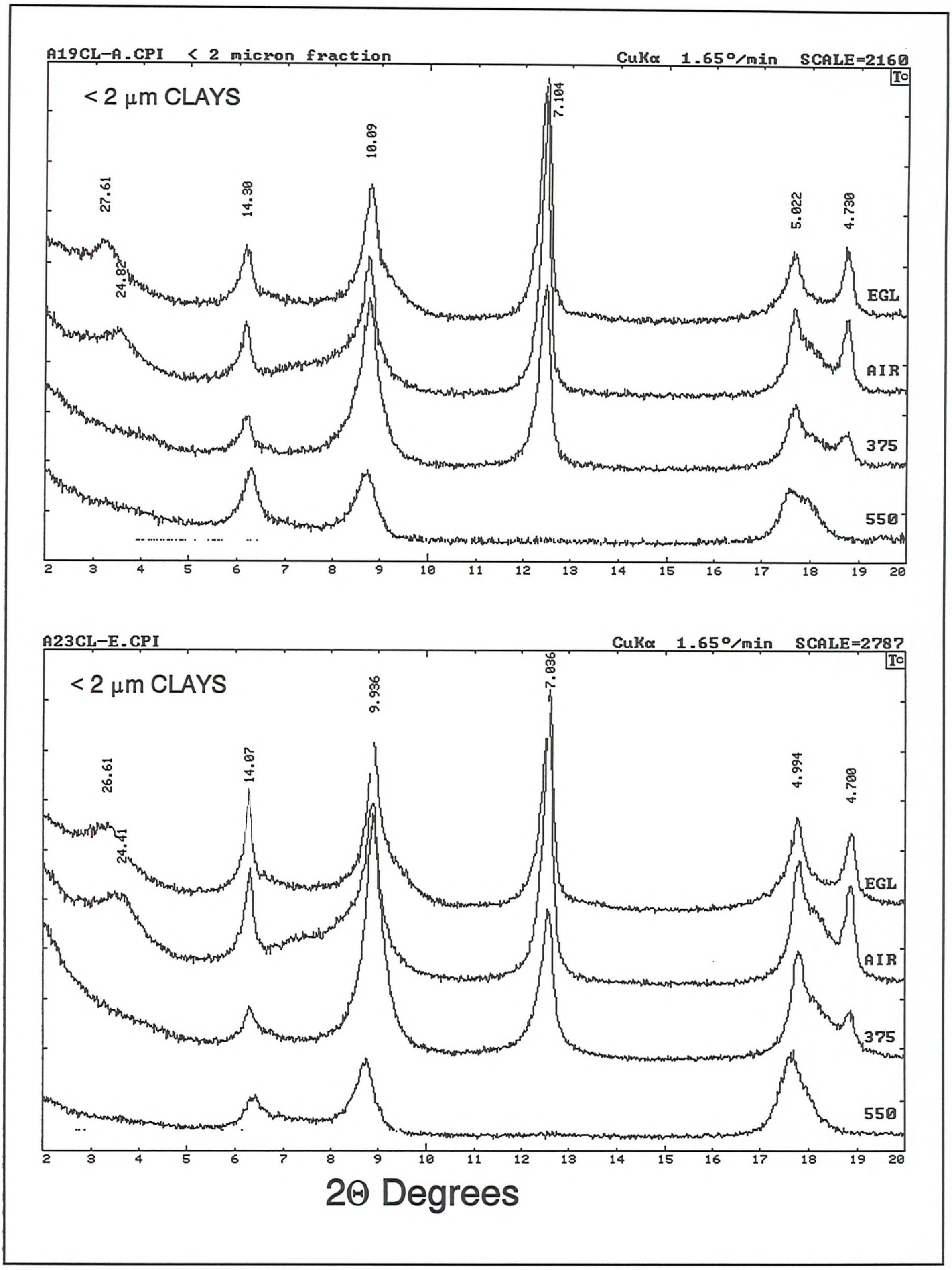

Figure 2-7: X-ray diffraction results for clay fractions of shales A19 and A23. See text for details.

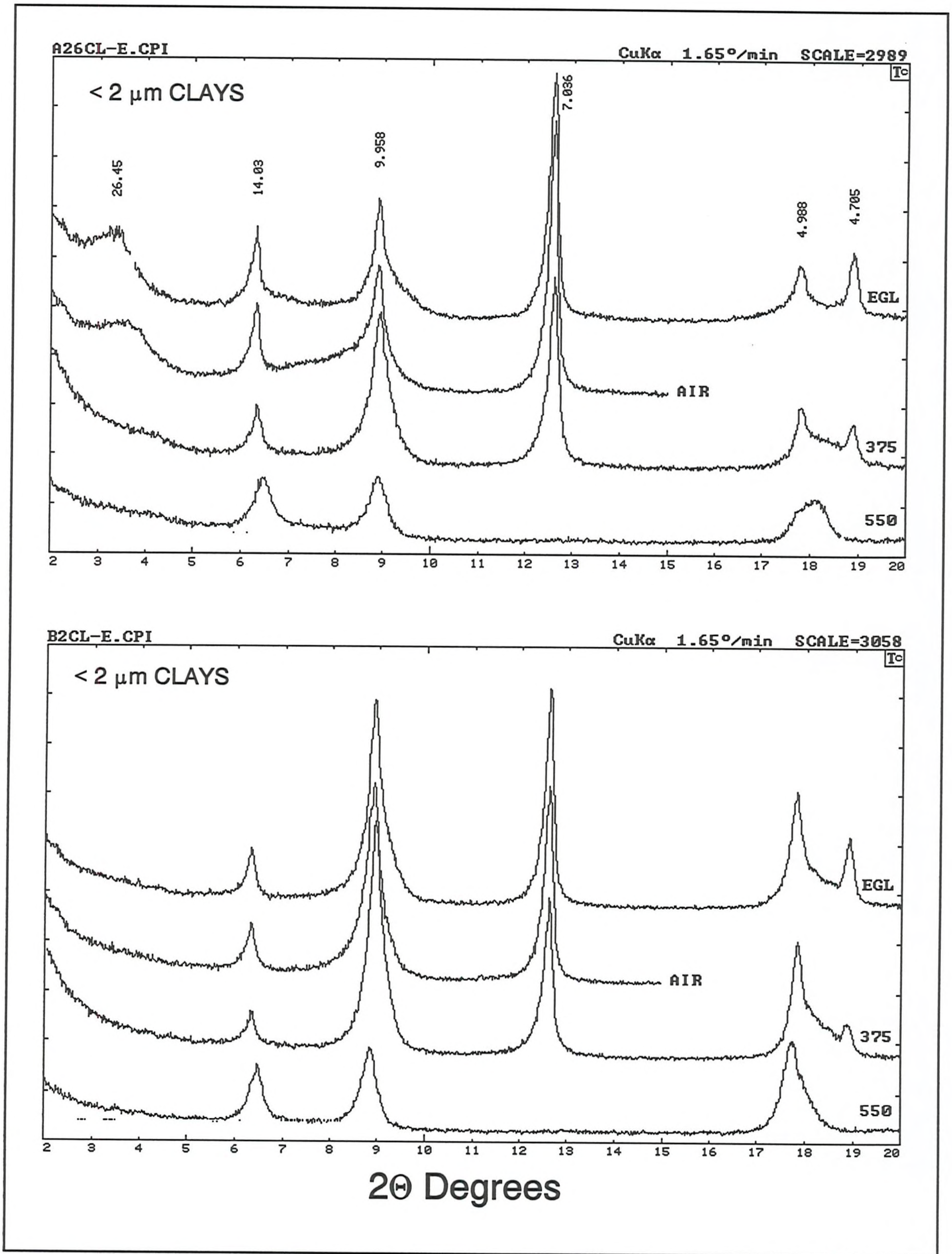

Figure 2-8: X-ray diffraction results for clay fractions of shales A26 and B2. See text for details.

illite-smectites, and mixtures of the two according to the XRD patterns of air-dried and glycolated material. Table 2-1 lists the diagnostic parameters for the nine specimens studied.

All the data plot as pure illites in figure 2-4 (figure 2 of Środoń, 1984). The spread to the left of the illite field is caused by the presence of small quantities of quartz in the clay fractions. The parameter I*r* is the ratio of 001 intensity divided by 003 intensity before and after glycolation. Values greater than one indicate the presence of small quantities of illite-smectite in illite-rich samples, as does a reduction in the spacing between the 001 and 002 peaks following glycolation. Six of the nine samples appear to contain a small amount (less than15%, but not more precisely quantifiable) of illite-smectite according to these criteria. The small values of BB1 (basal width of the 001 reflection) suggest this to be of the ISII type of layering (Środoń, 1984). The low-angle peaks at around 3.32 °2Θ correspond to a d-spacing of about 27.4 Å (glycolated) and 24.8 Å (air dried). Paradoxically, these peaks suggest the presence of an ordered IS type interlayered illite-smectite: allevardite in the sense of Velde (1985), or rectorite as defined by Bailey *et al.* (1982). In the data of Środoń (1984), occurrences of rectorite are characterised by much greater values of I_r and smaller values of $\Delta_{002\text{-}001}$ than are observed here. The explanation may lie in the fact that the superlattice phase is concentrated in the <0.1 μm fraction (figure 2-9).

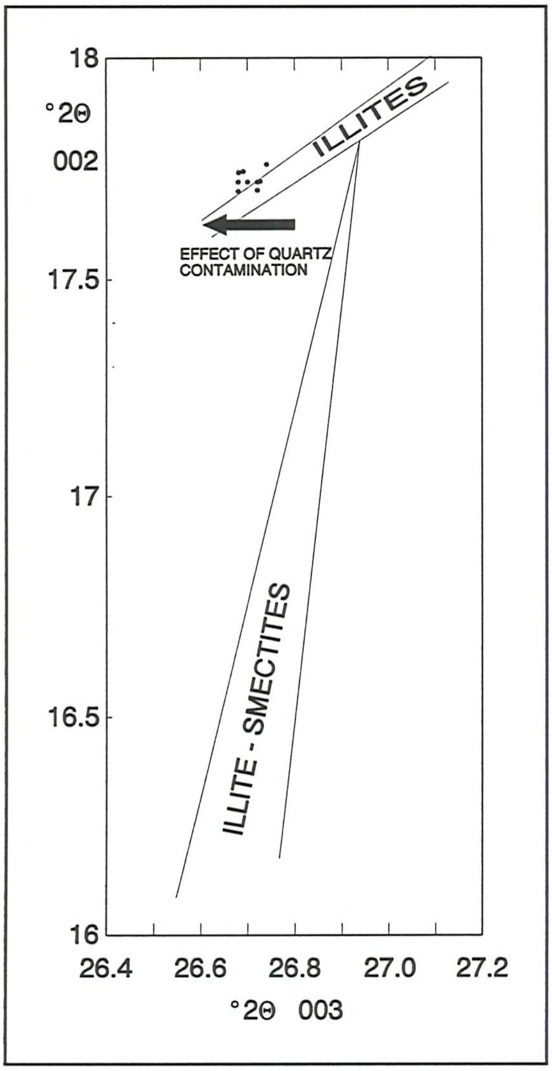

Figure 2-4: Data from table 2-1 plotted in the diagram of Środoń (1984).

The exact illite/smectite ratio cannot be estimated by the methods of Środoń (1980) because of the obscuring effect of chlorite peaks, but the peak at *circa* 29Å is strong

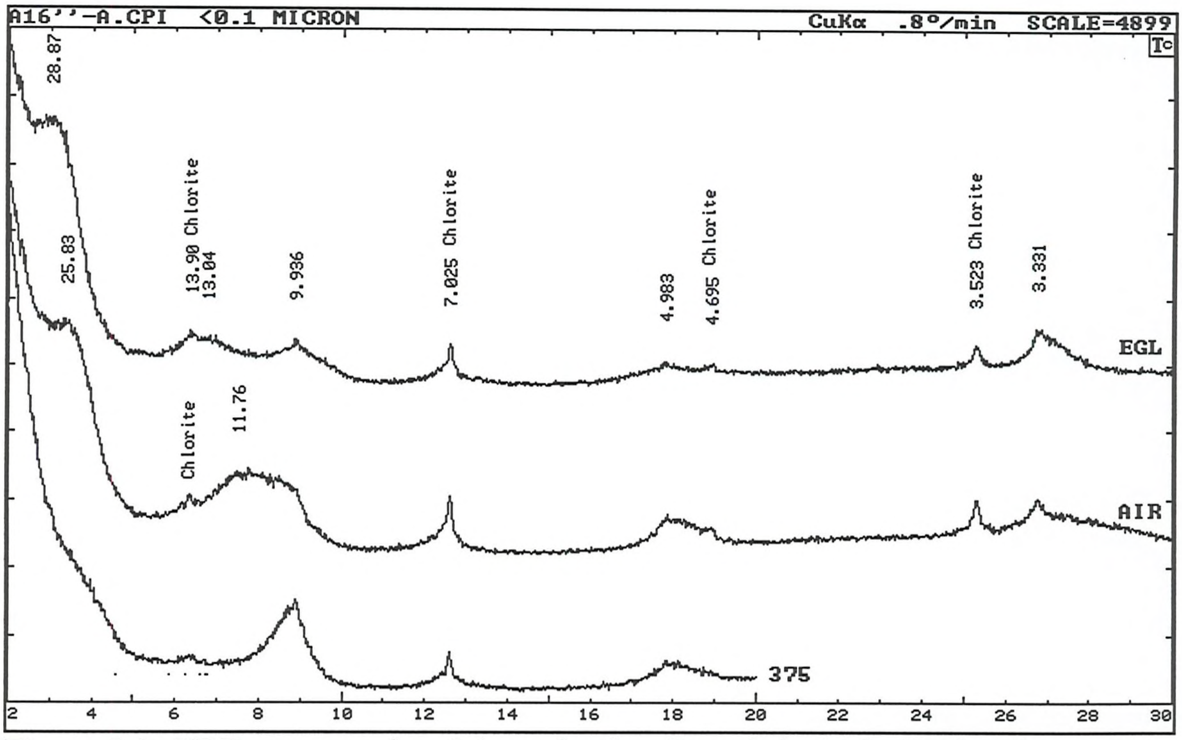

Figure 2-9: XRD patterns of a <0.1 μm fraction from shale A16, showing the presence of an allevardite-type superlattice phase. Peak labels in angstroms. EGL = glycolated; air = airdried and 375 = heated to 375 °C.

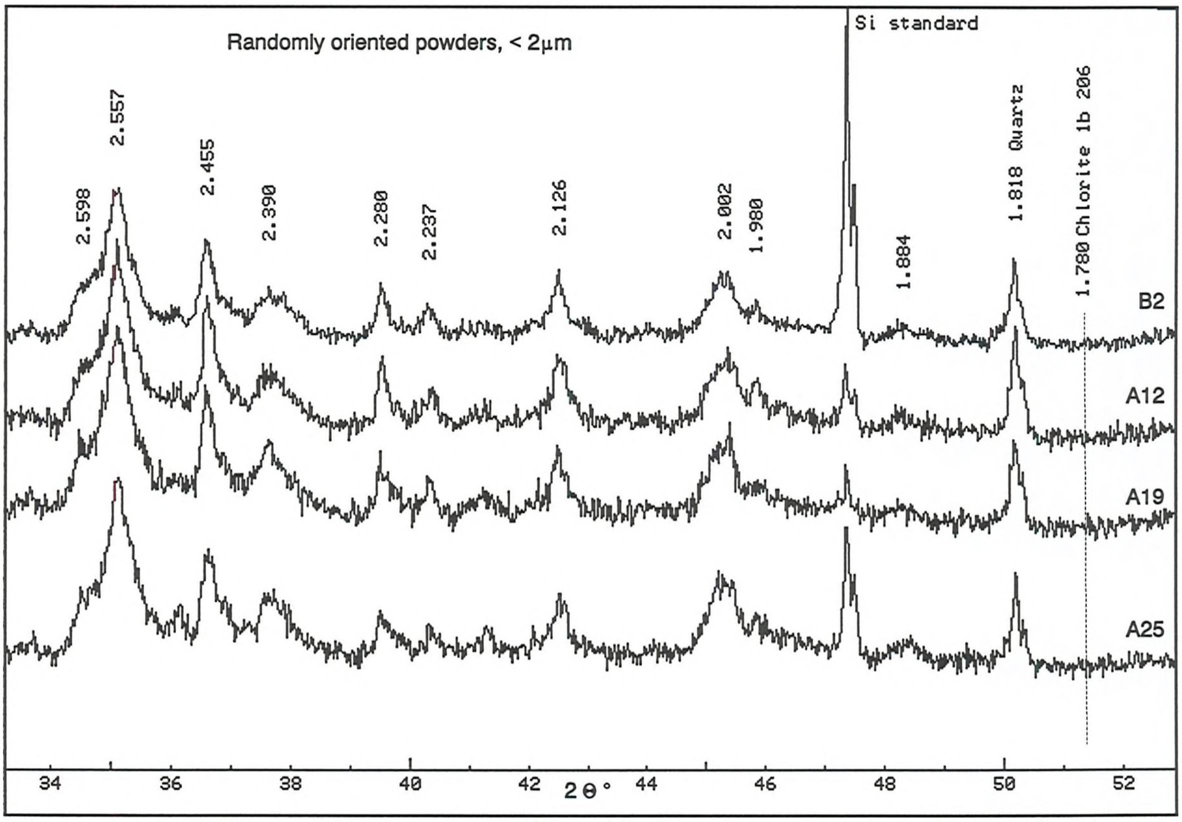

Figure 2-10: XRD powder patterns of illite-chlorite-quartz mixtures. Illite peaks obscure the diagnostic peaks for chlorite polytypes, but note that the chlorite 1b,90° 206 peak at 1.78 Å is absent.

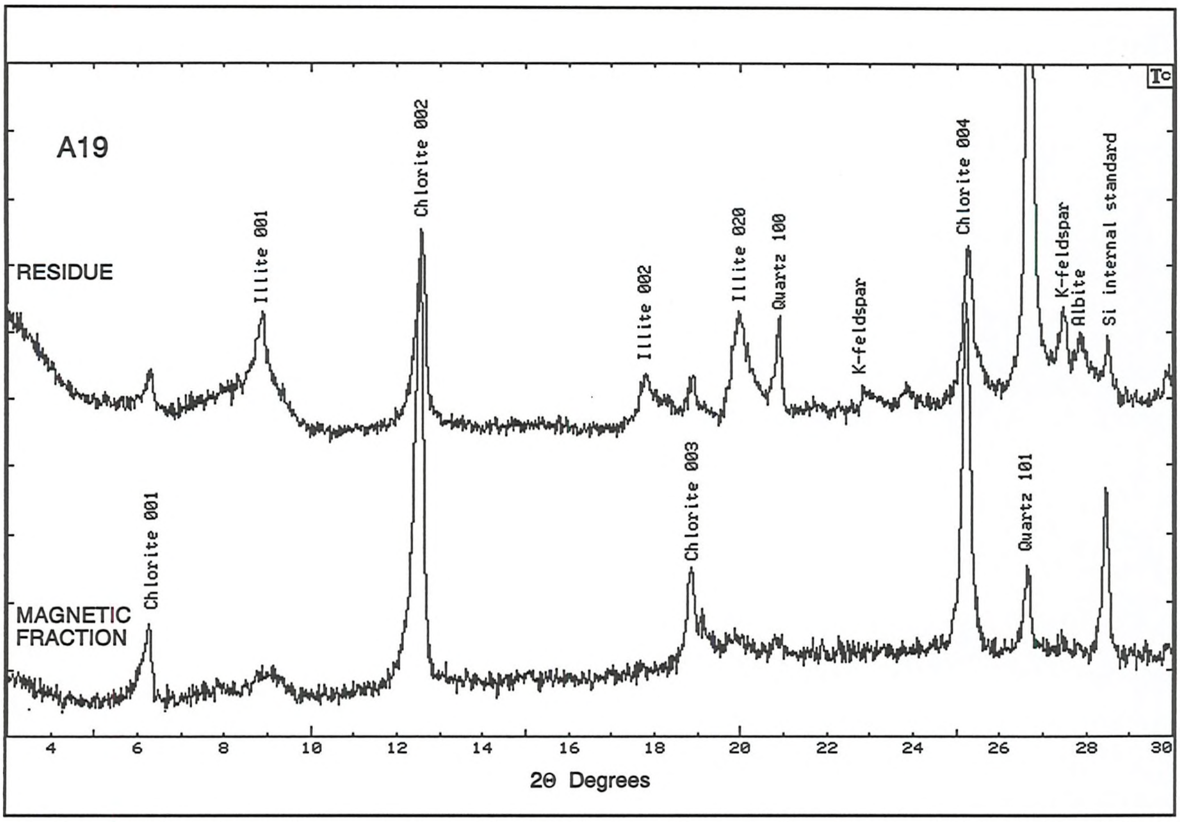

Figure 2-11: Magnetic separation of A19 clays. Magnetic fraction is chlorite plus silicon internal standard, plus traces of illite and quartz. Non-magnetic fraction is illite - chlorite - quartz mixture with k-feldspar and albite.

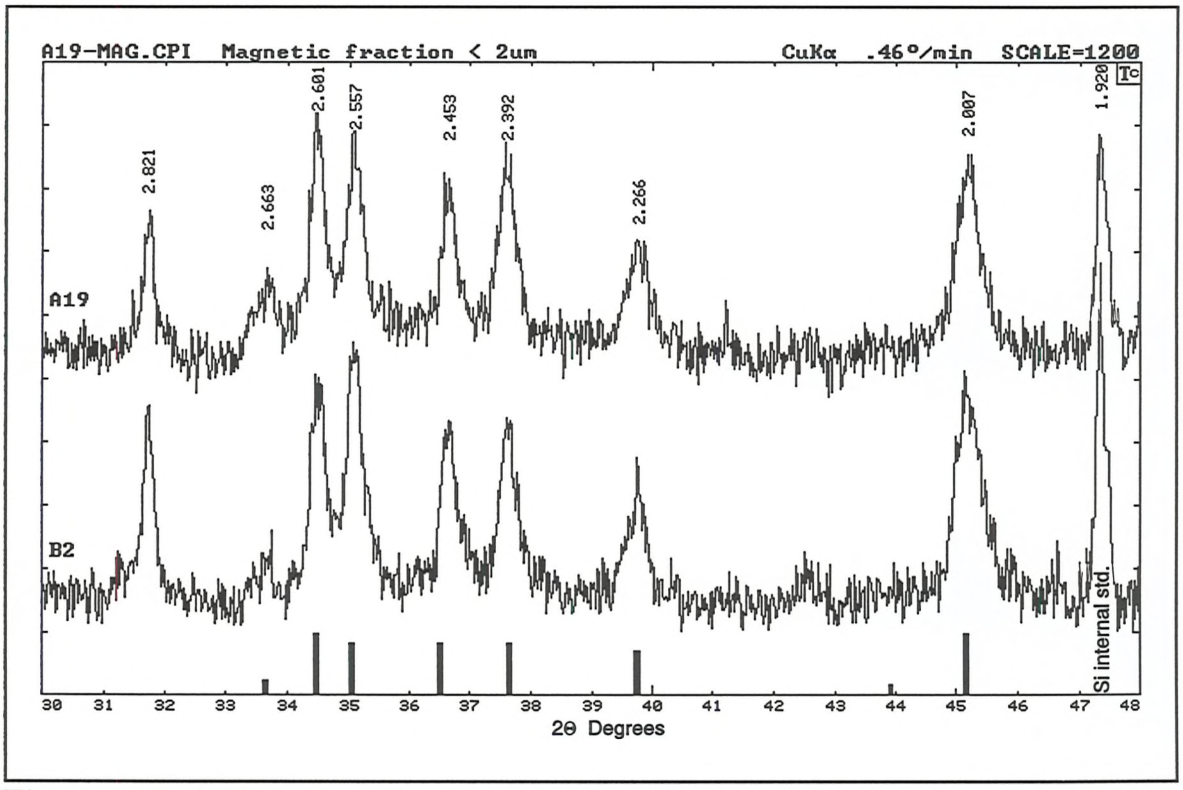

Figure 2-12: XRD patterns for magnetically concentrated chlorites from samples A19 and B2. Black bars are the diagnostic peaks for llb polytype (from Bailey, 1980).

evidence of the presence of rectorite. The concentration of this phase in the ultra-fine fraction suggests that it is either persisting metastably beyond its normal temperature range, or is retrograde material caused by late-stage alteration.

Hayes (1970) and Curtis *et al.* (1985) have described chlorites in sedimentary rocks. Authigenic sedimentary chlorites are mostly the Ib polytype; with an increase in metamorphic grade the IIb polytype prevails. In an effort to characterize the clay polytypes, some XRD runs with randomly oriented powders were made (figure 2-10). Because of the illite-chlorite mixture and the resulting peak overlaps, it was not possible to characterize the polytype of either chlorite or mica. However, the chlorite 1b, 90° polytype can be excluded because of the absence of a 206 reflection at 1.78Å. The clay fractions of samples A19 and B2 were separated magnetically using the technique of Tellier *et al.*(1988) to produce a magnetic concentrate rich in chlorite (figure 2-11). This material was identified unequivocally as the IIb polytype (figure 2-12). On the basis of this result, and the absence of the 1b polytype in figure 2-10, it is proposed that essentially all the chlorites in the Navas de Estena shales have transformed to the IIb polytype. Hayes (1970) places this reaction at 150 to 200 °C. However, a recent study by Walker (1993) suggests that these limits may be as broad as 80 to 300 °C.

The non-magnetic fraction of sample A19 (figure 2-13) contains a mixture of mostly $1M_d$ illite with some of the $2M_1$ polytype. This is often considered to represent a mixture between detrital illites from igneous or metamorphic terranes ($2M_1$) and newly formed illites ($1M_d$) (Frey, 1987; Velde, 1985). The transition from $1M_d$ to $2M_1$ occurs at around the anchizone/epizone boundary (evidence reviewed in Frey, 1987), so the presence of the $1M_d$ polytype is consistent with a peak metamorphic grade below the epizone for the shales.

Under the scanning electron microscope (SEM), the shales have a well-recrystallized texture composed principally of quartz, chlorite and illite (figures 2-14(a),(b)). There are thin black streaks of organic material, present at a relatively low concentration of < 0.5 weight % organic carbon (chapter 4). Many of the larger chlorite and illite grains show some development of chlorite-mica stacks (figure 2-14(b), (f)). These

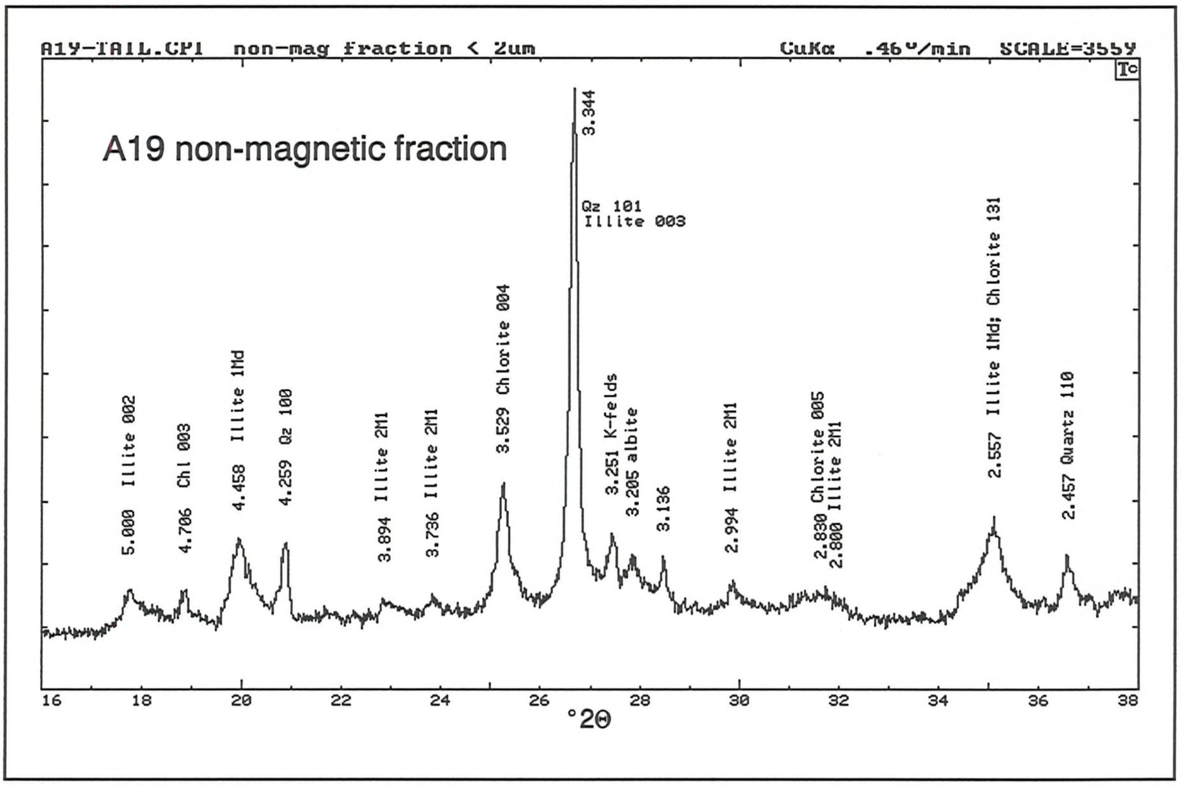

Figure 2-13: Non-magnetic fraction of shale A19 clays. Diagnostic peaks for illite polytypes are labelled.

interlayered growths of chlorite and illite are also described from monazite-bearing rocks by Milodowski and Zalasiewicz (1991b), who interpret them as diagenetic in origin, forming from detrital ferromagnesian precursors. Nonnon (1989) also reports chlorite-mica stacks from the Brabant massif in Belgium (See Fig. 1-2). The chlorite-mica stacks found in the Calymene Formation are not as well developed as those described by Milodowski and Zalasiewicz (1991b) from the Lower Ordovician of Wales; this may reflect the difference in metamorphic grade (anchizonal in Spain versus lower epizone in Wales). Accessory detrital zircon and rutile are present (figure 2-14(c),(e)), together with goethite which is probably a weathering product of pyrite. Authigenic anatase occurs, often as skeletal grains (figure 2-14(e)). Traces of albite and microcline show up on XRD scans (e.g. figure 2-13), but neither was detected with the SEM, suggesting that they might be present as very fine-grained detrital fragments. Rare crystals of florencite, an aluminium, REE phosphate isostructural with alunite, appear to be authigenic, intergrown with chlorite (figure 2-14(e),(f)). They have a rather skeletal appearance, and may be decomposing in favour of monazite concretions forming in their vicinity (figure 2-14(f)). Detrital monazites are very rare, and invariably fine-grained (figure 2-15(d)); they are readily

	300-2	300-3	300-4	300-5	300-6	300-7	300-8	300-9	300-10	300-13	300-14	300-15	300-16	300-17	300-20
	Chl	Chl	Chl					Chl		Chl		I	Chl		
SiO2	26.8	27.9	27.1	39.0	29.4	47.2	34.8	28.6	48.5	27.2	51.0	51.9	28.7	46.4	49.7
Al2O3	30.1	31.2	30.9	36.3	32.3	42.4	22.6	32.9	37.4	30.1	25.6	39.4	32.1	42.4	39.0
FeO	32.6	30.0	30.6	12.9	27.3	0.00	0.72	29.1	3.92	31.7	14.9	0.00	29.8	0.46	1.39
MgO	9.16	9.53	10.1	4.65	8.89	0.00	1.65	8.34	1.16	10.03	5.81	0.00	8.65	0.42	1.14
CaO	0.00	0.33	0.00	0.00	0.00	0.50	0.00	0.74	0.48	0.00	0.32	0.46	0.00	0.37	0.00
MnO	0.00	0.00	0.00	0.50	0.54	0.00	0.00	0.00	0.59	0.00	0.00	0.00	0.47	0.53	0.33
TiO2	0.63	0.30	0.00	0.39	0.29	0.50	34.35	0.00	0.00	1.00	0.00	0.00	0.00	0.00	0.27
K2O	0.00	0.13	0.00	3.78	0.60	7.44	4.71	0.29	6.18	0.00	0.95	6.93	0.23	7.49	6.39
Na2O	0.77	0.59	1.26	2.57	0.66	2.07	1.17	0.00	1.79	0.00	1.38	1.35	0.00	1.92	1.79
Atomic															
No. Oxygens	28	28	28	22	28	22	22	28	22	28	22	22	28	22	22
Si	5.02	5.15	5.04	5.18	5.35	5.86	4.55	5.23	6.11	5.06	6.58	6.36	5.28	5.80	6.16
Al	2.98	2.85	2.96	2.82	2.65	2.14	3.45	2.77	1.89	2.94	1.42	1.64	2.72	2.20	1.84
Al	3.66	3.93	3.80	2.85	4.27	4.05	0.03	4.32	3.65	3.65	2.46	4.04	4.21	4.03	3.84
Fe	5.10	4.62	4.74	1.43	4.15	0.00	0.08	4.44	0.41	4.91	1.60	0.00	4.57	0.05	0.14
Mg	2.58	2.64	2.81	0.93	2.43	0.00	0.32	2.29	0.22	2.80	1.12	0.00	2.38	0.08	0.21
Ca	0.00	0.07	0.00	0.00	0.00	0.07	0.00	0.15	0.06	0.00	0.04	0.06	0.00	0.05	0.00
Mn	0.00	0.00	0.00	0.06	0.08	0.00	0.00	0.00	0.06	0.00	0.00	0.00	0.07	0.06	0.03
Ti	0.09	0.04	0.00	0.04	0.04	0.05	3.37	0.00	0.00	0.14	0.00	0.00	0.00	0.00	0.03
K	0.00	0.03	0.00	0.64	0.14	1.18	0.79	0.07	0.99	0.00	0.16	1.08	0.05	1.19	1.01
Na	0.28	0.21	0.45	0.66	0.23	0.50	0.30	0.00	0.44	0.00	0.34	0.32	0.00	0.46	0.43

Table 2-2: Semi-quantitative analyses of phyllosilicates in shale B2. For sample location, see Fig. 1-9; for location of points see figure 2-14(a). Chl = chlorite; I = illite.

distinguished from authigenic monazites by their high thorium content. Tables 2-2 and 2-3 show semi- quantitative EDS analyses of mineral grains in figures 2-14(a) and (b), respectively. Because they are made without using standards, and normalised to 100%, these SEM-EDX analyses are best used for qualitative mineral identification. Quantitative electron microprobe data are discussed in a later section.

The silty "hard ground" horizons found in the Valleleor and Santa Maria sections (see chapter 1) have a similar mineralogy to the shales, being dominated by the assemblage quartz - illite - chlorite. They are richer in quartz and detrital heavy minerals such as rutile and zircon (figure 2-15). Chlorite-mica stacks (figure 2-15(b)) are more abundant than in the neighbouring shales, in accordance with the detrital affiliation suggested by Milodowski and Zalasiewicz (1991b). Florencite is again present (figure 2-15(c)), with a similar skeletal habit to that seen in the shales. Grey monazites are present only in low concentrations (see chapter 4), and none was seen

	301-01	301-02	301-03	301-04	301-08	301-09	301-10	301-11	301-12
	Chl	Chl						Chl	
SiO_2	27.7	26.7	48.4	47.3	40.9	47.5	49.3	27.5	47.0
Al_2O_3	31.0	31.1	41.3	42.7	36.8	39.8	40.5	30.8	42.3
FeO	29.2	29.9	1.21	0.60	13.4	2.17	1.08	29.2	1.6
MgO	10.4	10.3	0.00	0.26	3.35	0.88	0.80	9.80	0.00
CaO	0.00	0.00	0.00	0.46	0.00	0.00	0.00	0.61	0.26
MnO	0.62	0.36	0.00	0.00	0.00	0.84	0.00	0.00	0.00
TiO_2	0.00	1.00	0.64	0.00	1.22	0.95	0.25	0.25	0.00
K_2O	0.00	0.00	6.26	6.84	3.11	5.82	5.32	0.51	7.14
Na_2O	1.09	0.59	2.26	1.87	1.23	1.98	2.73	1.34	1.81
Atomic	Props.								
No. Oxygens	28	28	22	22	22	22	22	28	22
Si	5.12	4.95	5.98	5.86	5.36	5.93	6.07	5.09	5.85
Al	2.88	3.05	2.02	2.14	2.64	2.07	1.93	2.91	2.15
Al	3.85	3.74	4.00	4.09	3.03	3.78	3.94	3.81	4.06
Fe	4.50	4.61	0.12	0.06	1.47	0.23	0.11	4.51	0.16
Mg	2.88	2.86	0.00	0.05	0.66	0.16	0.15	2.73	0.00
Ca	0.00	0.00	0.00	0.06	0.00	0.00	0.00	0.12	0.03
Mn	0.10	0.06	0.00	0.00	0.00	0.09	0.00	0.00	0.00
Ti	0.00	0.14	0.06	0.00	0.12	0.09	0.02	0.03	0.00
K	0.00	0.00	0.99	1.08	0.52	0.93	0.84	0.12	1.14
Na	0.39	0.21	0.54	0.45	0.31	0.48	0.65	0.48	0.44

Table 2-3: Semi- quantitative EDS analyses of minerals from shale B2. See figure 2-14(b). Labels as per table 2-2.

in the three specimens examined. Occasional Th-rich detrital monazites were found, however (figure 2-15(b)).

2.4 Monazites

In thin section, monazite occurs as rare anhedral ellipsoidal grains, typically 0.5mm long, dark brown, with abundant silicate inclusions. Grains are optically homogeneous, with occasional sector zoning and a weak pink pleochroism. They show imperfect extinction because of the colour and the high inclusion density. Neighbouring grains in the same section are often in optical continuity (figure 2-16(b)). Wherever cleavage relations have been observed in monazite - bearing thin sections, the cleavage is seen to post-date the monazite grain (figures 2-15(e),(f);

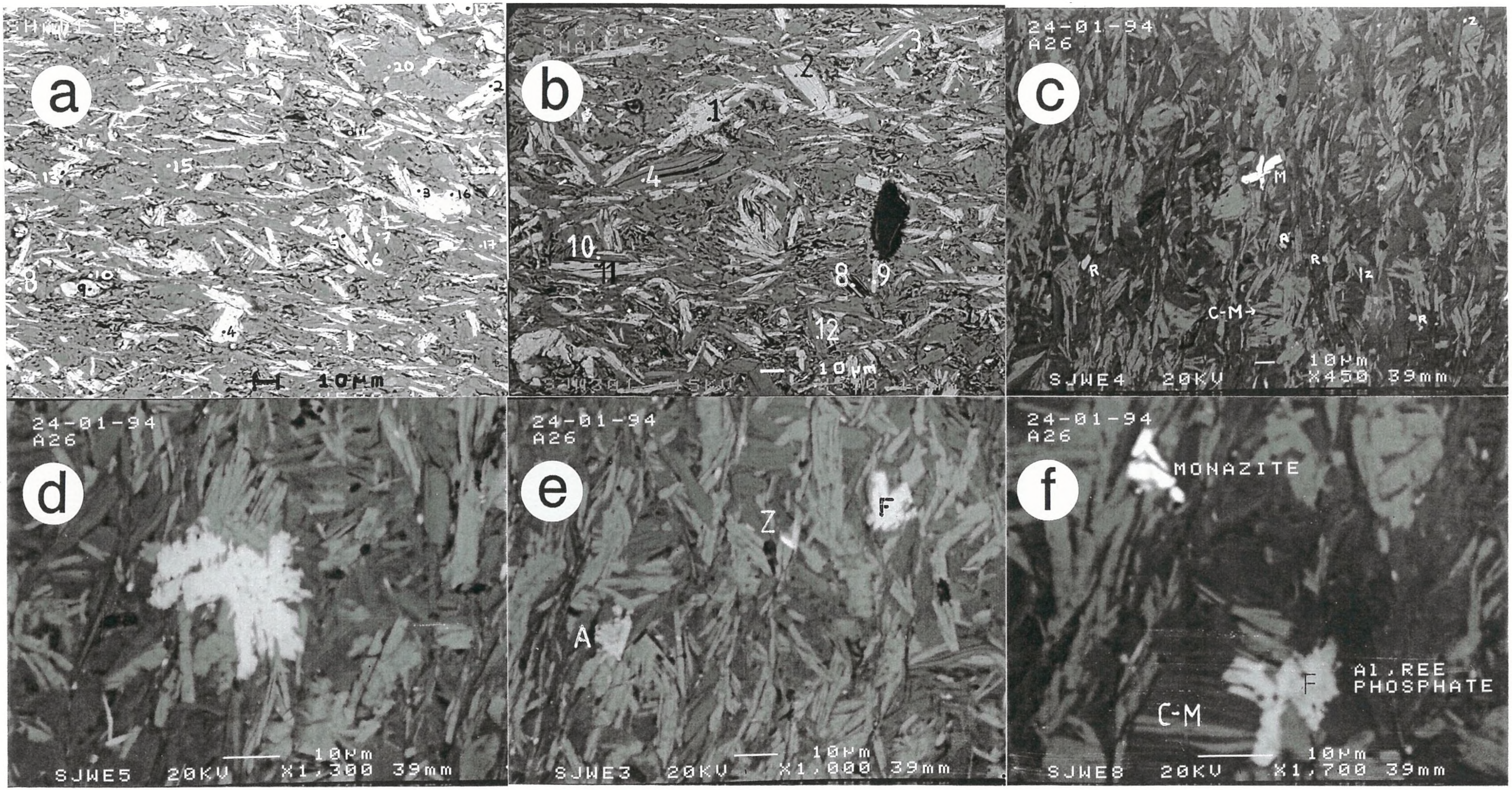

Figure 2-14: Back-scattered electron images of monazite-bearing shales. (a)&(b): Typical texture. Numbers refer to analyses in tables 2-2 and 2-3. Note incipient development of chlorite-mica stacks (points 2,3,10,11 in (b)). (c): Detrital rutile (R), tiny zircons (Z) and early-stage authigenic monazite (M) in qz.-illite-chl. matrix. (d): Authigenic florencite (Ce) intergrown with chlorite. (e): Florencite (F), anatase (A) and zircon (Z) in shale matrix. (f): Florencite, with corroded appearance, intergrown with chlorite-mica stack and in proximity to a euhedral early-stage authigenic monazite.

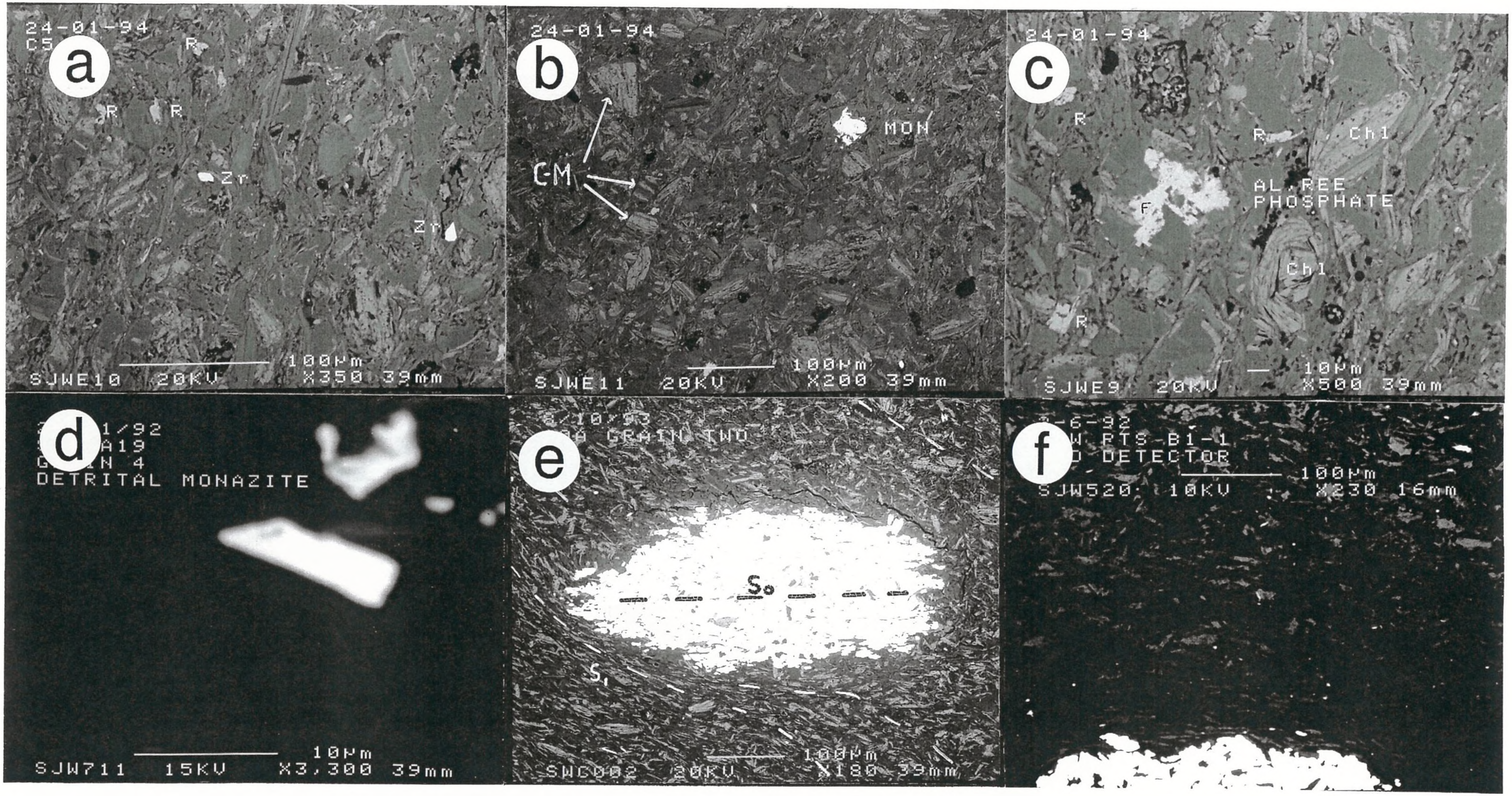

Figure 2-15: (a)-(c): "Hard ground" horizon, Santa Maria section (see Fig. 1-12). (a): Concentration of detrital xircon (Zr) and rutile (R) in quartz-rich matrix. (b): Abundant chlorite-mica stacks (C-M) along with Th-rich detrital monazite. (c): Authigenic florencite (F) and detrital rutile (R) in chlorite-quartz-illite matrix. (d): Rare Th-rich detrital monazite in shale A19, Valleleor. (e): Relict bedding fabric (S_0) aligned with long axis of monazite grain; cleavage in the host shale (S_1) is deflected around the end of the grain. (f): Shale texture in the vicinity of a monazite grain. There is a high strain zone where the cleavage is deflected around the relatively rigid monazite.

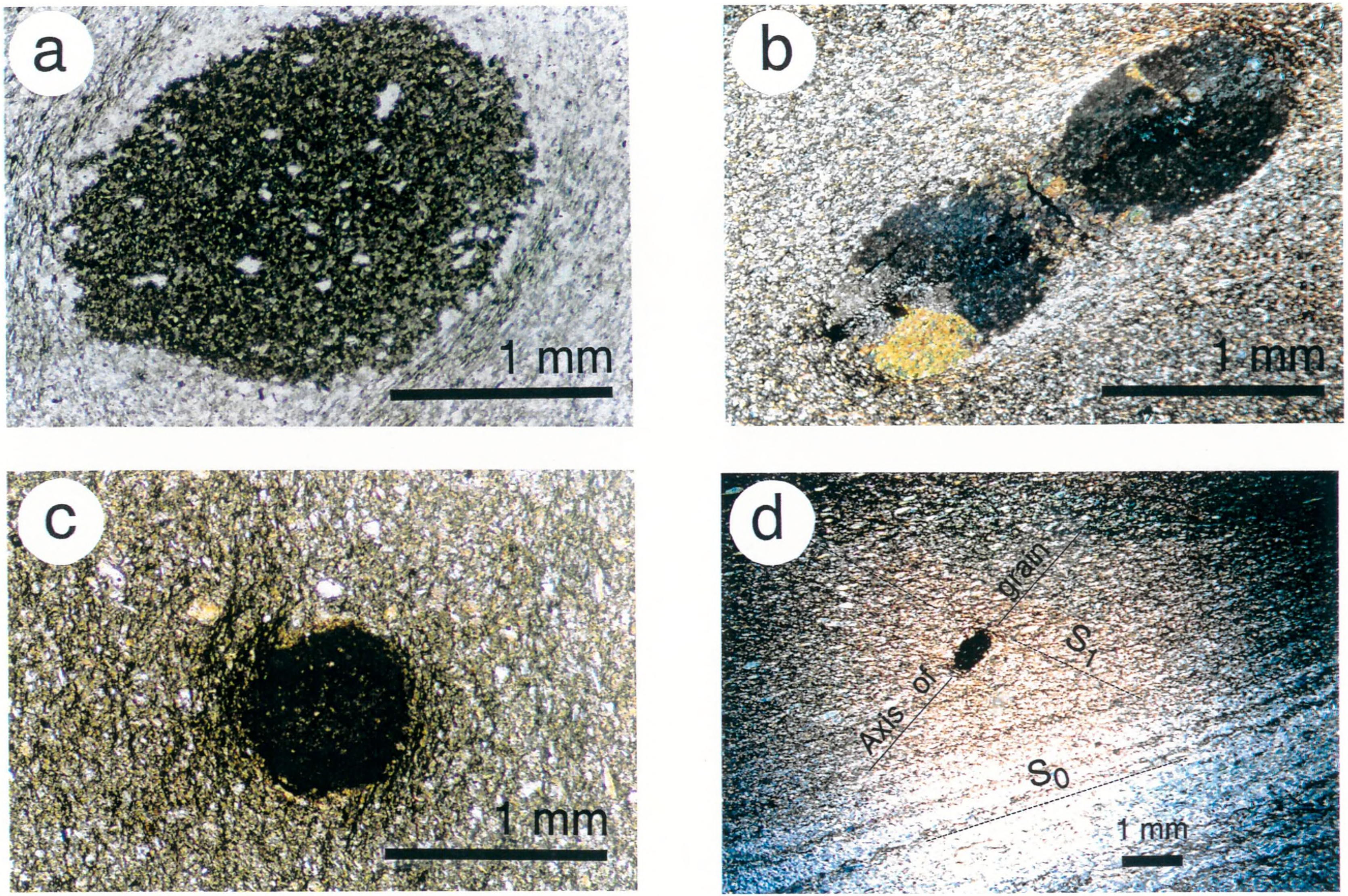

Figure 2-16: Grey monazites in thin section. (a): Extra-thin section, *circa* 10μm, showing the colour of the monazite and the texture of quartz and chlorite inclusions. Note the increased definition of the crenulation cleavage near the monazite grain. (b): Two monazites which have coalesced. Note the optical continuity between the main parts of the two grains, and the sector zoning of the left hand grain. (c): Deflection of cleavage around a monazite grain. (d): Typical cleavage-bedding relationships for grey monazite. The long axis of the grain is sub-parallel to bedding, with the cleavage at a high angle to both.

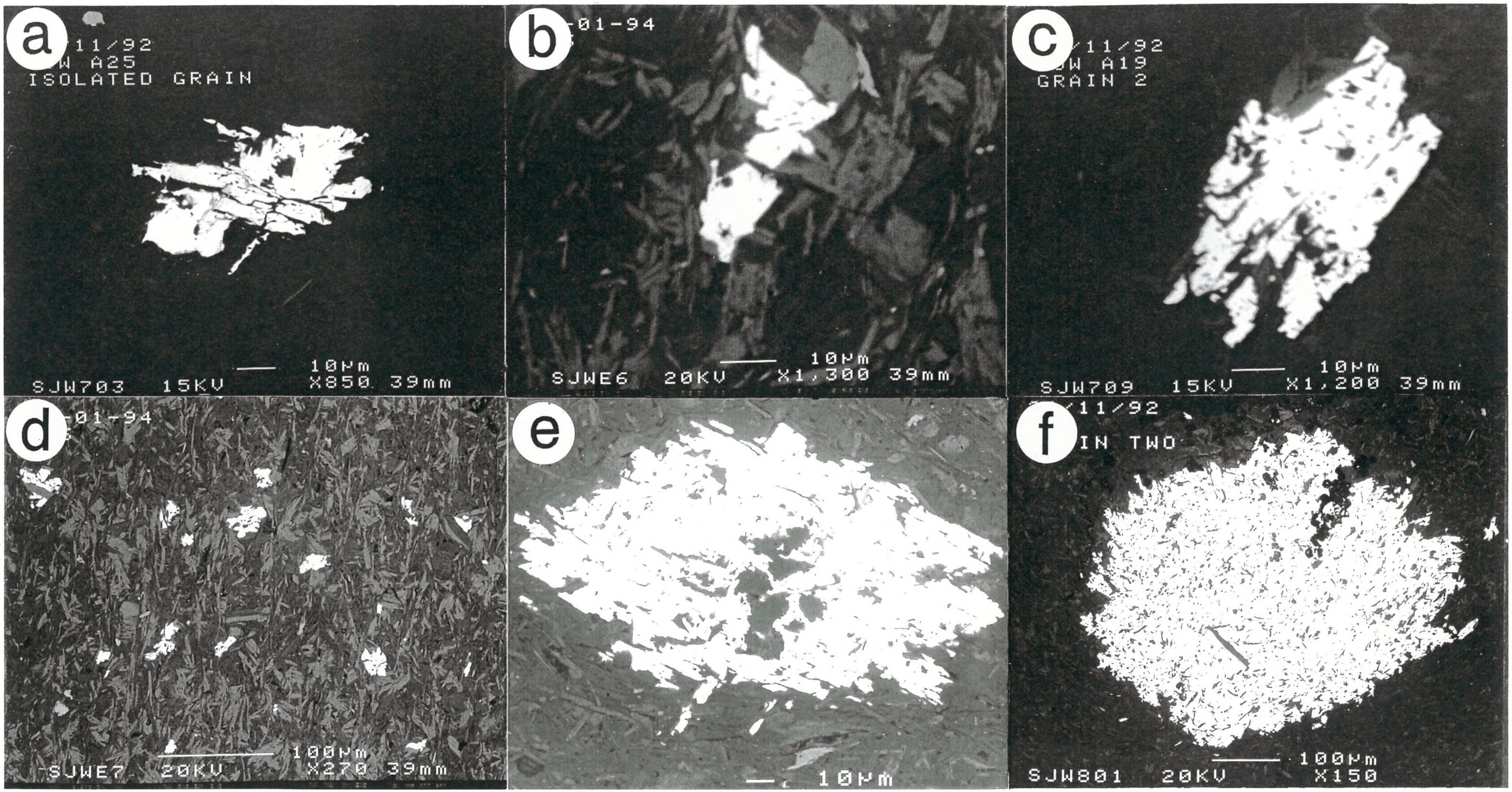

Figure 2-17: Stages of development of monazite concretions. (a) and (c): 40-50 μm grains coexisting with much larger grains in the same section. Note the development of euhedral crystal faces. (b): Isolated 10 μm grain in shale A26. (d): Cluster of small monazites nucleating in the same region of shale A26. (e) and (f): Two further grains from the same thin section as (c). (e) has well developed crystal faces and coarse inclusions of quartz, apparently preserved at the expense of phyllosilicates. (f) is fully developed grey monazite grain, with typical ragged outline.

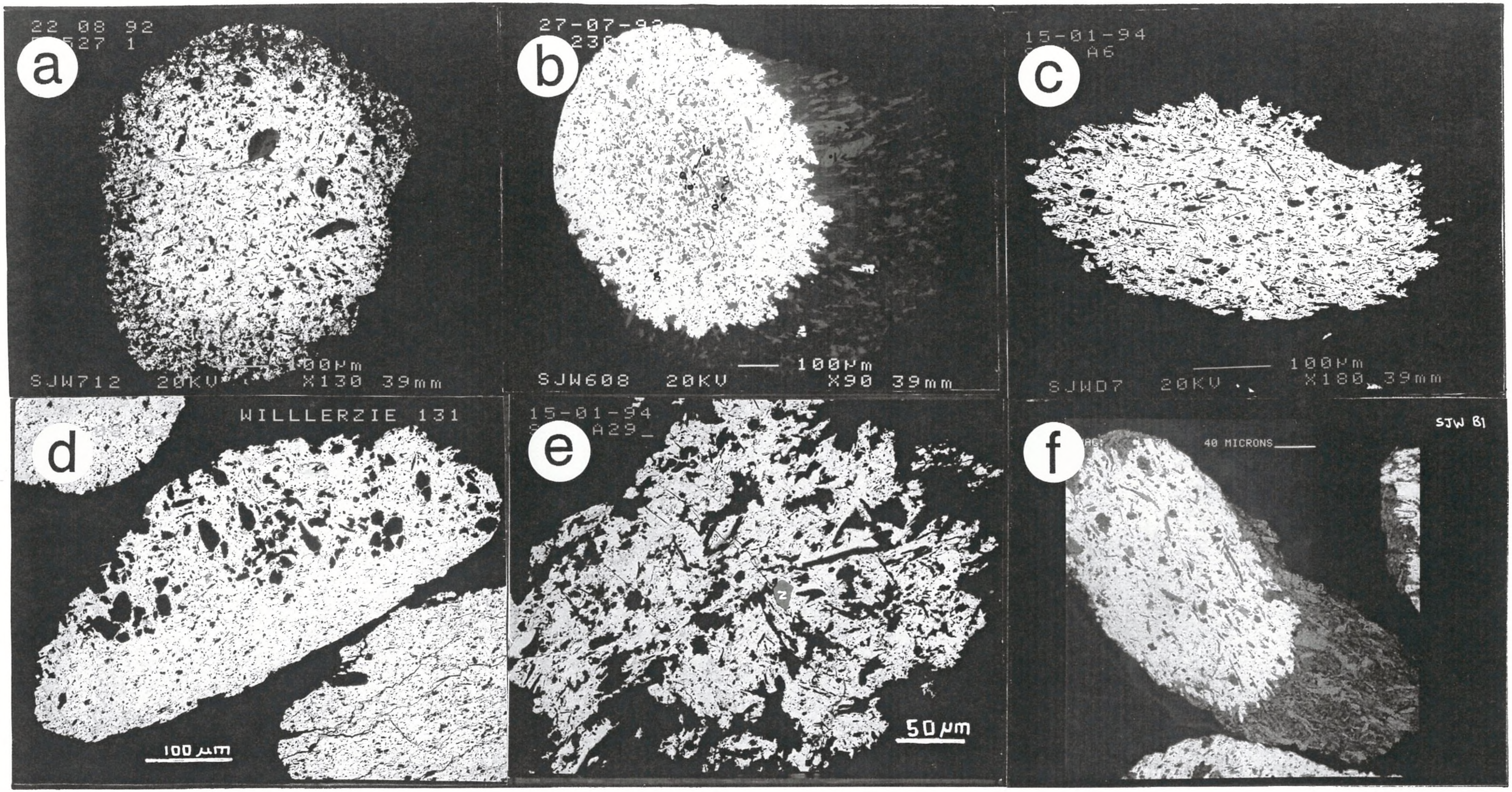

Figure 2-18: (a) and (b): Alluvial monazites from NW Spain showing contrasting patterns of inclusion density. (c): Monazite separated from shale A6, showing typical inclusion fabric parallel to the long axis of the grain, and a fairly high degree of cementing. (d): Alluvial monazite from Belgium. Note the sharp boundary which suggests the incorporation of a sedimentary bedding plane. (e): Monazite from the top of the Valleleor section, showing a skeletal fabric and inclusion of zircon (Z) and other silicates. (f): Digitised image of a monazite with an attached shale fragment, to illustrate the relative grain sizes of inclusions and shale minerals.

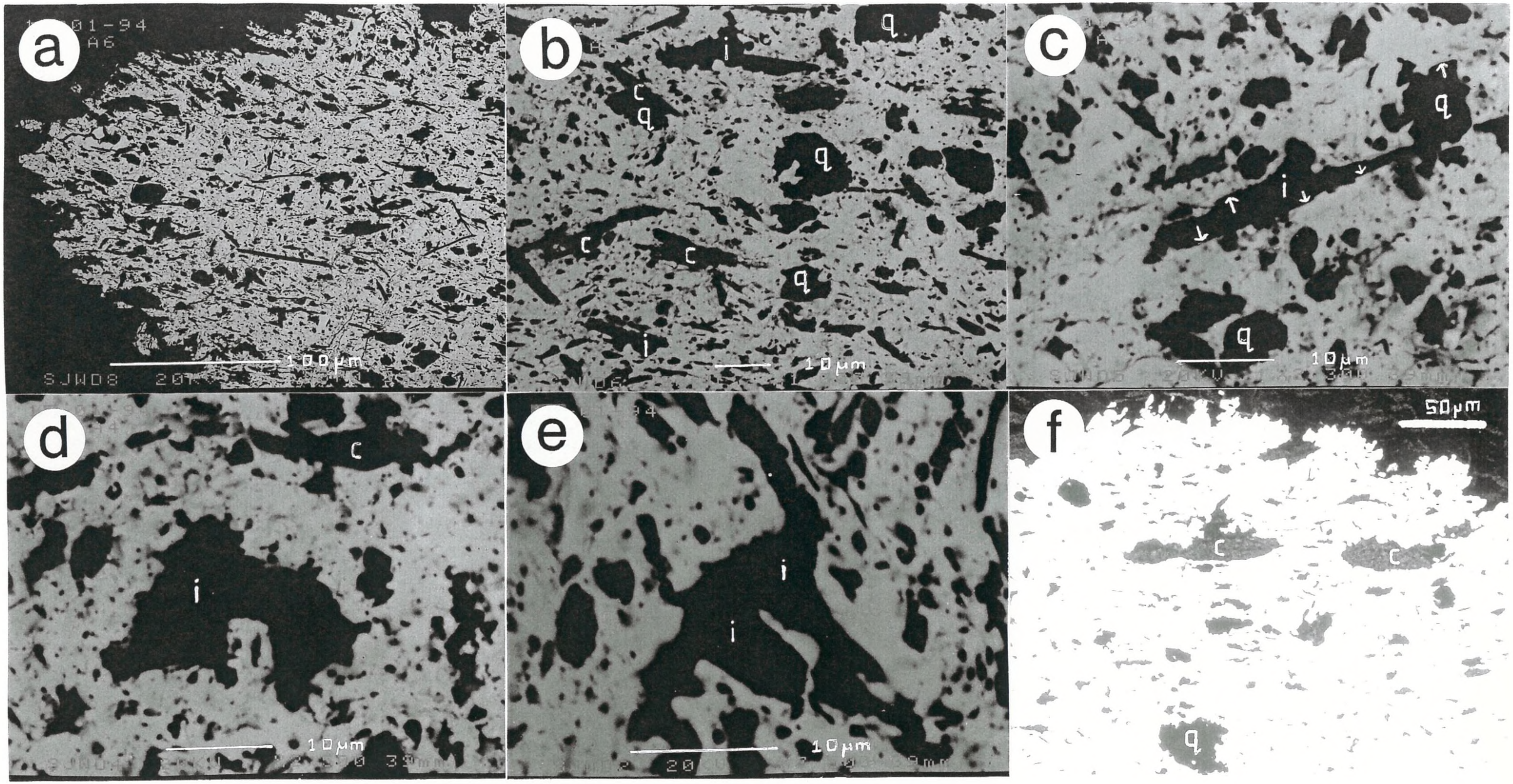

Figure 2-19: Textures of inclusions in monazite concretions. (a): Overview of typical inclusion texture. Acicular forms are mostly illites; equant to tabular are quartz and chlorite. (b): Inclusions of quartz (q), chlorite (c) and illite (i), all showing various degrees of replacement by monazite cement. (c): Development of crystal faces (arrows) in the growing monazite as it replaces illite and chlorite. (d) and (e): Illite grains partly replaced by monazite. (f): Chlorite and quartz inclusions partly replaced by monazite.

2-16(c),(d)). This is an important feature of grey monazite petrogenesis which has been observed in all the reported studies (e.g., Donnot et al., 1973; Burnotte et al., 1989; Milodowski and Zalasiewicz, 1991). It implies that in every case the monazites must have formed well before the peak of deformation, and presumably of metamorphism. The cleavage in Calymene Formation shales consists of a weak crenulation of a previous bedding-parallel compactional fabric; it is more pronounced in the immediate vicinity of monazites, which have behaved rigidly during deformation. The long axis of a grain is frequently rotated slightly with respect to bedding, and at a high angle to the cleavage (figure 2-16(d)). Grains frequently display an inclusion fabric oriented parallel to the long axis of the grain (figures 2-15(e),2-18(c)); Milodowski and Zalasiewicz (1991) equate this to original bedding for Welsh monazites. Figure 2-18(d) shows an alluvial monazite grain from Belgium which has clearly included a bedding plane within the concretion.

Monazite-bearing thin sections frequently contain a whole range of grain sizes, from 10-20 μm right up to several hundred microns (figure 2-17). Euhedral faces are commonly developed on these smaller grains (figure 2-17(a),(c),(e)). There is sometimes a tendency for a cluster of small grains to nucleate in a particular area (figure 2-17(d)). One has the impression that, of a large population of early-formed grains, a small number are favoured to grow large at the expense of the others.

The mineralogy of the inclusions in monazite grains is always the same as in the host shale: quartz, chlorite, and illite, along with occasional zircon and rutile. The inclusion minerals have a comparable grain size to those in the shale (figure 2-18(f)). Monazite growth is usually clearly replacive (figure 2-19); the silicate inclusions have a ragged appearance and have been partially replaced by monazite cement. At the boundaries between inclusions and the encroaching cement, euhedral crystal faces are often developed (figure 2-19(c)). Although both quartz and phyllosilicates can show replacement textures (figure 2-19(b)), there is some suggestion that quartz may be more resistant to replacement by monazite than the other included phases. Some grains are found with inclusions of coarse-grained quartz and little else (figure 2-17(e)); this may, however, reflect original sedimentary texture.

Relative proportions of cement and inclusions

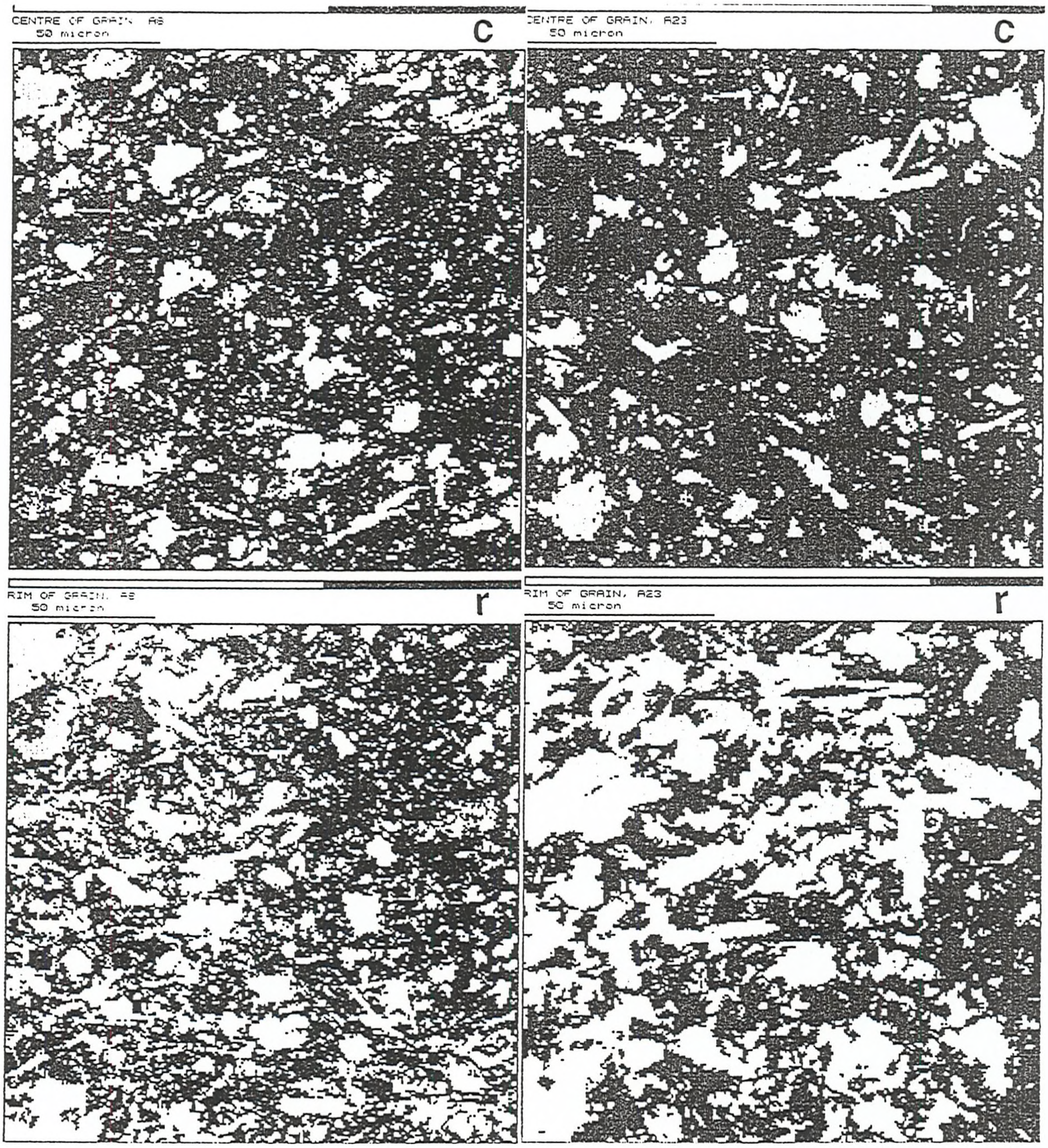

Figure 2-20: Binary maps showing textural contrast between core (c) and rim (r) areas of two monazite grains. Dark areas are monazite, light areas are silicate inclusions. The bar denotes pixel intensities in the original BSE image.

The proportion of a concretion occupied by cement potentially records information about the depth of its formation (e.g. Curtis et al., 1986). The monazites separated from Calymene Formation shales consist of between 50 % and 75% phosphate cement, with the remainder silicate inclusions. If it were assumed that the concretions had formed in soft sediment, as is the case for many carbonate concretions (e.g. Pye et al., 1990), then the cement might be assumed to have displaced pore water, in which case the proportion of cement would equate to the original porosity of the sediment at the time of formation. The porosity of compacting shales is a predictable function of depth (Baldwin and Butler, 1985); the limits of 50% and 75% would correspond to depths of 70 m and 0.9 m, respectively. This estimate depends on the concretion formation being purely displacive; if any replacement of clastic material by monazite cement has occurred, then the depth estimate will be too low. Since the textural evidence presented above supports largely replacive concretion growth, it seems unlikely that the proportion of cement is directly related to the original porosity.

Many concretions appear, subjectively, to be cemented to a greater degree in the core than the rim. This can be be quantified by using digitised back-scattered electron (BSE) images. The intensity of each pixel in a BSE image is proportional to the atomic number of the material under the beam; a threshold value was chosen by trial and error to distinguish inclusions from cement (in practice this value is not critical because of the high mass contrast between silicates and monazite). The binary maps of figure 2-20 could then be generated, along with a measured value for the proportion of inclusions versus monazite - a sort of automated point counting procedure. Core versus rim measurements for three monazites from the section at Valleleor seem to confirm the subjective impression:

	Percentage of monazite cement	
	Core	**Rim**
A8	71.5	53.9
A15	62.5	59.8
A23	77.2	51.1

Table 2-4: Degree of cementing in cores versus rims of three concretions.

Such a result can be interpreted in two ways:

1). The concretion formed while the sediment was still compacting, recording a greater apparent "porosity" in the core, or

2). Because the concretion grows from the centre outwards, the rim will always tend to be less well cemented than the core whenever growth stops.

Figures 2-18 (a) and (b) show contrasting patterns of inclusion density, with 2-18(b) having a higher density of inclusions in the core. In the case of grey monazites, it seems that no clear conclusion can be drawn from changes in inclusion density in different parts of the grain, and so great caution should be used in interpreting this kind of evidence.

Relative proportions of quartz and phyllosilicates

In order to assess the relative degree of replacement of quartz and phyllosilicates by monazite cement, polished thin sections of *in situ* monazites were examined on the SEM. Energy dispersive spectra were acquired of areas inside and outside the monazite nodules, leaving the beam on scanning mode. This provided a convenient way of averaging data from a large area of the specimen. The spectra were processed using the Tracor analysis program "SQ" to produce ZAF-corrected, semi-quantitative analyses. All the major elements including phosphorus were analysed, plus the light rare earths. Normative quartz, chlorite and illite were then calculated by assuming :

Molar chlorite = atomic (Fe + Mg) / 5.5

Molar illite = (K + Na) / 0.9

Molar quartz = atomic Si - 0.7(Fe + Mg) - 3.7(K + Na)

Results were then plotted as proportions in normative quartz - illite - chlorite space (figure 2-21). They reveal that the main difference between inclusions and host shale is a systematic quartz enrichment and illite depletion within the monazite grains. This tends to confirm the idea that phyllosilicate minerals, especially illite, are replaced by monazite more readily than quartz.

2.5 X-ray diffraction pattern of grey monazite

Figure 2-22 shows the XRD pattern measured on a monazite concentrate prepared from alluvial material from the Navas de Estena area. The sample was prepared for

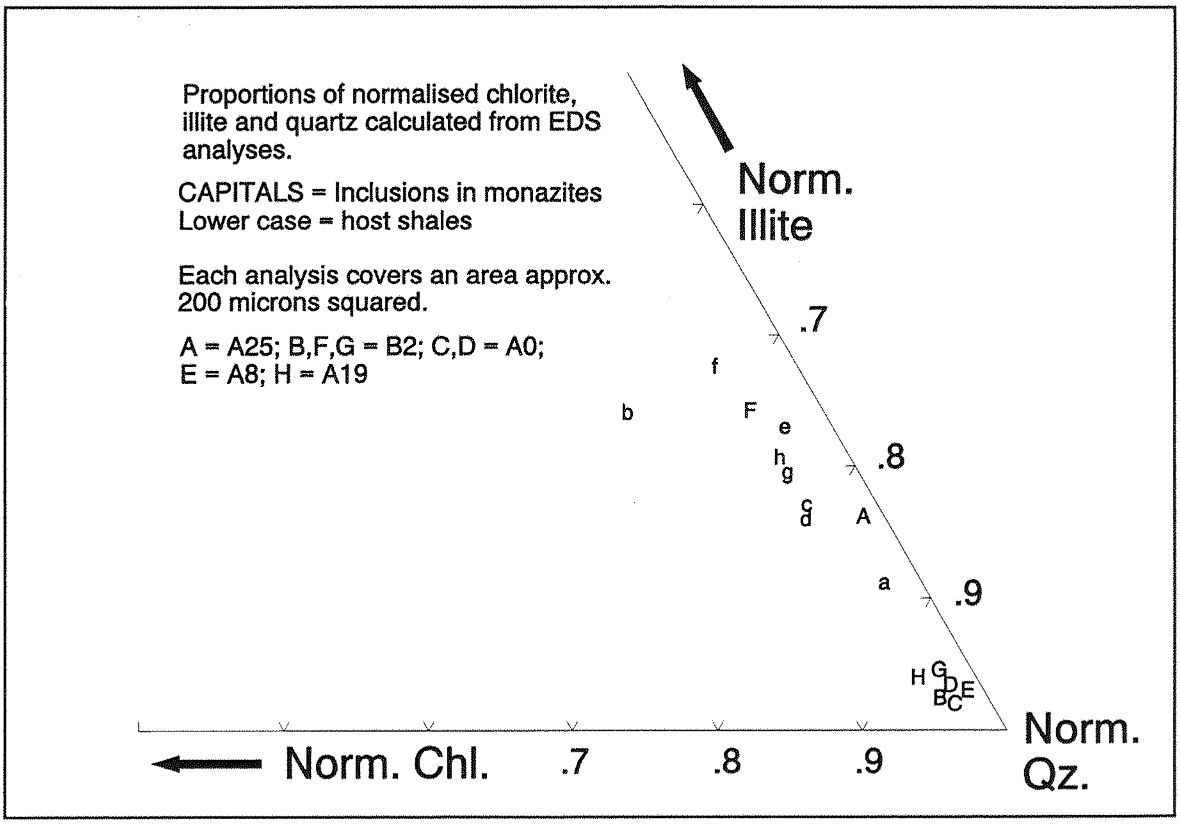

Figure 2-21: Silicate inclusions within monazites (capital letters) compared with the corresponding host shales (lower case letters) in the normative system chlorite-quartz-illite.

use as an ICP-MS standard (see appendix A); after grinding it finely in a ball mill, iron oxides were removed using a citrate-dithionite digestion and the powder was centrifuged in methylene iodide to try to separate the monazite cement of the nodules from silicate inclusions. The bars in figure 2-22 represent the XRD pattern of igneous monazite, for comparison. It is concluded that grey monazite has identical XRD characteristics to igneous monazite, in agreement with Nonnon (1984) and Rosenblum and Mosier (1983).

2.6 Comparison of the chemistry of inclusions versus host rock minerals

A quantitative electron microprobe study was carried out on several polished thin sections containing monazite grains *in situ*, in order to compare the compositions of silicate inclusions from different parts of the nodules and the same phases in the host shale. Analysis points were chosen using BSE images; in general, the coarser grains

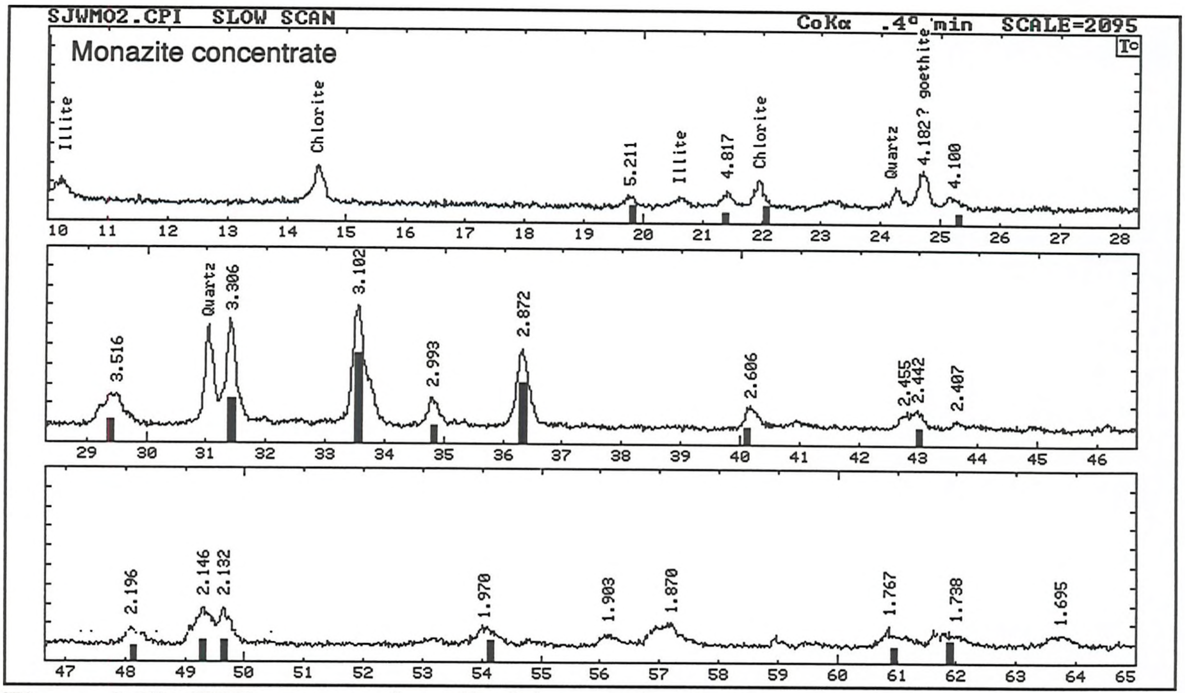

Figure 2-22: XRD pattern of an alluvial monazite concentrate. The black bars represent the reference peaks for igneous monazite. Quartz, illite and chlorite impurities are present from the silicate inclusions.

were chosen in the hope of getting clean analyses. Choice of analysis points was neither random nor systematic, and there is probably a numerical bias in favour of inclusions rather than host rock minerals, and phyllosilicates rather than quartz.

The results are given in table B-1, appendix B. Because of the presence of intergrowths of different phases on a scale finer than the probe beam (~2 μm), many of the analyses represent mixtures of silicates, sometimes with some monazite included. Only the major elements were analysed; the phosphorus content gives an indication of how much monazite is included in the analysed area. The totals are therefore uncorrected for REE, water content of hydrous minerals, and oxidation state of iron. Table B-1 includes an estimated total taking into account monazite and water content. Analyses with >1.5% P_2O_5 or with corrected totals < 90% were rejected. To facilitate comparison, all the analytical data were recalculated to a clay formula of 22 oxygens per formula unit. A plot of Si atoms per formula versus K + Na (interlayer charge) is shown in figure 2-23.

Essentially all the analyses fall within a triangle defined by the end members chlorite-illite-quartz, with the vast majority falling on well defined end members.

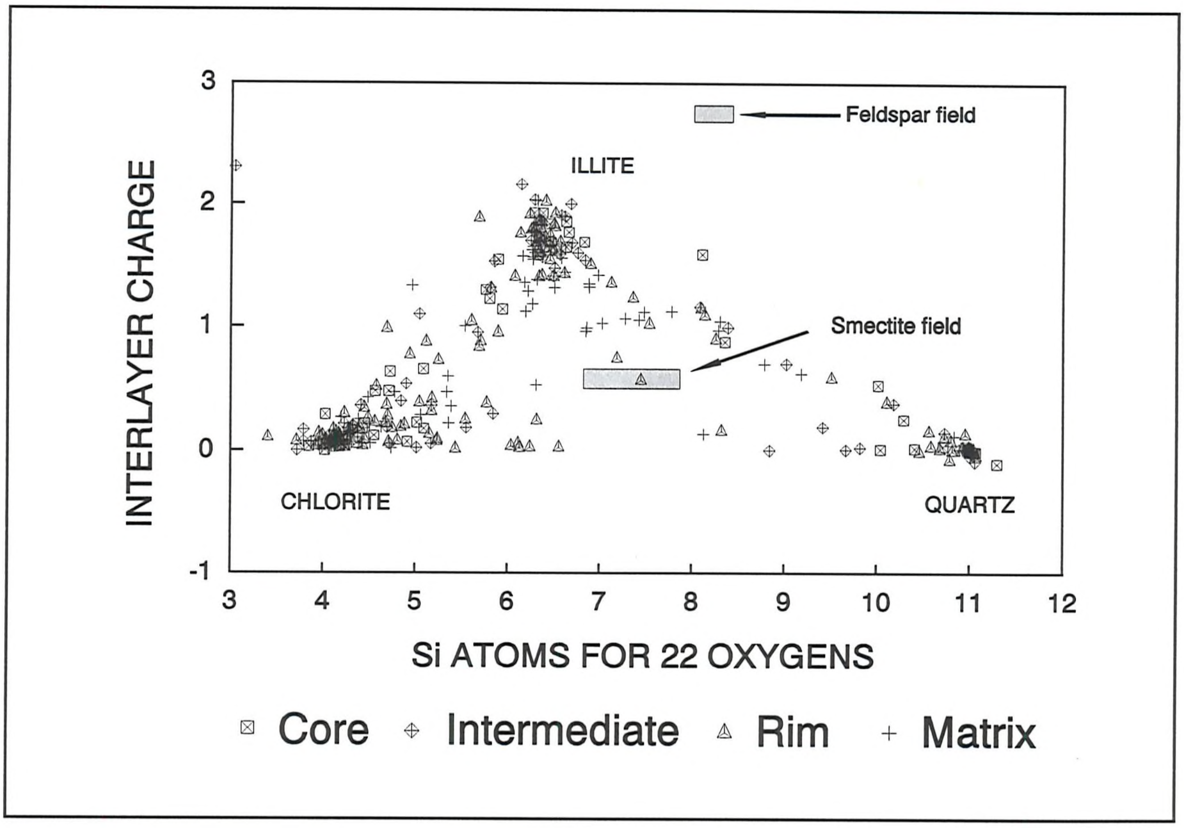

Figure 2-23: Microprobe data for Navas de Estena shales, recalculated to 22 oxygens per formula unit. Matrix = minerals in the host shale. Core, Intermediate, Rim refer to position of an inclusion mineral within a monazite nodule.

There is no evidence of either feldspars or smectites being preserved as armoured inclusions within the nodules. The apparent mixing trends between quartz and the phyllosilicate minerals, and at least to some extent the mixing between illite and chlorite, are caused by intergrowths on a scale too fine for the microprobe beam to resolve (i.e., < 2μm). The questions arise,

a) To what extent is there compositional variation in illlites and chlorites, or is the variation in figure 2-23 due to physical mixtures, and

b) Is there any distinction between inclusions and shale matrix?

Illites

In figure 2-24, the microprobe data are plotted in the coordinates described by Velde (1985). The system is assumed quartz saturated; M^+ is the proportion of monovalent

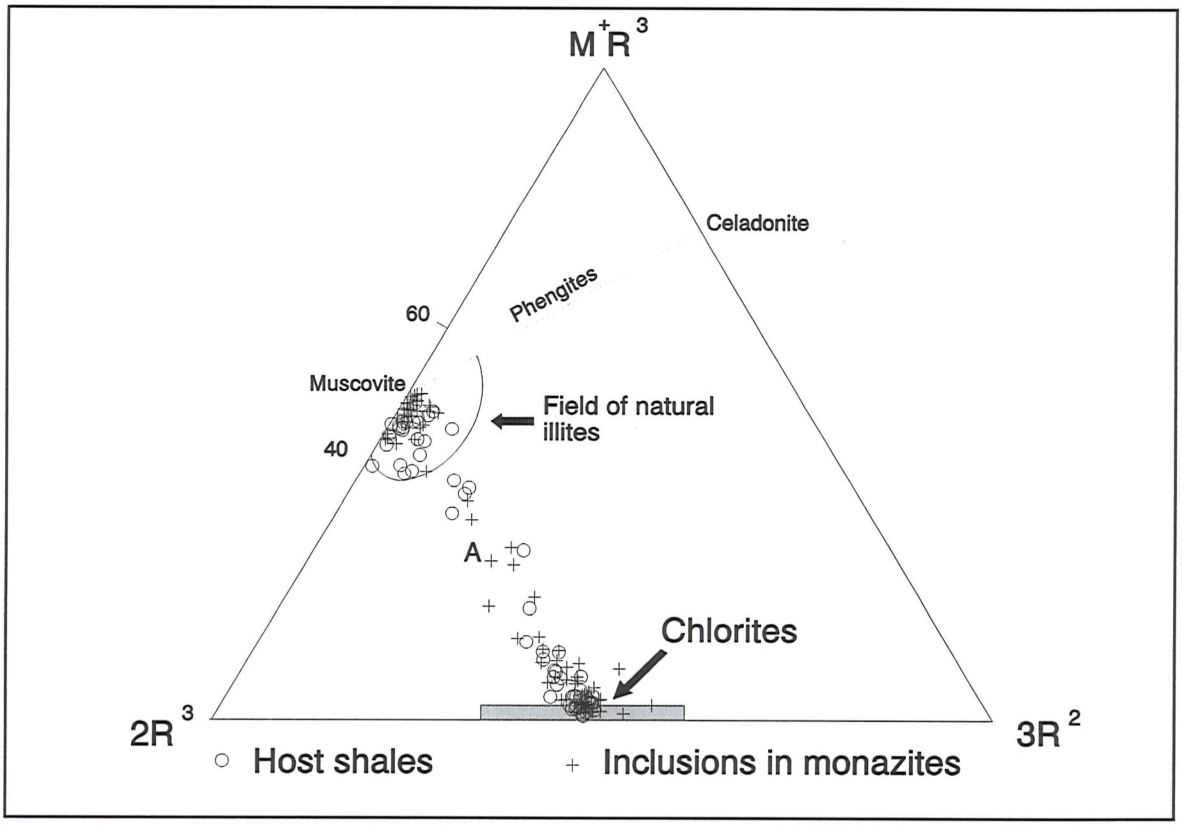

Figure 2-24: Velde plot of phyllosilicate analyses from Calymene Formation. A = average whole rock composition from XRF data.

cations in the formula; R^2 and R^3 are divalent and trivalent cations, respectively. In the absence of quartz, the whole rock composition of the system can be expressed as a simple mixture of illite and chlorite ("A" in figure 2-24). Relatively few illitic points plot outside the field of natural illites described by Velde (1985); there is more of an apparent mixing trend from chlorite towards illitic compositions. Figure 2-25(a) shows the illite field in more detail. Analyses which contain a component of chlorite can be recognised by cation totals higher than 4 (table B-1); in order to avoid any artificial displacement towards chlorite, only points with totals between 3.8 and 4.2 are plotted in the figure.

Figure 2-26 consists of the same data plotted as sodium v. potassium. There is a tendency for the more sodium-rich compositions to have anomalously low (Na + K) totals, which may reflect a systematic analytical error (sodium is a difficult element to measure using the EDS method).

In both cases, however, inclusions and host-rock illites have distinct characteristics.

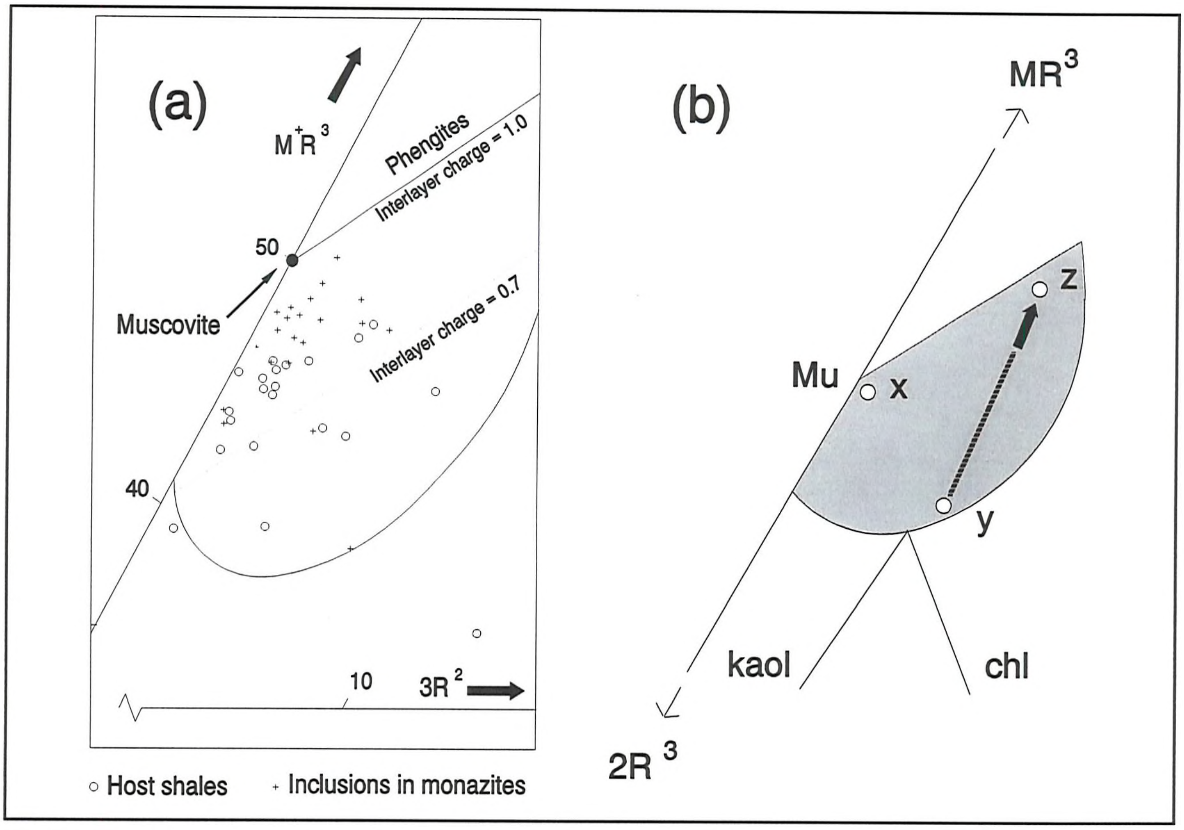

Figure 2-25: (a): Expanded view of illite field in figure 2-24. Points with cation totals > 4.2 have been excluded. (b): Phase relations near illite in MR^3-$2R^3$-$3R^2$ coordinates, after Velde(1985). See text for details.

Illites within monazite nodules are high charge, K-rich micas with interlayer charge > 0.85; minerals in the host shale are more illitic, with interlayer charge < 0.85, unusually high sodium, and a greater content of trioctahedral, divalent cations. Figure 2-25(b) illustrates schematically some different mica compositions formed during diagenesis in the presence of chlorite (Velde,1985). The symbol "x" denotes the position of detrital muscovite, probably of igneous origin, initially present in the sediment. Under upper anchizonal conditions, rims of illite with the composition "y" form on the original grains (Velde,1985). With further increase in grade, the illites tend to a phengite composition (z), typical of greenschist facies rocks.

The most likely origin for the high-charge, K-rich illites found as inclusions in the nodules is detrital igneous or metamorphic muscovite. The host-rock illites, with their high sodium content and lower interlayer charge, are probably authigenic products of diagenesis. This prompts the questions:

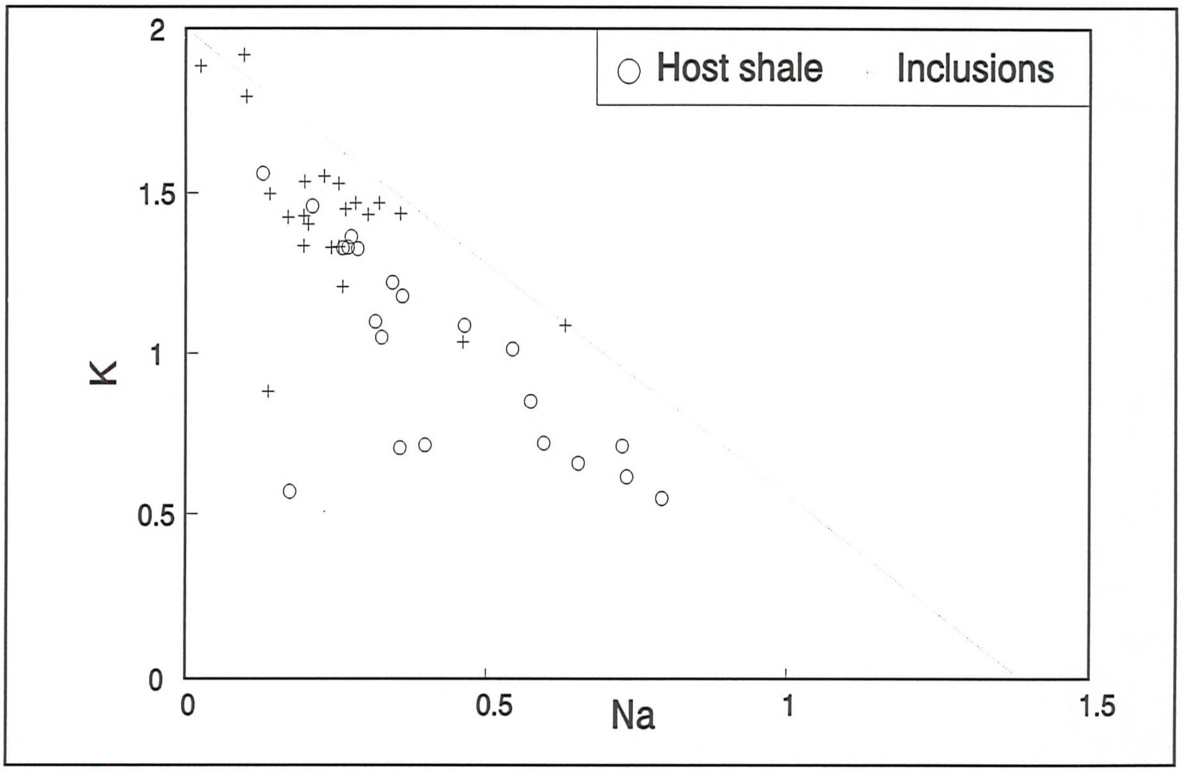

Figure 2-26: Illite data plotted as sodium v. potassium per 22-oxygen formula. The dotted line shows the tendency towards lower M^+totals for Na-rich compositions.

1. Are any high-charge detrital muscovites preserved in the groundmass?, and
2. Why are no lower-charge illites, either detrital or authigenic, found in the nodules?

In response to (1), some groundmass analyses do plot in the "inclusion" field of figure 2-26. As remarked earlier, the choice of analytical points was not statistically rigorous, and there may well be detrital muscovites present in the groundmass of the shale. The 2M polytype observed by XRD very probably corresponds to a detrital high-temperature mica component. The alternative, that they were present and have altered to illite, is hard to accept because it is muscovite which is the stable phase during low-temperature metamorphism, compared to illite, which is metastable.

In considering question (2), it is likely that the original sediment - in a mature, distal shelf environment - contained fine-grained detrital illite with interlayer charge around 1.4 per formula unit, as well as coarser grained muscovites. The absence of such illites within the nodules suggests that it was preferentially replaced by monazite as they grew. This is what would be expected on the grounds of grainsize and stability of muscovite relative to illite.

The absence of authigenic illites as inclusions in the monazite nodules argues for an early diagenetic origin for the monazite. However, the evidence of illite replacement (previous paragraph and figure 2-21) suggests that monazite concretion growth was kinetically favoured over illite, and so even if monazite and illite were cogenetic, neoformed illites would probably not be preserved as inclusions in monazite nodules.

Chlorites

A subset of chlorite analyses was selected according to the criteria: $SiO_2<30\%$; (FeO + MgO)>30%. The resulting 85 points were recalculated to a 28 oxygen formula and plotted in figure 2-27 as tetrahedral aluminium versus iron/magnesium ratio. Curtis et al. (1985) identified discrete chemical fields for the low temperature (Ib) and high temperature (IIb) polytypes by using analytical TEM. The present data cluster around

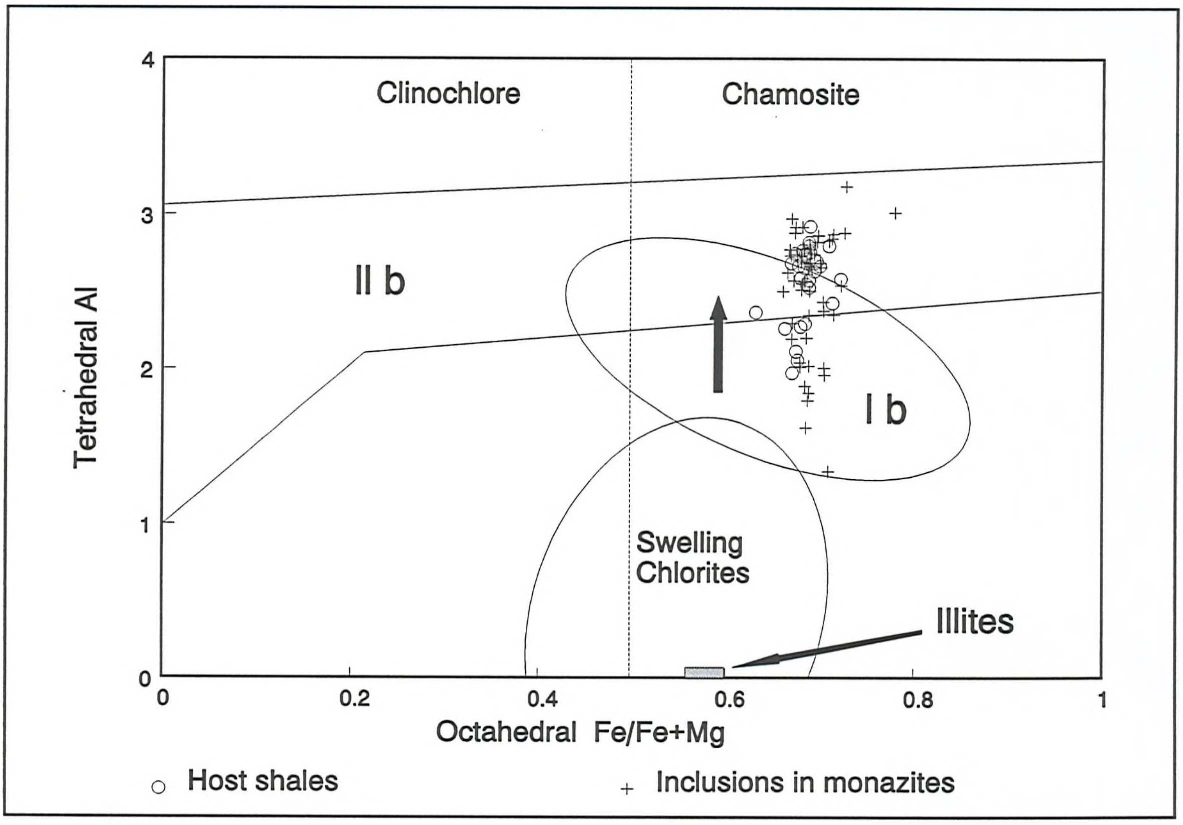

Figure 2-27: Chlorite compositions from Calymene Formation shales plotted in the diagram of Hayes (1970). Polytype fields from Curtis et al. (1985). The arrow shows the presumed evolution of stable chlorite compositions with increasing metamorphism.

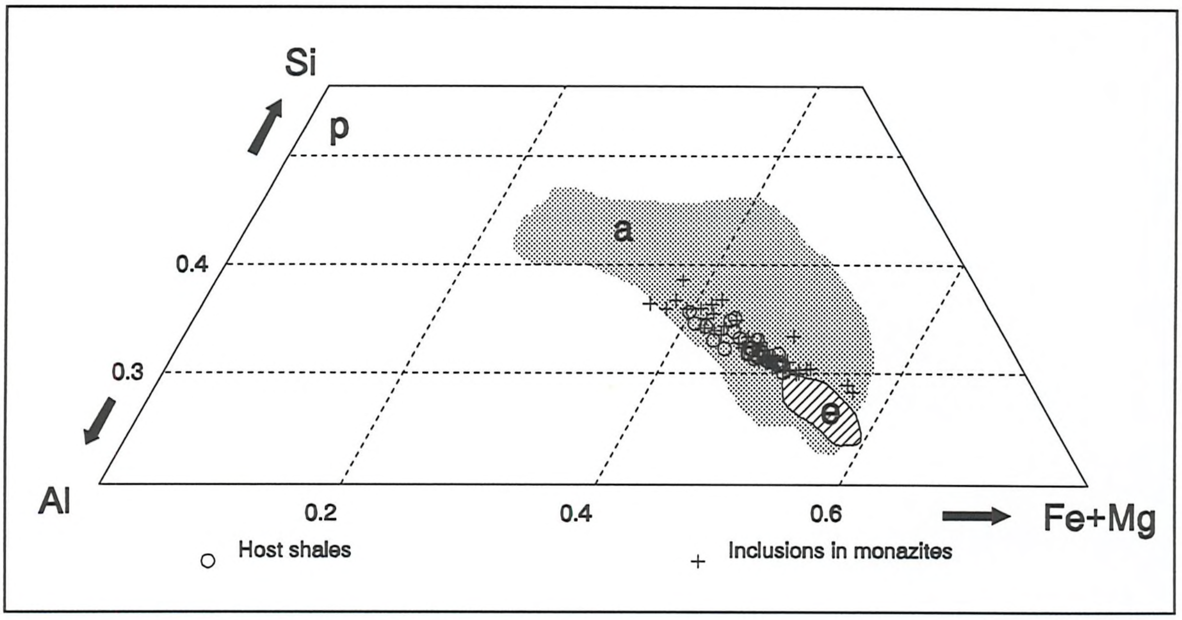

Figure 2-28: Chlorite compositions plotted in part of the triangle Si-Al-(Fe+Mg). Shaded areas are for anchizonal (a) and epizonal (e) chlorites from Wybrecht et al. (1985). P = phengite composition.

a lower temperature paragenesis, from very fine scale mixtures of higher temperature illite and chlorite. The absence of any lb polytype peaks (figure 2-10) favours the mixture option, but XRD methods are not sensitive at low concentrations and lb chlorite preserved as inclusions would probably go undetected.

Wybrecht et al. (1985) studied phyllosilicate compositions from a suite of Moroccan greywackes with metamorphic grade ranging from diagenesis through to the epizone. They found that chlorites were initially derived from detrital biotites. Under diagenetic and anchizonal conditions, a range of chlorite compositions occurs spanning much of the join between the greenschist facies chlorite - phengite end members (figure 2-28). The anchizonal "chlorites" were found to have an interlayer charge of up to ≈1.0 (K+Na+½Ca) per 14 oxygens - i.e., largely biotite chemistry. They still had true chlorite XRD patterns, with a 7Å basal peak (Wybrecht et al., 1985), suggesting that potassium is somehow loosely accommodated in a chlorite structure, rather than in microscopic mica domains. With an increase in grade to the epizone, the field of stable chlorite compositions contracts dramatically towards the ferromagnesian end of figure 2-28, and interlayer potassium is excluded (Wybrecht et al., 1985). A shrinking of the chlorite field with increasing temperature is also reported by Velde (1985).

structure, rather than in microscopic mica domains. With an increase in grade to the epizone, the field of stable chlorite compositions contracts dramatically towards the ferromagnesian end of figure 2-28, and interlayer potassium is excluded (Wybrecht et al., 1985). A shrinking of the chlorite field with increasing temperature is also reported by Velde (1985).

The data from the Navas de Estena shales (figure 2-28) lie within the anchimetamorphic field of Wybrecht et al. (1985), clustering towards the epizone field. The lower grade "tail" of the distribution contains a high proportion of inclusions inside monazite grains; these data points contain up to 0.2 alkali atoms per 14 oxygens (table B-1), well within the range of anchizonal chlorites of Wybrecht et al. (1985). This suggests that the K-rich, Al(lV)-poor, (Fe+Mg)-poor points of figures 2-27 and 2-28 could represent lower temperature chlorite compositions. It is likely that monazite concretions began to form when a relatively wider range of chlorite compositions was stable, and that some of these chlorites were trapped as inclusions, possibly of the lb polytype. With increasing metamorphic grade, chlorites evolved to more ferromagnesian compositions; concretions continued to form and trapped these higher grade chlorites in their turn. Earlier-formed chlorites would have tended to exsolve thin lamellae of illite, leaving a more evolved chlorite, as postulated by Wybrecht et al., (1985). Very fine intergrowths formed in this way are the more quartz-rich and Al(lV)-poor data points of figures 2-27 and 2-28; coarser intergrowths constitute the chlorite - mica stacks of figure 2-14(b) and (f).

2.7 Discussion: timing and temperature of monazite formation

The most reliable piece of evidence constraining the timing of the nodules is their undoubted pre-cleavage origin. Since the cleavage must have formed at or below the maximum temperature of 260 - 275 °C inferred from organic reflectance data, by which stage monazite nodules behaved as rigid concretions, the upper temperature limit for nodule growth must be a somewhat lower figure: perhaps 250 °C.

Monazites appear to have trapped lower temperature forms of chlorite as inclusions. The period of monazite concretion growth spans a significant range of chlorite compositions (figure 2-28), and hence, presumably, temperatures. The cluster of "evolved" chlorites, with (Fe+Mg)/(Fe+Mg+Si+Al)≈0.48 (figure 2-28) and Al(IV)≈2.7 (figure 2-27) contains data points from both inclusions and host rock, implying that chlorites of this composition were syngenetic with monazite.

The shrinking of the chlorite field has not been calibrated in terms of temperature, but in the study of Wybrecht et al. (1985) it is associated with the epizone. It seems likely, therefore, that the "evolved" chlorites included in monazite nodules were formed towards the high-grade end of the range of conditions experienced by the shale. This implies that nodule growth continued almost to the point of cleavage formation.

If this evidence from chlorite compositions is correct, it further supports the idea that authigenic illite was excluded from the growing nodules, leaving only detrital muscovites as inclusions. The compositions of illite-smectite minerals in the host shale cannot, therefore, provide any information about the timing of monazite growth.

The low temperature limit for nodule growth is difficult to constrain. The post-compactional origin of the nodules is not especially informative: Bennett et al. (1981) suggest that a well-compacted fabric can be formed at 80-100 m. burial depth, before any significant heating of the sediment. Although it seems implausible that monazite nodules were growing over the entire range of temperature from burial to almost the epizone, it is a difficult idea to disprove.

A possible low temperature limit is given by the absence of K-feldspar inclusions in monazites, or any K-feldspar pseudomorphs. The disappearance of feldspar during burial diagenesis of mudrocks has been documented by several workers (Boles and Franks, 1979; Hower et al., 1976, Awwiller, 1993). In Texas Gulf Coast cores, K-feldspar becomes unstable and apparently dissolves at temperatures between about 60 °C and 120 °C. While no general reaction has been established, it is likely that it is of the form:

K-feldspar + smectite ± kaolinite = illite + chlorite + quartz

If the monazite matrix acted as a barrier to the transport of K and Al (which is unproven), then any detrital K-feldspars enclosed by monazite would have been protected from this reaction. Alternatively, if only potassium were lost, illite + quartz pseudomorphing K-feldspar might be expected inside monazite nodules. The absence of any such evidence provides a very tentative low-temperature limit for concretion formation of 60-120 °C.

2.8 Distribution of REE within monazite grains

Zoning in grey monazites was first described by Read et al. (1987) from alluvial material; it has since been described in *in situ* monazites from Belgium (Burnotte et al., 1989), Wales (Milodowski and Zalasiewicz, 1991) and Rwanda (Laval et al., 1993). All workers who have investigated monazite chemistry report the same concentric zonation: the rims of the grains are enriched in Ce and La, and the cores in Sm and Nd. Three techniques were used in the present study to examine this zoning: (a) SEM traverses; (b) X-ray mapping on the SEM; and (c) Laser ICP-MS.

SEM Traverses

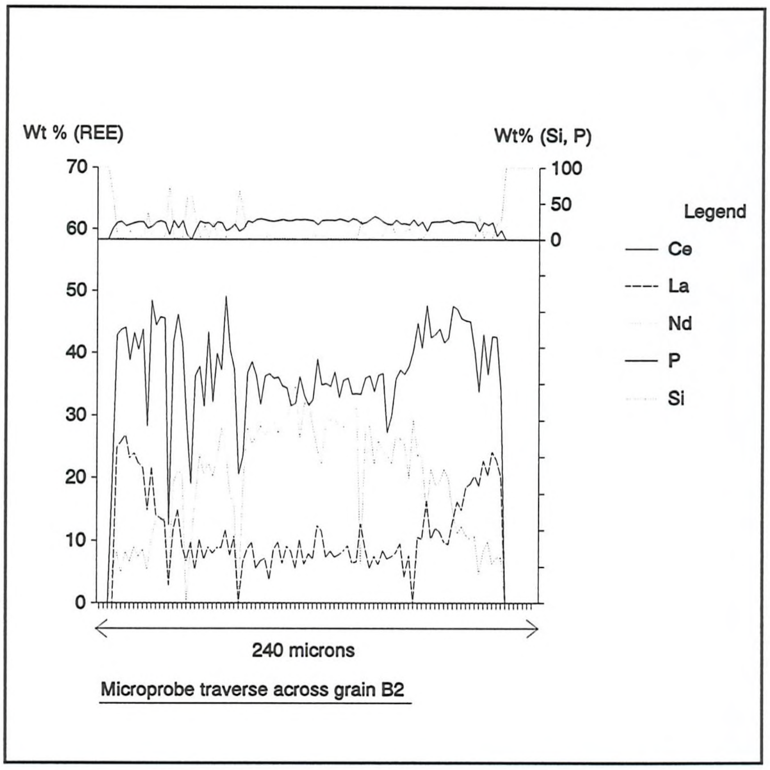

Figure 2-29: Typical traverse across a monazite grain, showing variation in La, Ce and Nd. Si and P variations illustrate the presence of silicate inclusions.

Monazite concentrates which had been separated from large shale samples (chapter 4) were mounted in polished blocks of resin and coated with a carbon film for SEM study. The instrument used was a JEOL JSM-6400 SEM fitted with a JEOL energy dispersive spectrometer and a Tracor series 2 image analysis system. The accelerating voltage was 20 KV, takeoff angle 40°, and working distance 39mm. Automated traverses of 25 points were made across six grains from different parts of the section at Valleleor. An energy dispersive spectrum was acquired for one minute for each data point; this was then processed using the Tracor programme "SQ" to produce a semi-quantitative analysis, normalised to 100%. The electron beam frequently lay partly or wholly on a silicate

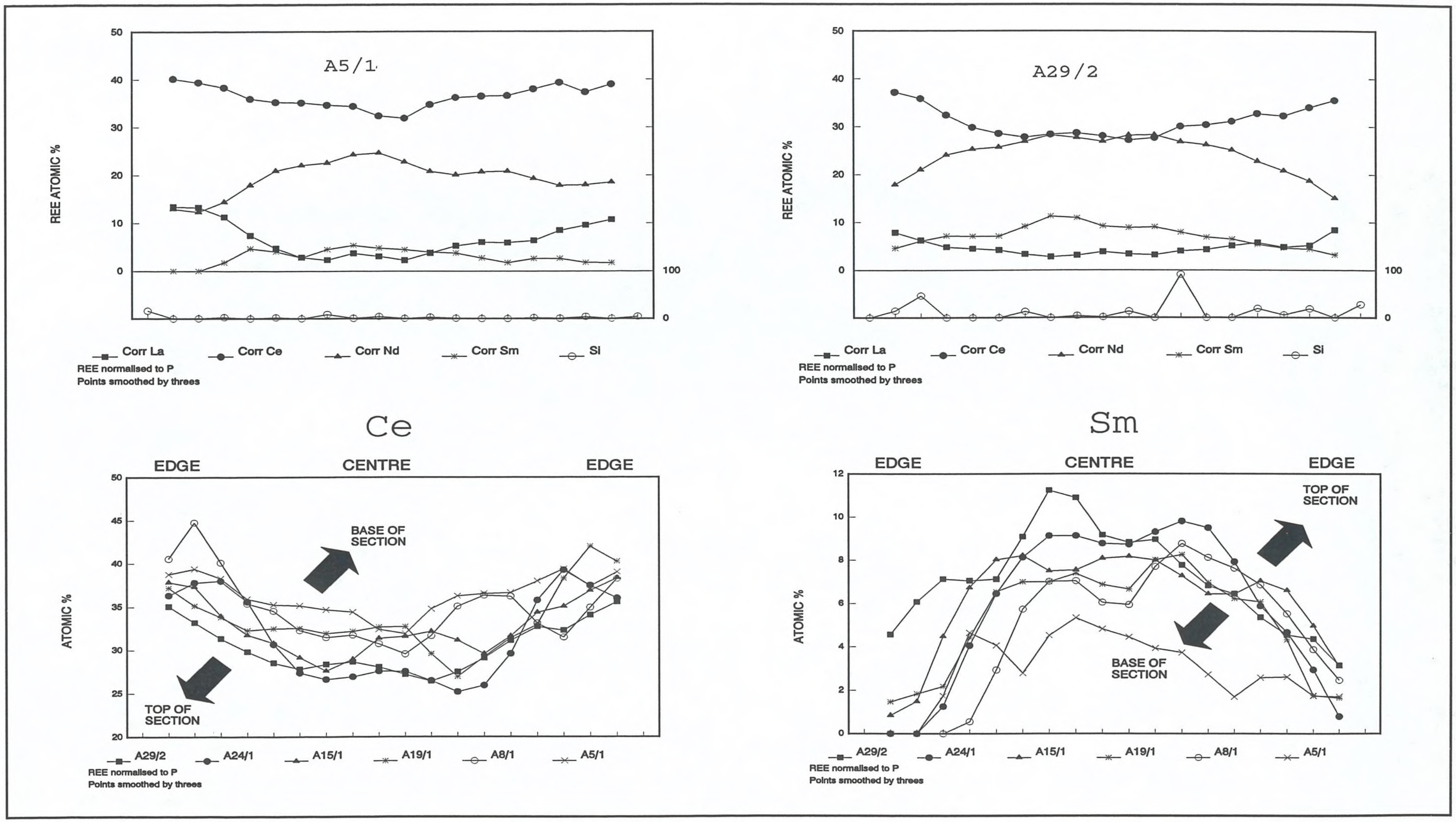

Figure 2-30: Top: Semi-quantitative EDS scans (~300μm long) across two monazites to show zoning. Si peaks denote inclusions. Bottom: comparison of five traverses from A5 (near base) to A29 (top) of section at Valleleor.

inclusion (figure 2-29) so the data were processed according to the following scheme:

1. Points with > 20% SiO_2 were deleted, and the average of their neighbours substituted.
2. Phosphorus was used to normalise all the points in a traverse to the average phosphorus value. Since virtually all the phosphorus is contained in the monazite cement rather than the silicate inclusions, this served to remove the effect of any silicate component in the analysis.
3. A running average of three points was applied across the traverse.

This procedure served to remove most of the noise on the raw data. The top two graphs of figure 2-30 illustrate the typical form of the REE distribution. The zoning of the Spanish monazites is similar to that reported from other locations, with light rims and heavy cores. The sense of the zoning appears to cross over at about praseodymium, which is either very weakly enriched in the cores, or completely unzoned (figure A-5, appendix A). The bottom two graphs of figure 2-30 show cerium and samarium traverses for the six Valleleor specimens. While the traces are all approximately parallel, core enriched for Sm and rim enriched for Ce, an intriguing feature of the Valleleor section is seen: the top of the section is systematically richer in Ce, and the base is richer in Sm. This is discussed further in chapters 4 and 6.

X-ray Mapping

X-ray mapping is a qualitative technique where the background-corrected counts are integrated over a small region of the EDS spectrum corresponding to a particular element. The procedure is repeated for each pixel of a digital image, so that the brightness is a measure of the concentration of the element. Mapping of La to Sm is possible using the Lα lines at 20 kV; for heavier REE, problems with overlaps are too severe to use these lines. Figure 2-31 shows maps of La, Ce and Nd for three monazite nodules. The Si map highlights the inclusions. The data are processed using a linear transform to maximise the contrast in each case. The sense of zoning is

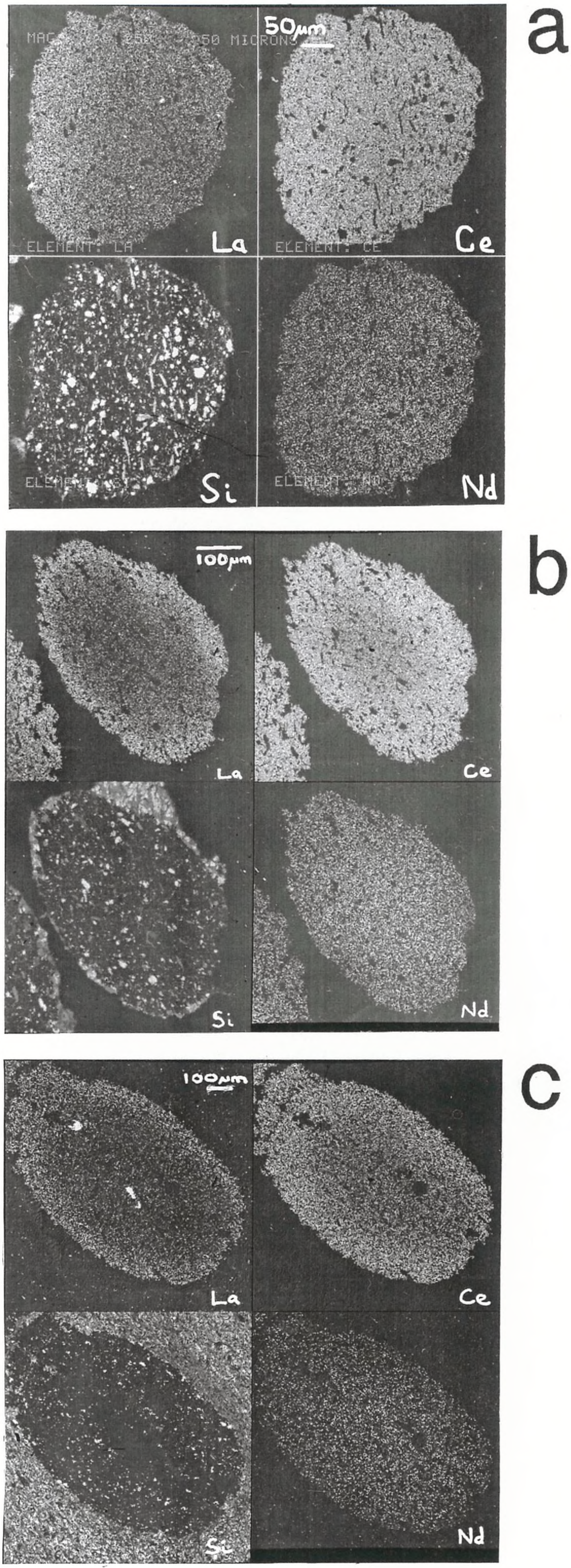

Figure 2-31: X-ray maps of grey monazites. (a),(b): specimen B1, heavy mineral fraction. (c)=B2, *in situ* (same grain as figure 2-16(b)). Bright spot in (c), La map, is rutile, caused by Ti peak overlap with La.

confirmed, with Nd in the cores and La, Ce in the rims. The zoning seems to be rather diffuse; there is no sign of an abrupt change , as might be expected if, for example, a detrital precursor grain had been overgrown. Furthermore, the annular "fringe" of maximum contrast in element concentration - the transition from dark to light in figure 2-31 - is in a different place for different elements. Whatever the process that generated the zoning, it appears to have varied with lanthanide atomic number as well as with time.

To investigate the zoning of heavier REE, mapping of Sm to Dy was done at 5 kV using the M-α lines. These lines, although faint, are free from overlaps with the other REE. Using the low value of 5 kV accelerating voltage maximises their intensity. Figure A-7, appendix A, shows a set of maps for a monazite separated from sample A24. The Gd, Tb and Dy M-α lines overlap with Mg, which is present in chlorite as inclusions and in the attached shale fragment. Mapping times were 12 hours for La to Nd, and 52 hours for Sm to Dy. The grain in figure A-7 shows a relatively sharp zonation of La and Ce, unlike those of figure 2-31. The sense of the zoning is again seen to change around Pr, which shows only very diffuse enrichment in the rim (some EDS traverses on other grains show a similarly diffuse Pr enrichment in the core). The REE from Sm to Dy show a consistent sense of zoning, enriched in the cores.

Laser ablation ICP-MS

This subject is considered in detail in the article included as appendix A. The key geological conclusions are:

1. Two types of chondrite-normalised REE pattern are distinguished. One type, typical of monazite rims, shows a uniform decrease in abundance from La to Lu, with a small negative Eu anomaly (figure A-8(f)). The other, typical of nodule cores, shows a smooth maximum in the light REE at about Nd or Sm, with a similar decrease towards the heavies and negative Eu anomaly (figure A-8(e)). Other patterns are intermediate between these two (figure A-8(b)), giving the impression of a smooth transition from core to rim.
2. The accuracy of the technique is insufficient to allow the measurement of, for

example, Yb concentration across a grain. The biggest problem lies in reproducibility of the quantity of material ablated per shot.

Since the above study, some further work was done using a more sensitive instrument (Plasmaquad PQ2+) at Southampton in 1993. The improved detection limits of the new instrument, and smaller spot size of a laser operating in the ultra-violet spectrum, have overcome some of the problems described in appendix A. It is now possible to measure all the REE even in shales, using a crater size of approximately 10μm (figure 2-32(a)). The method is only semi-quantitative; the laser is fired continuously at low power, 5 shots/second, and 30 seconds integration time used per site. A background measurement is made in the shale away from the monazite grain (figure 2-32(a)) and the subsequent raw counts are then divided by this value to produce shale-normalised plots directly.

Figures 2-32 and 2-33 show the results of two traverses at right angles through an *in situ* monazite grain. The cerium distribution (figure 2-32(c)) shows a much sharper peak in the x- direction than the y- direction. This probably reflects differential compaction: an originally even halo around the nodule has been distorted by subsequent deformation, indicating compaction parallel to x after the monazite had formed. This suggests that the present distribution reflects diffusion towards the monazite as it grew, rather than diffusion away from the grain after it was formed. Lead, thorium and uranium (figure 2-32(d)) are enriched in the monazite and also concentrically zoned: Th and Pb follow La and Ce in being more abundant in the rim, while the sense of U zoning is not entirely clear. This behaviour is not entirely consistent with the ionic radii of the species concerned (table 2-5):

Ion:	Pb^{2+}	La^{3+}	Pr^{3+}	Gd^{3+}	Th^{4+}	Ho^{3+}	U^{4+}	Lu^{3+}
Radius (pm)	129	116	113	105	105	101	100	98

Table 2-5: Ionic radii for selected elements in 8-fold coordination (CN of monazite = 8 to 9). From McLennan (1989).

The y- traverse intersects the core of the grain and shows the REE zoning best (figure 2-33(a),(b)). Only La and Ce are rim-enriched; all the other REE are more

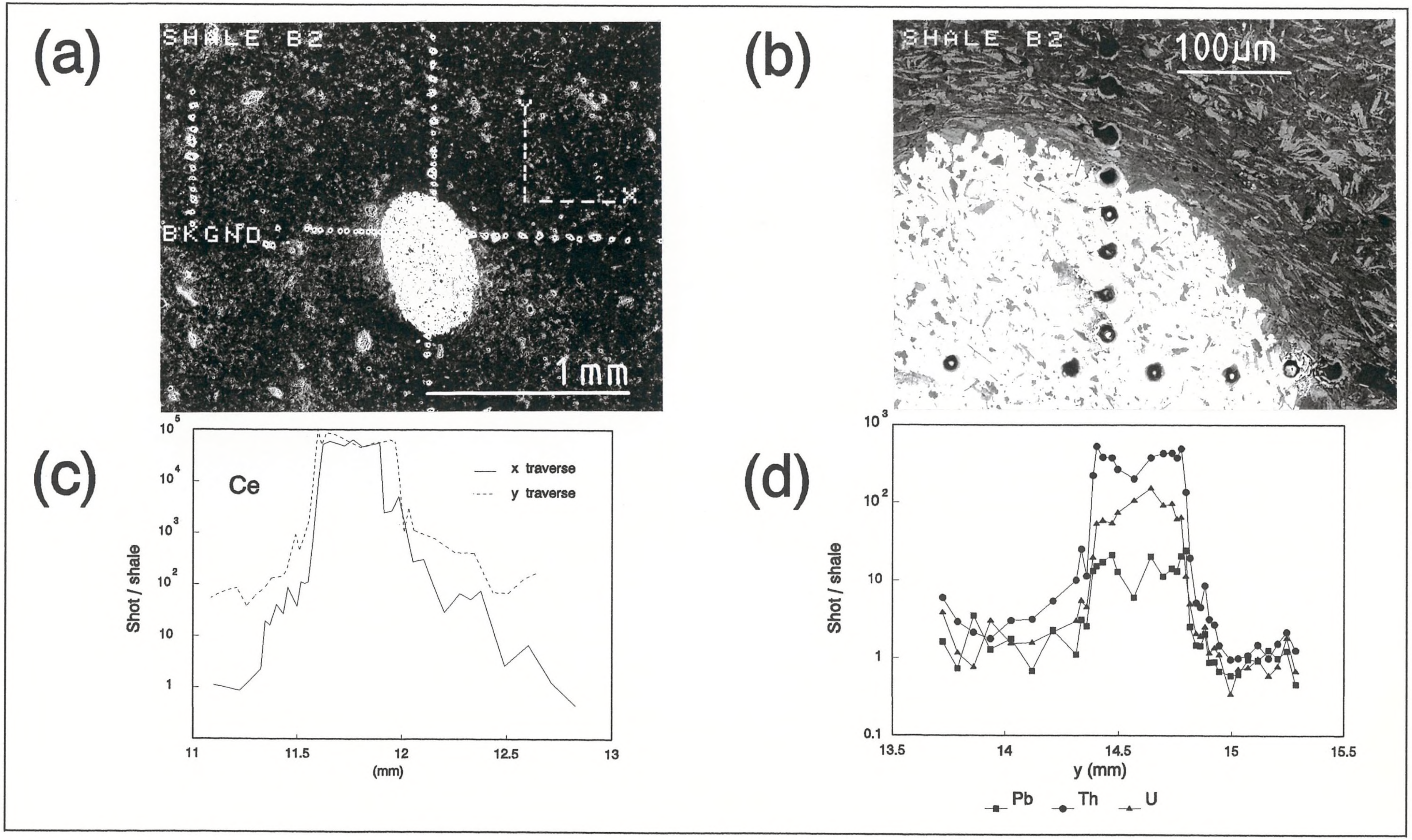

Figure 2-32: (a), scanning electron and (b), backscatter, images of a laser ICP-MS traverse across an *in situ* monazite grain (shale B2), showing x and y axis traverses. Vertical row of shots at left hand side of (a) is the background measurement. Note cleavage deflecting around the grain in (b). (c): cerium traverses. Note the greater dispersion in the y-direction. (d): Lead, thorium and uranium distributions. U is core-enriched like the heavy REE; Th and Pb are rim-enriched like the light REE.

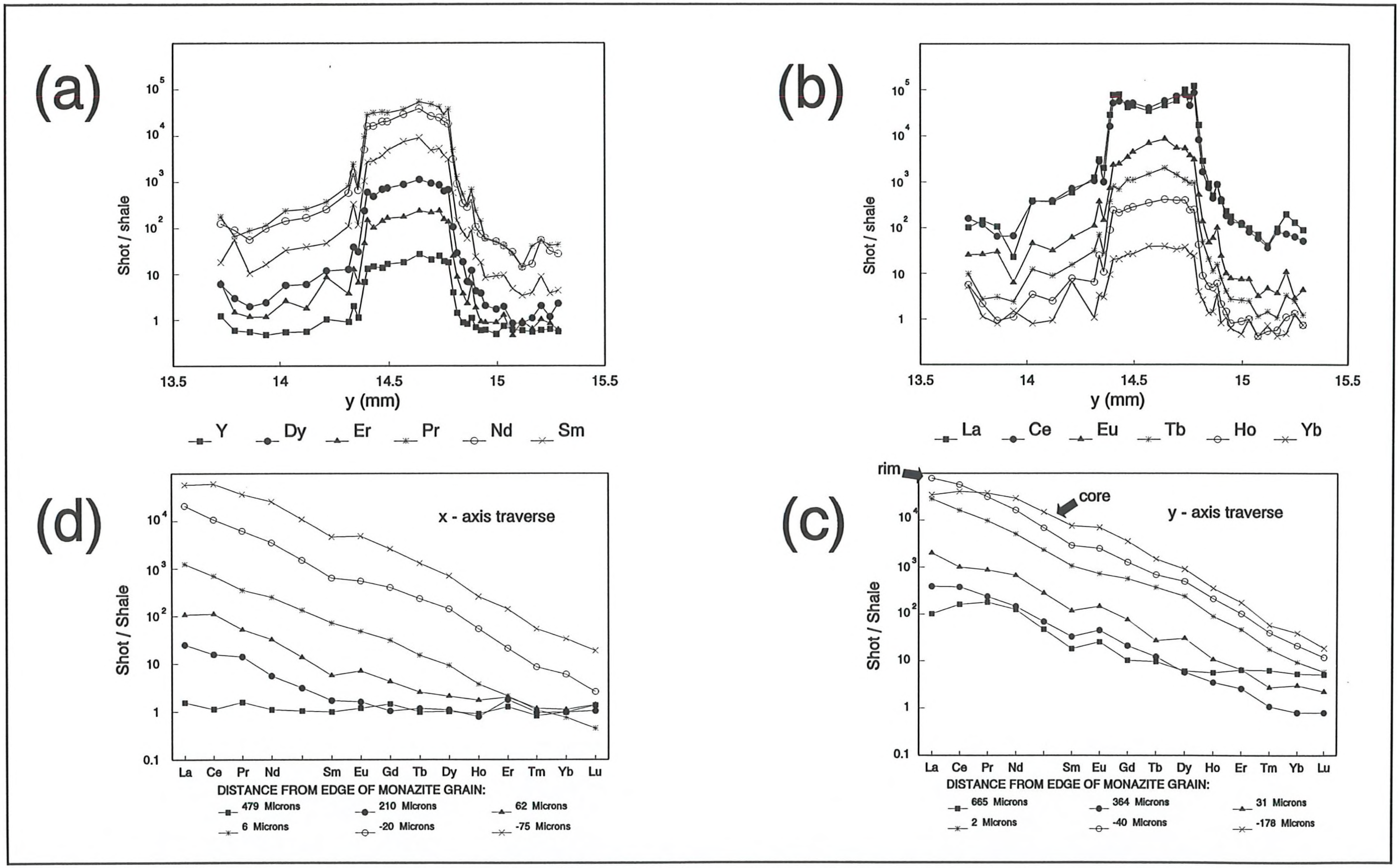

Figure 2-33: (a) and (b): REE traverses across the y- direction of figure 2-32(a), normalised to the surrounding shale. Note zoning of monazite, the sense of which changes between Ce and Pr. Note the dispersion of all the elements, with concentration falling about one order of magnitude per millimetre away from the nodule. (c) and (d): Shale - normalised REE patterns at various distances from the edge of the monazite grain, in the x- and y- directions, respectively. The y- traverse intersects typical core material, peaking around Pr; core and rim type patterns intersect at around Pr.

concentrated in the core, in accord with previous results. The core enrichment is most pronounced for the elements Nd to Eu.

Shale-normalised REE patterns (figure 2-33(c),(d)) are generally monotonously decreasing, light enriched patterns, with no anomalies. The origin of the slight dip at Sm on several patterns is not clear. Only in the very centre of the grain (labelled "core") is there a change to the typical core-type pattern noted in appendix A. This pattern appears to intersect the rim-type pattern (labelled "rim") at a mass just lighter than Pr. REE patterns in the shale approaching the monazite nodule are generally intermediate between flat shale patterns and the rim-type monazite pattern.

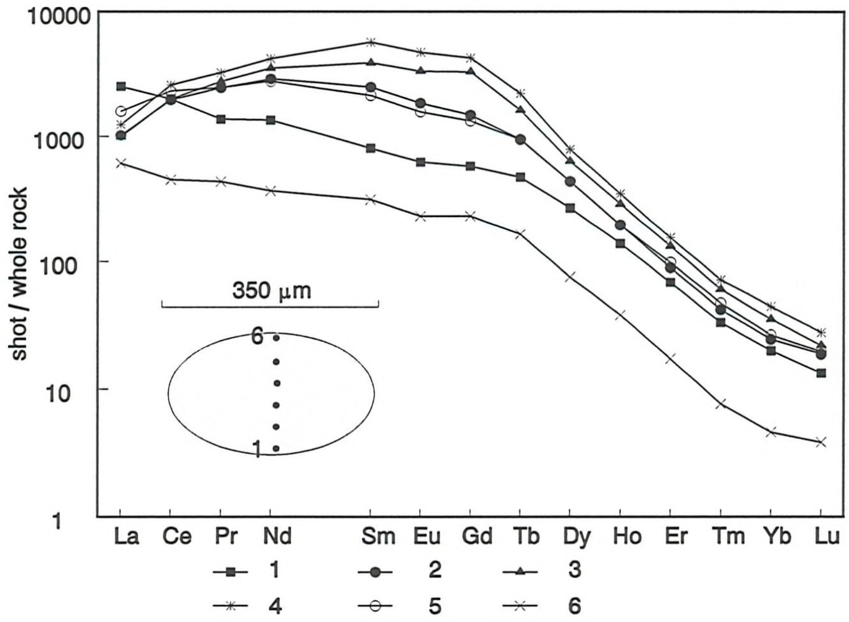

Figure 2-34: Monazite REE patterns normalised relative to the host shale for a nodule from shale B2. Shot 6 partly missed the nodule.

Figure 2-34 shows REE patterns obtained in a laser-ICPMS traverse across a monazite nodule from shale B2, normalised to the whole-rock abundances for B2 measured by solution ICPMS. The changing patterns from rim to core are again clear (shot 6 only partly hit the nodule, and so has lower overall abundances). There is essentially no europium anomaly for the monazite relative to the whole rock, and no distinction between core and rim patterns in this respect, strongly suggesting that Eu was in the 3+ state during monazite formation (see discussion in chapter 6).

2.9 Conclusions: REE zoning in monazites

The sense of zoning in grey monazites reported by previous workers is confirmed in the present study. La and Ce are concentrated in the rims of the concretions; Pr is either unzoned or else weakly enriched in the cores; the heavier REE are more abundant in the cores than in the rims. Refined laser-ICP-MS techniques demonstrate that the zoning exists in all the heavy REE and Y. U, Pb and Th are also zoned.

The monazite structure strongly favours the large REE ions Ce^{3+} to Nd^{3+} over the smaller heavy REE and yttrium. This preference may be thought of as an atomic-mass-dependent low-pass filter; the composition of a monazite concretion will be dictated by a combination of the prevailing fluid chemistry and this crystal-structural filter. A LREE-rich fluid will lead to LREE-enriched monazite, but if the fluid is HREE-rich, the resulting monazite will have a pattern showing a maximum at an intermediate mass (figure 2-35). The change in REE pattern of a concretion from core to rim could be explained by a steady evolution in fluid chemistry from HREE-rich to LREE-rich over the timespan of concretion growth. Whatever the mechanism, it appears to be a process ubiquitous in black shale sequences of widespread origin and age. Possible mechanisms to account for this fluid evolution will be considered in chapter 6.

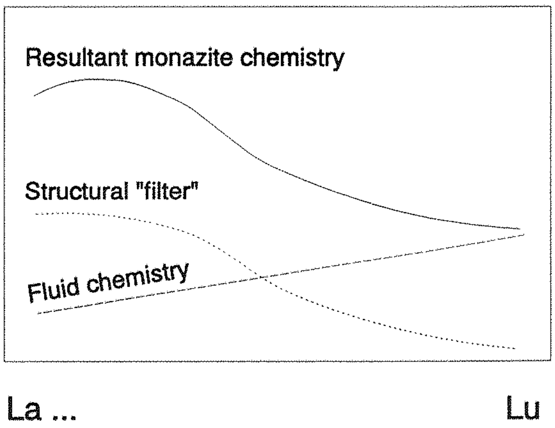

Figure 2-35: Sketch to illustrate how a core-type REE distribution may result from a combination of crystallographic control and fluid chemistry.

Chapter 3: The mineralogical and chemical evolution of silicified cone-in-cone concretions, Valleleor area

3.0 Introduction

Cone-in-cone concretions occur in a relatively narrow zone of the section at Valleleor (figure 3-1), between 10 and 30 metres below the first condensed section at about 290 m above the base of the Calymene Formation. They are texturally similar to other examples of cone-in-cone described from shale or mudstone formations, but differ in having a matrix of quartz and chlorite instead of calcite. A few large concretions were studied in detail to establish their relationship to the grey monazite nodules, and in the hope of gaining some insights into REE mobility during diagenesis.

3.1 Petrography of cone-in-cone concretions

Macroscopically, the concretions weather to a reddish brown colour, and are extremely indurated compared to the surrounding shale. They often weather out as loose cobbles, in which case they have an exfoliated appearance caused by the tendency for fragments of the outermost "cones" to break off. Figure 3-2 shows a section through a typical concretion. A light grey matrix contains thin laminae of darker grey shaly material which define nested "v" shapes, 2-3cm across, with their apices pointing in to the centre of the concretion. The apical angles are between 80° and 120° (Fig. 3-4(a),(d)). In the core of concretion F51, a septarian cavity is surrounded by a zone of cream coloured alteration, with an outer halo of brown coloured alteration (Figs. 3-2,3-3). The cone structures continue all the way to the centre of the altered zone. The mineralogy was investigated by X-ray diffraction; all the patterns obtained consist essentially of mixtures of chlorite and quartz. The bleached zone at the core is predominantly quartz, and the most chlorite rich material is at the rim (Table 3-1).

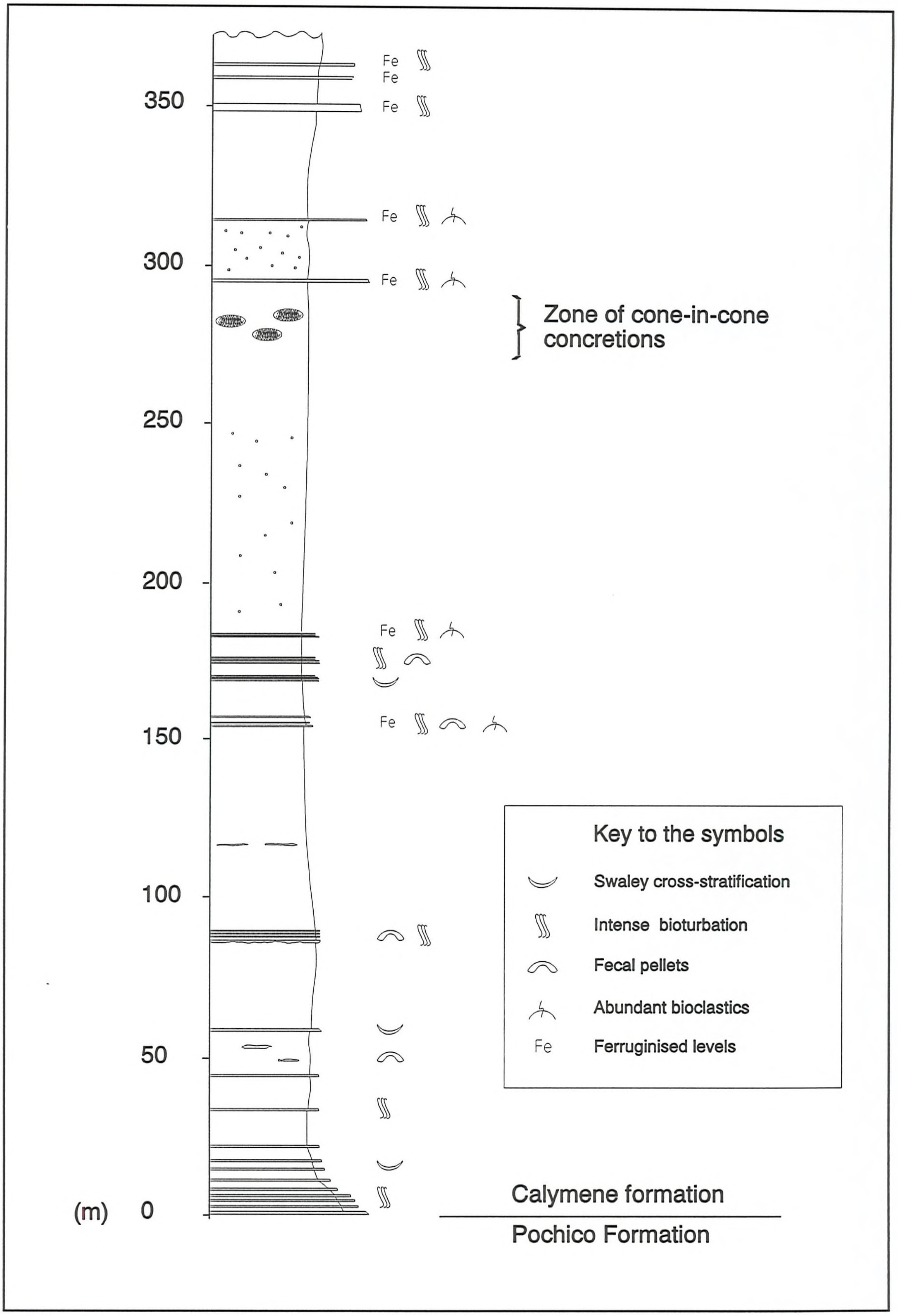

Figure 3-1: Log of Calymene Formation at Valleleor (after Gomez, 1991). For location, see figure 1-9.

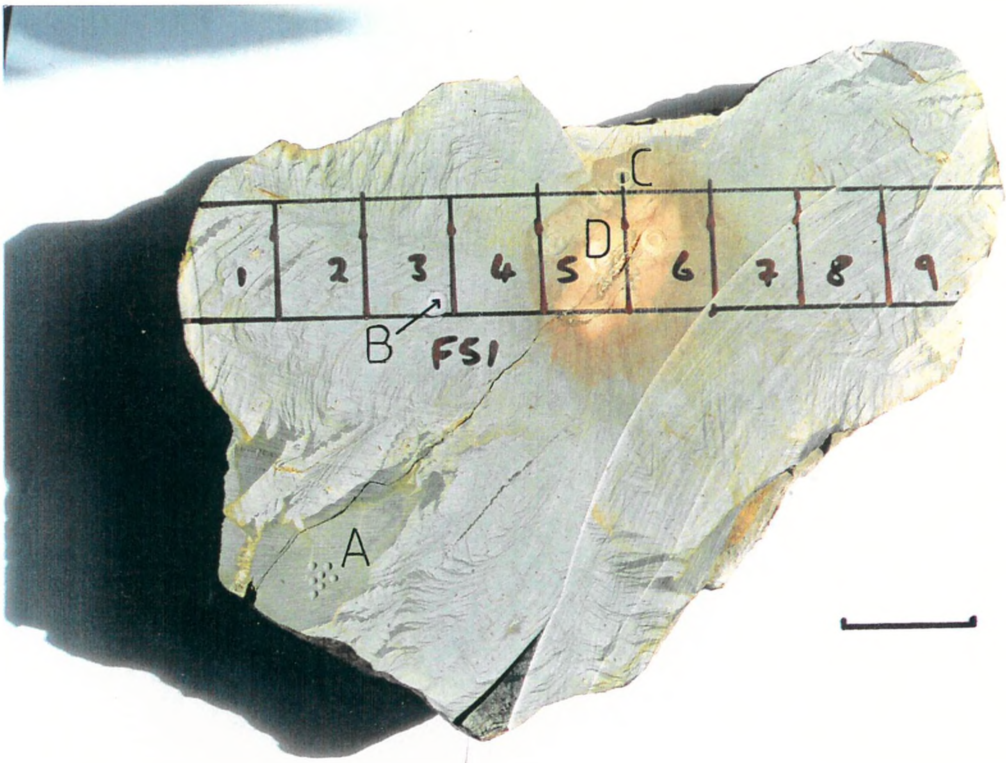

Figure 3-2: Large cone-in-cone concretion from Valleleor. The strip labelled 1 to 9 was ground up for geochemical study. Points A to D are the locations of XRD sampling (see table 3-1). Scale bar = 4 cm.

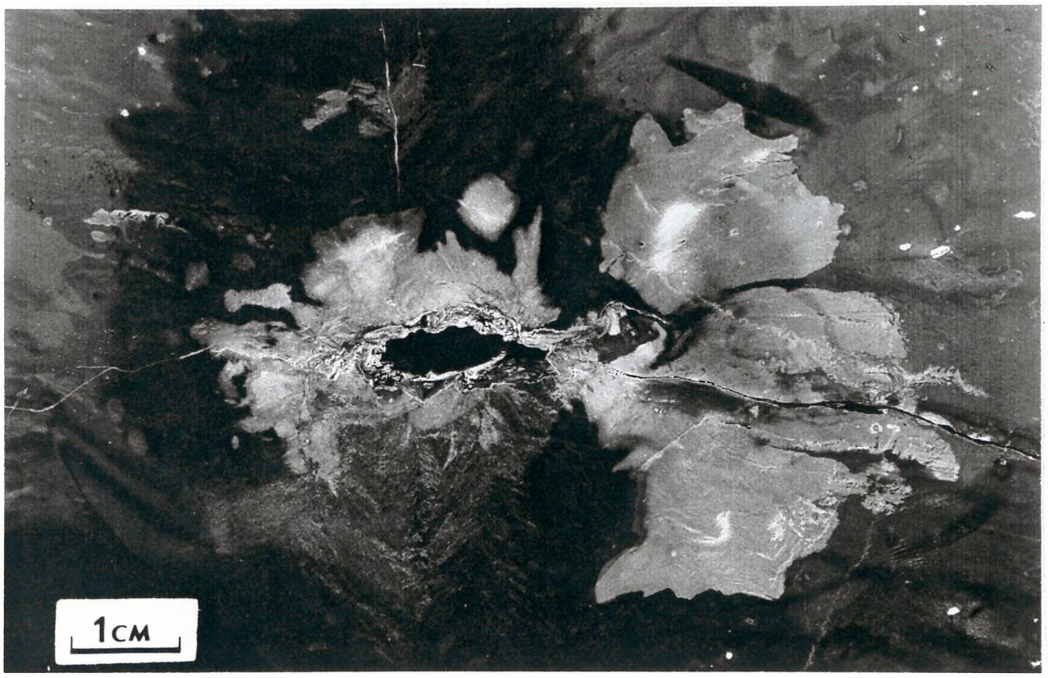

Figure 3-3: Core of concretion F51. Note the mineralised cavity, and the cone structures extending to the centre and overprinted by the bleached alteration zone.

Location:	**A (rim)**	**B (matrix)**	**B (clay fraction)**	**C (outer core)**	**D (inner core)**
Estimated chl/qz ratio	0.6	0.2	0.8	0.3	<0.1

Table 3-1: Rough proportions of chlorite and quartz estimated from XRD traces. A to D refer to positions shown in figure 3.

A <2μm fraction of the light grey matrix material was also found to consist solely of chlorite plus quartz, with a much higher proportion of chlorite. At the margins of the concretion, some larger fragments of shale have been included (Fig. 3-2). In thin section, the shale laminae defining the cone structures are seen to be continuous with these marginal shale fragments (Fig. 3-5(a)). The outside edge of each lamina has a sawtooth profile; the opposite edge is smooth. The sawtooth is formed by a series of *en echelon* blocks with listric shaped microfractures between them. Adjacent cones often intersect in small fractures (Figs. 3-4(a),(b)). Some of the textures give the impression of a plastic, soft-sediment style of deformation (Fig. 3-5(b)). Framboidal pyrites, up to 0.5mm in diameter, are intimately associated with the argillaceous cone laminae (Figs. 3-4(a), 3-5(c)). Larger euhedral pyrites (Fig. 3-5(d)) occur only in the matrix material, and are more abundant towards the rim of the concretion.
Crenulation cleavage is visible in the marginal shale fragments and in the thicker parts of the cone laminae (Fig. 3-5(a)); it has the same sense throughout the section and post-dates the formation of the cone structures. In back-scattered electron images (Fig. 3-6), the matrix consists of chlorite and quartz in roughly equal proportions, with grain size of about 100 μm. Neither mineral shows any preferred orientation, suggesting either a contrast in competence with the associated shale laminae, or a post-deformational origin for this matrix material. In one specimen, a 150 μm concretion of grey monazite was observed, apparently replacing the quartz-chlorite matrix of the cone-in-cone concretion (Fig. 3-6).

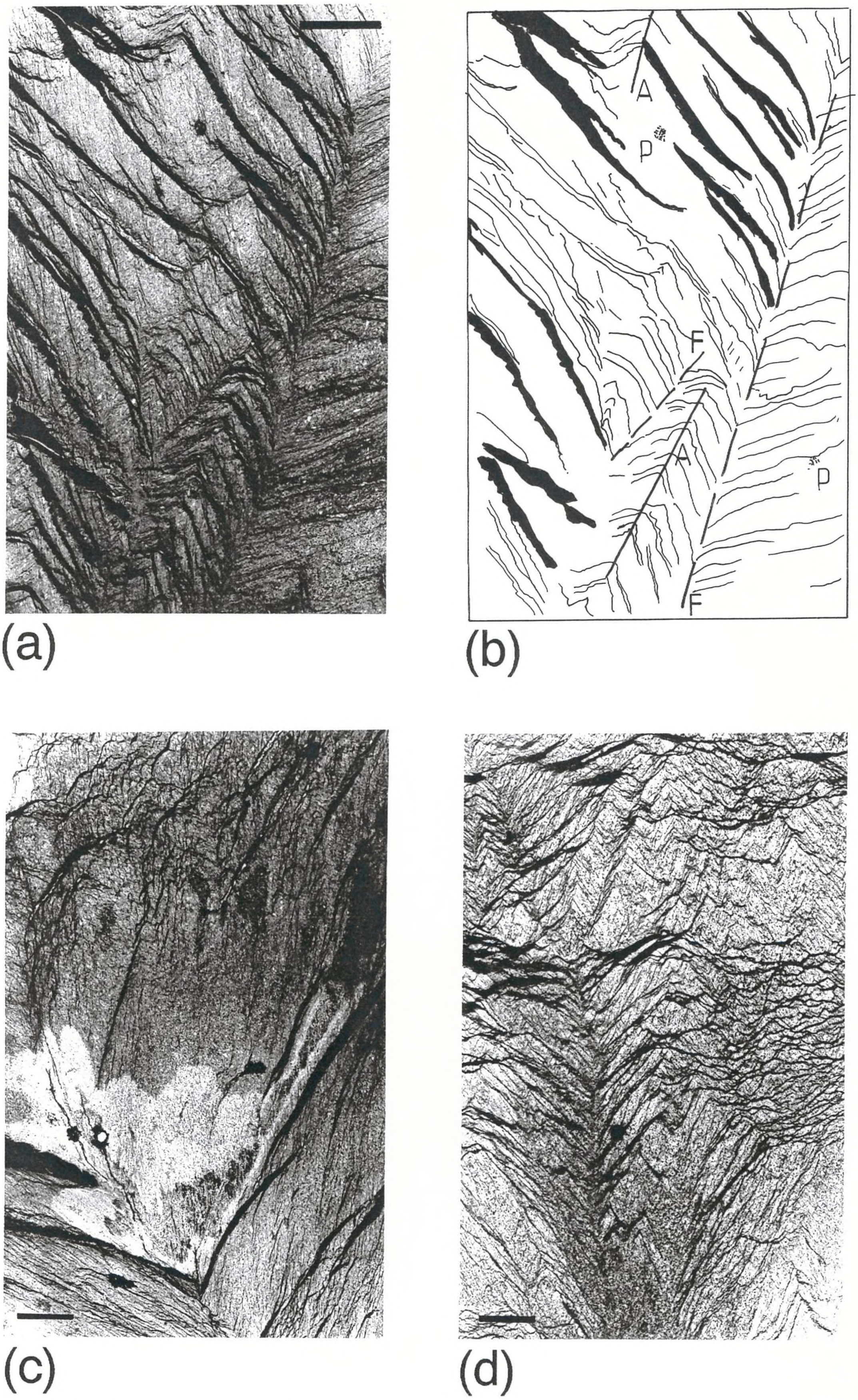

Figure 3-4: Photomicrographs of concretion texture. (a) and (b): nested cone structures intersecting in fractures (F). A = Axes of cones; p = framboidal pyrite. (c): Core of a concretion, showing late alteration. (d): Cone-in-cone texture. Scale bars = 3 mm.

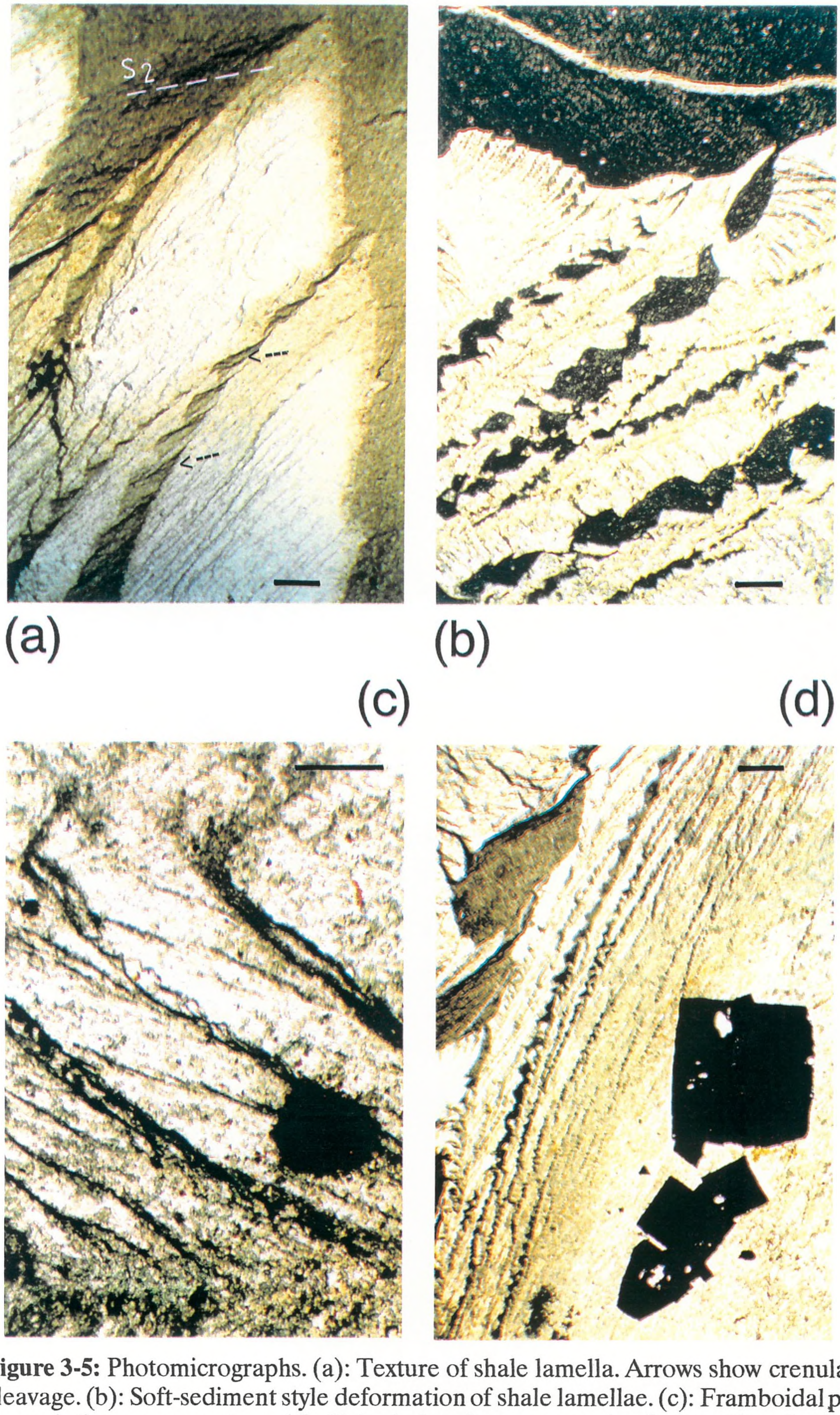

Figure 3-5: Photomicrographs. (a): Texture of shale lamella. Arrows show crenulation cleavage. (b): Soft-sediment style deformation of shale lamellae. (c): Framboidal pyrite overprinting cone structure. (d): Euhedral pyrite near margin of concretion. Scale bars = 0.5mm.

3.2 Mineralized cores

The septarian cavity in the core of concretion F51 is lined with a soft, reddish-brown, gossaniferous material. Study by X-ray diffraction revealed this to consist of some 70 % goethite. After the goethite had been removed by citrate-dithionate digestion, as described by Jackson (1975), the pattern of Fig. 3-8 was obtained. This is closely related to the patterns of alunite family minerals such as hidalgoite ($PbAl_3AsO_4SO_4(OH)_6$) or hinsdalite ($PbAl_3PO_4SO_4(OH)_6$) (Van Wambeke, 1971). A back-scattered-electron image (Fig. 3-7) reveals equant, possibly hexagonal, grains of a Pb-, Fe-, Al-, P- bearing mineral in a mammillary-textured mass of goethite. In order to overcome peak overlap problems with the electron microprobe, the grains of Fig. 3-7 were examined by laser ICP-MS. This gave a qualitative indication of the presence of high concentrations of lead, bismuth, aluminium, iron and transition metals (Fig. 3-9). Sulphur and arsenic are also present in moderate amounts (the technique is insensitive to phosphorus). The mineral in question may be intermediate between hidalgoite and corkite ($PbFe_3SO_4PO_4(OH)_6$), with a significant bismuth content. Iron is more abundant than aluminium, and phosphate is the dominant anion, although sulphate and arsenate are also present. The same mineral was also observed in a shale sample from the same formation, infilling a microfossil test.

3.3 Geochemistry of shales and cone-in-cone concretions

Two concretions, samples F50 and F51, were sampled in traverses of five and nine points, respectively. Major and trace elements were determined for each sub-sample by X-ray fluorescence, and rare earths were determined for concretion F51 by ICP-MS. The results are summarized in table 2 and figures 3-10 to 3-13.

Concentric Zoning

The septarian mineralization has created an anomaly at sub-sample F51-5, and to a lesser extent at F51-6 and F50-2. It consists of a strong enrichment in lead, arsenic, bismuth, iron and phosphorus (Fig. 3-11), clearly correlating with the presence of

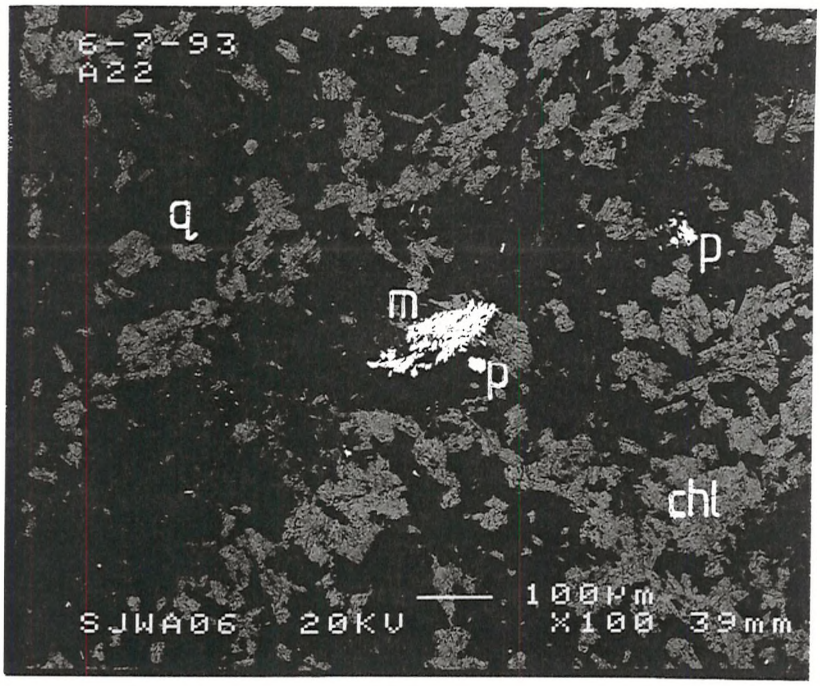

Figure 3-6: Back scattered electron image of concretion matrix, showing quartz (q) - chlorite (chl) cement, grey monazite (m) and pyrite grains (p).

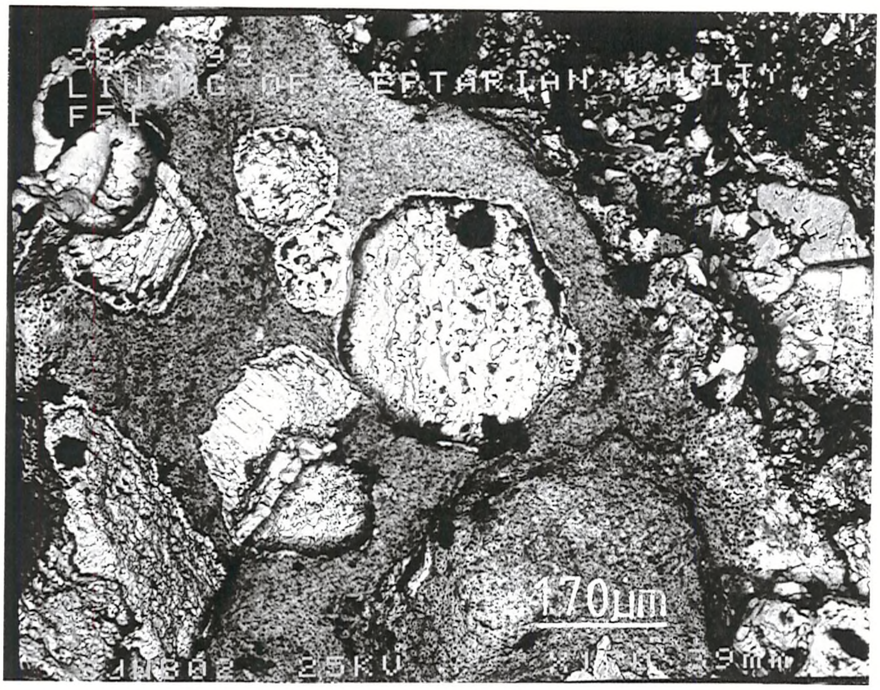

Figure 3-7: Back-scattered electron image of lead-bearing alunite family mineral plus goethite.

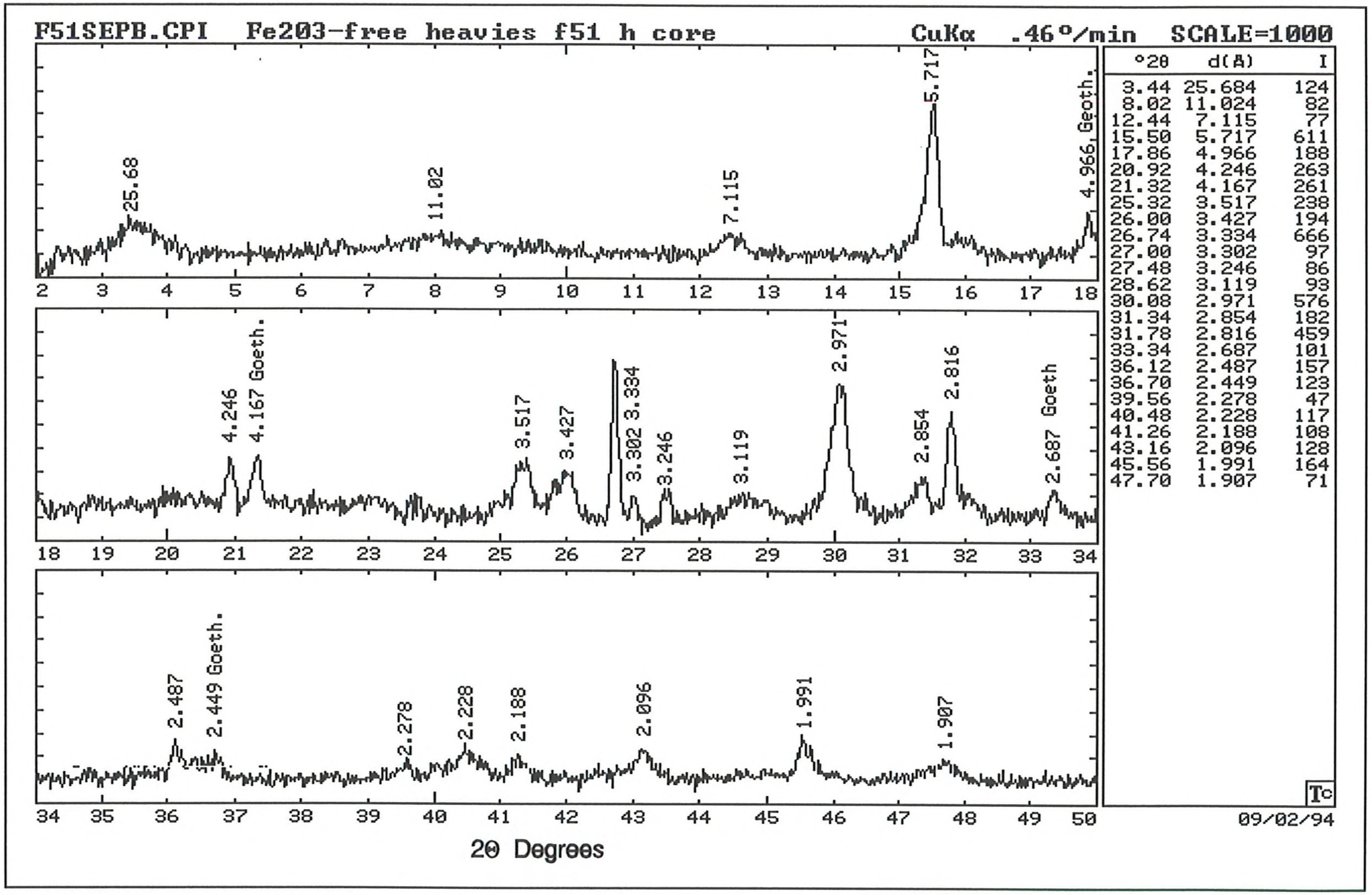

°2θ	d(Å)	I
3.44	25.684	124
8.02	11.024	82
12.44	7.115	77
15.50	5.717	611
17.86	4.966	188
20.92	4.246	263
21.32	4.167	261
25.32	3.517	238
26.00	3.427	194
26.74	3.334	666
27.00	3.302	97
27.48	3.246	86
28.62	3.119	93
30.08	2.971	576
31.34	2.854	182
31.78	2.816	459
33.34	2.687	101
36.12	2.487	157
36.70	2.449	123
39.56	2.278	47
40.48	2.228	117
41.26	2.188	108
43.16	2.096	128
45.56	1.991	164
47.70	1.907	71

Figure 3-8: Background-subtracted XRD pattern of the hidalgoite-hinsdalite mineral from the core of concretion F51. Labelled peaks may be due to goethite impurities.

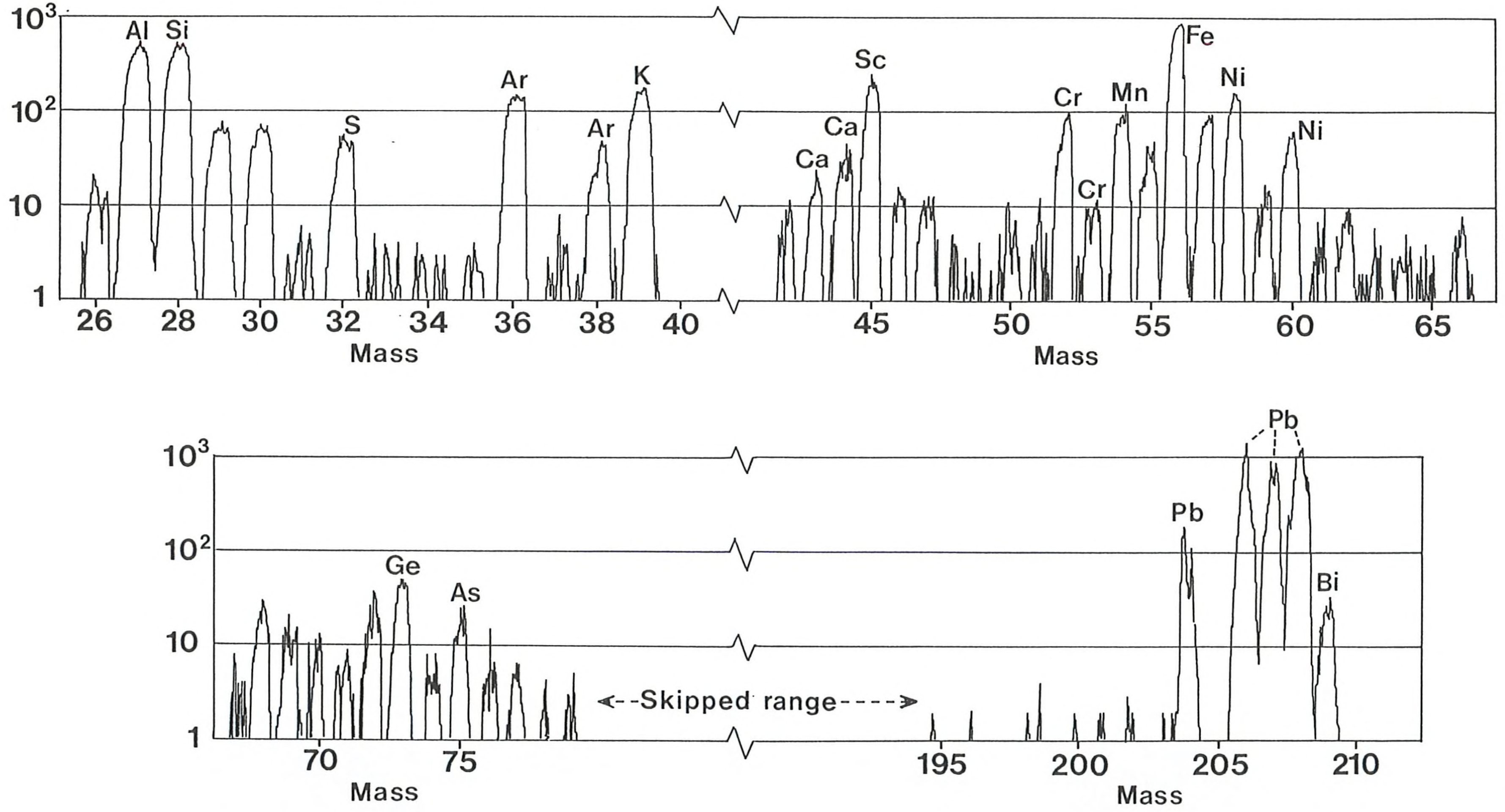

Figure 3-9: Laser ICP-MS scan of the mineral in figure 3-8. Peak area is a qualitative measure of concentration. ^{36}Ar and ^{38}Ar peaks are from the argon carrier gas.

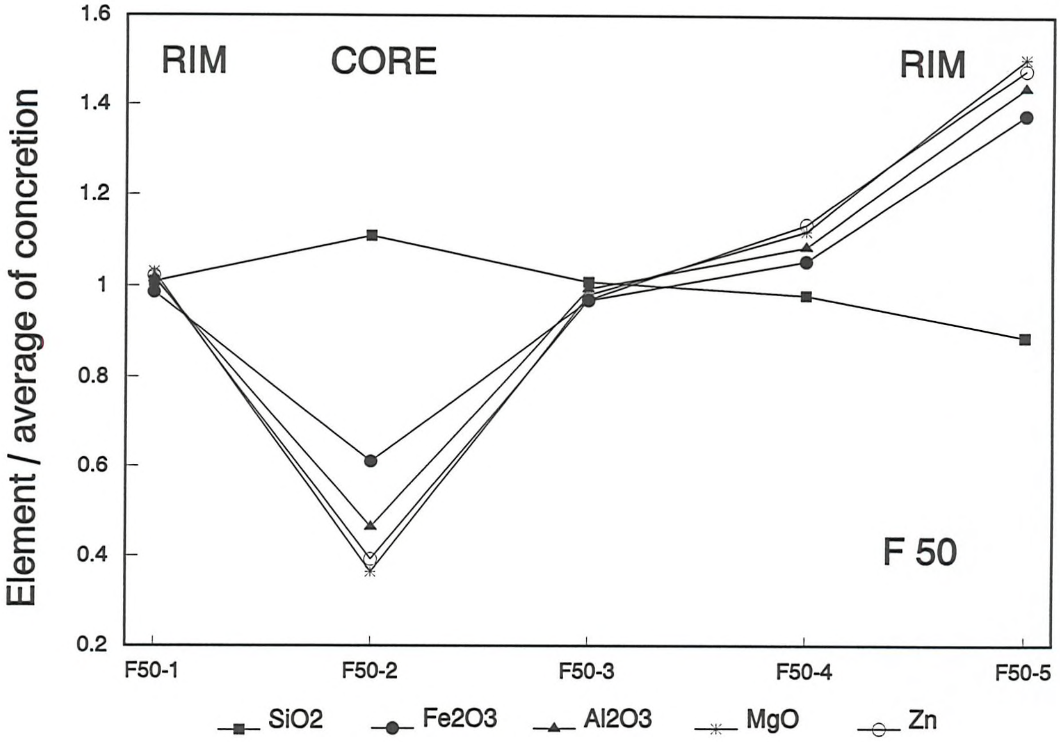

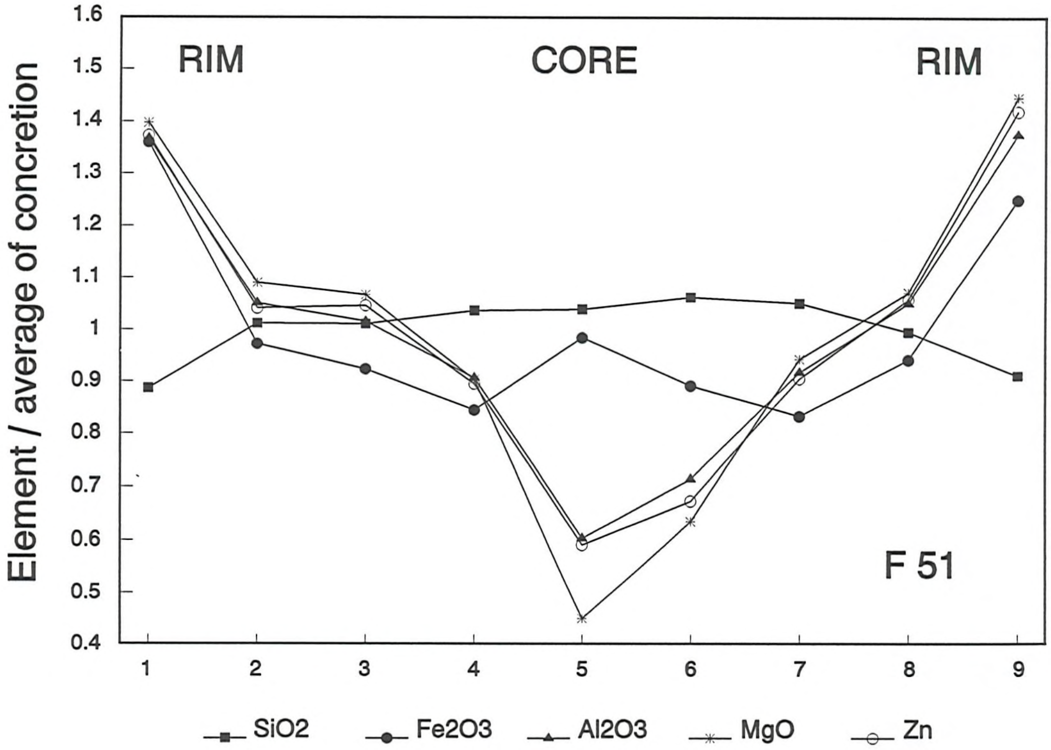

Figure 3-10: Relative variation of major elements across concretions F50 and F51.

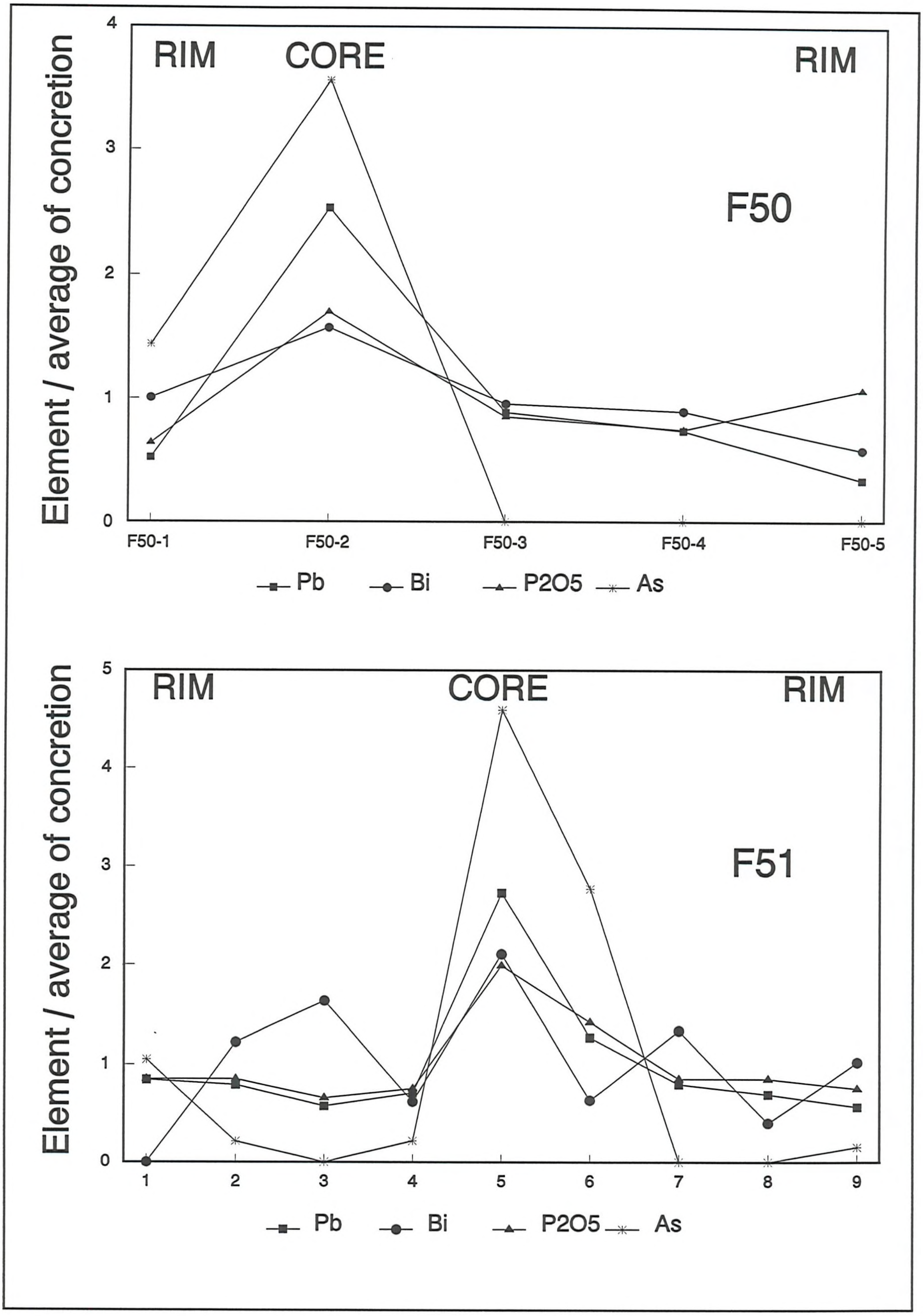

Figure 3-11: Relative variation of trace elements across concretions F50 and F51.

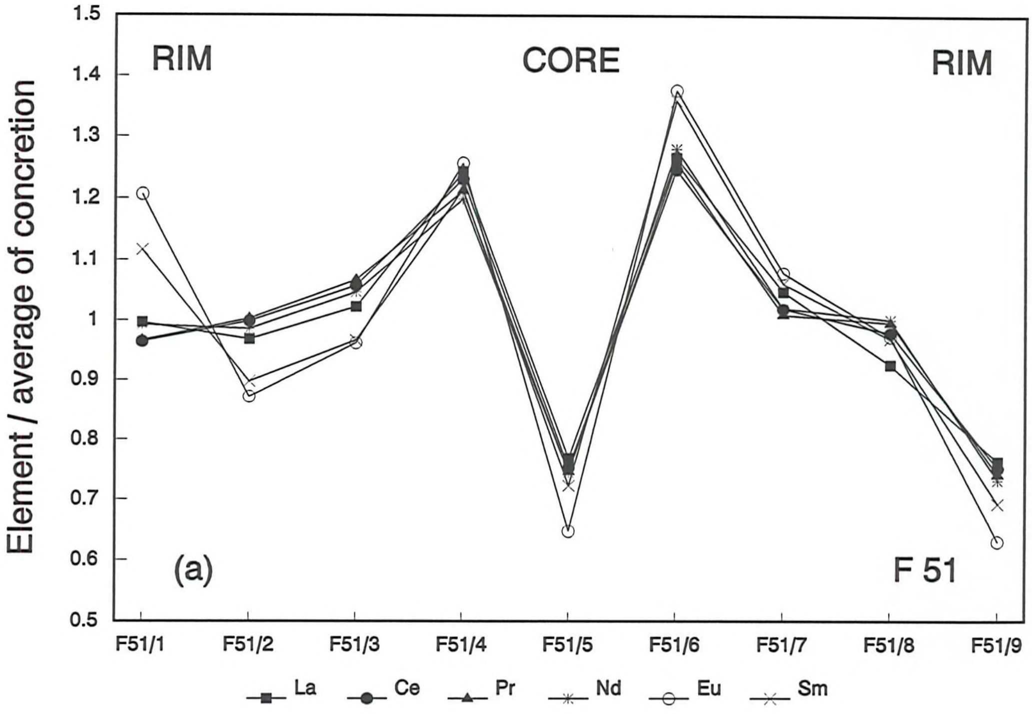

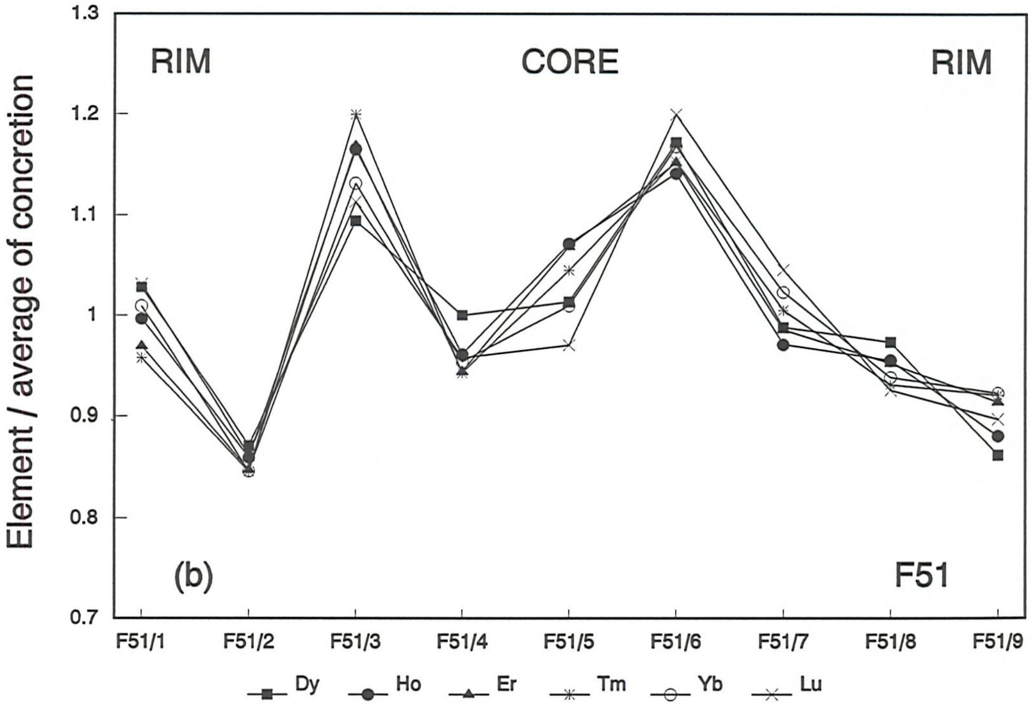

Figure 3-12: Relative variation of (a) light REE and (b) heavy REE across concretion F51.

Wt %	F51/1	F51/2	F51/3	F51/4	F51/5	F51/6	F51/7	F51/8	F51/9	F50/1	F50/2	F50/3	F50/4	F50/5	Shale
SiO_2	66.2	75.5	75.4	77.3	77.5	79.1	78.4	74.2	68.0	78.5	86.3	78.5	76.2	69.1	47.9
TiO_2	0.3	0.3	0.3	0.3	0.3	0.3	0.3	0.3	0.3	0.3	0.2	0.3	0.3	0.3	1.0
Al_2O_3	9.0	6.9	6.7	5.9	4.0	4.7	6.0	6.9	9.0	6.3	2.9	6.1	6.7	8.9	25.5
Fe_2O_3	15.4	11.0	10.4	9.5	11.1	10.1	9.4	10.6	14.1	9.8	6.1	9.7	10.5	13.7	17.2
MnO	0.1	0.1	0.1	0.1	n.d.	n.d.	0.1	0.1	0.1	0.1	n.d.	0.1	0.1	0.1	0.1
MgO	2.9	2.2	2.2	1.9	0.9	1.3	1.9	2.2	3.0	2.1	0.7	2.0	2.3	3.0	3.7
CaO	0.1	0.2	0.1	0.1	0.1	0.1	0.1	0.2	0.2	0.1	0.1	0.1	0.1	0.1	1.4
Na_2O	0.4	0.3	0.3	0.2	0.1	0.2	0.2	0.3	0.2	0.2	0.2	0.2	0.1	0.5	0.8
K_2O	0.1	n.d.	n.d.	n.d.	n.d.	n.d.	n.d.	n.d.	n.d.	n.d.	n.d.	n.d.	n.d.	n.d.	2.2
P_2O_5	0.1	0.1	0.1	0.1	0.2	0.2	0.1	0.1	0.1	0.1	0.2	0.1	0.1	0.1	1.2
LOI	4.7	3.1	3.1	2.7	3.2	2.8	2.6	3.2	3.8	2.7	3.0	2.9	3.0	3.4	
TOTAL	99.3	99.8	98.7	98.2	97.8	99.0	99.2	98.2	98.8	100.2	100.0	100.0	99.4	99.3	101.0
ppm															
As	13	3	n.d.	3	57	34	n.d.	n.d.	2	1	4	n.d.	n.d.	n.d.	24
Mo	n.d.	n.d.	n.d.	n.d.	n.d.	n.d.	n.d.	n.d.	n.d.	n.d.	n.d.	n.d.	n.d.	n.d.	1
Sn	n.d.	2	n.d.	n.d.	n.d.	1	2	n.d.	n.d.	n.d.	2	n.d.	2	n.d.	3
Bi	n.d.	2	2	1	3	1	2	1	1	1	2	1	1	1	n.d.
Cu	336	182	111	63	135	79	21	148	128	42	59	74	60	62	
Rb	2	1	2	2	5	3	1	2	2	0.9	2.5	2.5	1.3	2.0	105
Sr	54	45	39	22	6	10	20	58	49	8.3	10.1	8.4	8.9	14.2	134
Zr	31	31	30	32	40	37	32	30	33	30	31	37	32	35	111
Nb	7	8	7	7	9	9	7	7	8	7.5	6.7	7.7	7.5	7.5	18
Th	n.d.	n.d.	n.d.	n.d.	n.d.	n.d.	n.d.	n.d.	n.d.	n.d.	n.d.	n.d.	n.d.	2.3	17
U	16	6	2	19	39	12	2	n.d.	13	1.91	0.08	1.60	n.d.	0.40	4
Pb	982	925	671	827	3158	1472	929	810	662	425	2085	729	607	272	42
Zn	194	147	148	126	84	95	128	149	201	133	51	126	148	192	215
Ni	50	24	22	14	14	13	14	21	43	23	9	20	26	46	87
Ga	19	16	14	11	18	13	12	15	19	13	13	15	15	17	35
Cr	33	33	28	31	36	41	45	33	46	37	21	37	26	117	103
V	48	39	39	40	34	38	40	42	51	28	26	33	33	42	178
Ba	n.d.	n.d.	n.d.	n.d.	n.d.	n.d.	n.d.	n.d.	n.d.	n.d.	n.d.	n.d.	n.d.	n.d.	392
Y	4.7	4.2	6.1	4.7	5.3	5.6	4.8	4.5	4.4						39.1
La	15.6	15.2	16.0	19.5	12.0	19.8	16.4	14.5	12.0						43.8
Ce	31.0	32.1	34.0	39.6	24.2	40.1	32.7	31.5	24.2						93.7
Pr	3.8	3.9	4.2	4.7	2.9	4.9	3.9	3.9	2.9						11.2
Nd	15.6	15.4	16.4	18.8	11.7	20.1	16.0	15.7	11.5						41.3
Sm	4.2	3.4	3.7	4.6	2.7	5.1	4.0	3.7	2.6						10.0
Eu	1.2	0.8	0.9	1.2	0.6	1.3	1.0	0.9	0.6						2.5
Gd	3.8	3.0	3.3	3.9	2.7	4.4	3.5	3.3	2.5						11.1
Tb	0.4	0.3	0.4	0.4	0.3	0.4	0.4	0.4	0.3						1.7
Dy	1.6	1.3	1.7	1.5	1.5	1.8	1.5	1.5	1.3						8.9
Ho	0.2	0.2	0.3	0.2	0.2	0.3	0.2	0.2	0.2						1.8
Er	0.6	0.5	0.7	0.6	0.6	0.7	0.6	0.6	0.5						4.1
Tm	0.1	0.1	0.1	0.1	0.1	0.1	0.1	0.1	0.1						0.6
Yb	0.6	0.5	0.7	0.6	0.6	0.7	0.6	0.6	0.5						3.5
Lu	0.1	0.1	0.1	0.1	0.1	0.1	0.1	0.1	0.1						0.5

Table 3-2: Major and trace (by XRF) and rare earth element (by ICP-MS) traverses across concretions F50 and F51. See figure 3-2. Shale analysis was on an ignited powder (LOI = 0). n.d.=not detected.

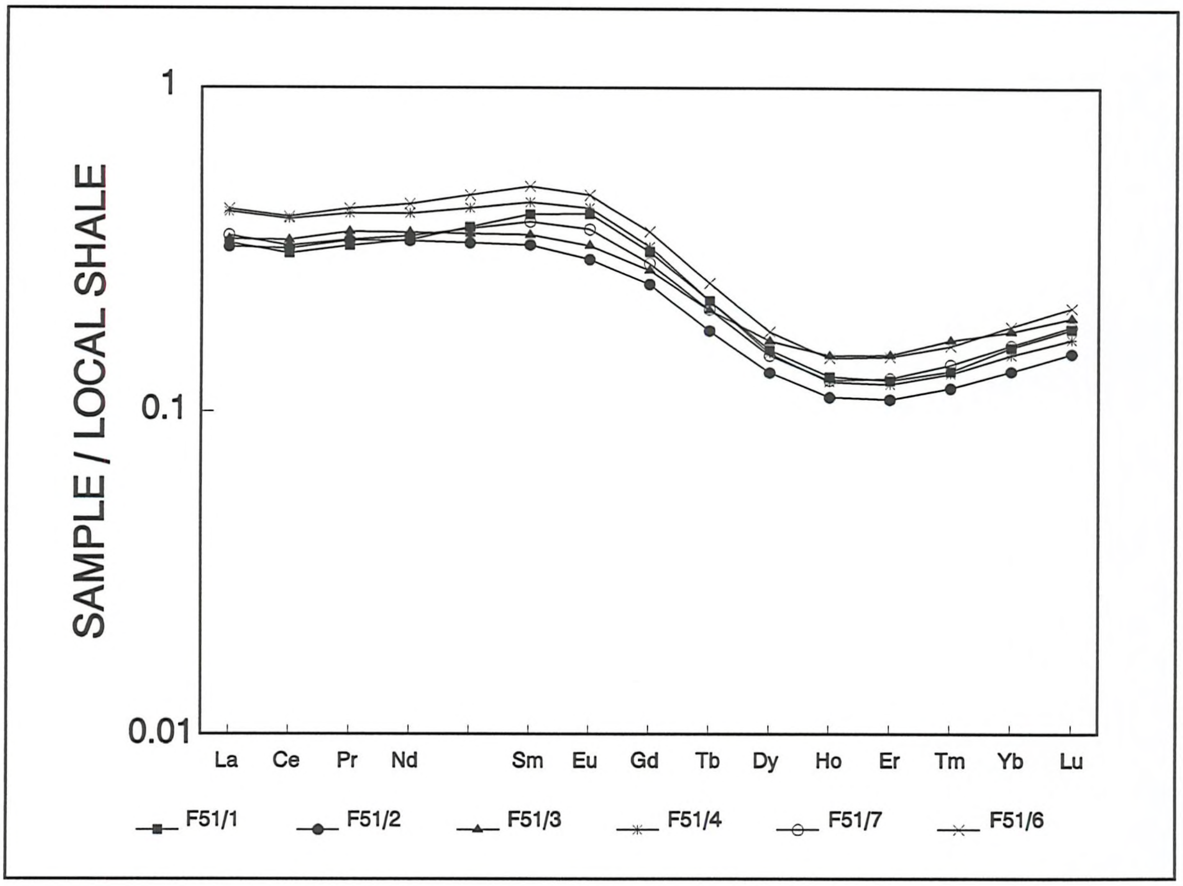

Figure 3-13: REE patterns of subsamples of concretion F51, normalized to the local shale (see table 3-2).

the alunite mineral described above. The same mineralizing process has apparently leached the light and middle REE from the core of concretion F51 (Fig. 3-12). Notwithstanding the anomalous core, there is a radial zonation in the concretions. Fe, Al, and the transition metals Mg, Ni, Zn and Cu are enriched in the rim relative to the core (Fig. 3-11). Si is slightly enriched in the core (Fig. 3-10). From the overall shape of the patterns in figure 3-12, the REE appear originally to have been enriched in the core of the concretion; subsequently the light REE (Fig. 3-12(a)), and to a lesser extent the heavy REE (Fig. 3-12(b)), were leached by late stage alteration.

Chemistry of the concretions compared to the host shales

The REE pattern of concretion F51, normalized to the surrounding shale, is shown in figure 3-13. The light REE are depleted by a factor of about three relative to the shale, and the heavies by a factor of about five, with a smooth minimum at erbium. The effects of the radial REE zonation are secondary compared with this overall heavy REE depletion. Other relatively immobile trace elements, Zr, Ti and Nb are likewise depleted by factors of 3.4, 3.6 and 2.3, respectively. The light REE depletion can thus plausibly be explained by a three-fold compaction of the shales after the formation of the concretion. This would correspond to an original porosity of about 67%, which equates to a depth of ten metres, according to the shale compaction curves of Baldwin and Butler (1985). The heavy REE depletion is discussed below.

3.4 Discussion

Cone-in-cone was reviewed by Tarr(1932), who ascribed its origins to a combination of overburden pressure and pressure solution of calcite. The argillaceous laminae were the insoluble residue of solution effects. The structures of figure 3-5(a) clearly result from extension parallel to the clay layers causing fracturing; other textures (e.g. Fig. 3-5(b)) appear characteristic of soft sediment deformation. These conclusions are in agreement with later authors (Gilman and Metzger (1967), Franks(1969)) who invoke pressures associated with the growth of carbonate minerals to explain the fracturing of the clay layers. Gilman and Metzger (1967) suggest that the inversion of aragonite to calcite, with its associated volume increase, was responsible for the deformation of the shale laminae in concretions from Devonian shales from New York State. They describe textures identical to those seen in the Calymene formation, and, in addition to the small *en echelon* style fractures already noted, recognize fractured boundaries on the opposite, smooth suface of each clay lamina:

> "In detail it is noted that one side of each major fracture is smooth and uninterrupted whereas the opposite side has a series of steplike offsets caused by the minor fractures. The uninterrupted side of the fracture always forms the outside of a cone or conic scale." (Gilman and Metzger (1967))

No clear evidence was found in the Spanish concretions for these "major fractures". Franks (1969) examined cone-in-cone from Cretaceous shales in Kansas. He rejects the idea of fractures, concluding:

> "The cone structures are the product of the growth of cone-shaped plumose aggregates of fibrous calcite in argillaceous sediment, either muddy or sandy. The clay films that outline the conic scales stem from the disturbance and displacement of the original sediment by the growing fibers of calcite. So-

> called cone fractures in Kiowa cone-in-cone are not the products of fracturing, but rather are growth boundaries between sets of plumose aggregates of fibrous calcite."

The cone-in-cone concretions from Valleleor differ from published descriptions in having a matrix of microcrystalline chlorite plus quartz, instead of carbonate. The similarity of the detailed structure of the shale laminae to the "conic scales" of Gilman and Metzger (1967) or Franks (1969), strongly suggests a common origin for all the concretions, i.e. that the Valleleor concretions originally had a calcitic or possibly sideritic matrix that has since been replaced. Development of the cone structures involved extension parallel to the clay laminae, resulting in a pattern of small fractures, and was probably associated with the growth of carbonate crystals. The resulting increase in volume of the concretions may have caused the development of septaria in their cores (Todd, 1903).

The concretions were formed at shallow depth, while the sediment was still able to deform plastically. After burial and compaction of the surrounding sediments until anchizonal conditions were reached, the carbonate matrix of the concretions was replaced by the present chlorite - quartz assemblage. The heavy-depleted shale normalised REE pattern of figure 3-13 may result from REE fractionation during diagenesis. Calculations by Wood (1990b) suggest that the solution behaviour of REE at temperatures of above 200 °C is dominated by fluoride complexing at all but very high pH values. Since the stabilities of REE-fluoride complexes increase from La to Lu (Wood,1990a), preferential dissolution of the heavy REE could have occurred, producing the observed pattern. The concentric zoning which is observed in the REE as well as in many more mobile elements was probably produced at the same time. At some intermediate stage of the alteration, the nodule would have existed with a carbonate-cemented core and a silicate rim; the resulting gradient in pH may have caused some migration of REE towards the core. The enrichment of iron and transition metals in the rim of concretion F51 is as a result of the greater modal abundance of chlorite there relative to the core. These relatively mobile elements were presumably introduced at the same time as the alteration of the matrix. The silica enrichment is associated with a greater modal abundance of quartz in the core relative to the rim, and is probably associated with the lead- and iron-bearing septarian alteration of the core. This alteration is characterised by oxidised mineralogy (goethite, corkite-hidalgoite) and fracturing of the concretion; it is probably related to recent weathering. The associated leaching of light REE from the core of the concretion probably occurred at near-surficial temperatures and neutral to acid pH. Under these conditions, REE are mobile as Ln^{3+} ions (Wood, 1990a; Lee and Byrne, 1992). The light REE ionise more readily than the heavy, which may account for the increased light REE depletion.

Raiswell (1987) presents models where the growth of carbonate concretions is localised at or above the zone of methanogenesis. He also points out that a hiatus in sedimentation is required if a discrete horizon of concretion growth is to occur, rather than a disseminated zone of carbonate precipitation. The occurrence of cone-in-cone concretions twenty metres below a "condensed section" suggests that a pause in sedimentation was likewise important at Valleleor. The horizon of the cone-in-cone concretions coincides with a minimum in whole-rock organic carbon (sample A22, Fig. 4-7). Despite the high iron content of the shale, there is very little pyrite ($S < 300$ ppm). This suggests that, of the mechanisms of concretionary formation proposed by Raiswell (1987), iron reduction in the zone of methanogenesis is the most likely to apply. Oxidation of an organic reducing agent would have produced excess bicarbonate ions (Coleman, 1985, reaction(9)), leading to the precipitation of an iron-rich carbonate. Although the original carbonate cement has been replaced, the high iron/calcium ratios of both shales and concretions suggest that it may have been sideritic.

3.5 Implications for monazite petrogenesis

The presence of monazite within the concretion matrix (Fig. 3-6) does not constrain the timing of monazite growth if, as is assumed here, the matrix was replaced under anchizonal conditions. In the few sections which have been examined, no monazite was found within the argillaceous part of the cone-in-cone, suggesting, but by no means proving, that monazite post-dated the early plastic-style deformation and the initial, presumably carbonate, cement of the cone-in-cone.

The fluids responsible for the formation of the chlorite + quartz cone-in-cone matrix were also capable of transporting REE; the patterns of figure 3-13 suggest that they were enriched in heavy REE. Figure 3-6 shows that monazite was either syngenetic with these fluids or slightly later. It is tempting to equate the fluid which removed the heavy REE from cone-in-cone concretions (figure 3-13) with the heavy REE enriched fluid of figure 2-34, which was present during the initial stages of monazite formation.

3.6 Conclusions

Cone-in-cone concretions were formed in unconsolidated muds of the Calymene formation about twenty metres below the sea floor. The environment was a distal part of the shelf with a low clastic input and oxic bottom waters which supported an abundant shelly fauna. The concretions were probably originally cemented by calcite and siderite. Thin stringers of unconsolidated mudstone were deformed extensionally during the growth of the concretion, fracturing into a series of small blocks and giving rise to the sawtooth profiles of the cones. After deep burial and the onset of anchizonal diagenetic conditions, but probably before the regional crenulation cleavage was formed, the carbonate matrix was replaced by the assemblage chlorite plus quartz. In the process, heavy rare earth elements were partially leached and all the REE were locally mobilized to produce concentric zoning of the concretion. More recently, the concretions were exhumed to a shallow depth characterized by brittle deformation and the presence of oxidised fluids. The cores of some concretions have been affected by iron-lead-bismuth mineralisation including a rare alunite family mineral intermediate between hidalgoite and corkite. All the REE, but especially the light REE, were leached during this late mineralization.

Chapter 4: Geochemistry

4.0 Objectives

Major, trace and rare earth element data are presented for material from the Navas de Estena syncline. The objectives of the geochemical study are:

1) To characterise the chemistry of the rocks of the Navas de Estena area.
2) To measure quantitatively the concentration of monazite in a given section.
3) To investigate the extent to which host rock geochemistry may control monazite abundance.
4) To establish the extent of REE mobility in the monazite-bearing shales.
5) To investigate the chemistry of the monazites themselves.

4.1 Geochemical sampling and sample preparation

Initially, the section at Valleleor (figure 1-9) was chosen for detailed geochemical study because the sedimentology had already been studied by Almaden Mining personnel (Gomez, 1991). A rather sporadic monazite distribution had been inferred from inspection of hand specimens in the field (shown as "mo" on figures 4-1 and 4-2). In an effort to be systematic, continuous chip sampling was performed over some 450 m of section, resulting in thirty samples, each of about 10 Kg, and each representing between 10 and 20 vertical metres of section. The bulk of each sample was jaw-crushed to approx. 0.5 cm size; a sample splitter was then used to separate about 100g of this, which was then ground up finely in a Tema mill for geochemical analysis. The remainder was ground using a disc mill and sieved into size fractions: <250 μm; 250 - 500 μm; and 500 μm - 2mm. Repeated passes were made through the mill, sieving each time to minimize losses in the fines, until the whole sample had passed through the 2mm sieve. By adjusting the pressure of the plates and the feed rate, recovery in the 250 - 500 μm fraction could be optimised. This fraction, which coincides with the mode of monazite grain size determined in previous alluvial studies (E.Ortega, Almaden Mining, *pers. comm.*) was then used for heavy liquid

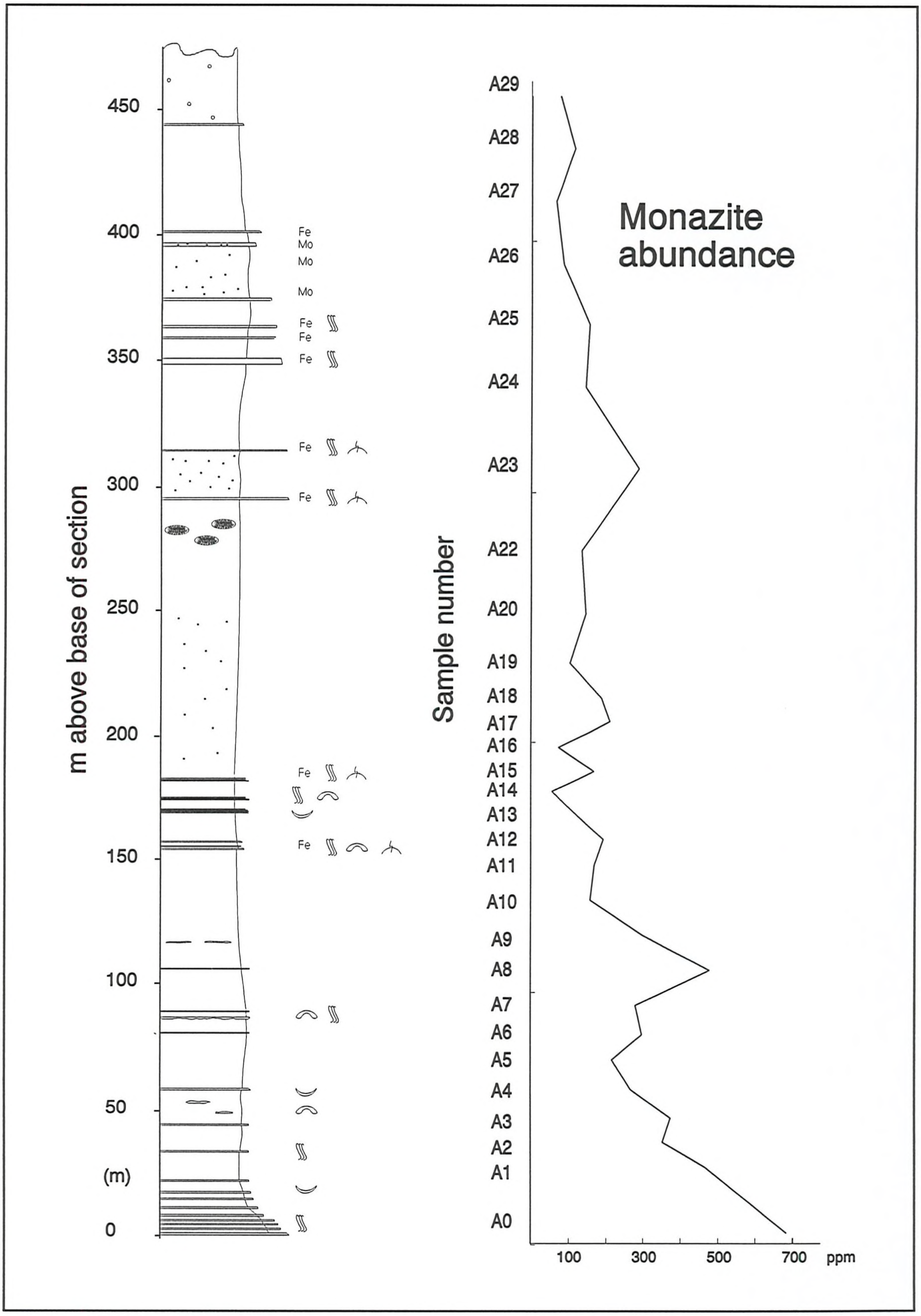

Figure 4-1: Valleleor section showing sedimentary log of the lower part of the Calymene Formation and measured monazite abundance. See text for detals of monazite estimation. For key to symbols see figure 1-10.

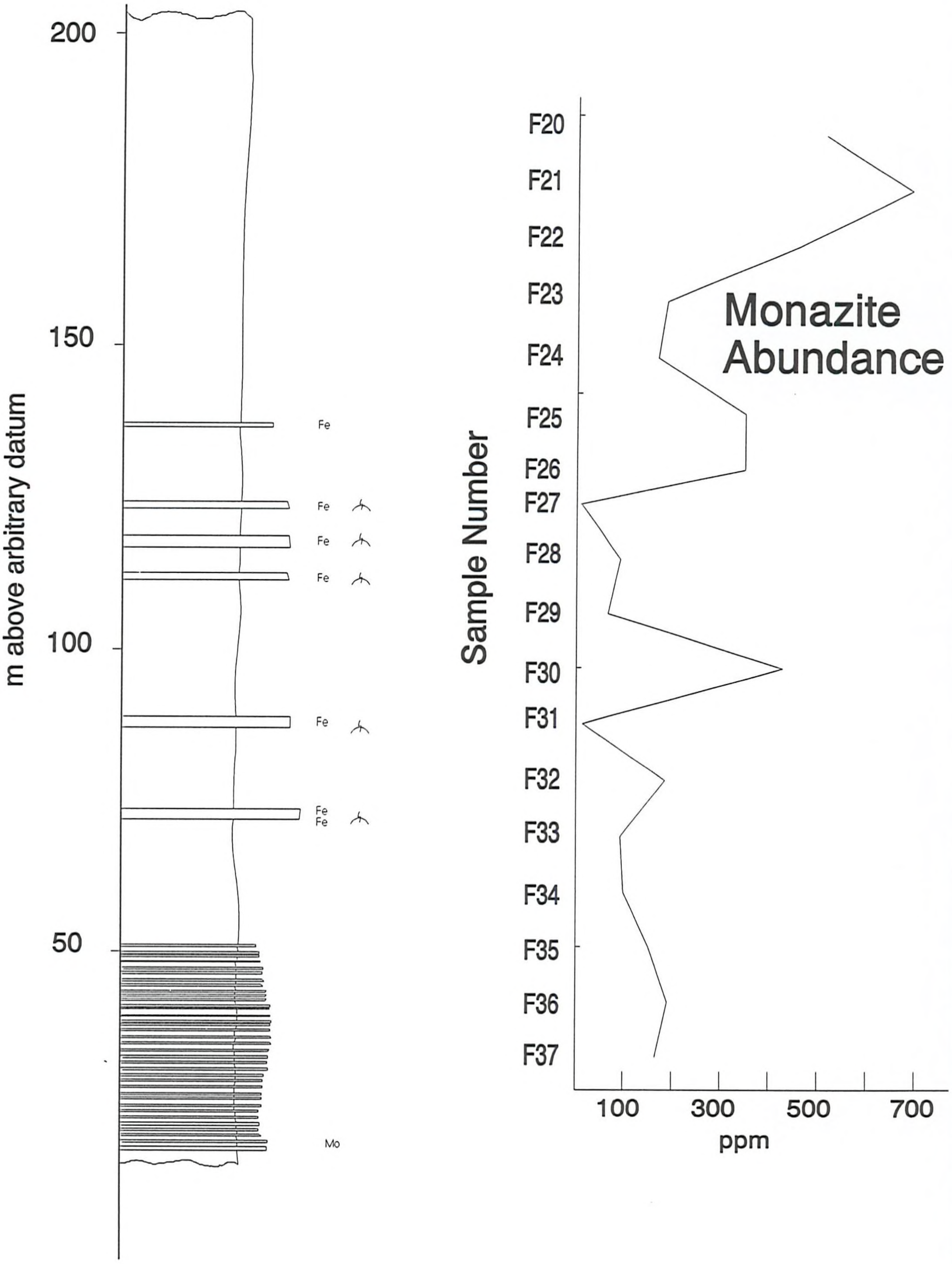

Figure 4-2: Santa Maria section, showing sedimentary log and measured monazite abundance. See text for details of monazite estimation. Same symbols as Fig 4-1.

separation.

Following the initial studies at Valleleor, a second section was sampled at Santa Maria, about 2 km east of the village of Navas de Estena. The sedimentary log for this section featured spectacular development of "hard grounds" (see chapter 2). Because of the lithological contrasts present in the section, single grab samples of about 10 kg were preferred to composite samples. Eighteen samples (F20 - F37) were collected on a measured traverse across the area of "hard grounds", representing 170 vertical metres of section (figure 4-2). These samples were processed in exactly the same way as the Valleleor material.

Many more conventional hand specimens were collected in the Navas de Estena basin; sampling concentrated on areas with abundant monazite visible in hand specimen (e.g. "B1", figure 1-9); and on concretions, especially large cone-in-cone concretions at Valleleor (chapter 3). At the base of the Calymene section at Navas de Estena, specimens were collected from adjacent beds in alternating sand/shale sequences, in order to study possible REE mobility between sand and shale layers. These specimens (figure 1-9) range from the Tremadoc (F40, 41) through the Arenig-aged Armorican quartzite (F42, F43) and Pochico formation (F44, F45) up to the contact with the Calymene formation in Llanvirn time (F61 - F63). Each sample number denotes a shale (a) - sandstone (b) pair.

Sample digestion techniques for ICP-MS and XRF sample preparation are described in appendix A.

4.2 Mineral separations and estimation of monazite abundance

A laboratory was established for heavy liquid separations using methylene iodide ("MEI": density = 3.32). The thirty samples from Valleleor (A0 to A29) and eighteen from Santa Maria (F20 to F37) were separated into heavy and light fractions. Each sample was shaken with MEI in a separating funnel; after settling, the heavy fraction was drawn off and the process repeated until no further heavies settled. Normally, three repeats sufficed; this ensured essentially complete recovery for any given size fraction. Lights and heavies were washed repeatedly with acetone; MEI was recovered from the washings using a water cascade apparatus. No attempt was made to extract all of the monazite in a sample; such an approach was rejected as being too time-consuming to be practicable. Instead, only the 250- 500 μm fraction was used throughout, coupled with the assumption that monazite grain size is relatively invariant. Examination of monazites in thin section from all parts of the Valleleor bears this out subjectively, with the majority of grains in this size bracket.

Heavy mineral fractions were examined under the binocular microscope and in some cases mounted in polished blocks to enable mineral identification from energy dispersive spectra in the SEM. Many of the heavy fractions consisted almost entirely of monazite (density = 4-5 gcm^{-3}, depending on the proportion of silicate inclusions), with small amounts of pyrite and arsenopyrite. In places, however, iron oxide minerals were predominant. No other REE-bearing minerals were found. It proved difficult, even by hand picking, to separate pure monazites, chiefly because of their strong resemblance to weathered iron oxide minerals.

The approach chosen was to measure the REE content of the heavy fractions by ICP-MS and thus to calculate the monazite concentration by assuming all the LREE (La - Dy) to be contained in monazite (*i.e.*, concentration of monazite = (mass of heavies/mass of sample)*(ΣLa-$Dy_{Heavies}$/ΣLa-$Dy_{Standard}$)). Biasing the estimate by using the light REE in this way will tend to minimise any errors caused by, for example, zircon or xenotime in the heavies. A hand-picked concentrate of alluvial monazites from the Navas de Estena basin was used as the standard. This approach has the benefit of being objective and systematic, and should yield a quantitative and reproducible measure of monazite abundance. However, it should be emphasised that the monazite concentration finally obtained, although hopefully proportional to the true value, will systematically err on the low side because of <250 μm sized grains, present in the bulk rock, which are lost in the fine fraction and not measured.

Monazite distribution at Valleleor

Figure 4-1 shows the concentration of monazite versus stratigraphic level at Valleleor, expressed as ppm monazite in the 250 - 500 μm size fraction. The greatest concentration is about 700 ppm at the base of the shales; further up in the Calymene formation, it falls to about 150 ppm. Apparent peaks occur at 110 and 300 metres above the base of the section. There is an apparent systematic decrease in monazite away from the base of the section, coinciding with increasing depth of sedimentation and increasing prevalence of fine grained muds over silty material (see chapter 2). It is not clear whether the silty horizons at *circa* 170 m or the "hard grounds" at 350 m have any influence on monazite abundance. It is clear, however, that observation of monazites in the field cannot serve as a guide to the true distribution. The tedious process of mineral separating, digestion and REE analysis is thus vindicated. Two specimens (B6 and B8, see figure 1-9) were processed from the Pochico Beds, below the Calymene Formation. B8 contains no monazite; B6, from a little lower in the formation, contains 50 ppm. Monazite is therefore not confined entirely to the Calymene formation, although regional panning (Ortega, 1993), indicates that the Calymene is the principal source of alluvial material.

Monazite distribution at Santa Maria

Figure 4-2 shows the sedimentary log for Santa Maria, featuring six prominent "hard grounds" in a sequence of otherwise massive shales. Traces of monazite had been observed in the finely intercalated silts and muds at the base of the section (Gomez, 1991), but not higher up. The relationship between sample points and sedimentology, and the measured monazite abundance, are also shown (figure 4-2). Samples F27 and F31 are ferruginised, quartz-cemented siltstones from the "hard ground" horizons; they both contain very little monazite. As in the Valleleor section, the maximum concentrations of monazite are in zones of massive shales with little internal structure.

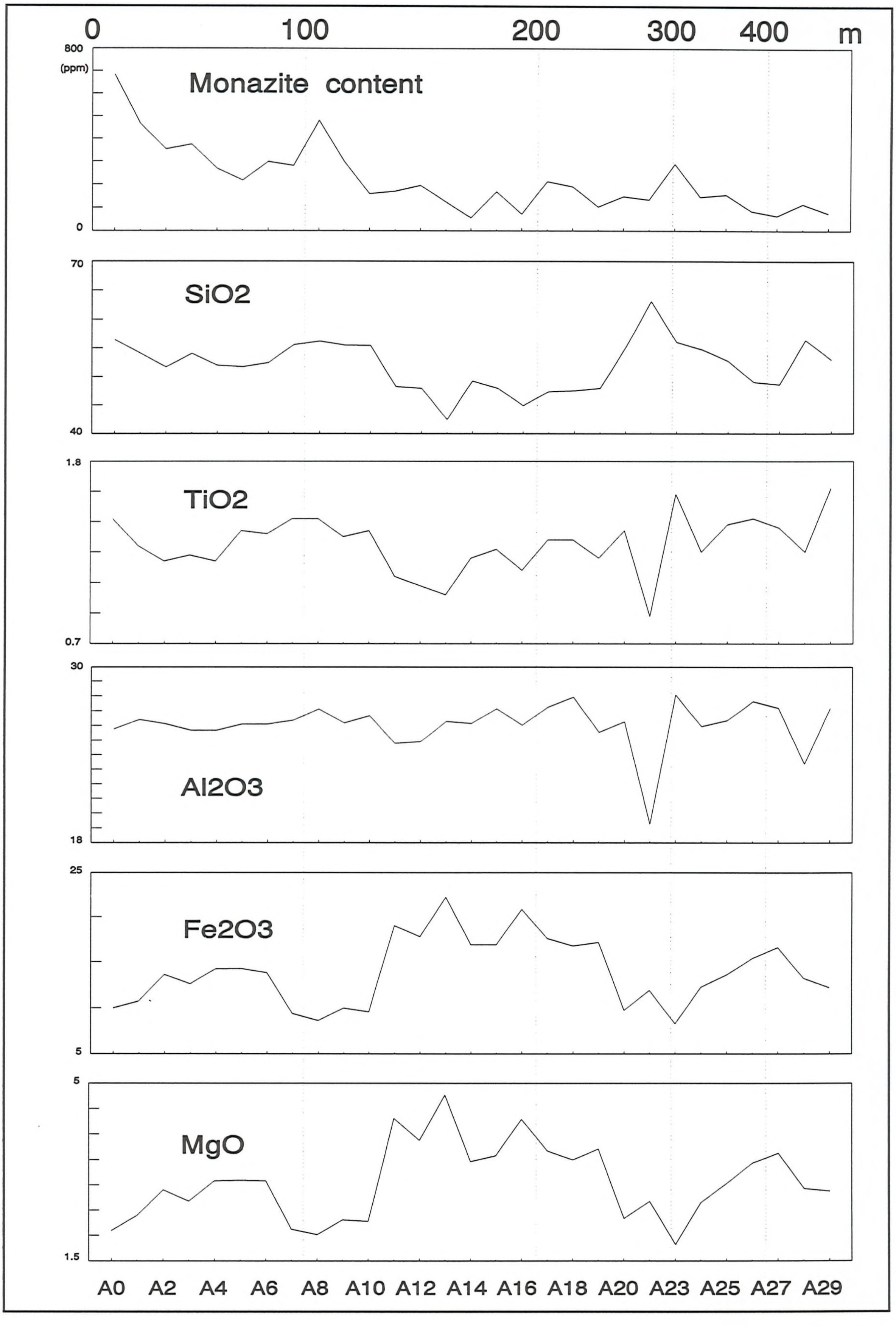

Figure 4-3: Major and trace element chemistry at Valleleor, compared with monazite abundance. A0 is base of section.

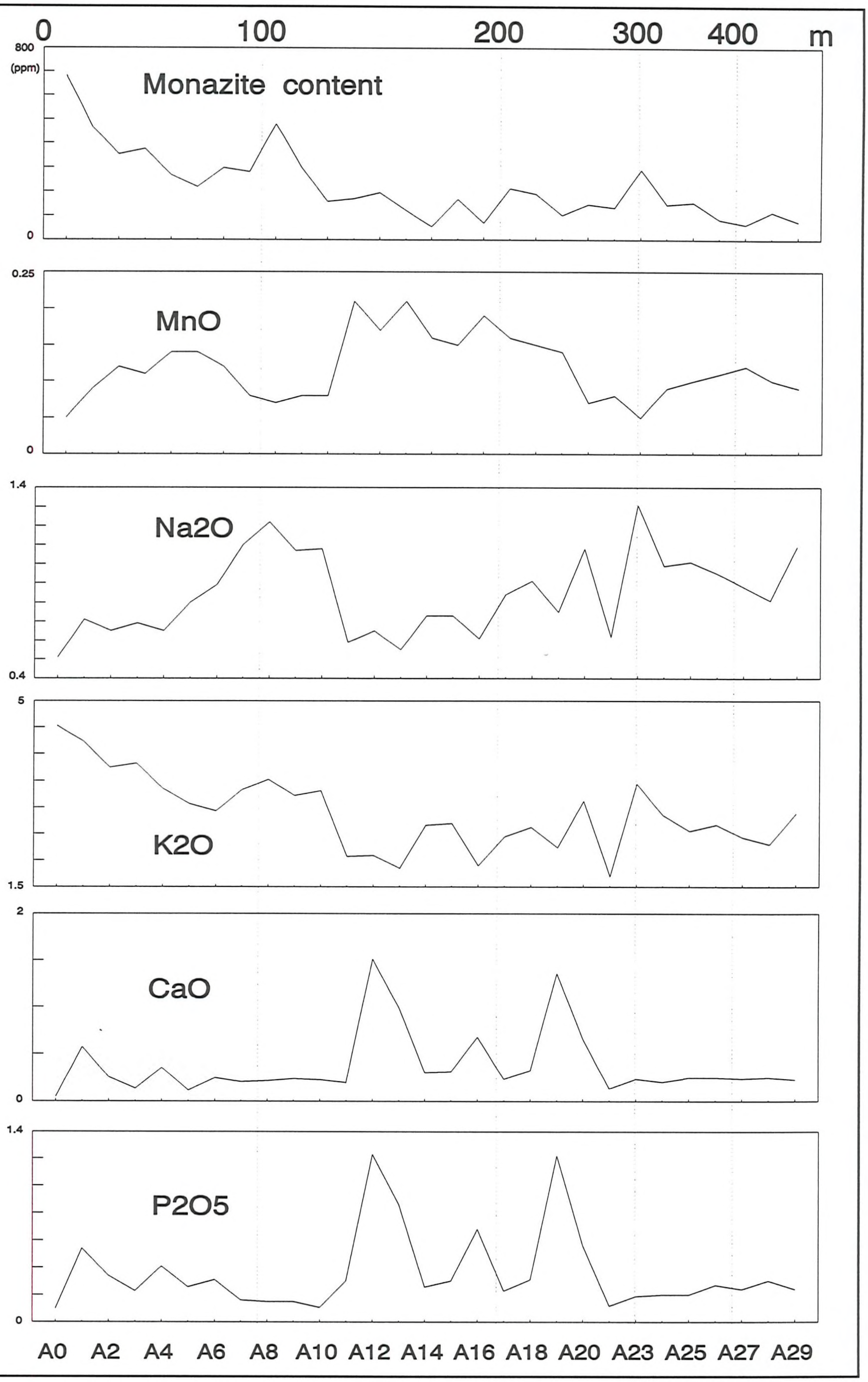

Figure 4-4: Valleleor major and trace chemistry continued.

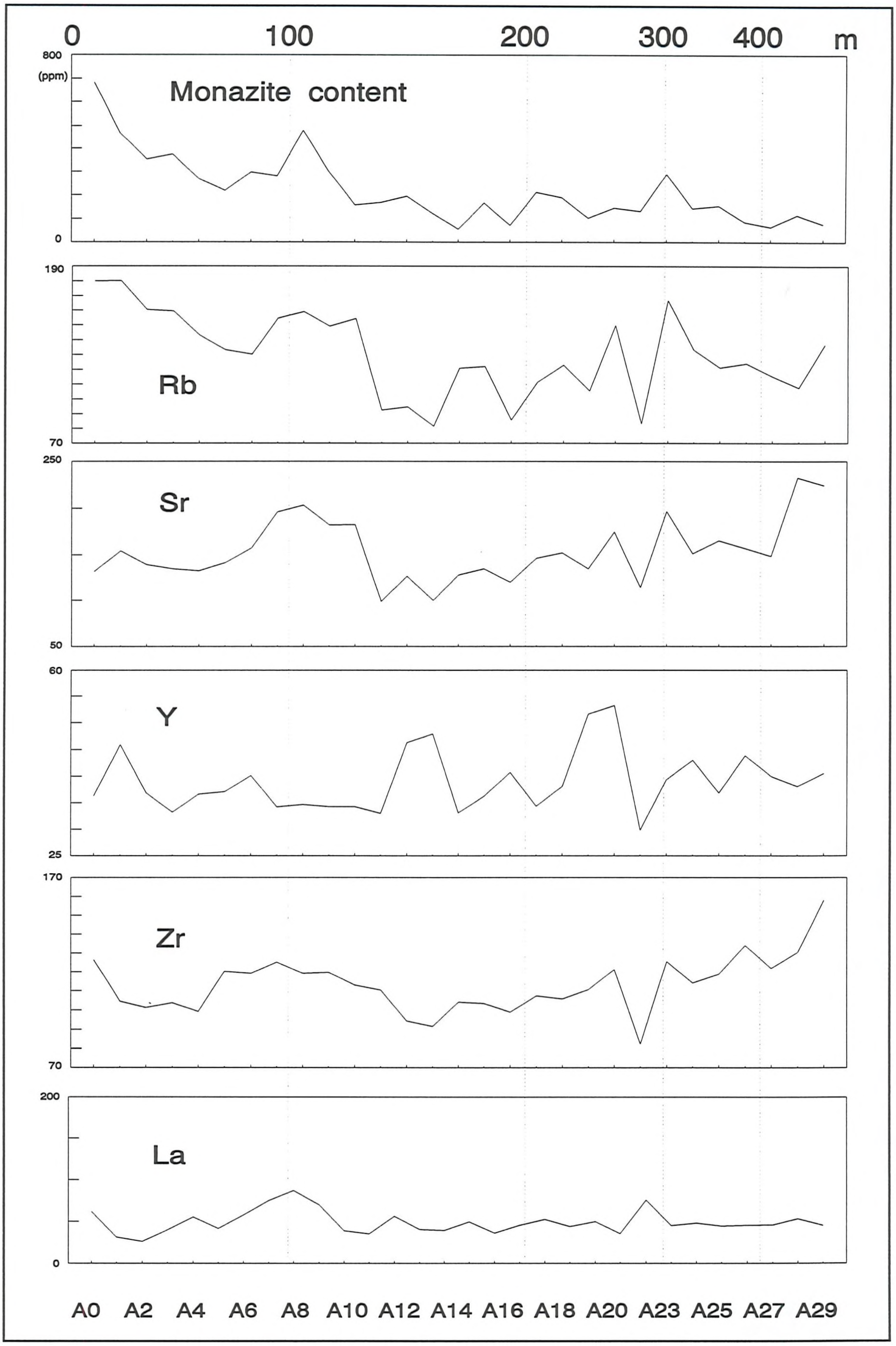

Figure 4-5: Valleleor major and trace element chemistry continued.

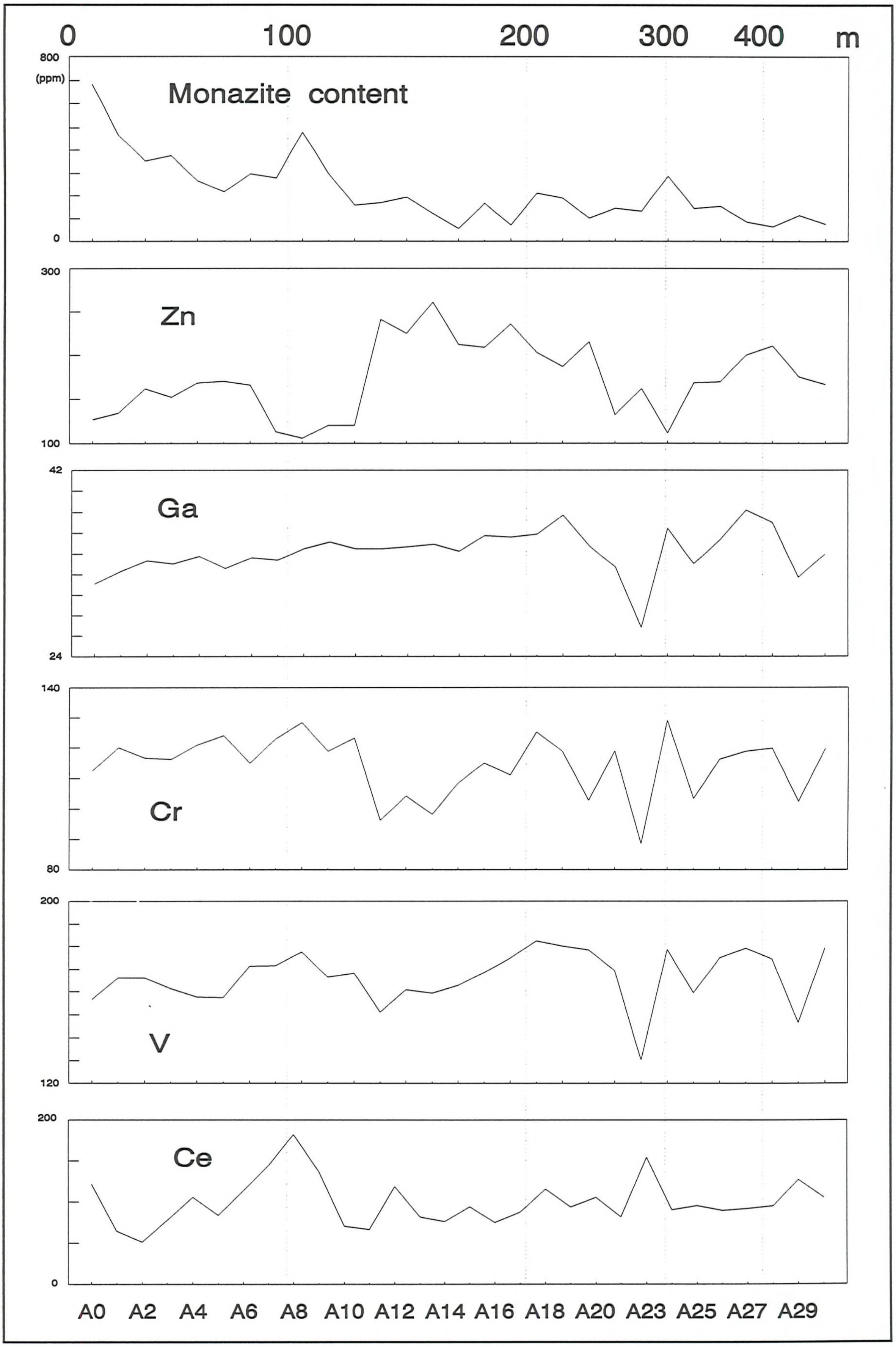

Figure 4-6: Valleleor major and trace element chemistry continued.

4.3 Geochemistry of the section at Valleleor

Major and trace elements

Major and trace element data for Valleleor (tables B-2, B-3; figures 4.3 - 4.6) define a number of distinct zones. The lowest 150 m of the section are characterized by a gradual decrease in potassium and increase in sodium and relatively high silica, about 55 wt.%. Iron and magnesium increase to reach a plateau at 80 m, but are low between 110 and 150 m. This lowest part of the section corresponds to the regional marine transgression at the base of the Llanvirn referred to by Rabano(1989). The next interval, from 150 m to 250 m, has low silica, titanium, sodium and potassium, but high transition metals, calcium and phosphorus. The correlation between calcium and phosphorus suggests the presence of apatite, possibly as a phosphatic cement produced during diagenesis. Monazite, by comparison, makes no significant contribution to the phosphorus budget of the shales. This middle section reflects deeper water, with a lesser amount of terriginous clastic input. The upper part of the section shows a gradual increase in Zr and Ti, indicating a change of facies towards greater clastic heavy mineral input.

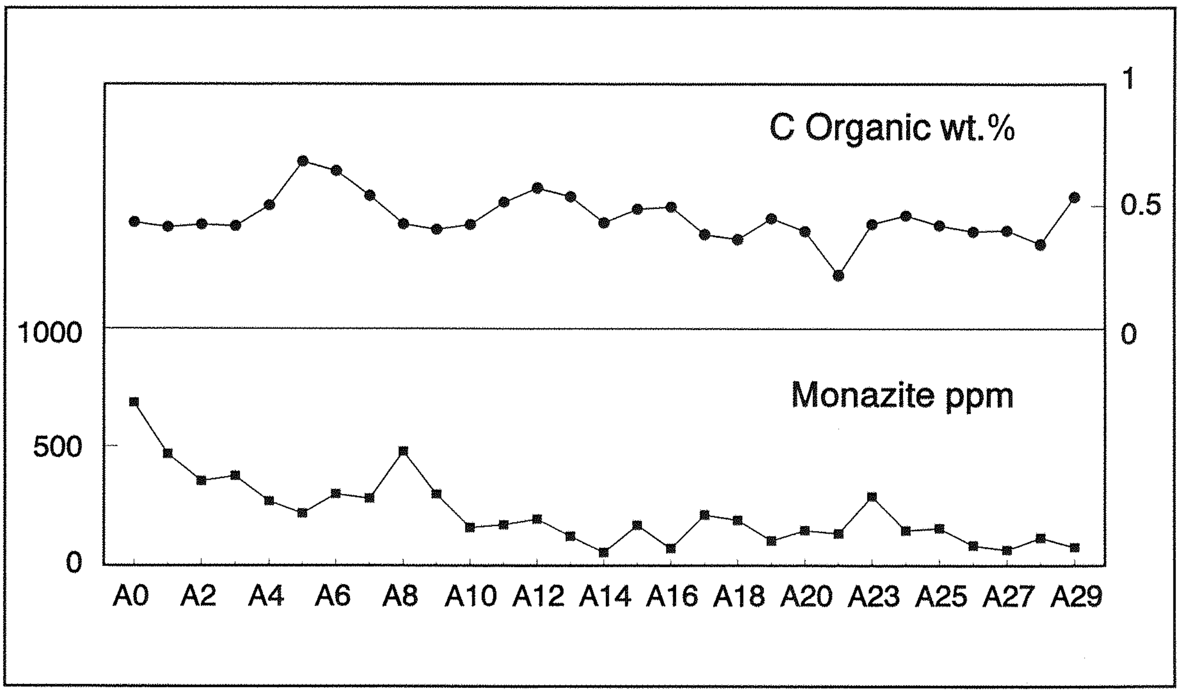

Figure 4-7: Total organic carbon content compared with monazite abundance for the section at Valleleor. Base of section is on the left.

Organic carbon

The total organic carbon content of the shales is of the order of 0.5 % (figure 4-7). The main sources of organic carbon in Lower Palaeozoic shales are graptolites, chitinozoans, spores, pollens and other microfossils, and bituminous material (Tricker et al., 1992). The peaks at around 70 m. and 150 m. may correspond to deeper water facies; both intervals are graptolite-bearing. The minimum at A22 is possibly related to cone-in-cone concretions (chapter 3). There is no correlation with monazite abundance.

Rare earth elements

Figures 4-8 and 4-9 show some whole-rock REE data for the Valleleor section. Chondrite-normalised patterns (chondrite values after Masuda *et al,* 1973) are typical of Palaeozoic shales, with a small negative Eu anomaly inherited from the source terrain. Normalising to PAAS (Post Archaean Australian Shale; McLennan, 1989) reveals an enrichment in the middle REE compared to average shales. The presence of coarser-grained material can have the effect of shifting the whole pattern downwards: sandstones have essentially flat shale-normalised patterns in the range 0.2 to 0.5 times shale abundances. Some vertical offsets in fig 4.8b may be due to such grain-size effects. The plots of figure 4.8 (c) and (d) illustrate much of the variation in the REE patterns. Fig. 4-8(c) shows chondrite-normalised Gd vs normalised Gd/Yb ratio. This ratio normally lies in the range 1 - 2 for post-Archaean sediments (McLennan, 1989). The anomalously high values for some of the Valleleor shales may in one case (A22) result from the inclusion of material from cone-in-cone concretions (see chapter 3) in the chip sampling; the other data define a trend which suggests a mineralogical control. Sedimentary mixing is implausible because one end member would have to have an unrealistically high value of $[Gd/Yb]_N$. Table 4.1 shows the most significant correlations between Gd/Yb, La/Yb and the major and trace element geochemistry. These demonstrate that the MREE enrichment (Gd/Yb) is associated with lead, yttrium, calcium, phosphorus and strontium. A variable degree of enrichment in apatite is a possible cause of this effect. Apatite commonly contains strontium, and high concentrations of the light to middle REE (Mineyev, 1968).

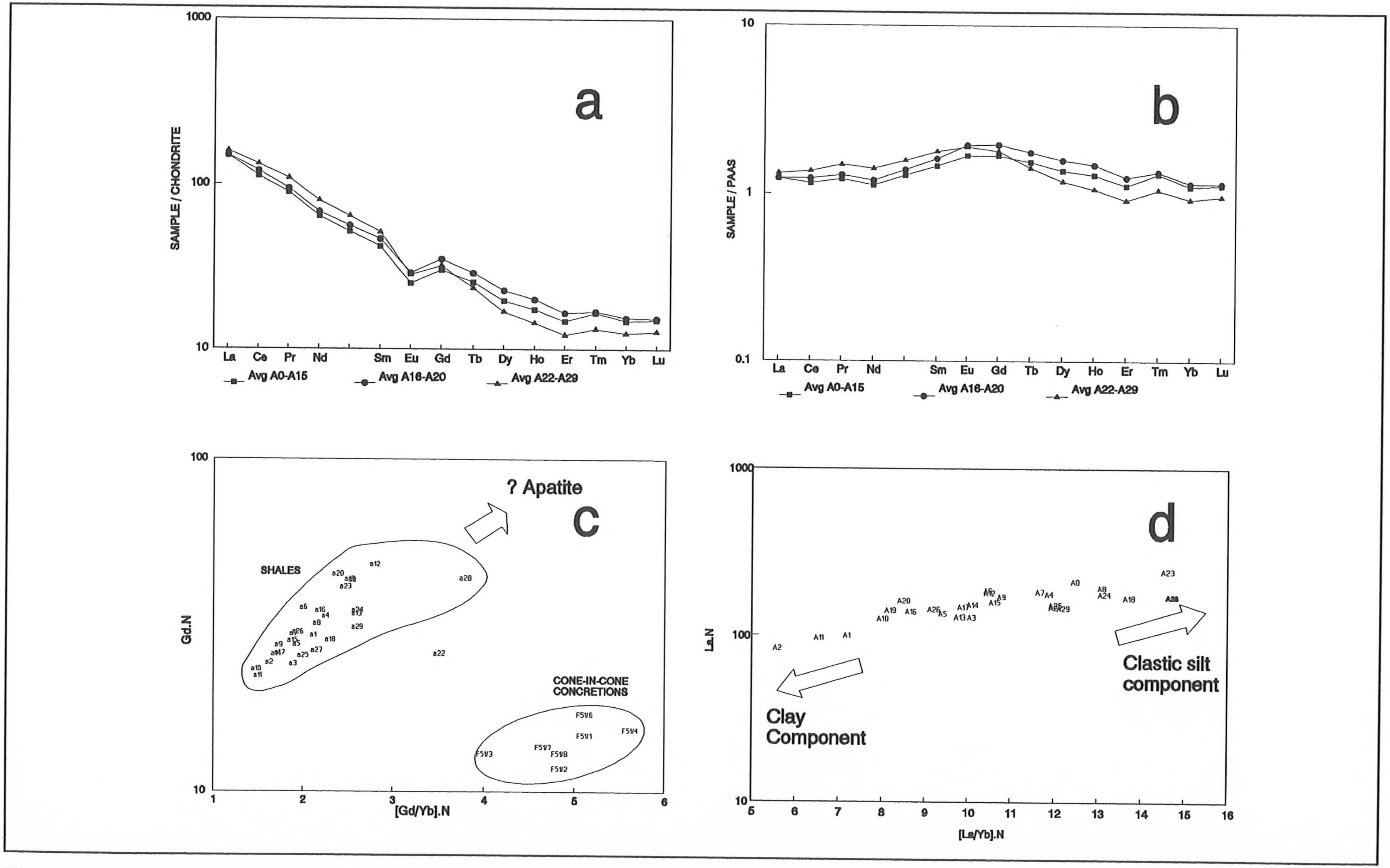

Figure 4-8: Valleleor shales. (a): Variation in chondrite-normalised REE patterns. (b): PAAS-normalised patterns. (c): Normalised Gd vs. Gd/Yb for shales and c-in-c concretions. (d): Normalised La vs. La/Yb.

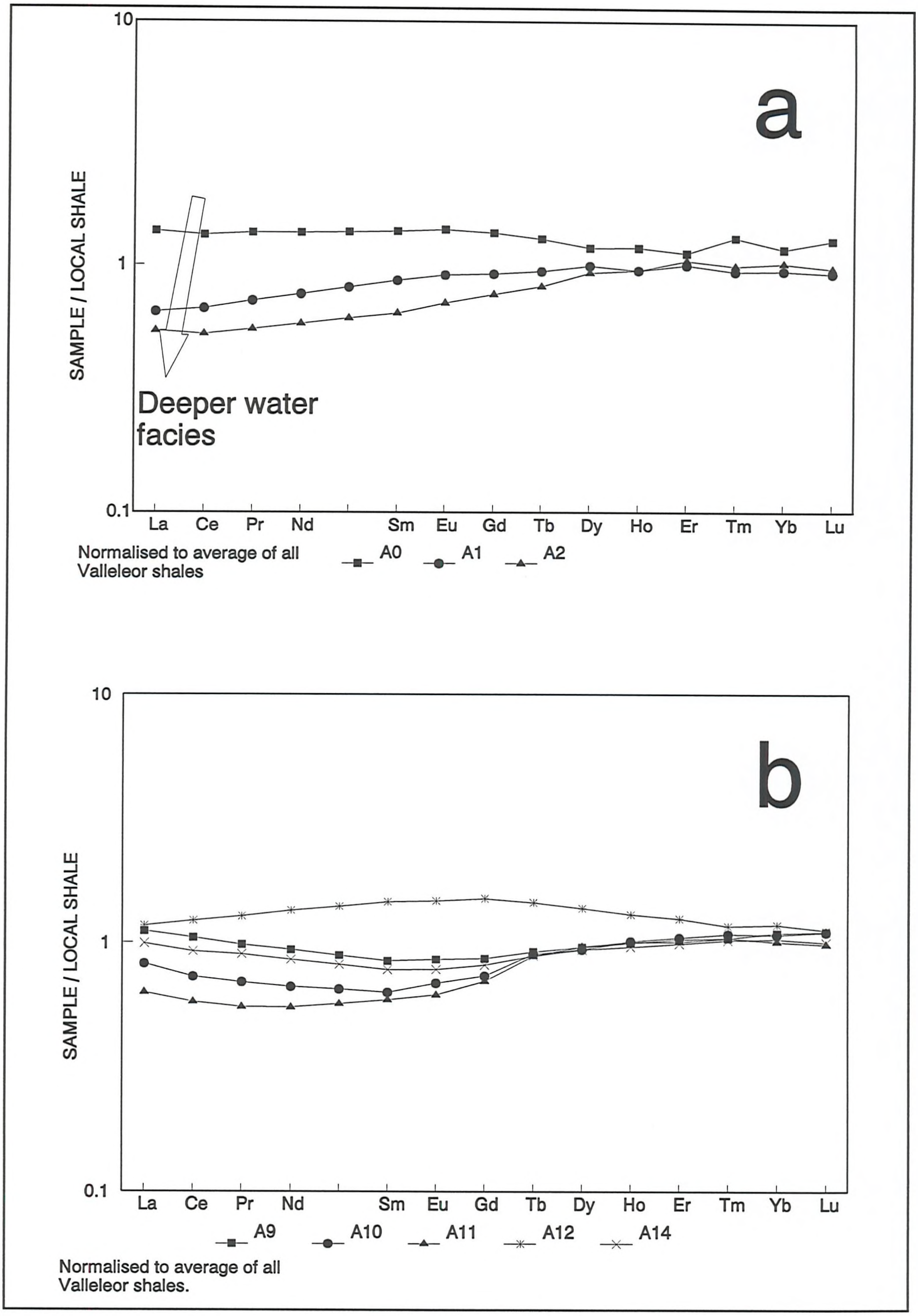

Figure 4-9: Valleleor shales continued. Plot (a) demonstrates the variation of La/Yb in the first three samples at the base of the Calymene, which coincides with the Llanvirn marine transgression.

n=28	$[La/Yb]_N$	$[Gd/Yb]_N$
La_N	0.81	0.41
Gd_N	0.32	0.79
SiO_2	0.33	0.11
TiO_2	0.42	-0.04
MnO	-0.38	-0.13
CaO	-0.26	0.34
P_2O_5	-0.32	0.35
LOI	-0.07	-0.09
Sr	0.51	0.32
Zr	0.38	0.22
Th	0.25	-0.30
Pb	0.13	0.56
Y	-0.18	0.47

(1% confidence >0.44; 5% >0.32)

Table 4-1: Pearson correlation coefficients of chondrite normalised La/Yb and Gd/Yb ratios with other elements at Valleleor.

Detrital monazite can be ruled out because of the absence of a thorium correlation. The correlation with lead is not clear. The normalised La vs La/Yb plot has a linear array of values, but these are within typical limits (La/Yb<20: McLennan, 1989), and probably result from mixing of sedimentary components. The La/Yb ratio correlates with strontium, titanium, silicon and zirconium and negatively with manganese and phosphorus. This can most easily be interpreted as a silty component richer in detrital heavy minerals (containing Zr and Ti) versus a fine grained mud component rich in transition metals.

Figures 4-9(a) and (b) are REE plots normalised to the local shales in order to illustrate best the variations between patterns. Samples A0, A1 and A2 show a steady change in La/Yb ratio which is associated with increasing depth of sedimentation during the basal Llanvirn marine transgression (see figure 4-1). Similarly, A9..A11 represent increasing depth of sedimentation in a sequence of massive black shales (Gomez, 1991). A12 includes a horizon of silts which are ferruginized, rich in fauna, and probably contain biogenic apatite. A14 also includes silty material.

In conclusion, the whole - rock REE patterns are controlled by three factors:

1). The ratio of clay minerals to quartz, which causes a simple dilution.

2). An enrichment in the middle REE, probably controlled by apatite and possibly associated with biogenic material.

3). A light REE depletion, associated with manganese and the absence of silica and "heavy mineral" tracers; probably linked to grain size and depth of sedimentation.

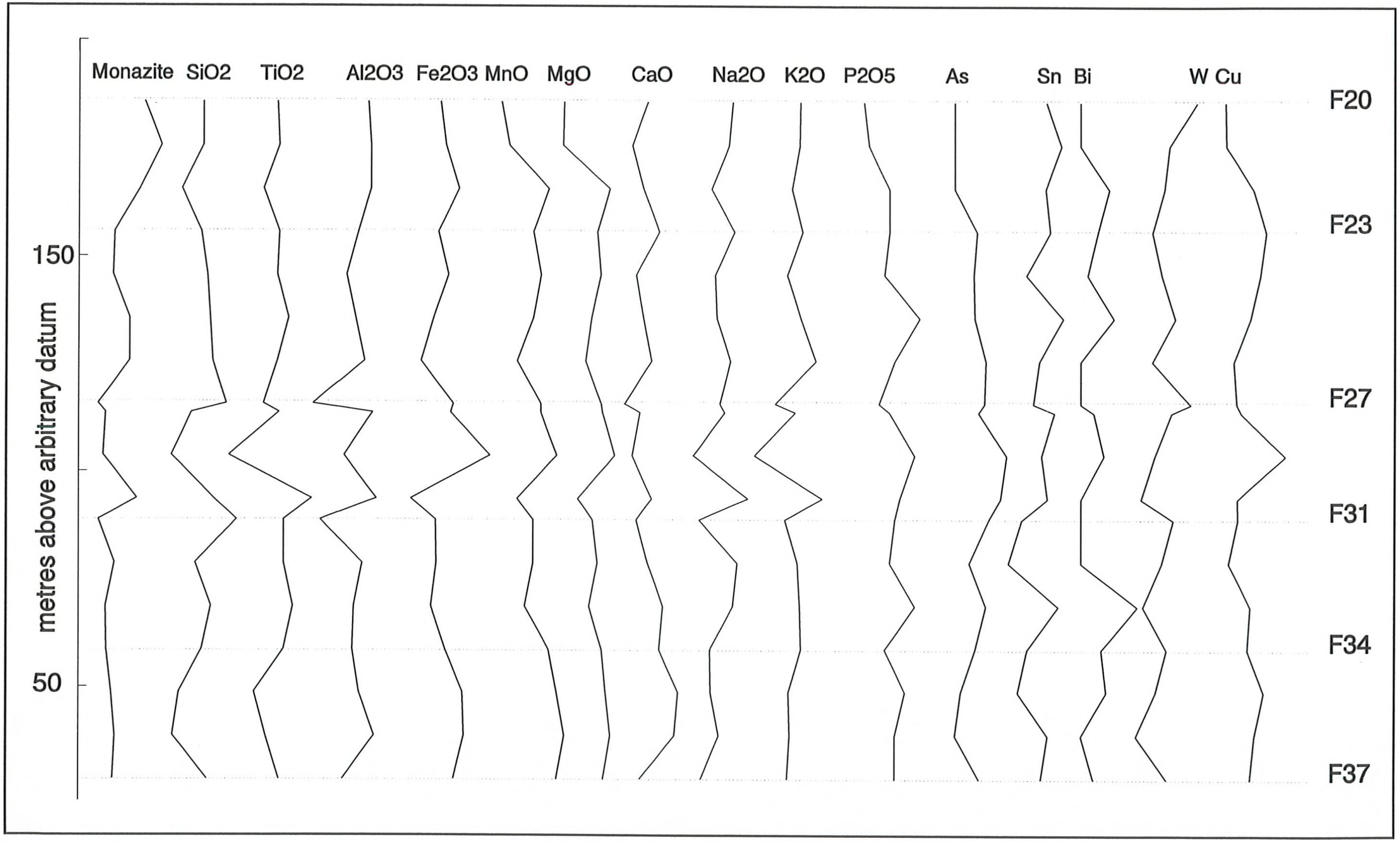

Figure 4-10: Santa Maria geochemistry. Data are normalised using standard deviation for each element. Compare sample locations to figure 4-2.

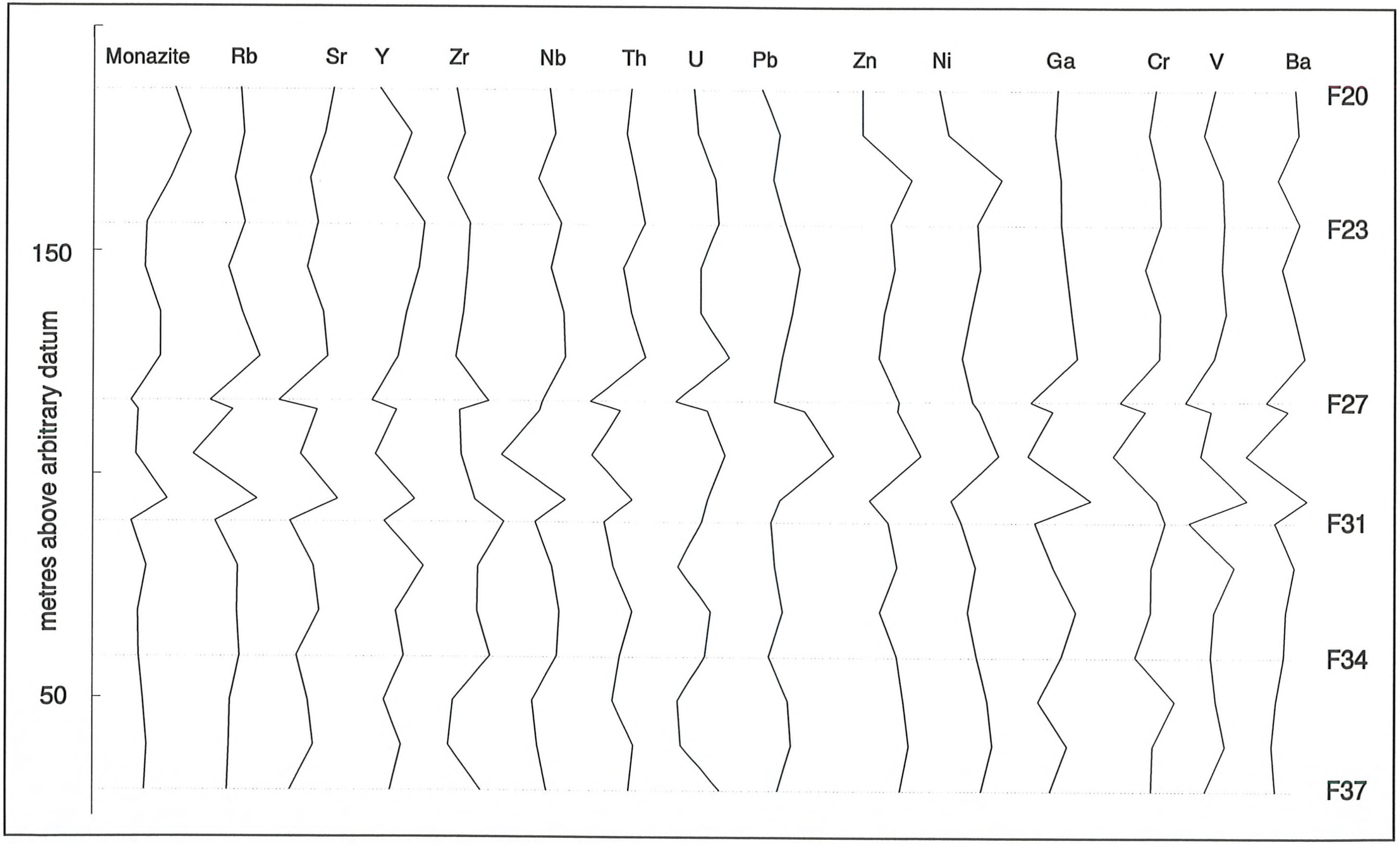

Figure 4-11: Santa Maria geochemistry, continued. Data are normalised using standard deviation for each element. Compare sample locations to figure 4-2.

4.4 Geochemistry of the section at Santa Maria

Major and trace elements

Figures 4-10 and 4-11, and tables B-2 and B-3, show major and trace element data for Santa Maria. Each element is standardised by subtracting the mean and dividing by the standard deviation, so that all the curves show comparable variation at the same scale. Monazite abundance is at the left of each figure, and some sample locations are shown to facilitate cross-referencing to figure 4-2. Not surprisingly, the greatest chemical variation coincides with the location of the large ferruginised silt "hard grounds" between 80 and 130 metres (e.g., F27 and F31, from two of the hard grounds). Monazite over this interval appears to correlate with a number of elements, notably Ti, Al, K, Rb, Sr, Nb, Ba; and to vary inversely with Fe, Mn, Mg, Ni and Zn. The "hard ground" horizons themselves have the lowest monazite concentration of the whole section. Chemically, they have a relatively high silica content, which is sedimentologically controlled, and are rich in transition metals, relating to their obvious ferruginous alteration, which is probably late-stage. The remainder of the section shows little chemical variation.

Rare earth elements

PAAS-normalised plots (figure 4-12 (b)) show considerable variation in the light and middle REE, with a similar peakiness around Gd to that observed at Valleleor. The greater variation seen in figure 4-12 (b) probably stems from the nature of the sampling: at Valleleor, chip sampling tends to exert an averaging effect. The Gd vs. Gd/Yb plot (figure 4-12 (a)) again shows a trend towards high values. However, at Santa Maria this effect carries a quite different chemical signature from the Valleleor data.

High Gd/Yb values correlate strongly with lead, copper and transition metals, and with the absence of silica, alkalis and the more mobile trace elements (table 4-2). There is an important correlation with LOI (loss on ignition), which is not found at

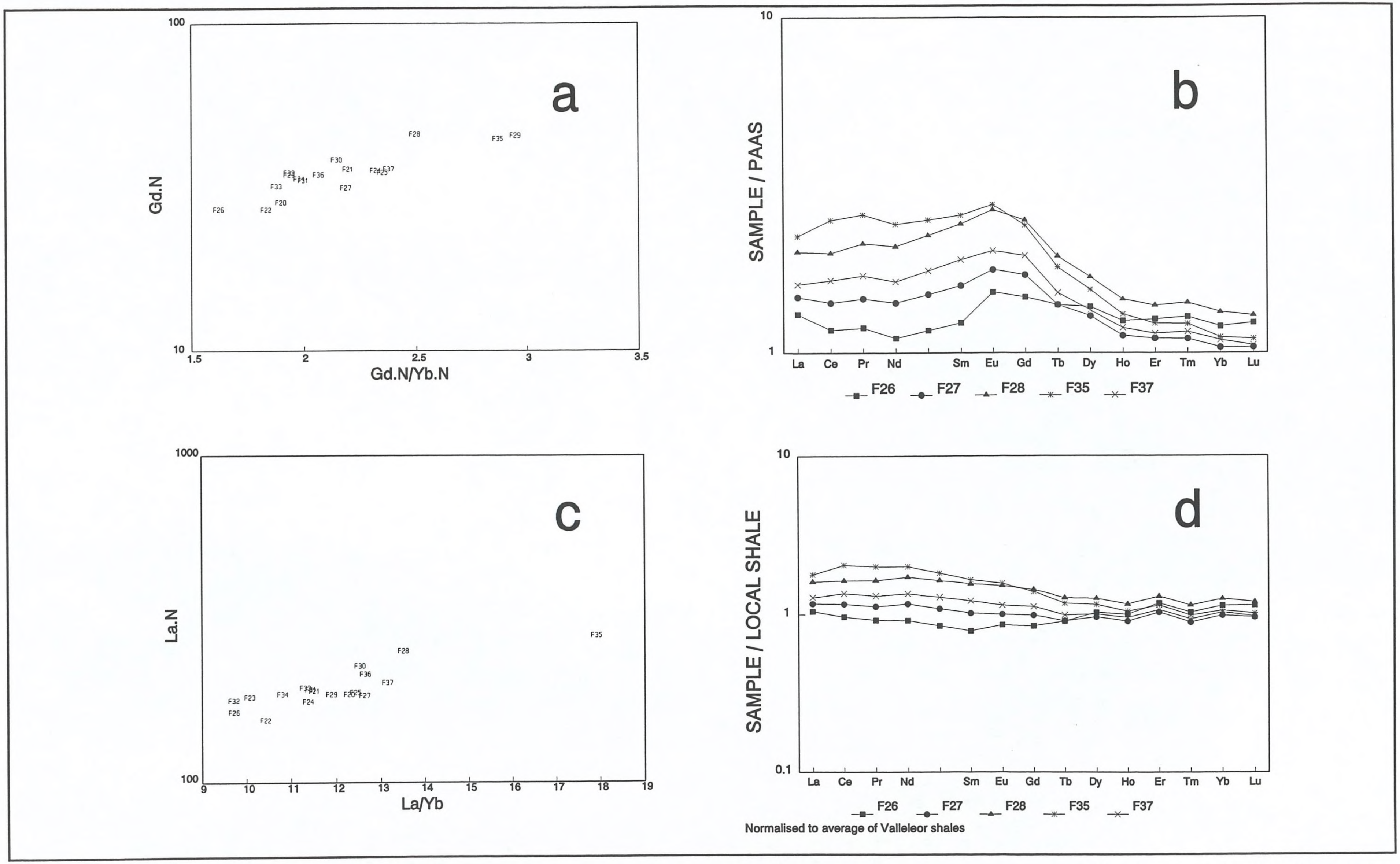

Figure 4-12: Santa Maria section. (a): Chondrite-normalised Gd vs. Gd/Yb. (b): Selected REE patterns normalised to PAAS. (c): Chondrite-normalised La vs. La/Yb. (d): Selected REE patterns normalised to local shale. Sample locations in figure 4-2.

Valleleor and which suggests an association with hydrous silicates or carbonates. Mineralization found in the cores of cone-in-cone concretions (chapter 3) has a similar association with lead, transition metals and REE depletion, clearly demonstrating the mobility of the light and middle REE during such late stage processes. The mineralization, consisting of goethite and alunite family minerals, is also occasionally seen in the shales hosting the concretions. Overall, the Gd/Yb enrichment is very probably attributable to late-stage alteration during weathering.

Pearson correlation coefficients between Gd/Yb ratio and whole-rock chemistry. Only coefficients > 0.4 ($\equiv$ 5% significance for n=18 samples) are shown.

SiO_2	-0.47	Rb	-0.57
TiO_2	-0.54	Nb	-0.64
Fe_2O_3	0.64	Th	-0.56
MnO	0.50	Pb	0.70
Na_2O	-0.50	Zn	0.44
K_2O	-0.61	Ni	0.40
LOI	0.48	Ga	-0.53
Cu	0.57	Ba	-0.57

Table 4-2: Variability in Santa Maria REE data compared with major and trace element data. See figure 4-12(a), and text for details.

The La vs. La/Yb plot (figure 4-12 (c)) shows a much smaller range of compositions than at Valleleor, with no $[La/Yb]_N$ values lower than 9.5. This probably reflects the restricted range of facies seen at Santa Maria: shallower water, with more silty material than Valleleor and without the development of thick graptolitic black shale intervals. There are no significant correlations between La/ Yb and major or trace element chemistry. In figure 4-12 (d), some REE patterns normalised to local shale are plotted, chosen to illustrate the range of variation in the data. The heavy REE plot very close together, suggesting that the overall variation in quartz/clay ratio is small.

In conclusion, the REE chemistry at Santa Maria is controlled by:

1). The limited range of sediment types, leading to less variability than the Valleleor shales.

2). Late-stage weathering, associated with lead mobility, which has caused an enrichment in the middle REE. The geochemical signature of this MREE enrichment is quite distinct from that at Valleleor described above; at Santa Maria, there is no evidence of any mineralogical control.

	MON	SiO2	TiO2	Al2O3	Fe2O3	MnO	MgO	CaO	Na2O	K2O	P2O5	Rb	Sr	Zr	Nb	Th	U	Pb	Zn	Ni	Ga	Cr	V	Ba	As	Sn	Y	La	Ce	Pr	Nd	Sm	Eu	Gd	Tb	Dy	Ho	Er	Tm	Yb	Lu
MON	1.00	-0.07	0.25	0.63	-0.31	-0.60	-0.70	-0.05	0.45	0.52	-0.38	0.59	0.69	-0.49	0.39	0.55	0.09	-0.29	-0.61	-0.47	0.46	0.35	0.40	0.59	-0.48	0.46	-0.05	-0.20	-0.24	-0.27	-0.27	-0.26	-0.24	-0.33	-0.39	-0.34	-0.26	-0.16	-0.14	-0.12	-0.08
SiO2	0.52	1.00	0.60	-0.54	-0.68	-0.52	-0.47	-0.41	0.17	0.30	-0.16	0.17	-0.15	0.72	0.52	-0.05	0.02	-0.50	-0.57	-0.65	0.11	0.09	-0.30	0.34	0.34	-0.05	-0.34	-0.26	-0.41	-0.41	-0.39	-0.39	-0.45	-0.42	-0.45	-0.38	-0.27	-0.12	-0.13	0.00	0.10
TiO2	0.19	0.59	1.00	0.22	-0.90	-0.55	-0.55	0.09	0.62	0.82	-0.08	0.72	0.43	0.38	0.85	0.49	0.02	-0.53	-0.69	-0.63	0.71	0.41	0.44	0.78	0.06	0.19	0.23	-0.01	-0.18	-0.21	-0.23	-0.28	-0.27	-0.29	-0.22	-0.01	0.19	0.34	0.39	0.48	0.49
Al2O3	-0.01	-0.10	0.57	1.00	-0.19	-0.23	-0.27	0.47	0.54	0.58	-0.07	0.66	0.83	-0.70	0.28	0.67	0.11	0.03	-0.25	-0.07	0.63	0.39	0.75	0.54	-0.42	0.38	0.47	0.20	0.16	0.14	0.11	0.06	0.15	0.06	0.16	0.28	0.35	0.37	0.43	0.40	0.36
Fe2O3	-0.54	-0.96	-0.70	-0.15	1.00	0.72	0.64	-0.09	-0.71	-0.87	0.07	-0.79	-0.52	-0.29	-0.88	-0.51	-0.09	0.55	0.77	0.72	-0.70	-0.47	-0.41	-0.86	-0.14	-0.12	-0.03	0.13	0.32	0.34	0.36	0.43	0.40	0.44	0.33	0.10	-0.10	-0.29	-0.32	-0.42	-0.50
MnO	-0.47	-0.90	-0.77	-0.22	0.95	1.00	0.94	0.21	-0.68	-0.60	0.38	-0.57	-0.63	-0.06	-0.59	-0.33	-0.09	0.40	0.93	0.90	-0.41	-0.23	-0.15	-0.74	0.01	-0.31	0.12	0.25	0.42	0.44	0.43	0.43	0.39	0.40	0.36	0.22	0.08	-0.08	-0.09	-0.18	-0.31
MgO	-0.58	-0.95	-0.68	-0.17	0.99	0.95	1.00	0.14	-0.60	-0.59	0.44	-0.57	-0.61	-0.04	-0.56	-0.34	0.02	0.46	0.97	0.95	-0.38	-0.29	-0.12	-0.71	0.16	-0.34	0.03	0.11	0.26	0.30	0.30	0.32	0.30	0.33	0.36	0.27	0.14	-0.01	-0.03	-0.10	-0.21
CaO	-0.27	-0.49	-0.55	-0.25	0.45	0.42	0.47	1.00	0.22	0.36	0.27	0.39	0.33	-0.31	0.18	0.44	-0.17	-0.13	0.05	0.16	0.36	0.52	0.47	0.18	-0.31	-0.07	0.48	0.43	0.43	0.37	0.27	0.08	0.12	0.04	0.15	0.28	0.35	0.32	0.39	0.31	0.26
Na2O	-0.09	0.54	0.75	0.51	-0.65	-0.65	-0.62	-0.30	1.00	0.76	-0.25	0.75	0.74	-0.15	0.70	0.51	-0.14	-0.32	-0.65	-0.56	0.66	0.26	0.60	0.81	-0.11	0.26	0.20	0.00	-0.15	-0.17	-0.20	-0.26	-0.18	-0.24	-0.10	0.16	0.33	0.45	0.49	0.52	0.55
K2O	0.83	0.73	0.45	0.17	-0.79	-0.73	-0.82	-0.46	0.16	1.00	-0.15	0.98	0.71	-0.07	0.88	0.76	0.11	-0.52	-0.70	-0.57	0.84	0.59	0.62	0.94	-0.15	0.24	0.23	0.01	-0.15	-0.18	-0.23	-0.33	-0.29	-0.37	-0.26	-0.03	0.17	0.34	0.40	0.48	0.51
P2O5	-0.27	-0.55	-0.61	-0.32	0.53	0.50	0.54	0.98	-0.43	-0.47	1.00	-0.16	0.00	-0.03	-0.17	-0.06	0.27	0.52	0.35	0.41	0.10	0.06	0.17	-0.26	0.51	0.11	0.07	0.21	0.24	0.24	0.24	0.27	0.33	0.36	0.39	0.34	0.24	0.08	0.10	0.04	0.11
Rb	0.73	0.80	0.58	0.27	-0.88	-0.83	-0.91	-0.48	0.36	0.97	-0.51	1.00	0.75	-0.21	0.87	0.82	0.14	-0.46	-0.65	-0.50	0.84	0.59	0.65	0.94	-0.25	0.26	0.23	-0.02	-0.15	-0.18	-0.23	-0.31	-0.27	-0.36	-0.26	-0.04	0.15	0.30	0.36	0.42	0.44
Sr	0.03	0.70	0.72	0.14	-0.70	-0.73	-0.67	-0.33	0.79	0.25	-0.41	0.40	1.00	-0.54	0.49	0.68	0.16	-0.02	-0.62	-0.47	0.73	0.45	0.72	0.74	-0.17	0.48	0.21	0.08	-0.03	-0.05	-0.08	-0.10	0.00	-0.07	0.02	0.16	0.25	0.31	0.36	0.37	0.44
Zr	-0.03	0.52	0.83	0.19	-0.52	-0.61	-0.46	-0.45	0.59	0.19	-0.47	0.29	0.74	1.00	0.15	-0.43	-0.07	-0.34	-0.12	-0.28	-0.24	-0.23	-0.41	-0.08	0.48	-0.37	0.04	-0.13	-0.18	-0.17	-0.15	-0.14	-0.17	-0.07	-0.04	0.01	0.09	0.15	0.11	0.17	0.18
Nb	0.30	0.63	0.94	0.58	-0.75	-0.78	-0.74	-0.62	0.71	0.57	-0.67	0.68	0.70	0.73	1.00	0.68	0.05	-0.56	-0.70	-0.58	0.77	0.41	0.46	0.88	-0.12	0.24	0.09	-0.19	-0.32	-0.36	-0.39	-0.45	-0.45	-0.49	-0.41	-0.19	0.03	0.20	0.25	0.31	0.34
Th	0.30	0.41	0.77	0.72	-0.58	-0.61	-0.58	-0.45	0.65	0.50	-0.52	0.60	0.49	0.41	0.78	1.00	0.38	-0.28	-0.42	-0.20	0.82	0.60	0.60	0.71	-0.34	0.48	0.18	-0.16	-0.24	-0.28	-0.33	-0.38	-0.36	-0.43	-0.34	-0.17	-0.01	0.11	0.19	0.24	0.23
U	-0.42	-0.36	-0.03	0.06	0.37	0.27	0.37	0.09	-0.12	-0.34	0.15	-0.34	0.05	0.09	-0.02	0.08	1.00	0.29	-0.00	0.07	0.26	-0.05	0.01	0.09	0.47	0.39	-0.12	-0.35	-0.38	-0.34	-0.30	-0.17	-0.15	-0.07	-0.03	-0.06	-0.07	-0.05	-0.04	0.09	0.17
Pb	-0.23	0.05	-0.05	-0.39	0.08	-0.05	0.07	0.09	-0.08	-0.21	0.13	-0.21	0.34	0.23	-0.03	-0.17	0.54	1.00	0.48	0.51	-0.20	-0.42	-0.01	-0.46	0.42	0.19	-0.02	0.21	0.30	0.37	0.44	0.60	0.64	0.70	0.69	0.52	0.30	0.11	0.09	0.03	0.08
Zn	-0.61	-0.92	-0.67	-0.20	0.98	0.91	0.98	0.47	-0.63	-0.82	0.54	-0.90	-0.66	-0.42	-0.73	-0.62	0.37	0.15	1.00	0.96	-0.50	-0.36	-0.17	-0.78	0.09	-0.35	0.01	0.06	0.24	0.27	0.28	0.32	0.31	0.34	0.35	0.24	0.09	-0.07	-0.10	-0.18	-0.30
Ni	-0.64	-0.95	-0.61	-0.07	0.97	0.91	0.98	0.44	-0.56	-0.81	0.51	-0.88	-0.65	-0.43	-0.67	-0.50	0.41	0.09	0.98	1.00	-0.32	-0.23	-0.02	-0.66	-0.02	-0.20	0.05	0.05	0.24	0.27	0.27	0.30	0.30	0.31	0.32	0.23	0.09	-0.06	-0.08	-0.17	-0.29
Ga	-0.47	-0.54	0.08	0.64	0.39	0.30	0.40	0.10	0.25	-0.48	0.04	-0.40	-0.11	-0.07	0.05	0.31	0.25	-0.21	0.37	0.47	1.00	0.38	0.75	0.73	-0.05	0.42	0.17	-0.13	-0.25	-0.27	-0.30	-0.35	-0.29	-0.35	-0.25	-0.03	0.13	0.24	0.32	0.35	0.39
Cr	0.31	0.42	0.72	0.68	-0.59	-0.56	-0.61	-0.46	0.61	0.54	-0.52	0.64	0.48	0.31	0.79	0.89	0.01	-0.19	-0.67	-0.55	0.18	1.00	0.42	0.56	-0.42	-0.01	0.13	0.25	0.21	0.15	0.08	-0.06	-0.07	-0.21	-0.18	-0.08	0.01	0.10	0.13	0.16	0.14
V	-0.16	-0.15	0.52	0.80	-0.06	-0.17	-0.07	0.04	0.54	-0.06	-0.03	0.06	0.25	0.23	0.45	0.64	0.24	-0.13	-0.11	0.01	0.65	0.56	1.00	0.57	-0.15	0.11	0.27	0.08	0.07	0.07	0.04	0.00	0.11	0.00	0.12	0.32	0.41	0.40	0.43	0.39	0.34
Ba	0.81	0.74	0.48	0.10	-0.79	-0.72	-0.81	-0.45	0.14	0.98	-0.45	0.94	0.30	0.28	0.57	0.44	-0.30	-0.18	-0.81	-0.82	-0.56	0.51	-0.10	1.00	-0.19	0.25	0.17	-0.07	-0.20	-0.23	-0.25	-0.30	-0.26	-0.33	-0.23	-0.01	0.18	0.35	0.39	0.46	0.49
As	-0.35	-0.27	0.06	-0.04	0.27	0.12	0.29	0.35	-0.02	-0.39	0.39	-0.36	0.00	0.20	-0.04	-0.06	0.22	0.30	0.32	0.35	0.32	-0.10	0.35	-0.39	1.00	-0.03	-0.19	-0.03	-0.10	-0.04	0.03	0.14	0.18	0.29	0.33	0.29	0.21	0.15	0.12	0.21	0.36
Sn	0.05	-0.16	-0.01	0.11	0.13	0.07	0.11	-0.05	-0.02	-0.12	-0.06	-0.13	0.01	-0.07	-0.04	0.12	0.25	0.06	0.06	0.12	0.10	0.03	0.23	-0.13	-0.01	1.00	-0.00	-0.05	-0.17	-0.19	-0.16	-0.09	-0.08	-0.05	-0.11	-0.16	-0.16	-0.16	-0.07	-0.02	0.06
Y	0.04	-0.10	-0.27	-0.24	0.07	0.06	0.06	0.67	-0.14	-0.12	0.65	-0.13	-0.25	-0.27	-0.31	-0.28	-0.10	-0.04	0.08	0.03	-0.16	-0.27	0.00	-0.12	0.24	0.06	1.00	0.29	0.28	0.25	0.21	0.16	0.22	0.26	0.47	0.65	0.77	0.78	0.82	0.73	0.62
La	0.24	0.39	0.44	0.18	-0.40	-0.47	-0.44	-0.09	0.44	0.16	-0.17	0.22	0.39	0.30	0.35	0.32	-0.19	-0.04	-0.40	-0.43	0.04	0.26	0.15	0.13	-0.07	0.09	0.25	1.00	0.96	0.94	0.92	0.82	0.80	0.73	0.64	0.48	0.34	0.23	0.26	0.24	0.25
Ce	0.14	0.37	0.43	0.10	-0.36	-0.46	-0.39	-0.01	0.44	0.07	-0.08	0.14	0.48	0.37	0.30	0.25	-0.14	0.13	-0.33	-0.38	0.02	0.16	0.13	0.06	0.02	0.06	0.23	0.96	1.00	0.99	0.97	0.89	0.87	0.79	0.69	0.51	0.34	0.19	0.19	0.14	0.11
Pr	0.14	0.38	0.40	0.02	-0.35	-0.46	-0.38	0.03	0.39	0.06	-0.03	0.13	0.49	0.39	0.29	0.19	-0.07	0.25	-0.31	-0.37	-0.06	0.11	0.07	0.07	0.05	0.03	0.25	0.92	0.98	1.00	0.99	0.93	0.91	0.84	0.73	0.55	0.36	0.21	0.21	0.16	0.13
Nd	0.13	0.38	0.33	-0.05	-0.33	-0.44	-0.35	0.10	0.34	0.04	0.05	0.11	0.46	0.36	0.22	0.12	-0.07	0.30	-0.28	-0.35	-0.11	0.03	0.01	0.05	0.06	-0.01	0.31	0.88	0.96	0.99	1.00	0.96	0.94	0.89	0.77	0.56	0.36	0.19	0.18	0.15	0.13
Sm	0.12	0.28	0.15	-0.20	-0.23	-0.35	-0.24	0.31	0.18	-0.01	0.28	0.03	0.33	0.24	0.05	-0.05	-0.05	0.36	-0.16	-0.26	-0.21	-0.13	-0.08	0.01	0.14	-0.04	0.47	0.75	0.85	0.91	0.96	1.00	0.98	0.96	0.83	0.60	0.37	0.19	0.16	0.13	0.12
Eu	0.10	0.22	0.07	-0.26	-0.18	-0.29	-0.18	0.44	0.09	-0.03	0.42	-0.01	0.26	0.19	-0.04	-0.13	-0.06	0.35	-0.12	-0.21	-0.26	-0.20	-0.09	-0.00	0.20	-0.03	0.61	0.65	0.76	0.82	0.88	0.97	1.00	0.98	0.90	0.70	0.48	0.29	0.27	0.22	0.22
Gd	0.07	0.13	-0.04	-0.32	-0.09	-0.19	-0.09	0.55	-0.02	-0.08	0.54	-0.07	0.15	0.10	-0.14	-0.21	-0.03	0.34	-0.03	-0.12	-0.26	-0.26	-0.11	-0.06	0.25	-0.03	0.71	0.56	0.67	0.74	0.80	0.92	0.98	1.00	0.94	0.74	0.52	0.33	0.30	0.26	0.25
Tb	0.04	-0.03	-0.18	-0.29	0.03	-0.04	0.04	0.69	-0.11	-0.13	0.67	-0.14	-0.09	-0.09	-0.27	-0.26	-0.08	0.12	0.07	-0.01	-0.19	-0.32	-0.09	-0.12	0.26	0.01	0.89	0.40	0.45	0.50	0.57	0.74	0.85	0.92	1.00	0.92	0.77	0.61	0.58	0.52	0.51
Dy	0.03	-0.07	-0.20	-0.26	0.04	0.02	0.05	0.68	-0.12	-0.12	0.67	-0.12	-0.13	-0.13	-0.24	-0.23	-0.05	0.09	0.07	0.02	-0.17	-0.25	-0.02	-0.11	0.31	0.01	0.94	0.24	0.27	0.31	0.37	0.55	0.70	0.80	0.95	1.00	0.95	0.85	0.83	0.76	0.72
Ho	0.07	-0.05	-0.19	-0.20	0.00	0.01	0.01	0.62	-0.08	-0.06	0.60	-0.06	-0.19	-0.19	-0.22	-0.19	-0.15	-0.07	0.01	-0.02	-0.16	-0.20	0.02	-0.07	0.25	0.03	0.97	0.22	0.20	0.22	0.27	0.44	0.59	0.69	0.90	0.97	1.00	0.96	0.94	0.89	0.83
Er	0.07	-0.05	-0.18	-0.14	-0.01	0.01	-0.01	0.57	-0.09	-0.00	0.56	-0.00	-0.22	-0.22	-0.16	-0.14	-0.08	-0.07	-0.01	-0.03	-0.13	-0.11	0.05	-0.02	0.22	0.02	0.94	0.13	0.08	0.11	0.16	0.32	0.47	0.58	0.81	0.93	0.97	1.00	0.99	0.96	0.90
Tm	0.28	-0.01	-0.17	-0.08	-0.06	-0.02	-0.06	0.38	-0.15	0.14	0.36	0.10	-0.37	-0.26	-0.14	-0.15	-0.26	-0.29	-0.07	-0.12	-0.20	-0.12	-0.08	0.12	-0.02	-0.01	0.86	0.22	0.09	0.09	0.13	0.25	0.37	0.46	0.71	0.78	0.87	0.87	1.00	0.97	0.92
Yb	0.21	0.09	0.01	-0.00	-0.18	-0.14	-0.18	0.33	0.05	0.15	0.29	0.16	-0.15	-0.11	0.05	0.09	-0.09	-0.19	-0.19	-0.19	-0.08	0.08	0.13	0.13	0.07	0.05	0.85	0.30	0.17	0.17	0.19	0.27	0.36	0.46	0.68	0.80	0.88	0.92	0.90	1.00	0.96
Lu	0.34	0.15	0.16	0.14	-0.27	-0.24	-0.27	0.19	0.12	0.26	0.14	0.27	-0.11	0.01	0.19	0.18	-0.19	-0.30	-0.28	-0.30	-0.07	0.16	0.16	0.25	-0.03	0.04	0.75	0.38	0.23	0.22	0.22	0.27	0.35	0.41	0.62	0.70	0.79	0.81	0.92	0.94	1.00

Figure 4-13: Matrices of Pearson correlation coefficients for Valleleor (bottom left) and Santa Maria (top right). 5% Confidence limit is 0.32 (Valleleor) and 0.4 (Santa Maria).

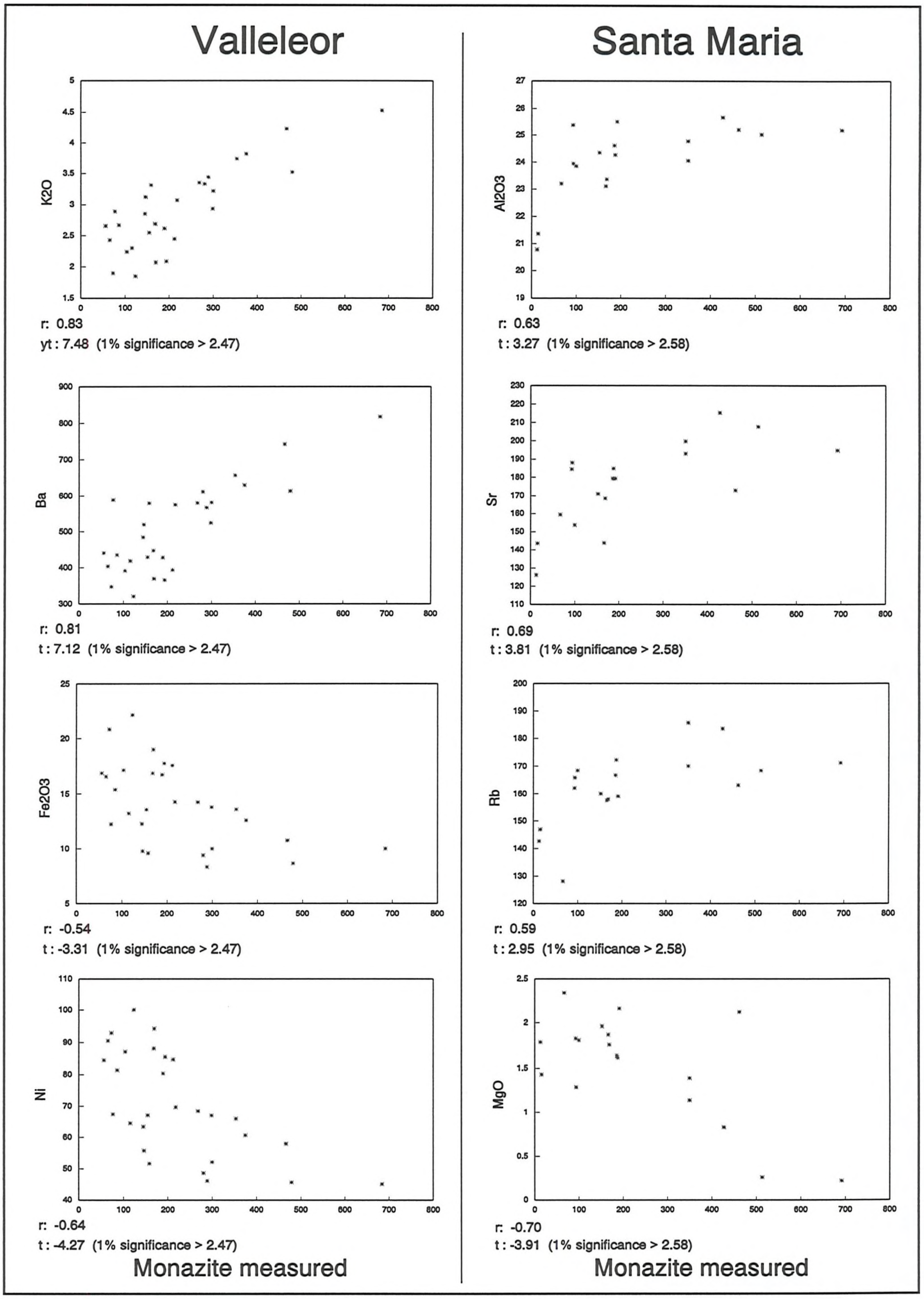

Valleleor:

r: 0.83
yt : 7.48 (1% significance > 2.47)

r: 0.81
t : 7.12 (1% significance > 2.47)

r: -0.54
t : -3.31 (1% significance > 2.47)

r: -0.64
t : -4.27 (1% significance > 2.47)

Santa Maria:

r: 0.63
t : 3.27 (1% significance > 2.58)

r: 0.69
t : 3.81 (1% significance > 2.58)

r: 0.59
t : 2.95 (1% significance > 2.58)

r: -0.70
t : -3.91 (1% significance > 2.58)

Figure 4-14: Scatterplots illustrating the correlation between monazite abundance and selected elements at Valleleor and Santa Maria. r is Pearson correlation coefficient; t is t-statistic for testing significance of correlations.

4.5 Correlation between monazite abundance and host-rock chemistry

Figure 4-13 consists of Pearson correlation coefficients between monazite and all analysed elements at Valleleor and Santa Maria. At Valleleor, monazite correlates strongly with K, Rb and Ba, and negatively with Ni, Zn, Fe and Mg. At Santa Maria, it correlates positively with Al, K, Rb, Sr, Th and Ba, and negatively with Ni, Zn, As and Zr. For the Valleleor data (n=28), the 1% and 5% confidence limits correspond to r=0.44 and r=0.32; at Santa Maria (n=18) they correspond to r=0.54 and r=0.40. Figure 4-14 illustrates some of these relationships graphically.

It is notable that monazite shows no correlation with either rare earth elements or with phosphorus. This demonstrates that **monazite formation has involved a local redistribution of rare earths**, rather than REE transport into the system from elsewhere. The role of phosphorus is equivocal: most of the P budget of the rock is associated with calcium, probably as apatite, but if this were somehow immobile during diagenesis, as suggested by Burnotte et al., (1984), then the availability of *mobile* phosphorus could be germane to monazite formation.

Statistical modelling

To investigate further the way in which monazite abundance might depend on the composition of the host rock, a stepwise regression model was evaluated using the program SYSTAT (Wilkinson, 1990). The model attempts to express monazite as a linear combination of all the geochemical variables. The least significant variable is rejected and the process repeated until only the significant predictors remain. A problem arises in that there is considerable autocorrelation within the dataset (e.g. Fe with Mg, K with Rb) which causes instability in the regression coefficients. The approach taken to overcome this problem was first to extract the principal components from the geochemical dataset, and then perform the regression using the first ten principal components. In the case of the Valleleor data, these ten components accounted for 96% of the total variance (see appendix B, table B-6). Table 4-3 shows the result of this procedure. The tolerance values are now close to

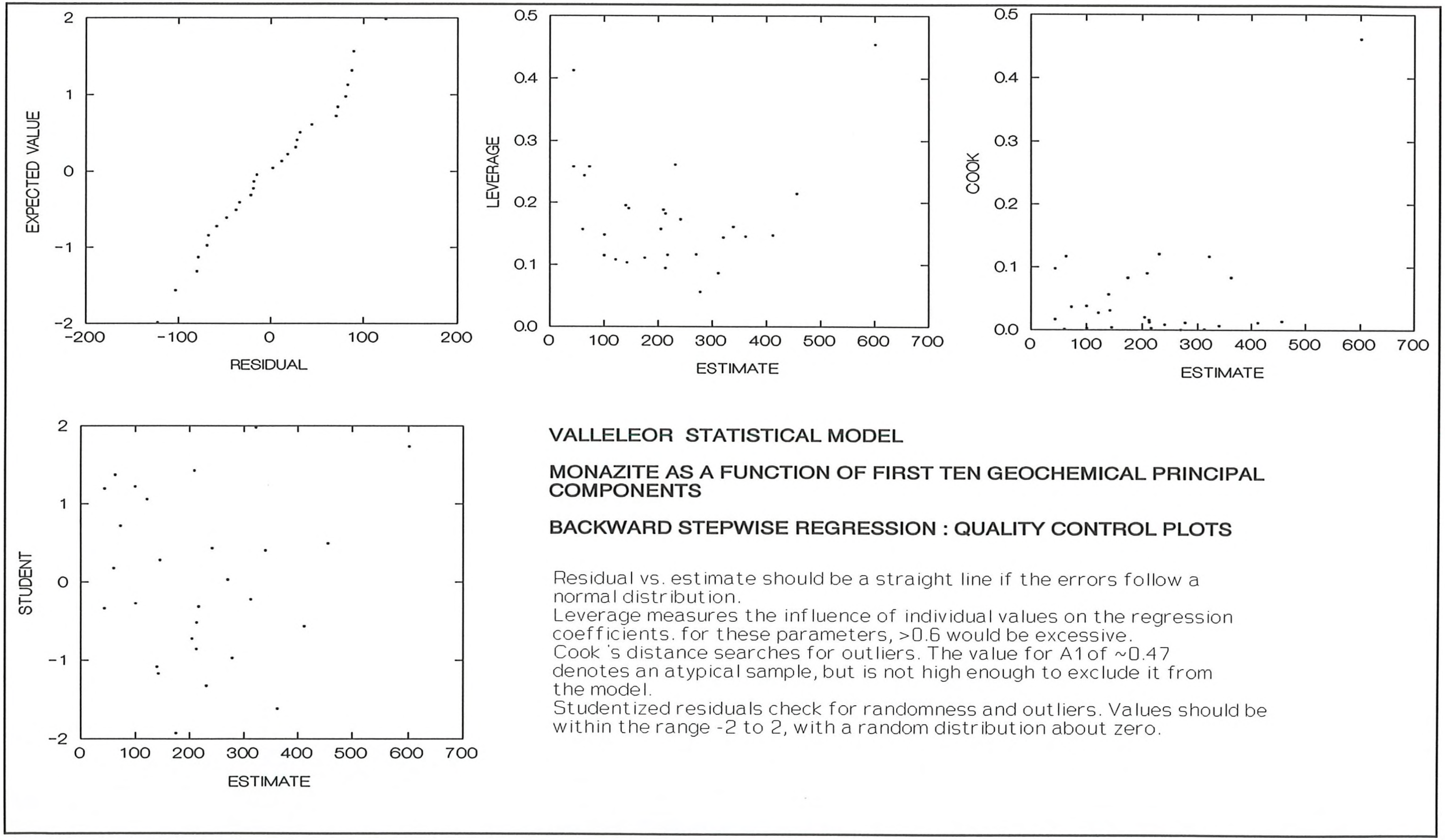

VALLELEOR STATISTICAL MODEL

MONAZITE AS A FUNCTION OF FIRST TEN GEOCHEMICAL PRINCIPAL COMPONENTS

BACKWARD STEPWISE REGRESSION : QUALITY CONTROL PLOTS

Residual vs. estimate should be a straight line if the errors follow a normal distribution.
Leverage measures the influence of individual values on the regression coefficients. for these parameters, >0.6 would be excessive.
Cook 's distance searches for outliers. The value for A1 of ~0.47 denotes an atypical sample, but is not high enough to exclude it from the model.
Studentized residuals check for randomness and outliers. Values should be within the range -2 to 2, with a random distribution about zero.

Figure 4-15: Quality control plots for Valleleor linear regression model.

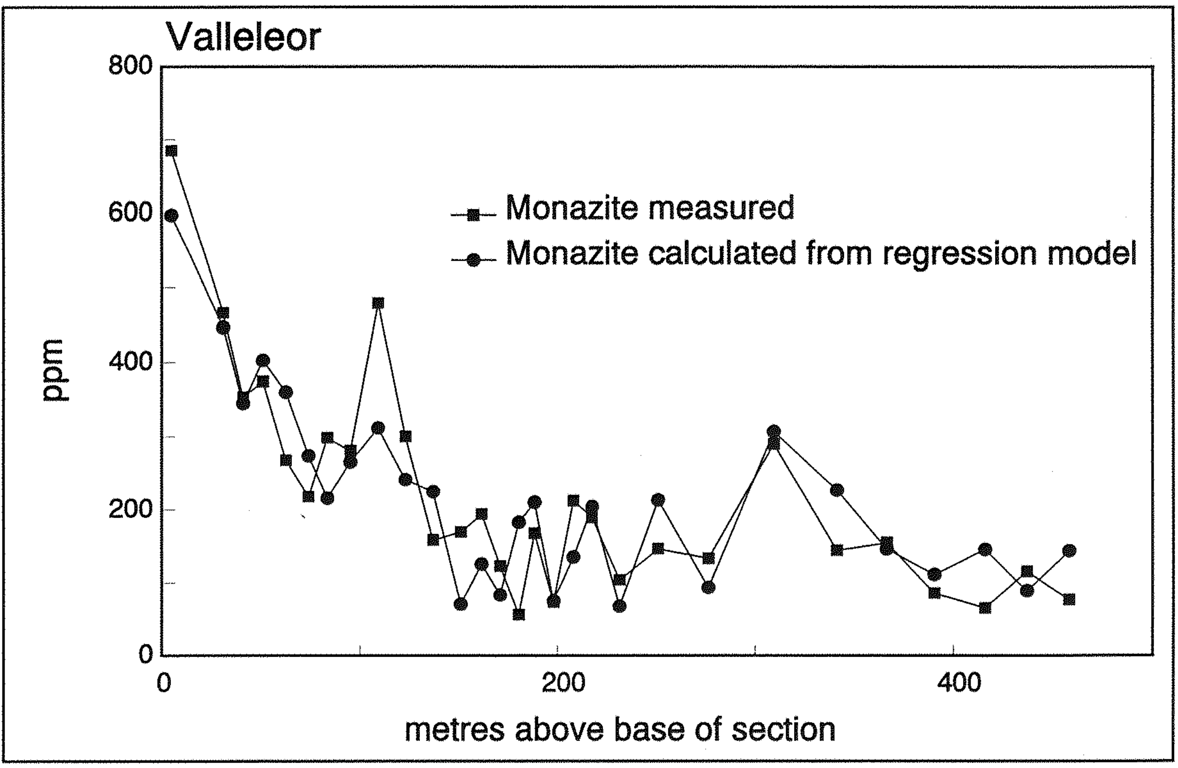

Figure 4-16: Measured versus predicted monazite at Valleleor.

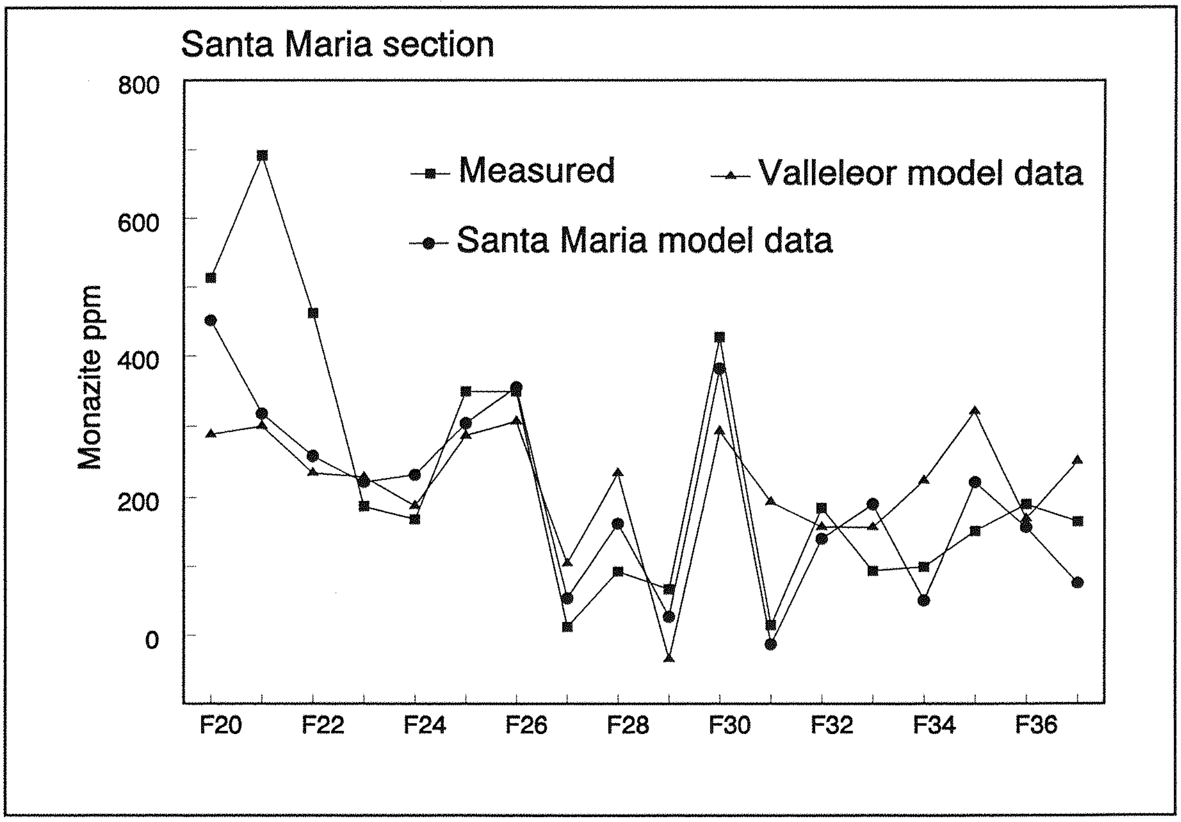

Figure 4-17: Measured monazite abundance at Santa Maria compared with abundance calculated from a best-fit linear regression model, and with abundance calculated from the Valleleor best-fit model.

VARIABLE	COEF	STD	STD COEF	TOLERANCE	T	P(2TAIL)
CONSTANT	217.427	13.469	0.000		16.143	0.000
PC(1)	106.304	13.716	0.709	1.000	7.750	0.000
PC(5)	-29.044	13.716	-0.194	1.000	-2.117	0.045
PC(6)	-72.680	13.716	-0.484	1.000	-5.299	0.000
PC(10)	-27.444	13.716	-0.183	1.000	-2.001	0.057

Dependent Variable: Monazite N: 28 Multiple R: 0.899 Squared multiple R: 0.808
Adjusted squared multiple R:.774 Standard error of estimate: 71.272

Table 4-3: Regression output for Valleleor principal components. PC(n) refer to the principal components in table B-6, appendix B.

an ideal value of 1, reflecting the absence of autocorrelation between the principal components. The near-zero P value for the regression indicates that a fit has been obtained with a high degree of significance, *i.e.*, monazite abundance is almost certainly a function of rock chemistry. The standard error value of 71.2 is the error that would be expected if the model were used to predict monazite concentrations from further geochemical data points. Figure 4-15 consists of plots of statistical parameters designed to test the applicability and validity of the linear regression model.

The coefficients of principal components 1,5,6 and 10 can be combined according to the proportions above to produce a vector of coefficients which relate the whole-rock geochemistry to the measured concentration of monazite ("Vlmodel" in table B-6, appendix B); figure 4-16 compares the predicted values so obtained with the measured values. The fit is good, which is not surprising because these are the very data from which the predictor function was derived.

A more rigorous test of a statistical model is to apply it to new data; in figure 4-17, the regression coefficients derived from Valleleor are applied to the Santa Maria section. The three traces are measured monazite, modelled monazite based on the Santa Maria data themselves, and modelled monazite based on the Valleleor data (point F21 was omitted from the Santa Maria model as an outlier). The Valleleor model fits the measured data at Santa Maria with a correlation coefficient of 0.64, which is significant at the 0.3% confidence level. Apparently, the chemical

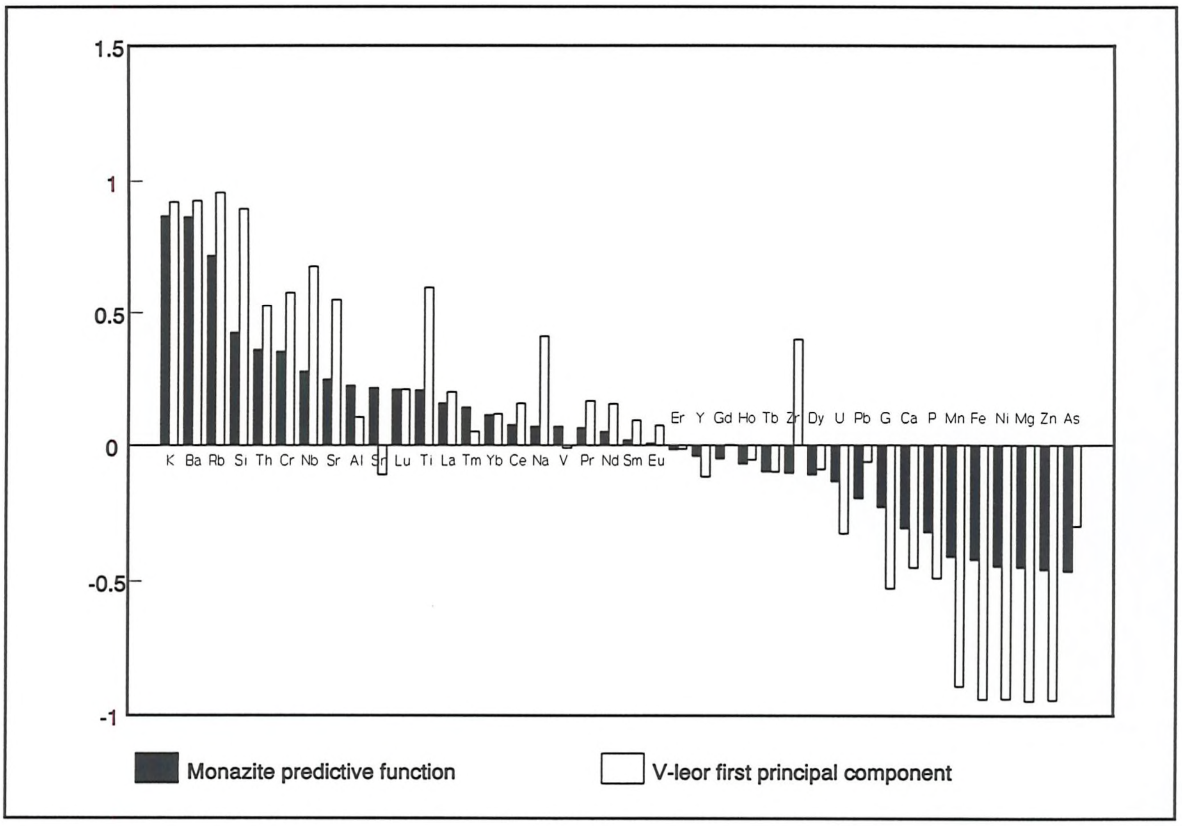

Figure 4-18: Element loadings for the monazite predictor derived from linear regression modelling, compared with the loadings for the first principal component of the Valleleor data.

characteristics of monazite mineralization in the basal Calymene formation can be used to predict the amount of monazite in rocks a few kilometers away, higher in the sequence, and with distinctly different sedimentology.

A best-fit predictive function for monazite derived from the entire dataset ("All" in table B-6) is illustrated in figure 4-18. For comparison, the loadings of the first principal component at Valleleor are shown. Absolute values of greater than about 0.3 are significant; *i.e.* monazite has strong positive loadings for K, Ba, Rb etc. and negative loadings for Mn, Fe, .. As. (The loading values are correlations of the mathematically generated component with individual chemical components).

Interpretation of modelling

The principal component depicted in figure 4-18 expresses the maximum possible amount of variance that can be expressed by a single variable. In a system comprising mixtures of different end members, it is likely to express the degree of mixing between the main end member compositions (e.g., Jarvis and Pearce, 1993). In the Navas de Estena syncline, the bulk of the sediments are shelf muds, of either primary or reworked origin; the thin silty layers seen occasionally at Valleleor and more frequently at Santa Maria are probably very distal storm sand layers. Brenchley et al.(1986) infer transport of such sand layers more than 100 km offshore on the Ordovician Iberian shelf. It is likely that the principal component of figure 4-18 is expressing mixing between a clastic silty component - quartz, feldspar (K,Rb,Ba), and heavy minerals (Th, Zr, Ti, Nb) - and a muddy, perhaps partly authigenic, component with detrital clays (Fe, Mg, Ni, Zn), iron and manganese oxides, and authigenic apatite. Very thin silt layers could easily be incorporated into the sediment by bioturbation or physical reworking such that they would no longer be recognizable in the field, but they would still affect the chemistry.

In summary, the amount of monazite in a particular specimen in the study area is related to the bulk major and trace element chemistry of that specimen. The "monazite" function of figure 4-18, essentially the best fit "whole rock chemistry associated with monazite", is very similar to the first principal component. It seems reasonable to infer that:

1). Monazite abundance is proportional to the amount of original silty material in a sediment comprising a mixture of a silty component and a clay component.

2). In particular, monazite is associated with K, Rb, Ba and Si rather than the "detrital heavy" tracers Ti, Zr, Nb, which suggests that the feldspathic component of the silt was important. A possible explanation for such a link is for the REE in the monazites originally to have been derived from detrital alkali feldspars.

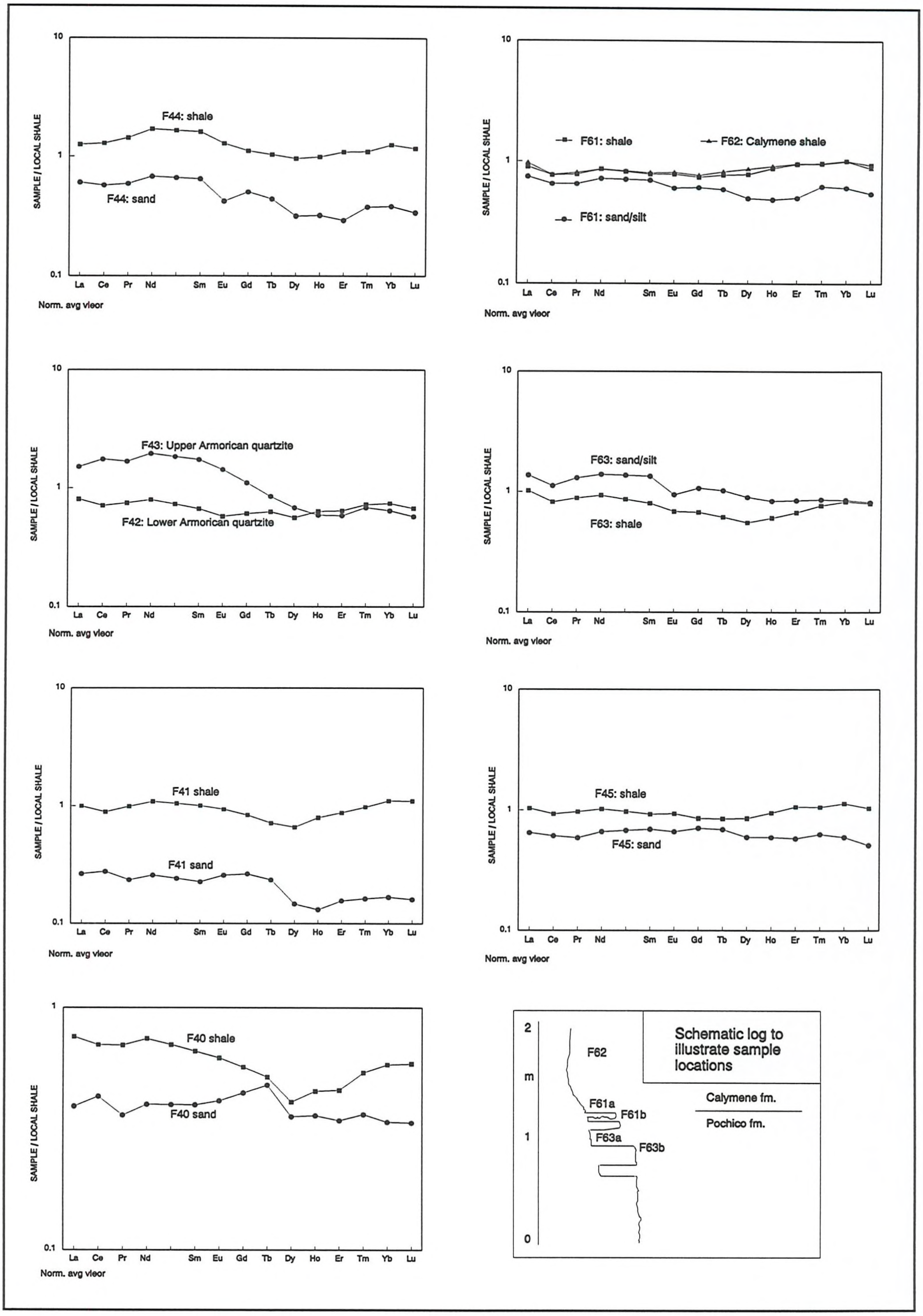

Figure 4-19: REE patterns of sandstone / shale pairs from the Lower Ordovician section in the Rio Estena. For sample locations see figure 1-9.

4.6 Comparison of interlayered shales and sandstones

In their study of turbidite-hosted grey monazites in Wales (reviewed in chapter 1), Milodowski and Zalasiewicz (1991) found LREE enrichment of fine grained hemipelagite horizons relative to the interbedded turbidite siltstones, which was attributed to monazite formation in the hemipelagites. They found clear evidence for REE transport on a scale of about ten centimetres. To check for a similar process at Navas de Estena, a number of interbedded shale/sandstone or shale/siltstone specimens were collected from the base of the Ordovician sequence in the Rio Estena up through the Armorican quartzite and Pochico formation and into the Calymene formation. The REE patterns are shown in figure 4-19.

F41, of Tremadoc age, shows a possible LREE enrichment, but overall lower REE levels, in the sandstone fraction. Two specimens from the Armorican quartzite have REE levels comparable to shales; F43 is notably enriched in the light REE, possibly reflecting detrital monazite or allanite content. F44 and F45, from the lower and middle Pochico formation respectively, have sandy interbeds with REE patterns parallel to, and with lower abundance than, the neighbouring shales. Even at the Pochico / Calymene boundary there is no sign of light REE depletion in the sandstone/siltstone layers. This boundary is transitional over about ten metres, with a gradual increase in the proportions of shale over sands or silts. Monazite is visible in the shale layers, and was measured in high concentrations at the same horizon to the north at Valleleor. In figure 4-12(d), F26, F27, F28 are above, in and below a silty "hard ground" horizon at Santa Maria. F26, which has the greatest concentration of monazite, actually has a slightly light-depleted pattern; the silty horizon F27 has an almost flat shale type pattern.

In conclusion, no light-REE enriched shales, with complementary light-depleted sandstones, of the sort described by Milodowski and Zalasiewicz (1991) were found. It would seem that vertical transport of REE to form monazite is not a significant mechanism and that the REE transport which does occur must be on a scale of centimetres or less.

4.7 Mass balance considerations

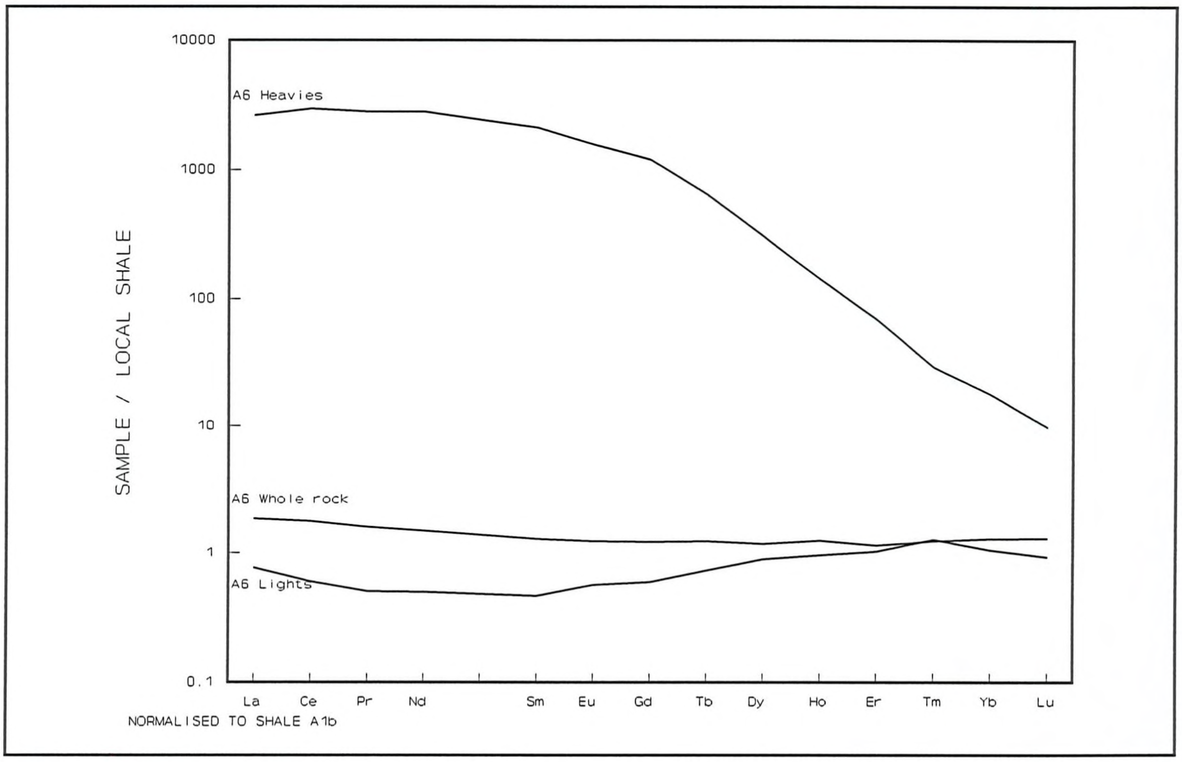

Figure 4-20: Shale-normalised REE pattern for monazites separated from sample A6 compared to the whole rock pattern and the light fraction remaining after mineral separation.

Figure 4-20 shows shale normalised patterns for sample A6 from Valleleor; the heavy fraction consisting of virtually pure monazite which was separated from it; and the light fraction ($\rho<3.3$) from which the monazites have been removed. The monazites are strongly LREE enriched, with the light fraction showing a complementary depletion in LREE. Nearly all of the difference is accounted for by the LREE content of the separated monazites (table 4-4).

Since only the 250-500μm fraction of shale was separated using heavy liquids, any smaller monazites will be either lost in the fines or not freed from the light fraction. Thin sections typically contain a range of monazites of different grain sizes, so the calculation in table 4-4 indicates that at least 40% of the Ce in the whole rock is contained in monazite, and probably much more when the finer grained monazite is included.

Mass of Ce in 1g shale(μg)		114
Mass of Ce in 1g 250-500μm lights (μg)	39	
Mass of Ce in heavy fraction separated from 1g of 250-500 μm fraction(μg)	57	
	96	114

Table 4-4: Mass balance for shale A6.

If we assume the following parameters:

Average monazite grain diameter = 350μm (based on SEM photographs)

REE content of grey monazites = 44.1 % (Based on alluvial monazites)

REE content of pure $LnPO_4$ = 60 %

Monazite concentration in shale = 350 ppm (estimated from figure 4-1)

Density of inclusion - free monazite = 5.1 gcm^{-3}

Density of silicate inclusions = 2.8 gcm^{-3}

Density of shale = 3.0 gcm^{-3}

Then,

Calculated density of grey monazite = 4.19 gcm^{-3}

Mass of a 350μm grain = $4/3 * \pi * (175 * 10^{-4})^3 * 4.19 * 10^6 = 94\mu g$

Number of monazites in 100g shale = 350 * 100 / 94 = 372 grains

Volume of 100g shale = 33 cm^3

Volume of shale occupied by one monazite grain = 33 / 372 = 0.09 cm^3

∴ Spacing between grains = $\sqrt[3]{(0.09)}$ = 0.45 cm

This estimate seems reasonable for specimens with abundant monazite, where experience suggests that a random slice through a fist-sized hand specimen has about 50 % chance of intersecting a monazite grain. The evidence presented above concerning shale/sandstone pairs demonstrates that there is no REE transport on a scale of about 10 cm. This estimate of the spacing between nodules reinforces the other geochemical evidence by suggesting that only very localised REE transport on a scale of < 1 cm may be necessary for monazite formation.

4.8 REE chemistry of monazites

Rare earth element patterns of monazites are strongly enriched in the LREE with respect to their host shales (e.g., figure 4-20). The curve shows a smooth variation without any anomalies at Eu or Ce. The REE data measured on heavy mineral concentrates (specimens with the suffix "h" in table B-4) have been used to deduce the monazite content of the heavies, and so cannot be used to deduce absolute values of REE concentrations in monazites for fear of circular reasoning. However, since monazite is the only REE-bearing phase in the heavies, it is safe to assume that ratios of REE measured in the heavies will reflect the true values of the monazites.

The Valleleor data show a remarkable systematic variation REE behaviour with

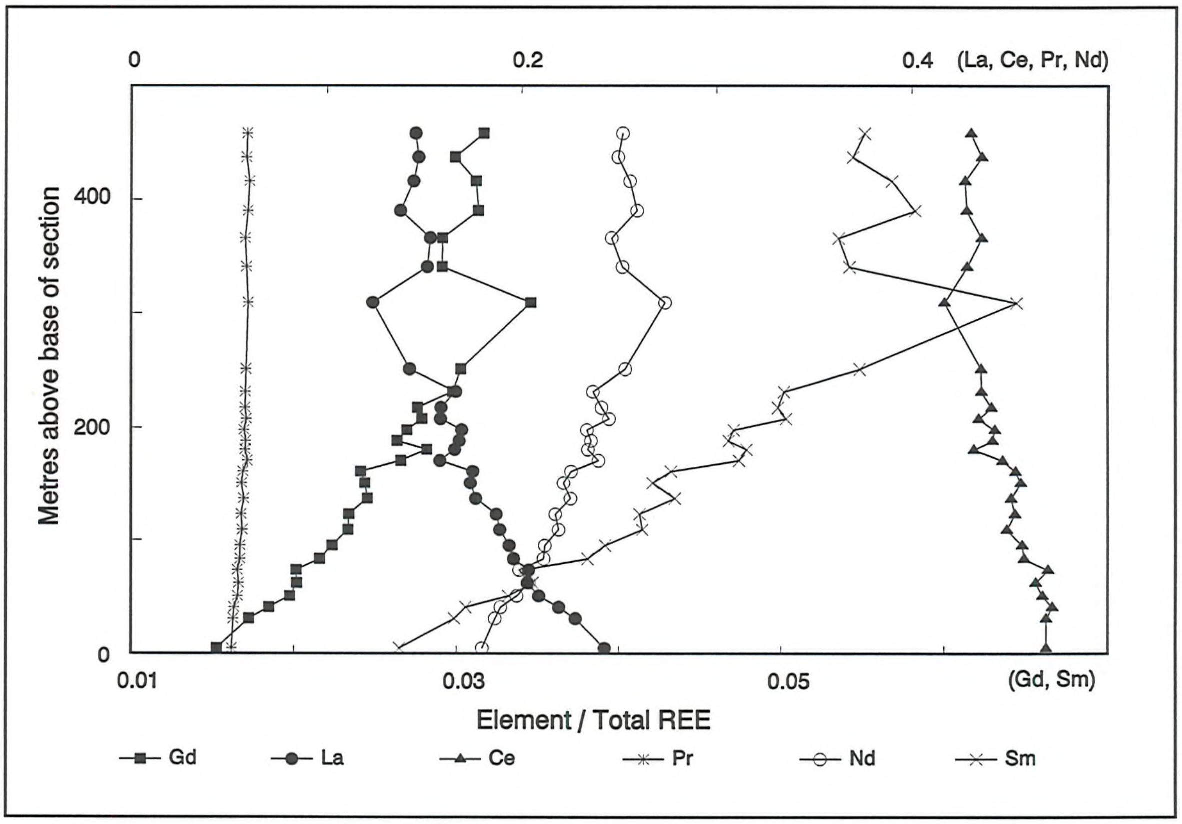

Figure 4-21: Variations in relative proportions of REE in monazite at Valleleor as a function of stratigraphic level.

Valleleor:

	La	Ce	Pr	Nd	Sm	Eu	Gd
Height	-0.88	-0.87	0.82	0.88	0.90	0.90	0.89
Monazite	0.77	0.65	-0.79	-0.72	-0.71	-0.73	-0.75
Ba	0.69	0.56	-0.75	-0.65	-0.61	-0.63	-0.64
K_2O	0.65	0.51	-0.71	-0.61	-0.57	-0.60	-0.60
Ga	-0.59	-0.56	0.63	0.59	0.58	0.57	0.57
Rb	0.49	0.35	-0.57	-0.45	-0.41	-0.44	-0.44
LOI	-0.48	-0.41	0.57	0.46	0.42	0.44	0.45
Na_2O	-0.46	-0.49	0.41	0.48	0.51	0.49	0.48
V	-0.37	-0.48	0.39	0.42	0.43	0.40	0.44
As	-0.37	-0.39	0.35	0.37	0.41	0.44	0.45
Ni	-0.33	-0.24	0.42	0.29	0.25	0.28	0.30
Zn	-0.31	-0.21	0.38	0.27	0.23	0.26	0.28

Santa Maria:

	La	Ce	Pr	Nd	Sm	Eu	Gd
Monazite	0.67	0.63	-0.43	-0.65	-0.66	-0.59	-0.69
Th	0.67	0.65	-0.29	-0.64	-0.69	-0.69	-0.70
Al_2O_3	0.62	0.72	-0.04	-0.60	-0.74	-0.68	-0.74
Zr	-0.53	-0.63	0.16	0.52	0.59	0.56	0.66
Rb	0.50	0.47	-0.13	-0.46	-0.52	-0.51	-0.52
Sr	0.45	0.55	0.06	-0.43	-0.58	-0.49	-0.59
U	0.42	0.40	-0.37	-0.46	-0.41	-0.40	-0.36
As	-0.40	-0.38	0.22	0.37	0.39	0.40	0.45
Ga	0.40	0.46	0.01	-0.38	-0.48	-0.47	-0.48
Ba	0.40	0.35	-0.12	-0.36	-0.40	-0.37	-0.41
Sn	0.38	0.35	-0.26	-0.34	-0.35	-0.33	-0.41
K_2O	0.37	0.33	-0.03	-0.33	-0.39	-0.37	-0.38
V	0.35	0.53	0.13	-0.36	-0.51	-0.46	-0.51
SiO_2	-0.33	-0.48	-0.02	0.34	0.43	0.42	0.44
Height (m)	0.29	0.23	-0.34	-0.27	-0.21	-0.18	-0.28

Table 4-5: Correlation coefficients between various lanthanides in monazite (expressed as Ln/Total REE) and height, monazite abundance and whole rock geochemistry at Valleleor and Santa Maria. Only elements with significant correlations are shown.

stratigraphic level. The relative proportions of La and Ce decrease steadily up-section, while Pr, Nd, Sm, Eu, etc. increase up-section (figure 4-21). The partial matrices of correlation coefficients in table 4-5 suggest that, at Valleleor, the effect appears to be primarily a function of height in the section. The relative concentration of light v. heavy REE in the monazites is also strongly correlated with the total amount of monazite, and other "monazite indicators" such as Ba, K and Rb. At Santa Maria, although there is no correlation with height, the REE proportions of monazites are still correlated with monazite abundance and associated elements. However, the correlations are weaker (the same r value is less significant at Santa Maria than at Valleleor because of the different number of samples).

In conclusion, the REE chemistry of monazites shows two types of variation:

1). At Valleleor, the relative proportions of light to heavy REE in monazites vary according to the height above the base of the section.

2). At both Valleleor and Santa Maria, they vary according to the amount of monazite present.

In both cases, La and Ce have an inverse relationship to Pr, Nd, Sm ..., such that the more monazite is present, the more La, Ce rich it is and the more Pr, Nd, Sm... poor. This phenomenon is reminiscent of the fluid evolution documented by the zoning described in chapter 2, where the REE chemistry evolved from an initial HREE-rich fluid to a later LREE-rich composition (figure 2-35). The positive correlations between La, Ce and monazite in table 4-5 suggest that this later fluid was the more favourable for the growth of the nodules. Because of the constraints already established on REE transport, the correlations with height in the section at Valleleor are seen as largely coincidental. They most likely stem from geochemical factors linked to the steady evolution in sedimentary environment from the base of the section upwards.

Chapter 5: Nd and Sm isotopic data.

5.0 Objectives

The experiment which was performed sought to measure a Sm-Nd isochron age by sequential leaching of individual monazite nodules. Because the REE pattern of the monazite changes from core to rim (chapter 2), the Sm/Nd ratio is higher in the core of a nodule than in the rim. If this zoning could be sampled by successive acid leaching of the nodule (and if the different areas of the nodule were originally isotopically homogeneous), then a Sm-Nd isochron should yield the age of formation of the nodule. The age of the sediment is known from the biostratigraphy to be Lower Llanvirn (≈475 Ma), so a radiometric age would potentially date the nodules as synsedimentary or diagenetic, and allow an estimate of burial depth at the time of nodule formation.

5.1 Methods

Stage #	Acid used	Time	Temperature
1	5 drops HNO_3 + 5 drops HCl	30 hours	150 °C
2	5 drops HNO_3 + 5 drops HCl	30 hours	150 °C
3	5 drops HNO_3 + 5 drops HCl	7 hours	150 °C
4	0.1 ml HF + 5 drops $HClO_4$	12 hours	150 °C

Table 5-1: Summary of sequential leaching procedure.

Two ≈1mm sized nodules from heavy mineral concentrate A29 (the top of the Valleleor section) were placed in 30 ml size Teflon® bombs. The four stages of leaching are summarized in table 5-1. Because of the high concentration of REE in the leachates, with only a small proportion of Fe, Mg and Al from the inclusions, it was possible to separate Nd from each fraction using a single stage of ion-exchange chromatography. A Teflon® resin was used (KELF® coated with HDEHP, adapted from White and Patchett, 1984), with 0.2 M HCl as eluant. Aliquots of the leachate solutions were analysed for REE by ICP-MS, in order to check whether the patterns obtained were consistent with the laser-ICPMS results presented in chapter 2. The original leachate solutions were spiked directly, using the ICP-MS results as a rough guide, in order to measure Sm and Nd concentrations precisely by isotope dilution.

All the residues were loaded onto a VG Sector 54 Thermal Ionisation Mass Spectrometer (TIMS), equipped with seven collectors. The isotope dilution measurements were performed in static mode; Nd isotope ratios were measured in multidynamic mode. Three standard solutions were employed to monitor precision, as detailed in table 5-2.

5.2 Results

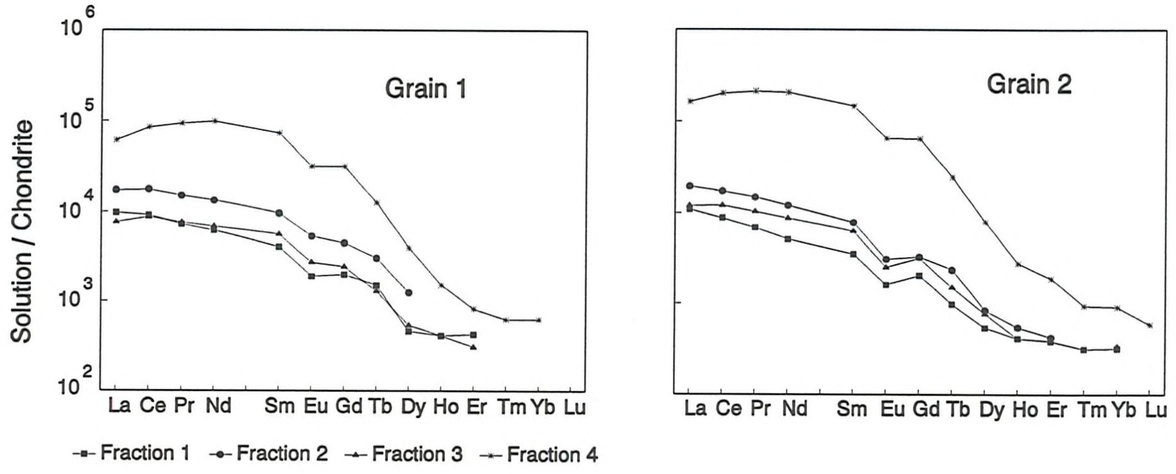

Figure 5-1: Chondrite-normalised REE patterns obtained for the four leachates, showing how the material sampled initially has $La_N > Nd_N$ and the latest fraction is a Nd-rich "core"-type pattern (see chapter 2).

The ICP-MS results (Figure 5-1) suggest that the leaching is indeed sampling first the rim of the nodule and then the cores, resulting in a range of Sm/Nd ratios.

The results of the TIMS measurements are summarized in table 5-2, and plotted as an isochron diagram in figure 5-2. Neither grain yields an isochron; there is a range of approximately 1.4 ε_{Nd} units, calculated at the inferred age of sedimentation. It is concluded that either:

	Sm Recovered (μg)	Nd Recovered (μg)	^{147}Sm/^{144}Nd (atomic)	^{143}Nd/^{144}Nd (atomic)	ε_{Nd} (t=475 Ma)
Grain 1					
#1	0.786	4.15	0.1146	0.511923±6	-9.0
#2	2.16	10.88	0.1198	0.511958±6	-8.6
#3	1.13	5.71	0.1191	0.511968±6	-8.4
#4	13.57	53.76	0.1525	0.512047±6	-8.9
Grain 2					
#1	0.766	4.27	0.1085	0.511961±6	-7.9
#2	1.79	9.36	0.1155	0.511965±6	-8.2
#3	1.35	6.63	0.1232	0.512020±6	-7.6
#4	22.56	95.05	0.1435	0.512038±8	-8.5
Standards					
JMC321	(n=9, ±2σ)			0.511120±13	
	Max			0.511132	
	Min			0.511112	
CIT nNd*β*	(n=14, ±2σ)			0.511916±18	
	Max			0.511929	
	Min			0.511901	
"Soton"	(n=20, ±2σ)			0.512226±16	
	Max			0.512240	
	Min			0.512212	

Table 5-2: Results of the sequential leaching experiment on monazite nodules from shale A29.

1) The system has not been closed since formation of the nodules, or that
2) The original source of the REE had a slightly heterogeneous Nd isotope composition.

There is some evidence for both of these possible explanations. Late-stage alteration of cone-in-cone concretions (chapter 3) was accompanied by REE mobility, which could conceivably have upset the isotope systematics of the monazite nodules.

Alternatively, REE in the monazites may have been derived from two different

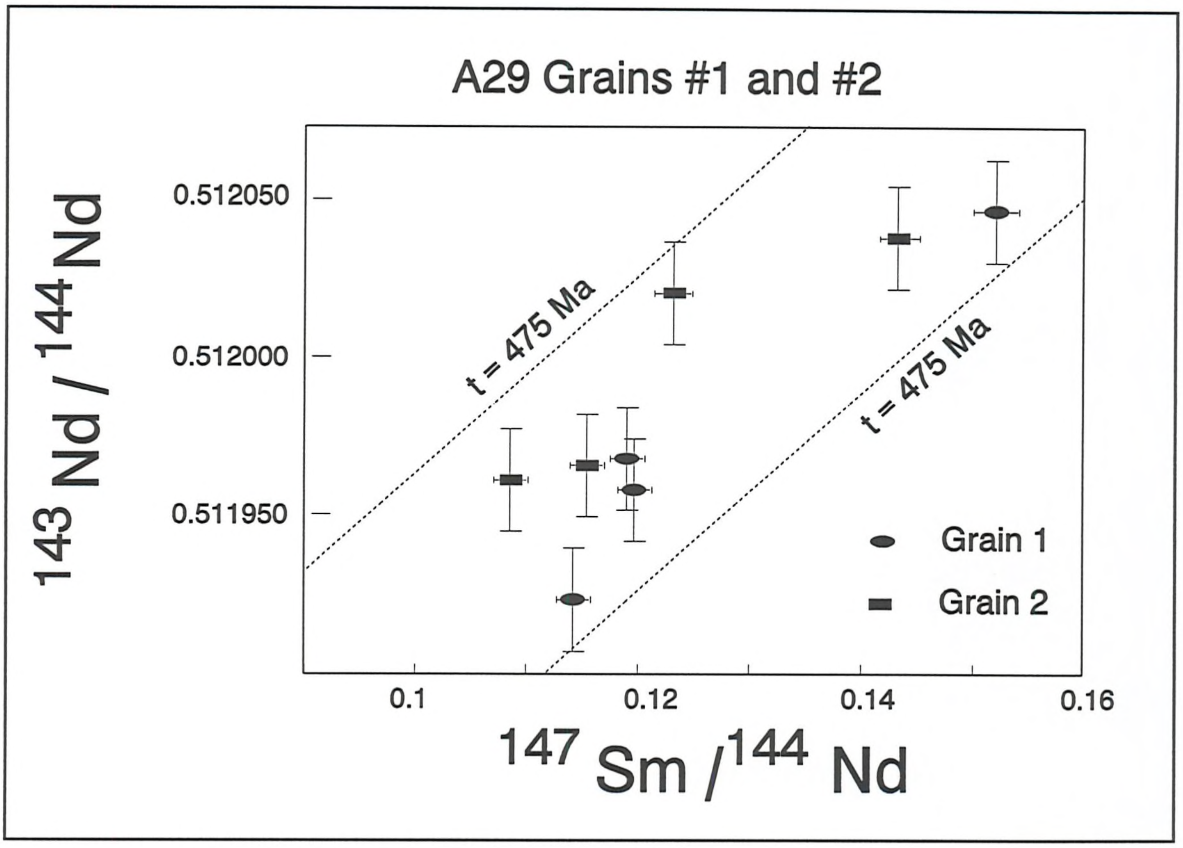

Figure 5-2: Sequential leaching results for the two monazite nodules plotted in an isochron diagram. Error bars are ±2σ.

sedimentary components (see discussion in chapter 6) which were incompletely mixed at the time of nodule formation. The age of the sediment, 475 Ma, is relatively small compared to the half-life of Sm (106 Ga), and the leaching process sampled only a small range of Sm/Nd values. Thus, although the range of initial ε_{Nd} values was relatively small, there is insufficient radiogenic ^{143}Nd to overcome the initial heterogeneities present in the sediment.

Chapter 6: Discussion

6.1 Previous models

This topic was briefly addressed in chapter one. Here, the principal models for grey monazite formation which have been proposed in the literature will be discussed in the light of this study and others.

Contact metamorphism

A granite-related origin for grey monazite was proposed by Rosenblum and Mosier (1983) after their study of alluvial panning concentrates. They found a spatial correlation between monazite occurrences and granite plutons in Alaska, and noted that the well-known locality at Kivu, Zaire, was also within the contact aureole of a granite.

In Spain, the only granites in the area of the monazites are late Hercynian and post-date the cleavage formation in the shales (Ortega, 1993). These post-S_2 plutons cannot, therefore, be responsible for the formation of the pre-S_2 monazites.

Similarly, monazite nodules from Belgium, Wales and Rwanda occur in host rocks which have been unaffected by contact metamorphism. The contact-metamorphic model is therefore rejected.

Hydrous precursors

Donnot et al. (1973) proposed that grey monazite formed via an initial hydrous REE phosphate phase, rhabdophane ($LnPO_4.H_2O$, where Ln=lanthanide). This was inferred to have formed blebs of radiating, fibrous crystals, which later dehydrated to produce monazite. In support of this idea, Donnot et al. (1973) describe monazite nodules with textures pseudomorphing the fibrous rhabdophane. They also cite the ease of dehydration of rhabdophane to produce monazite. A recent study by Akers et al. (1993) bears this out, concluding that monazite is the stable phase with respect to rhabdophane at temperatures of less than 200 °C.

In the present study, hundreds of monazite nodules were examined as BSE images in the course of identifying heavy mineral concentrates. In addition, alluvial concentrates from Rwanda, Belgium and the Grand Fougeray material originally studied by Donnot et al. (1973) were examined. No traces of rhabdophane were ever found, nor were any structures suggesting replacement of fibrous material by monazite. All the textural evidence (chapter 2) suggests the direct replacement of silicate minerals in the shale by monazite. It is concluded, therefore, that the texture described by Donnot et al. (1973) is not important, and that there is no direct evidence for the existence of a rhabdophane precursor.

However, the above does not preclude the formation of precursor REE minerals during early diagenesis, followed by remobilisation of REE to form monazite at another site. The model proposed by Milodowski and Zalasiewicz (1991) (figure 1-6) envisages REE liberated in early diagenetic reactions being concentrated in zones rich in organic material, either as phosphates or adsorbed onto the organic material itself. These REE could later recrystallize at higher temperature to form the monazite concretions.

The presence of florencite, $LnAl_3(PO_4)_2(OH)_6$, in some Navas de Estena shales (chapter 2) may be indicative of such a process. Florencite grains in figure 2-14 (d) to (f) have a rather ragged appearance which may be indicative of dissolution. If this is the case, then florencite may act as a temporary reservoir for REE which were released at a very early stage of diagenesis, held in florencite, and then made available again for the later stages of monazite growth by florencite breakdown. However, McKie (1962) found florencite to be hydrothermally stable to more than 500 °C.

Recrystallization of detrital monazites

This theory was proposed by Read et al. (1987) for the grey monazites of the Welsh basin, and subsequently dismissed by Burnotte et al. (1989), working in Belgium, and

Milodowski and Zalasiewicz (1991) in their more detailed study in Wales. The latter authors concluded that there was no sedimentary control of nodule distribution comparable to that seen for detrital heavy minerals such as zircon, which were concentrated in fining-upward layers at the base of turbidite units. They reported very rare instances of monazite nodules nucleated on Th-rich detrital cores; in these cases, however, there is a sharp boundary between the detrital core and the later overgrowth, with no sign of recrystallisation of the core.

In the present study, no such overgrowths on detrital monazites were seen. Detrital monazite is very rare in the Calymene Formation shales; when seen, it tends to be fine-grained and euhedral, and shows no evidence of instability under diagenetic conditions. Grey and yellow monazite have identical XRD patterns (this study, figure 2-22; Rosenblum and Mosier (1983); Nonnon (1984)) and are presumably identical crystallographically. It is difficult, therefore, to imagine a mechanism which would cause yellow monazite to be unstable at the same time as grey monazite was forming. In conclusion, there is no evidence to support the theory of Read et al. (1987).

Role of phosphate

Burnette et al. (1989) attach importance to the role of phosphorus in monazite genesis:

"The availability of phosphorus during diagenesis requires that it be trapped in the sedimentary sequence at an early stage either as authigenic phosphorus (phosphorite, phosphatic shale, etc.) or detrital phosphorus (organic matter, phosphorite gravels, etc.)."

Their model (see chapter 1) invokes transport of phosphate vertically through the sediment from such enriched horizons to the site of mineralization, *i.e* they move the phosphorus to the REE, not the other way around.

At Valleleor, P is associated strongly with Ca (chapter 4), implying that the P budget is dominated by apatite. Ca^{2+} content is 69 mmol/kg, which will consume on average

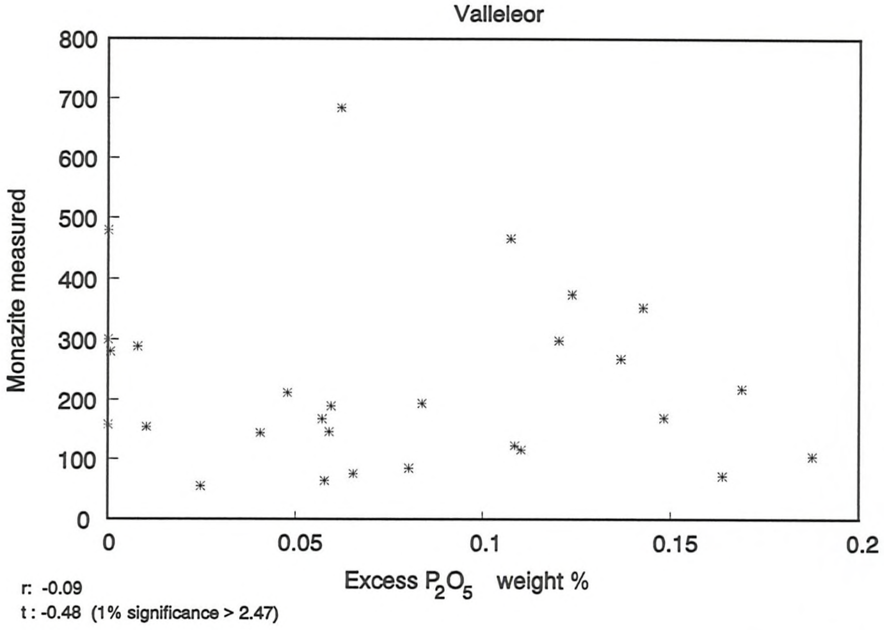

Figure 6-1: Scatterplot illustrating lack of correlation between phosphate content in excess of that required to form apatite, and monazite abundance.

41 mmol/kg phosphate as apatite. Average P content is 52 mmol $(PO_4)^{3-}$ per kg of shale, leaving 11 mmol/kg of excess phosphate ions. This compares with 1.9 mmol/kg of Ln^{3+}. Thus, even if most of the phosphate is assumed to be immobilised in apatite, there remains five times as much phosphate as is required to form monazite. This "excess phosphate" shows no correlation with monazite abundance (figure 6-1). Hence, availability of phosphorus does not seem to be a factor controlling the monazite distribution within the sections studied and there is no need to invoke vertical movement of phosphate of the sort proposed by Burnotte et al. (1989).

However, phosphate may be significant in explaining the geographical distribution of grey monazites. The association of phosphorus with organic material in marine black shales is well known (e.g. Demaison and Moore, 1980). Milodowski and Zalasiewicz (1991) propose that the release of phosphorus from organic material during early diagenesis serves to concentrate REE as phosphates in organic rich horizons. If, as Burnotte et al. (1989) maintain, only a small fraction of total P is mobile during diagenesis, then the availability of sufficient free phosphate to precipitate REE could become important. This "mobile fraction" could equate to biogenic phosphorus associated with organic material. In sediments deposited under oxic bottom waters, organic material is poorly preserved because of bioturbation and oxidation. Any associated phosphate would probably be incorporated into authigenic apatite, and subsequently would be unavailable during diagenesis. As was observed in chapter 1, monazites in Spain and in Wales seem to be restricted to the deeper water parts of the shelf, around the oxic/anoxic boundary. There may thus be a link between water depth, the incorporation of organic material into the sediment, and the availability of mobile biogenic phosphate during diagenesis.

It is worth noting that, at 1600 ppm P, the Calymene Formation has about twice the phosphorus concentration of average shale (700 ppm: Mason and Moore, 1982). However, there is insufficient evidence to elaborate this theme any further.

Local remobilisation of REE

In the Llandovery of Central Wales, Milodowski and Zalasiewicz (1991) demonstrate convincingly that REE from turbidite units have been redistributed and concentrated in thin overlying hemipelagite units, where they form grey monazite nodules (chapter 1: figure 1-6). In this particular case, it is clear that the source of the REE is the coarser-grained fraction of the sediment, and that transport of REE is over a matter of tens of centimetres. The monazite nodules, which are indistinguishable from those found in Spain, predate the cleavage and are not found in early diagenetic carbonate concretions, and are therefore inferred to form during late diagenesis. The origin of the zoning is less clear; Milodowski and Zalasiewicz (1991) attribute it to initially greater mobility of heavy REE, so that the source material evolves to more LREE-rich compositions with time.

In Spain, the rocks are possibly distal analogues of the Welsh turbidites; there are thick intervals of fine mudstones, probably bioturbated, with little internal structure, and only occasional thin silty layers. Monazite is not associated with any sedimentary feature of the sort described by Milodowski and Zalasiewicz (1991). However, the correlation between monazite abundance and silt component described in chapter 4 is consistent with the source of the REE being the coarser-grained part of the sediment, as it is in Wales. Although transport of REE is more local in Spain, perhaps by a factor of ten times, the overall chemistry of the process is very likely to be the same in both cases.

6.2 Constraints on monazite formation

These can be subdivided into observations which are in common to all grey monazite occurrences (summarized in chapter 1), and those which are restricted to the present study. Chief conclusions to be drawn from the first category are:

1. Grey monazite nodules form during diagenesis, after the initial compaction of the host sediment, and before the peak of metamorphism when the cleavage is formed.
2. The host is nearly always a fine-grained mudrock, but does not necessarily contain anomalous levels of REE, phosphate or organic matter.
3. The identical zoning, found in nodules of all ages and from different continents, must be caused by a process which is a ubiquitous part of burial metamorphism.

These ideas can be refined slightly in the case of the present study:

1. The nodules probably form somewhere in the temperature range 90±30 °C (disappearance of K-feldspar) to the middle anchizone (i.e. 220 - 250 °C). Monazite formation is not a sudden event, but, rather, spans a range of temperatures.
2. REE are only very locally redistributed, probably on the scale of about one cm.
3. The REE chemistry of the fluid is inferred to change from an initial HREE-rich pattern to a later flat or LREE-rich pattern during the interval of concretion growth (figure 2-35). The concept of two fluids, early and late, and the possible reasons for the change in fluid REE chemistry, is central to this discussion. They will be referred to as an "early, heavy" fluid and a "late, light" fluid.

4. Sm - Nd isotopic data (chapter 5) suggest that the REE contained in the monazites were not derived from an isotopically homogeneous reservoir. A plausible explanation is that REE were derived from two sedimentary components with different provenances: one, shelf muds which comprised the bulk of the sediment, and two, silty material from further up the shelf deposited as a result of storm events (Brenchley et al., 1986).
5. Although neither parameter can reliably be estimated in the field, the abundance of monazite correlates geochemically with the proportion of silty material in the sediment (chapter 4). In particular, monazite abundance correlates with the La- and Ce- rich component of monazite chemistry which is characteristic of the "late, light" fluid (table 4-5). It is tempting, therefore, to attribute the origin of this fluid to the silty component of the sediment, derived from distal storm sand layers.

6.3 Components of a genetic model

The process of monazite formation during diagenesis can be considered as the resultant effect of three stages, the first two of which vary chemically with time and temperature, and the third of which is a constant:

1. REE are released from some source material in the sediment.
2. They are transported, possibly as complex ions, through the sediment for a distance of from about one centimetre (Spain) to about ten centimetres (Wales).
3. The REE precipitate as monazite.

As discussed in chapter 2 (figure 2-35), stage 3 can be thought of as a sort of "filter", whereby the monazite crystal lattice excludes the smaller HREE ions in favour of the larger LREE ions with higher coordination number. Since this crytallographic control is more or less constant, the concentric zoning of the nodules must result from a combination of the first two processes. These will be considered in turn.

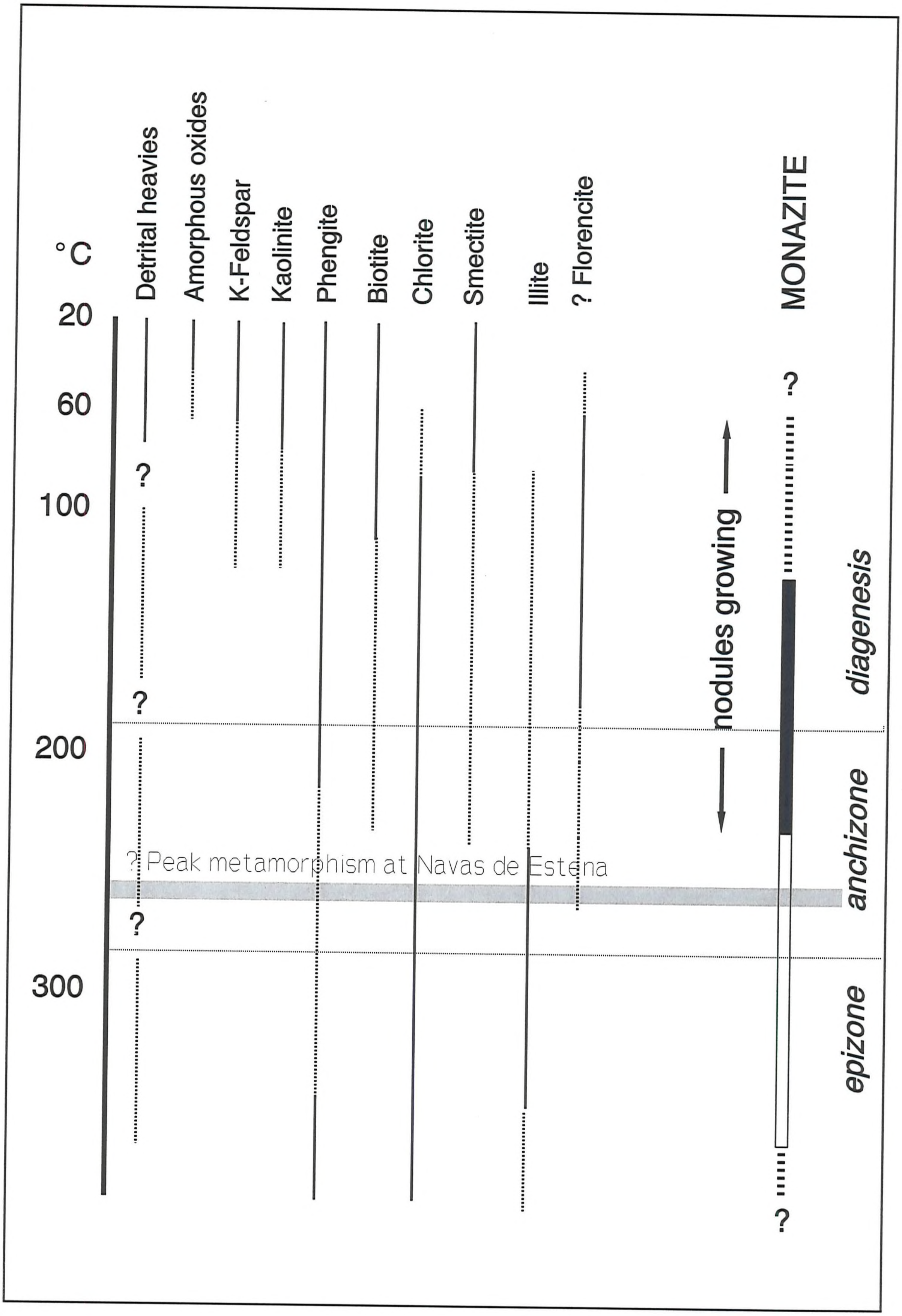

Figure 6-2: Possible scheme of mineral parageneses in a pelitic sediment, to illustrate potential sources of REE available to a growing monazite nodule.

6.4 Possible sources of REE during diagenesis

The sedimentary assemblage initially buried at the sea floor consists of detrital material from various sources, authigenic minerals formed near the water/sediment interface, and interstitial fluid (initially sea water, but very quickly changing to a sediment-buffered composition); the mixture is far removed from equilibrium. REE are contained in a number of reservoirs within the sediment, ranging from relatively unstable (e.g. adsorbed on the surface of amorphous oxide grains) to very stable (e.g. contained in the lattice of detrital zircon). As the sediment is buried and diagenetic reactions begin to restore the system to equilibrium, REE are released from each reservoir in turn, depending on its relative stability. Figure 6-2 illustrates some possible mineral transformations taking place in Calymene Formation shale during diagenesis, based on the discussion in chapter 2. This figure is necessarily speculative, firstly because the temperatures of the anchizone boundaries, many of the mineral transformations and the peak metamorphic grade are poorly constrained and secondly because the early stages of diagenesis are not preserved at Navas de Estena. However, some reasonable guesses may be made concerning the sequence of events.

Among the first materials to break down are fine grained amorphous iron and aluminium oxides (Curtis, 1985). These are followed by K-feldspar, kaolinite and the beginning of the long transformation of smectite into illite. Any REE associated with these early-destabilized phases are likely to be released into solution early on during diagenesis, probably before monazite nodules have begun to form.

The mobility of REE in mudrocks during early diagenesis has been studied by Balashov and Girin (1969). These authors conducted leaching experiments using 2% HCl (which attacks authigenic apatite) and ammonium oxalate (which dissolves only ions adsorbed onto clays). They concluded that between 20 and 90% of the total REE content was in a mobile form, either in dispersed apatite or adsorbed onto clay minerals. In particular, smectites contain a greater proportion of mobile REE than an illite-chlorite mixture (table 6-1). The leachates obtained by Balashov and Girin (1969) were all middle- or heavy-REE enriched (figure 6-3). This is an important result, because the study of Balashov and Girin (1969) is virtually the only direct

Fraction containing REE	Mineralogical composition and specimen number						
	Kaolinite; 31m	Illite-chlorite; 1397	Montmorillonite; 137m	Illite-chlorite-kaolinite; 800	Illite-chlorite; 1397	Illite-chlorite; 385	Illite-chlorite; 119
Dispersed apatite	5	25	40	30	25	30	20
REE adsorbed on clays	25	40	55	5	35	20	0
REE firmly bound in clays	70	35	5	65	40	50	80
Treatment used	Ammonium oxalate			2% HCl extraction			

Table 6-1: Distribution of REE in clays, from Balashov and Girin (1969).

experimental work undertaken on real mudrocks. Their results imply that the desorption of REE from clay minerals could plausibly produce the "early, heavy" type of fluid, the imprint of which is preserved in the Sm - rich cores of the monazite nodules. Figure 6-2 suggests that the conversion of smectite to illite continues throughout the likely temperature range of nodule formation, and that REE released during this reaction are likely to contribute to all phases of monazite nodule growth.

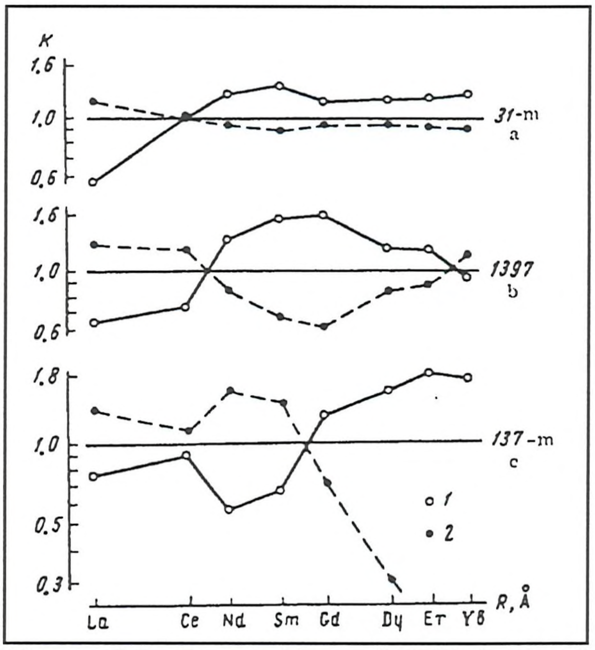

Figure 6-3: Composition of REE (Ln/total REE) for (1) leachates and (2) residue. a=kaolinite; b=illite/chlor; c=smectite. From Balashov and Girin (1969).

Despite the correlation of K and Ba with monazite abundance (see chapter 4), detrital K-feldspar is probably not a significant REE reservoir, with REE abundances only about one tenth of average shale (Grauch, 1989). In any case, it is inferred to break down before the onset of nodule growth (figure 6-2), and so should be associated, if anything, with the "early, heavy" type of fluid. If the coarser fraction of the sediment is a significant source for REE, as is suggested by the statistical modelling of chapter 4, and as was established by Milodowski and Zalasiewicz (1991) in Wales, then the chief candidates are detrital heavy minerals and detrital mafics.

The REE budget of sandstones is often dominated by a few heavy minerals (McLennan, 1989). However, heavy mineral concentrates are usually enriched in the heavy REE and so the breakdown of heavy minerals is unlikely to be the source of the "later, lighter" fluid in the Navas de Estena shales. While a small amount of, for example, allanite or bastnaesite could perhaps deliver the light-REE enrichment without affecting the whole-rock chemistry, the ubiquitous nature of the monazite zoning worldwide argues against it. Any explanation which requires unusual circumstances or exotic mineralogy is unlikely to be correct. Authigenic apatite can be ruled out as a source of REE because of the absence of a cerium anomaly in the monazites. Oceanic REE chemistry is typified by a negative anomaly at Ce, which is oxidised to Ce^{4+} and separated from the other REE, chiefly by incorporation into manganese nodules (Elderfield, 1988). Any minerals formed at the sea water-sediment interface would be expected to show a negative Ce anomaly in their REE patterns.

Detrital mafic minerals are a more likely source for the "later, lighter" fluid associated with the nodule rims. The widespread presence of coarse chlorite grains attests to the former presence of detrital mafics. Electron microprobe data presented in chapter 2 suggest that the later stages of nodule growth coincided with the breakdown of detrital biotite to form chlorite and illite. Greenschist facies micas have slightly heavy-enriched shale-normalized REE patterns (Roaldset, 1975), with similar light REE abundances to shales. Breakdown of such material would be unlikely to produce a light-REE-enriched fluid, and so it is likely that the explanation of the La- and Ce- rich nodule rims lies in the second step of the monazite-forming process: the evolution of fluid chemistry during diagenesis.

6.5 REE transport and the evolution of fluid chemistry

Three possible effects can influence the REE pattern of the fluid phase in water-rock interaction (Bau, 1991):

1. The REE pattern of the minerals with which the fluid is in contact;
2. Sorption of REE onto mineral grains; and
3. Complexation reactions.

Bau (1991) notes that, in the case of straightforward Coulombic interaction, the following controls apply to the second two processes:

1. The higher the ratio of ionic charge to radius, the stronger are REE sorption effects and the more stable is REE complexing in aqueous solution.
2. As temperature increases, sorption effects become weaker and all complexes become more stable.

He illustrates this effect by suggesting that the REE pattern of a fluid will be HREE-enriched with respect to its host rock if complexing reactions dominate, and LREE-enriched if sorption effects dominate (figure 6-4). If Eu^{2+} is present, Eu anomalies opposite in sense will be introduced.

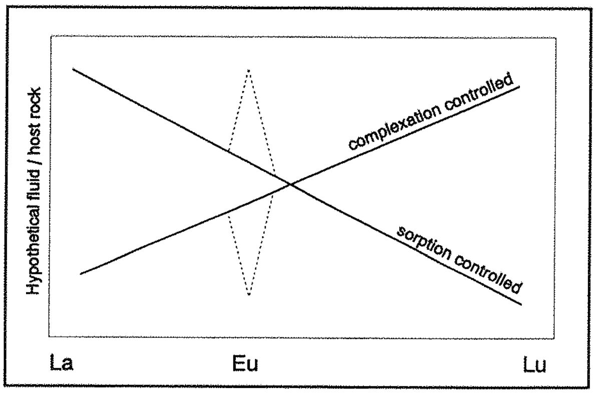

Figure 6-4: Sketch (from Bau,1991) illustrating the differing effects of complexation versus sorption processes on fluid chemistry.

This reasoning suggests a possible origin for the fluid evolution at Navas de Estena. The composition of the "early, heavy" fluid was dominated by REE complexing, probably with carbonate (see below). The REE were easily desorbed from the surface of smectites and amorphous oxide minerals, and reprecipitated to form the cores of the monazite nodules. Later on, after the easily-mobilised REE had been removed, the fluid chemistry was controlled by the ease of desorption of REE ions from their host minerals. The main source of REE was now detrital mafic minerals, to which the REE were more firmly bound than they had been to the clays. Because the light REE were more weakly bound than the heavies, a fluid with a light-enriched REE pattern resulted. Because of the absence of observed Eu anomalies, and the consistent behaviour of Eu form core to rim of the nodules (figures 2-33 and 2-34), it is concluded that no divalent europium was present.

Another effect contributing to the fluid evolution is the REE mass balance of the clay minerals: once heavy REE had been preferentially removed from the early source minerals, they would be left light-REE enriched (Milodowski and Zalasiewicz, 1991). This effect alone, however, cannot account for the correlation between monazite abundance and La, Ce-enrichment of monazites which is seen in Spain: if, as the correlation suggests, the "late, light" fluid is responsible for more monazite than the "early, heavy" fluid, then they cannot be complementary components of an initial source material unless some of the "early, heavy" fluid was lost from the system. However, the whole rock is a closed system for REE, and so an additional source must be found for the "late, light" fluid.

Possible REE complexes

A change in the stability of one lanthanide complex ion in favour of another could potentially affect the REE pattern of the fluid. The inorganic speciation of REE in natural waters is reviewed by Wood, (1990a). The amount of experimental data is limited and so Wood (1990a) uses a thermodynamic approach to calculate the speciation of Eu in a model groundwater at 25 °C (figure 6-5). The most important species appear to be $LnCO_3^+$ and Ln^{3+}, at neutral and low pH values, respectively. Lee and Byrne (1992) use thermodynamic data to extrapolate the stability constants from any one lanthanide to all the REE for a variety of ligands. Their results (figure 6-6), using the same groundwater as Wood (1990a), suggest that phosphate complexes may be important at pH 7 to 9. At acid pH, REE should be mobile as Ln^{3+} ions, while at higher pH, phosphate (for HREE) and carbonate (for LREE) complexes become significant.

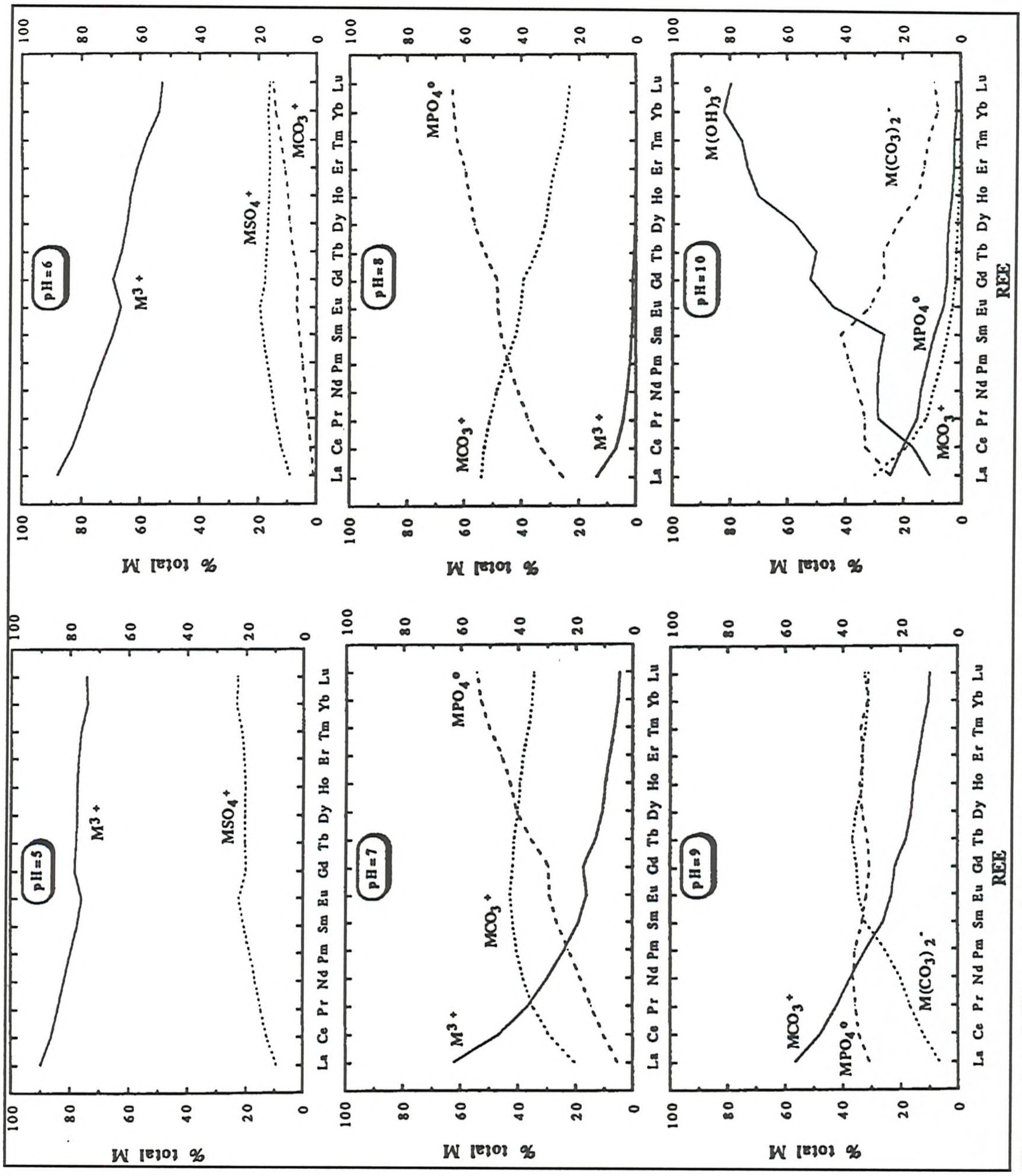

Figure 6-4: REE speciation in the model groundwater of Wood (1990a) (table 6-2) at 25 °C. From Lee and Byrne (1992).

Molarities	ΣEu	ΣF^-	ΣCl^-	ΣSO_4^{2-}	ΣPO_4^{3-}	ΣCO_3^{2-}	ΣNO_3^-
A	10^{-7}	10^{-6}	$2*10^{-4}$	10^{-4}	10^{-6}	10^{-4}	10^{-4}
B				10^{-6}	10^{-2}		
C		10^{-4}		10^{-6}			
D				10^{-6}		10^{-3}	

Table 6-2: Model groundwater composition of Wood(1990a) used to calculate figure 6-5. Compositions B-D same as A unless noted otherwise.

Clearly, speciation is strongly dependent on pH and REE atomic number. Stability data are also strongly temperature dependent; Wood (1990b) calculates that the stability of fluoride complexes will increase sharply with temperature. He suggestst that, at 100°C, LnF_3^0 will dominate at near - neutral pH with carbonate complexes at higher pH; at higher temperatures, fluoride should be the stable complex for all likely pH values, even if F^- concentrations are low (e.g. 10^{-5} molar). He does not consider the temperature - dependence of $LnPO_4^0$ complexes. All complexes, however, become more stable at higher temperatures, i.e. the solubility of REE will increase as temperature increases. The only ligand which could potentially produce a light-enriched REE pattern is chloride (Wood, 1990a; Bau, 1993) which forms stronger complexes with La than Lu. However, for Cl^- complexing to prevail requires very high salinity coupled with the absence of other more stable ligands, very low pH, and low temperature (Wood, 1991a). Chloride complexing is therefore very unlikely to be the cause of the "late, light" fluid.

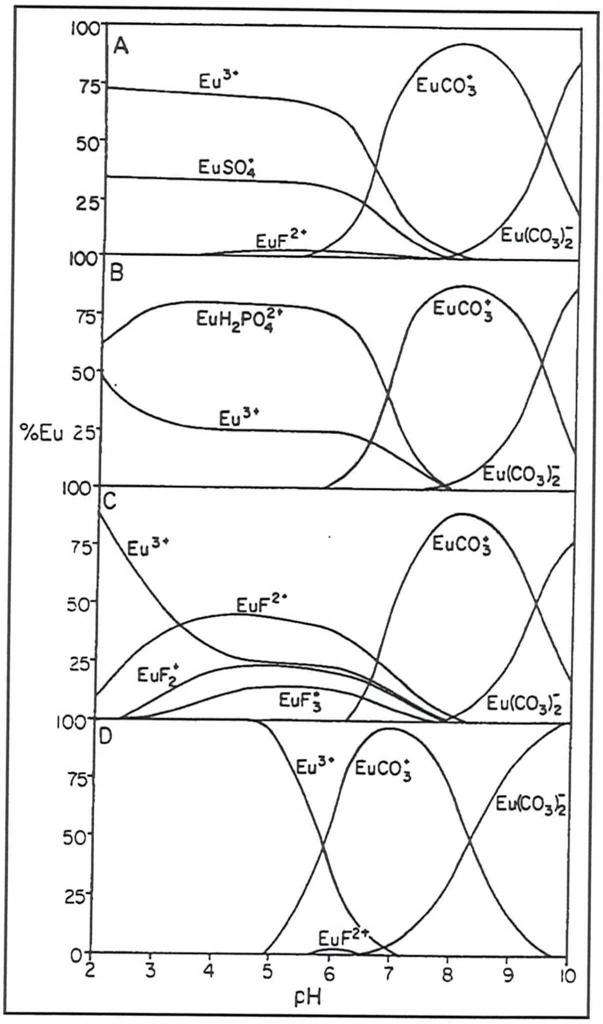

Figure 6-5: Distribution of Eu between different complexes at 25 °C (from Wood, 1990a). Water compositions in table 6-2. Y-axis is the proportion of aqueous Eu as each species.

It seems likely that, over the interval of monazite formation, carbonate and possibly phosphate complexes will be present at lower temperatures, and fluoride at higher temperatures. This would be consistent with REE mobility observed in cone-in-cone concretions (chapter 3). Because the stability of LnF_3^0 complexes increases from La to Lu, it also implies that REE complexing behaviour was probably not responsible for the "late, light" fluid which formed the monazite rims.

6.6 Conclusions: model for the formation of monazite nodules

Regional considerations

Grey monazites occur in fine-grained clay-rich sediments of distal facies. Monazite mineralization is probably linked to the preservation and burial of organic material and biogenic phosphate, and so is more likely to occur in sediments deposited at or below the oxic/anoxic boundary. Detrital clastic material in the form of distal turbidites or fine silt layers is a necessary component and probably constitutes the major source of mobile REE for monazite formation.

REE redistribution during diagenesis

Monazite nodule formation in the Calymene Formation probably begins at between 60 and 120 °C, after an initial compactional fabric has developed in the sediment. REE are initially desorbed, probably as carbonate complexes, from clays and fine-grained oxides, to which they were only weakly bound. The fluid at this stage is heavy REE enriched, because $LuCO_3^+$ is more stable than $LaCO_3^+$. The presence of phosphate ions, released into solution by the early oxidation of organic matter with which they were associated, causes REE to precipitate as monazite. The monazite forms nodules which grow by partially replacing the silicate minerals of the mudstone; phyllosilicates are replaced in preference to quartz. The combination of a fluid with Lu > La and the crystallographic control exerted by the monazite results in these early-formed nodules having the "core"-type patterns described in chapter 2, with a maximum at Sm or Nd and an overall LREE enrichment.

As diagenesis continues and the weakly-bound REE have mostly been released into solution, the fluid chemistry changes to a lighter REE composition. This is because Lu^{3+}, with its higher charge density, is more strongly bound to its host minerals than La^{3+}. The smectite to illite transformation continues to release REE, now lighter in composition as a result of early depletion of heavy REE. The main source of REE, however, is now from the detrital, clastic component of the sediment. It is probably mafic minerals such as biotite, but heavy minerals may also be important. The La-and Ce- rich rims of the nodules are precipitated from this second fluid. The amount of monazite precipitated in this second stage, which depends on the amount of coarser-grained detrital mafic material present, determines the final monazite abundance in the rock.

The monazite nodules had finished growing before the peak of deformation and cleavage formation, which probably occurred at 250 °C. This is therefore a likely upper limit for monazite formation.

Appendix A: Analytical methods

A1: The study of REE zoning in grey monazites by Laser ICP-MS and scanning electron microscopy.

A-1.1 Introduction

Grey monazites occur as sub - millimetre sized concretions in some Palaeozoic and older black shales. Like their yellow igneous counterparts, they are rare earth element, Y,Th phosphates, but are typically Th- poor and Eu- rich by comparison (Rosenblum and Mosier, 1983). They comprise between 15 and 40 % silicate inclusions, which have the same mineralogy as the host shale, enclosed by the monazite cement. The concretions are thought to form during the late stages of diagenesis, under anchizonal conditions. Grey monazites are invariably zoned, with La and Ce enriched rims and Nd / Sm enriched cores. The zoning was first described by Read et al. (1987) from alluvial material; it has since been described in *in situ* monazites from Belgium (Burnotte et al., 1989), Wales (Milodowski and Zalasiewicz, 1991) and Rwanda (Laval et al., 1993). Laser ICP-MS is a rapidly developing technique with the potential for microanalysis of geological materials at trace element detection levels (Jarvis and Williams, 1993).

Monazites are attractive and challenging subjects for laser ablation inductively coupled plasma mass spectrometry (LA-ICP-MS) because:

(i) They are rich in REE, typically 20% cerium by weight, with the promise of a strong signal from a small ablation spot;

(ii) A strong zonation of the light REE has been observed in electron microprobe studies (Burnotte et al., 1989; Milodowski and Zalasiewicz, 1991; this study, unpublished data), but the heavy REE distribution is unknown since it cannot easily be measured by existing techniques;

(iii). REE exhibit more than four orders of magnitude variation, with steeply LREE-enriched abundance patterns.

Chenery and Cook (1993) have examined monazites from Wales using a UV laser and a solid-liquid calibration, in which a standard solution is nebulised and mixed with the argon gas flow containing the laser ablated material. The present study avoids this approach and its potential problems by using a dry plasma fed only by argon from the laser ablation cell, and relies on a solid, matrix-matched standard for calibration. This method has the theoretical advantage of allowing for different elemental sensitivity induced by the ablation process, whereas the solid-liquid method assumes that the composition of the laser microplasma is the same as that of the solid sample. The object of this study is to develop a method of calibration for monazite analyses, with the ultimate aim of measuring the distribution of the heavy REE which are present at concentrations of a few ppm.

A-1.2 Sample preparation

The monazites in this study are from the Montes de Toledo area of central Spain, where a detailed study of monazites from a Lower Ordovician shale section (Windle, this volume) includes scanning electron microprobe traverses and elemental X-ray maps of individual grains as well as solution ICP-MS data. For this study, samples of about 10 Kg were crushed and sieved, then passed through methylene iodide (density = 3.32). Monazites were picked from the resulting concentrates and mounted in polished blocks. These were carbon coated as necessary for SEM imaging and electron microprobe analysis. Five grams of alluvial monazites from the same area were ground up very finely in a ball mill, and pressed into a pellet for use as a calibration standard for LA-ICP-MS. Three cycles of hydrofluoric/perchloric acid, evaporating to incipient dryness at 180 °C, were used to digest 0.5g of this material. The REE content of the resulting solution was determined by conventional solution ICP-MS; the results are shown in table 1.

Element	Concentration in standard pellet (ppm)	Chondrite value (after Masuda et al.(1973)
Yttrium	2484	
Lanthanum	90792	0.315
Cerium	200132	0.813
Praseodymium	24576	0.12
Neodymium	92325	0.597
Samarium	15792	0.192
Europium	2787	0.0722
Gadolinium	9163	0.259
Terbium	749	0.047
Dysprosium	1999	0.325
Holmium	175	0.073
Erbium	230	0.213
Thulium	17	0.032
Ytterbium	58	0.208
Lutetium	5	0.0323

Table A-1: Composition of the monazite standard pellet, and chondrite values used for normalization.

ICP-MS Instrument operating conditions

Instrument	VG Elemental PlasmaQuad PQ2+
Forward power	1.5 kW
Reflected power	<5 W
Plasma gas	Argon
Flow rate:	
coolant gas	14 l min^{-1}
carrier gas	1.0 l min^{-1}
auxiliary gas	0.5 l min^{-1}

ICP-MS Data acquisition parameters

Dwell Time / channel	80μs
Channels	2048
Sweeps	100
Scan width	30 - 179 m/z
Skipped regions	32-87, 91-129 m/z
Acquisition time	30 s

Laser

Laser type	Spectron Nd-YAG, max energy 600mJ
Wavelength	1064 nm
Laser mode	Fixed Q (free running)
Laser energy	750 V
Shot rate	20 Hz
Shots per site	10

Table A-2: LA-ICP-MS operating conditions for monazite analysis.

A-1.3 Experimental details and calibration strategy

Laser ablation ICP-MS

Table 2 summarises the laser ICP-MS operating conditions and data acquisition parameters. A number of experiments were performed using the pressed pellet of alluvial grey monazites to determine the optimum operating conditions, and to verify the homogeneity of the pellet. Fixed Q rather than Q-switched mode was chosen because of the greater spatial resolution available in the former. In fixed Q, the pits formed are typically parallel-sided with approximately similar diameter and depth, and in general material is removed from within the pit rather than from the area surrounding it. A critical parameter is the laser input energy, which determines the amount of material ablated and thus the amount of signal. Response increases approximately linearly with voltage until detector saturation is reached (figure A-1); for ^{140}Ce this was observed at about 5*10^{6} counts. The Ce signal is about 10^{4} times that of Lu; therefore, to avoid Ce saturation, an operating level of 750 volts was chosen, which gave a few hundred counts for lutetium.

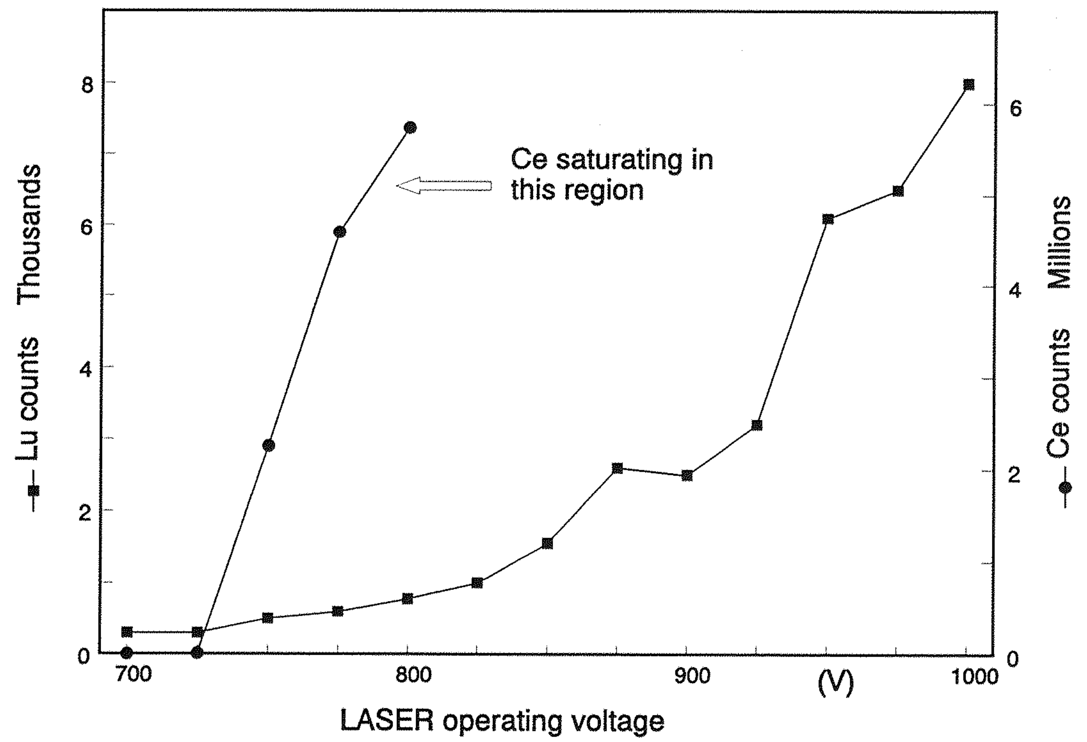

Figure A-1: Lu and Ce response as a function of laser power.

Figure A-2: Pattern of 24 craters in pressed powder monazite standard. Field of view = 1.7mm.

The crater size was of the order 80 to 100 μm (figure A-2). This still gave useful resolution for the approximately millimetre sized monazites. Repeat shots on a single point (figure A-3) produced significant amounts of signal after ten shots and in some

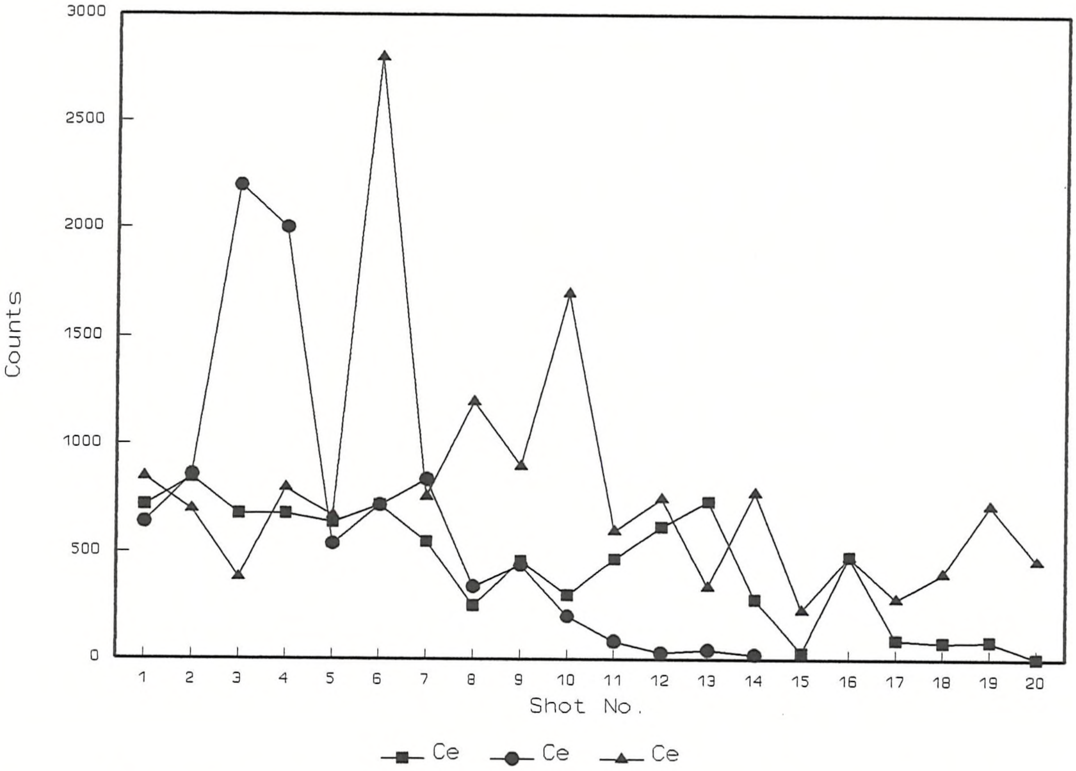

Figure A-3: Response for Cerium with successive shots on the same site, for three different sites.

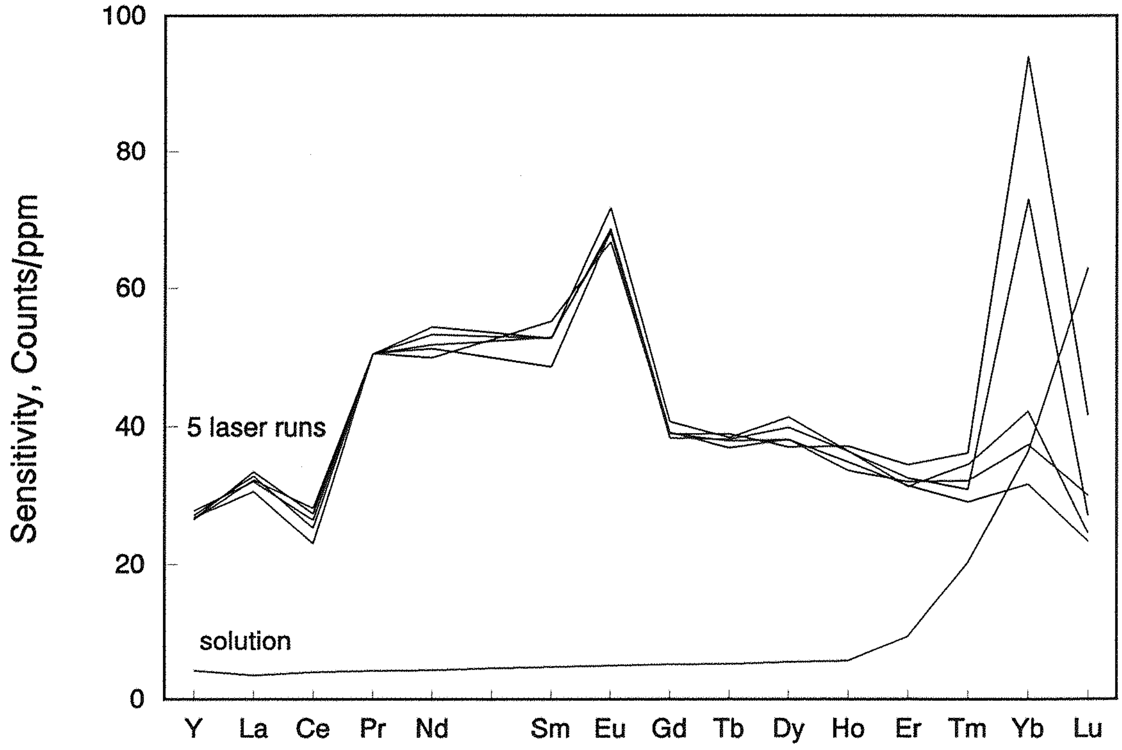

Figure A-4: Variation of sensitivity for the REE for five laser replicates (mutually normalised to Pr), on the pressed powder standard and for the same material analysed in solution.

cases as many as twenty. However, the amount of material ablated with each shot was not reproducible. Multiple shots per site can reduce the effect of this variation by averaging, and so ten shots per analysis point was adopted as standard. When ablating the calibration standard pellet, the average of five or more ablation sites, with ten shots per site, was taken in order to increase the sampled volume and reduce any effects of inhomogeneity in the pellet. Sensitivity varied by a factor of about two across the rare earths (figure A-4), exacerbating the effects of low lutetium concentration. It would also appear that sensitivity as a function of atomic number has a quite different profile during the laser ablation from that determined using conventional solution nebulisation (figure A-4). If this effect is due to the ablation process, rather than to running a dry plasma instead of a wet one, then the solid-liquid calibration of Chenery and Cook (1993) might not be reliable. The sensitivity was markedly improved by tuning the quadropole lenses using a heavy element signal, in this case uranium.

The calibration strategy has to address three sources of error:

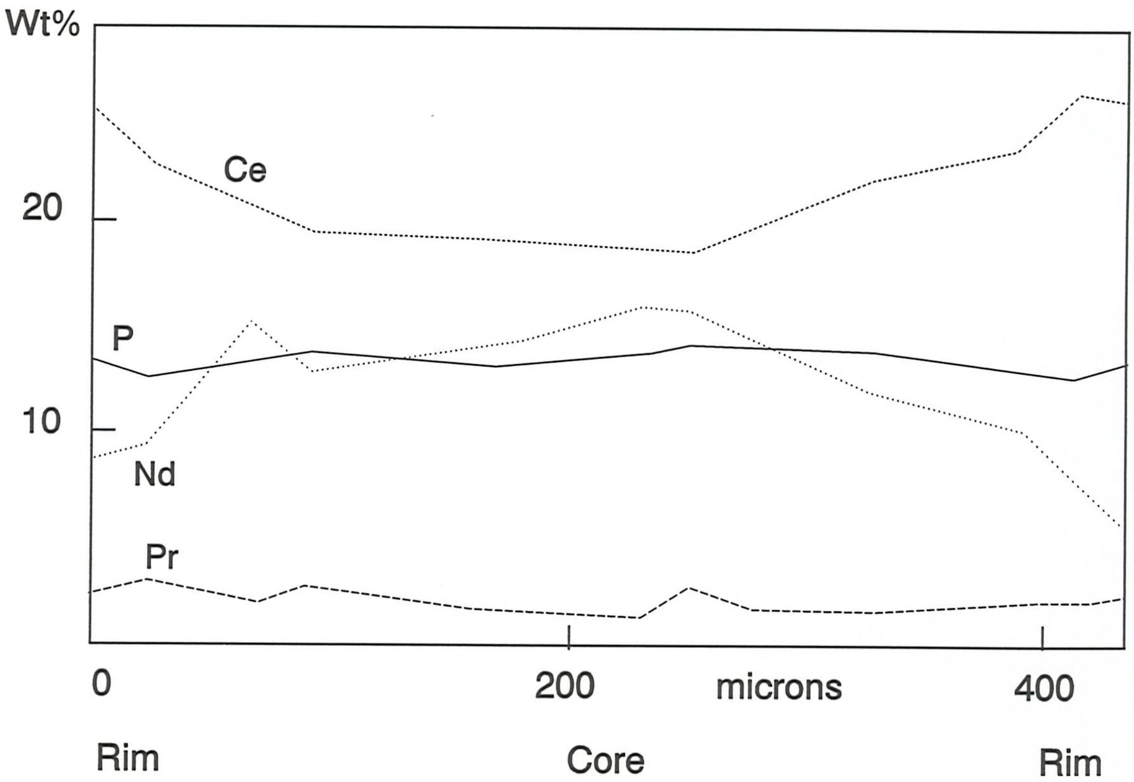

Figure A-5: Quantitative EDS traverse across monazite grain A29 showing the zoning of La and Ce, and the relative invariance of P and Pr.

1). The variable sensitivity of the different elements analysed.

2). The variable amount of material ablated with each shot.

3). Drift in the instrument sensitivity to analyte ions.

The first of these is readily compensated for by the use of a matrix-matched standard, as advocated by Hirata et al. (1988) for the analysis of geological materials by solution ICP-MS. The second problem is more intractable; it can be broken down into ablation consistency within a grain, and ablation consistency between an unknown and the standard. One possibility is to use phosphorus as an internal standard to normalise between shots on the same grain. In theory, if the monazite is stoichiometric, phosphorus should be at a constant concentration despite the REE zoning. Electron microprobe traverses of monazite grains tend to bear this out (figure A-5). However, REE patterns mutually normalised using the phosphorus counts show poor consistency within an individual grain (figure A-8a); they should essentially overlay at the heavy REE end, where the monazites are unzoned and have close to shale abundances. The observed differences probably result from the very different mass and physical properties of phosphorus compared with the rare earths, which

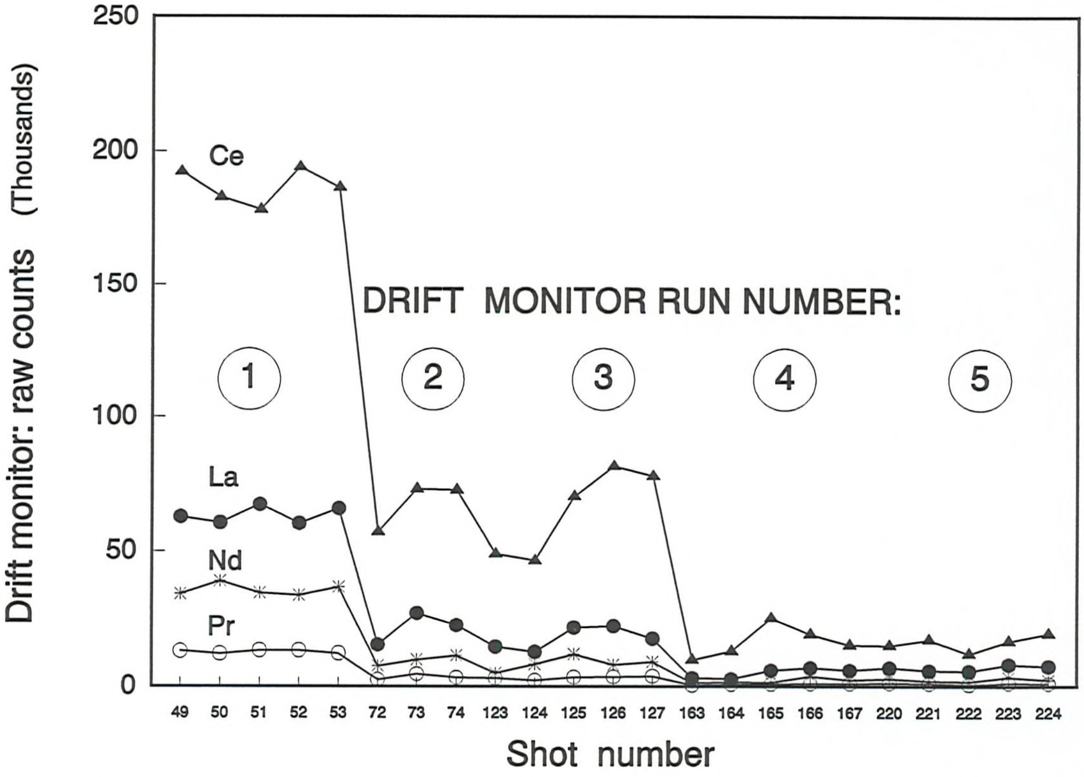

Figure A-6: Drift in sensitivity probably caused by buildup of material on the sampling cone.

influence the ablation behaviour. Phosphorus is apparently too far removed in mass from the other REE to be useful as an internal standard.

An alternative approach is to use one of the rare earths themselves. This is complicated by the existence of concentric zoning; however, X-ray mapping from the SEM (figure A-7), as well as quantitative electron microprobe traverses (figure A-5), suggests that praseodymium is almost unzoned, being that point in the mass spectrum at which the sense of the zoning changes from rim-enriched to core-enriched. When Pr is used as an internal standard for a particular grain, normalising to the average Pr counts, the precision increases dramatically (figure A-8b), suggesting that the REE do indeed behave coherently as a group during ablation. When comparing the unknown grain with the standard, there are two possibilities:

1) Assume that the internal standard (Pr) has the same concentration in the unknown as in the standard, or
2) Assume that the average volume of material ablated is a constant, and average many analysis points in the standard to improve the statistics.

In the case of the monazites, procedure (2) was preferred. The first method will inevitably be in error, because different grains have different proportions of silicate inclusions; the second makes the unsubstantiated, but not unreasonable, assumption that the pressed powder will ablate with the same characteristic as the actual mineral. A consequence of this calibration procedure is that accuracy increases with the number of shots for a particular grain, because a greater number of shots gives a truer representation of the average volume of material ablated.

To assess the analyte signal drift, the standard was run at twenty minute intervals during the sessions. Figure A-6 shows the steady decline in sensitivity, probably caused by build up of material on the sampling cone. The peak integrals were corrected for signal drift prior to calibration.

Scanning electron microscope

X-ray mapping and EDS analyses were performed on a JEOL JSM-6400 SEM fitted with a JEOL energy dispersive spectrometer and a Tracor series 2 image analysis system. The accelerating voltage was 20 kV, takeoff angle 40°, and working distance 39mm. X-ray mapping is a qualitative technique where the background-corrected counts are integrated over a small region of the EDS spectrum corresponding to a particular element. The procedure is repeated for each pixel of a digital image, so that the brightness is a measure of the concentration of the element. Mapping of La to Nd was done using the Lα lines at 20 kV; mapping of Sm to Dy was done at 5 kV using the M-α lines. These lines, although faint, are free from overlaps with the other REE. The Tb and Dy M-α lines overlap with Mg, which is present in chlorite as inclusions and in the attached shale fragment. Mapping times were 12 hours for La to Nd, and 52 hours for Sm to Dy.

A-1.4 Results

Figure A-7 shows X-ray maps of the first nine lanthanides for grey monazite grain A24. The maps for La to Sm confirm the results reported from other geographical locations (e.g. Milodowski and Zalasiewicz, 1991). The long-exposure maps of Eu to

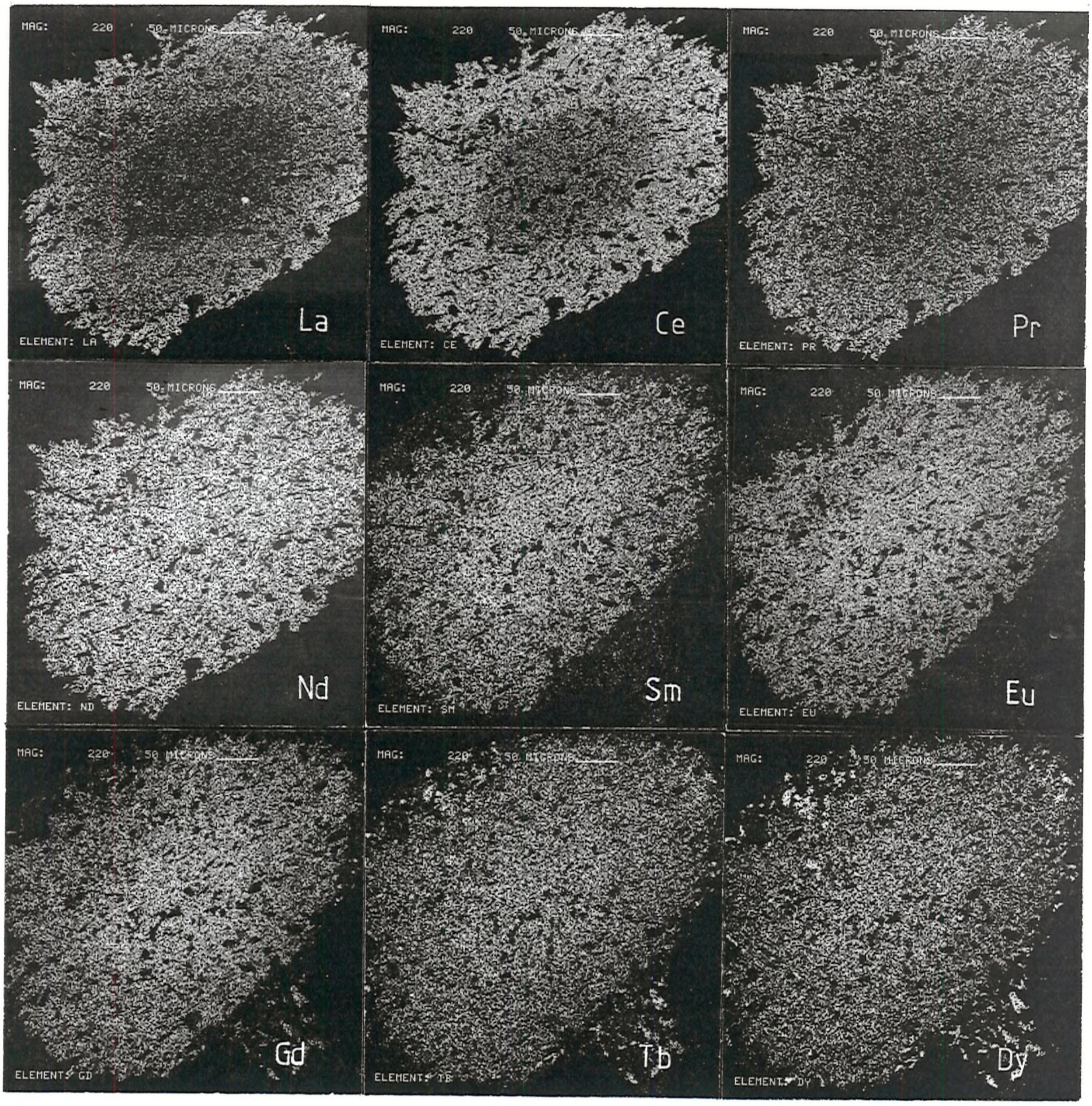

Figure A-7: Scanning electron microscope X-ray maps of grey monazite grain A24. See text for details

Dy show that the sense of the zoning, although faint, remains the same as for Sm with the middle REE enriched in the core of the grain.

The laser ICP-MS results (figure A-8) show reasonably smooth chondrite-normalised patterns, which are noisier at the heavy end where the analyte signal is close to background. Lutetium, at about 5μg.g^{-1}, is close to the detection limit. Correlations between shots are heavily dependant on the normalising method and internal standard used (figure A-8a,b). "Core" type patterns, with a peak around Nd or Sm (e.g. shot 18, figure A-8g) are distinguished from "rim" type patterns (e.g. shot 16), which have La >Nd and a straightforward light-enriched pattern. Some grains (figures 8b,g) show the same MREE zoning as was observed by X-ray mapping. Because of the

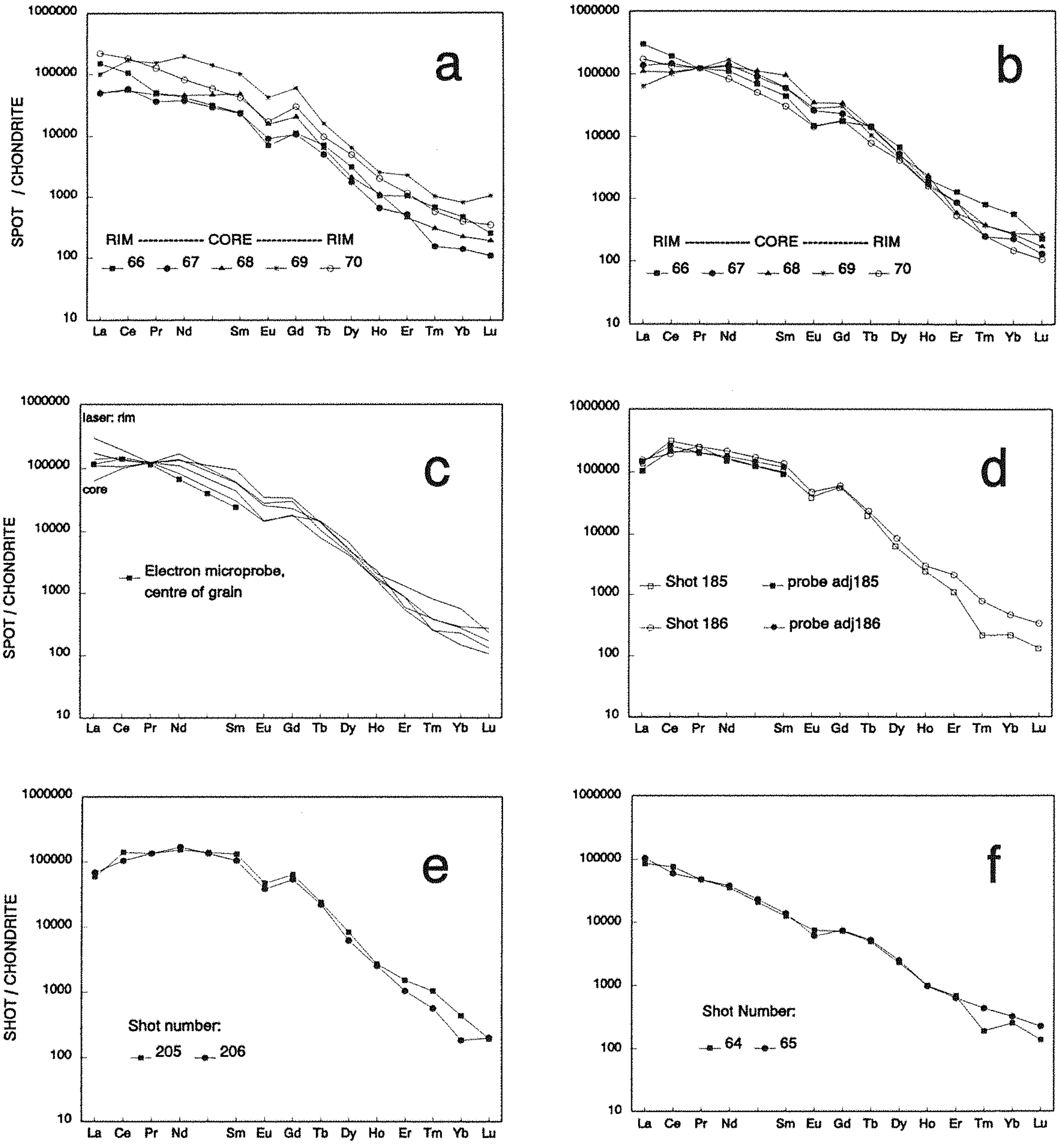

Figure A-8: Chondrite-normalised plots of REE abundances. (a): A traverse of five shots across a single grain, mutually normalised using phosphorus. (b): The same data, mutually normalised using the average praseodymium value of the five shots. (c): The same plot as (b) with electron microprobe data (La to Sm) from the same grain superimposed. (d): Two LA-ICP-MS patterns for another grain (open symbols), with electron microprobe analyses from points adjacent to the laser craters (solid symbols). (e) and (f): Two further monazite grains, each with two LA-ICP-MS sites, which appear not to show any zoning.

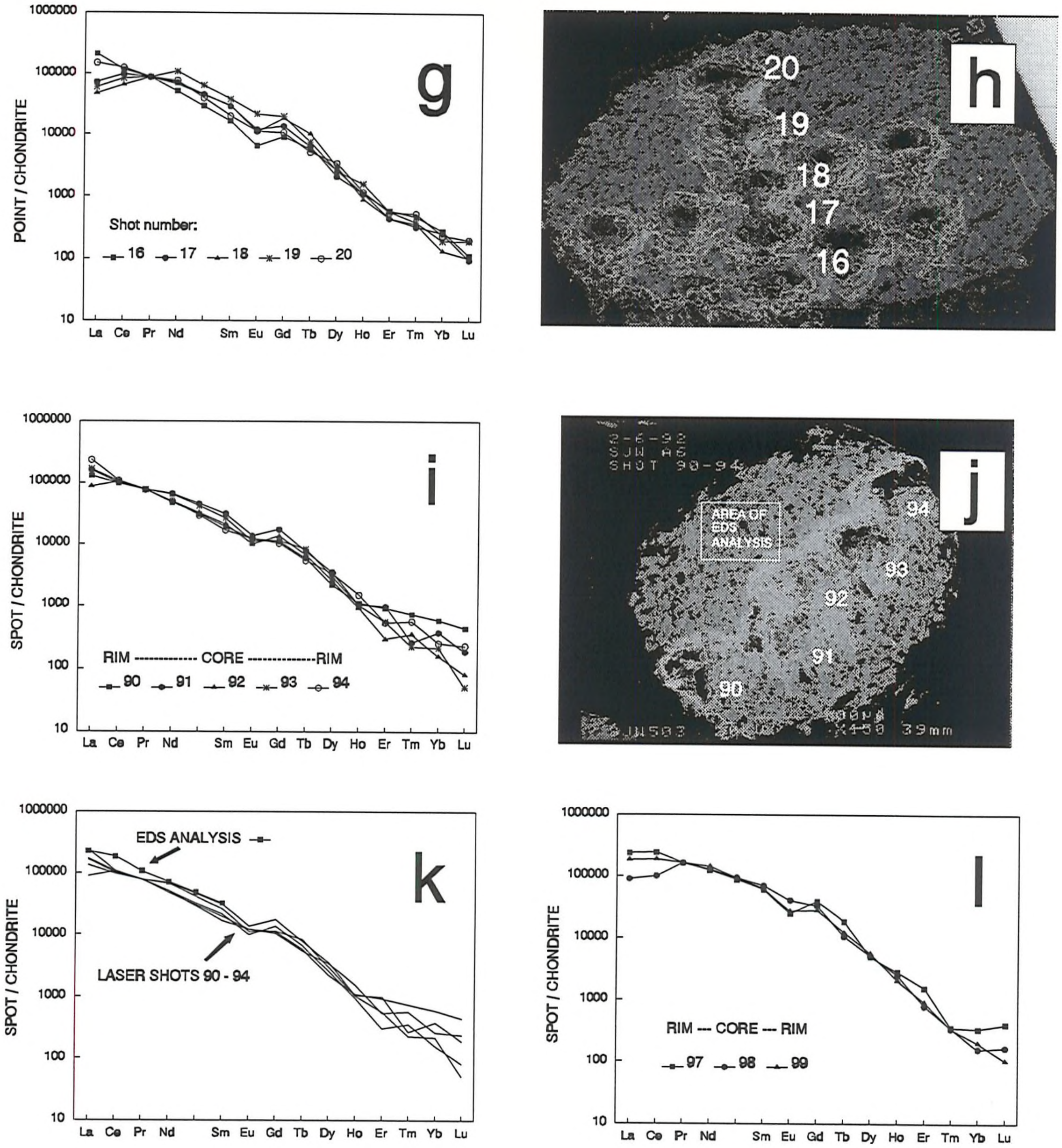

Figure A-8 cont: Zoned monazites. (h) and (j) show location of shots in (g) and (i) respectively. (k) shows results of the EDS analysis shown in (j). See text for details.

poorer precision for the heavy REE and the somewhat arbitrary use of Pr as an internal standard, it is not possible to infer any sense of zoning for elements heavier than Dy. There is some suggestion (figures 8g,8l) that the negative Eu anomaly shown by the monazites is smaller in the core of the grain than at the rim. Some measurements (figures 8d,8e,8f) show no zoning, probably because of the random nature of the sample sectioning or an accident of shot site selection. These patterns can be classified either as "cores" (figures 8d,8e) or "rims" (figure A-8f). Comparison with electron microprobe data shows generally good agreement. Figures 8c and 8d show the results of electron microprobe point analyses adjacent to the respective laser craters. Figure A-8k shows the results for an analysis area of a similar size to the laser crater. In every case, the microprobe results are within the range of values which might result from heterogeneity of the monazite, in particular from the proportion of silicate inclusions contained in the sampled volume.

A-1.5 Conclusions

Grey monazites from central Spain show similar concentric zoning to those described from other geographical areas, with La and Ce enriched rims and Nd, Sm enriched cores. The sense of the zoning crosses over more or less at praseodymium, and the REE, at least as heavy as Dy, are enriched in the cores. LA-ICP-MS is a useful technique for such studies at the $200\mu g.g^{-1}$ level (e.g. holmium) provided that a matrix matched standard is available for calibration. The technique is also very fast - less than one minute per ablation site - and requires little sample preparation. Accuracy is difficult to assess without a set of well characterised reference materials. The accuracy improves with the number of shots per grain, which is presently limited by the spot size of circa 100 µm. Good precision depends on the use of an internal standard; in zoned grains, differences of a few percent can be measured. The detection limit was about 5 ppm for lutetium, but for elements heavier than erbium, precision was compromised by background noise and quantitative measurement was impossible.

A2: ICP-MS analysis of standard reference materials: comparison of data reduction techniques

(Internal report to departmental ICPMS users, November 1993)

A-2.1 Introduction

Many possibilities exist for the normalisation and calibration of solution ICP-MS data. The raw integrals output by the machine must be corrected for :

1. Background noise
2. Instrumental drift, largely caused by buildup of material on the sampling cone and not necessarily the same for each element
3. Matrix effects: the interaction of different ions of the analyte solution in the plasma. The effect is mass-dependent, but not in any well-understood way. Possible approaches to correction are via the use of internal standards, or by comparison with well-characterised reference materials with a similar matrix.
4. Calibration: instrument operating conditions are not reproducible from session to session so it is always necessary to include standards in a run to establish the sensitivity (in counts/ppm) for each analysed element.

This experiment is an attempt to compare different methods of data reduction, using whatever reference materials were available in solution at the time. In this respect, it is not rigorous and internally consistent, because of the different sample preparation procedures used for the various reference materials.

A-2.2 Run details.

The following reference materials were run (mainly on the grounds of their availability):

BIR-1, JB-2 (2 solutions),BCR-1 (2 solutions), BHVO (3 solutions), BEN,
SDC-1, JG-3 (2 solutions), SCo-1, ACE (2 dilutions), NIMG, JG-1A, JG-2.

Three repeats of 60 seconds were used. Calibration was by three standards DR10, DR20 and DR30 prepared by Dr. Rex Taylor at Egham using multi-element standard solutions and used recently by Dr. Catherine Deniel. All the solutions were spiked with 50ppb rhenium and indium; it transpired that solutions DR10 - DR30 already contained Re and In, so the *1.1 dilution involved in the spiking gave rise to final concentrations of 9.09, 18.18 and 27.27 ppb of all other elements and 59.09, 68.18, and 77.27 ppb Re and In in solutions DR10, DR20 and DR30, respectively. In addition, a REE standard solution prepared in Southampton was run; it contained 50ppb of all the REE, Y and Sc.

The procedure consisted of:

Acid blank; first procedural blank
Four standards
Six unknowns
Standard DR30
Six unknowns
Four standards again
Second procedural blank
Six unknowns
Standard DR30

The drift was relatively severe for the first 1500 seconds (graph (2)), which was the reason for re-running all the standards at about 9000 seconds. This second batch of standards were used for calibration.

A-2.3 Data reduction.

The first step was to background subtract all the counts, using either the acid blank, or the appropriate procedural blank. Next, the indium and rhenium counts for DR10..DR30 were normalised to a standard level of 50ppb to allow for their erroneous concentrations as detailed above. The result of this correction is shown in graph (2).

Re-In internal standardisation

This procedure applies a mass-weighted correction factor to all measurements such that the corrected indium counts are equal to the indium counts in the standard, and the corrected rhenium counts are equal to the rhenium counts in the standard. The correction factors for other elements are a linear function of mass, constrained to pass through the two points Re and In. This is a one-step correction, assuming that the drift and the matrix correction are linear functions of mass (equation (1)). Note that standard DR30 is used as the normalising reference.

Sample	Mass	DR30	Unknown	DR30b	DR30c
Time		t_0	t	t_2	t_3
Ind	m_{Ind}=115	Ind_0	Ind_t	Ind_2	Ind_3
Ln	m_{Ln}	Ln_0	Ln_t	Ln_2	Ln_3
Re	m_{Re}=187	Re_0	Re_t	Re_2	Re_3

Table A-3: : Notation for data normalisation. Ln = lanthanide

$$Ln_{corr}=Ln_t\left(\left(\frac{(m_{Ln}-m_{Ind})}{(m_{Re}-m_{Ind})}\right)\left(\frac{Re_3}{Re_t}-\frac{Ind_3}{Ind_t}\right)+\frac{Ind_3}{Ind_t}\right) \qquad (1)$$

An alternative algorithm, suggested by Dr. I. Croudace, interpolates by mass between In and Re for both the standard and the unknown, then applies a correction factor equal to the ratio of these two "internal standard counts" for a particular mass element. i.e. (equation (2)):

$$Ln_{corr} = Ln_t \left(\frac{(m_{Ln}-m_{ind})Re_3 + (m_{Re}-m_{Ln})Ind_3}{(m_{Ln}-m_{Ind})Re_t + (m_{Re}-m_{Ln})Ind_t} \right) \tag{2}$$

This correction factor is a hyperbolic function of mass (graph (3)). In the mass interval 139 - 175, it is often nearly linear, and gives results little different from equation (1) (graph (4)). Since there is no theoretical reason to suppose that the sum of drift and matrix correction should have this functional form, the linear function (1) is preferred.

Drift correction

This procedure normalises all the drift monitor standards to the values of one particular standard. Normally, this will be the first standard of the run, although in the present case the third was preferred in order to keep most of the corrections to smaller values. Each element is corrected individually, avoiding the need to make any assumptions about the mass dependency of the drift. The correction factors for each element are then interpolated linearly with time between adjacent drift monitor standards. Graph (1) shows the effect of this correction on the raw indium and rhenium counts. This algorithm has the added complexity that it must be made in blocks, between two standards; the precise standards involved vary according to where the unknown lies in the whole run. e.g. (equation (3)):

$$Ln_{corr} = Ln_t \left(\left(\frac{Ln_3}{Ln_2} - \frac{Ln_3}{Ln_0} \right) \left(\frac{t-t_0}{t_2-t_0} \right) + \frac{Ln_3}{Ln_0} \right) \tag{3}$$

Both corrections

To evaluate the possibility of non-linear drift, the data were also reduced using first the time-interpolated drift (3) and then the mass-interpolated internal standard (1).

Calibration

For each element, a four point calibration was made using solutions DR10, DR20 and DR30 and constraining the line to pass through the origin. The reference values were thus 0.0, 9.09, 18.18 and 27.27 ppb. The best fit line had $r^2 > 0.99$ for all elements except tantalum, which habitually shows an offset of about 5ppb, presumably as a result of instrumental contamination (e.g. graphs 9,10).

A-2.4 Results

Each data reduction technique was evaluated by plotting the measured values, in ppb, against the reference values. These were derived by dividing the published values by the appropriate dilution factors. Reference values used are detailed in table 2. A best fit line was plotted for each element: ideally, it should have slope = 1 and $r^2 = 1$. A full set of plots are enclosed for the one - step Re-In method (equation (1)). The points are labelled as follows (prepared by) (dilution factor):

> a: BIR-1 (Rex)(1081); b: JB-2 (Rex)(1837) c: BCR1-1 (Rex)(2231); d: BCR1-2 (Rex)(1114); e: BHVO (Rex)(1842); f:BHVO1 (CD)(1402); g:BHVO2 (CD)(1531); h:BEN-2 (Rex)(1030); i: SDC-1 (SJW)(941); j: JG-3 (SJW)(420); k: SCo-1 (SJW)(5002); l: JB-2 (CD)(1448); m: ACE (IWC)(6300); n: NIMG (IWC)(6300); o: JG-3 (IWC)(6300); p: ACE (IWC)(1575); q: JG1a (IWC)(1575); r: JG-2 (IWC)(1575); s: JG-3 (IWC)(1575).

Values of accuracy (closeness of the gradient to one, expressed as a percentage) and r^2 were tabulated for the different methods; the results are summarized in graphs (5) to (8).

Linearity

It is clear from graph (7) that internal standardisation yields superior results to mere drift correction - in other words, there is a matrix effect. The simple Re-In procedure of equation (1) is just as good as the two - step procedure (equation (3) followed by equation (1)). Because the calibration (counts to ppb) is a linear transformation, the choice of standard (DR30 versus Soton STD50) does not influence the r^2 values.

Accuracy

Graph (6) shows that, firstly, the two-step correction of drift followed by internal standard is superior to the single step method. The difference, however, is small and the single step method may suffice for REE. Secondly, the overall accuracy is relatively poor (10 - 15%). This is ascribed to three factors:

1). The solution used for calibration (DR30) was rather old.
2). There was excessive drift during the run (graph (1)).
3). The standard solutions used were from a variety of sources, compromising the internal consistency of the experiment.

Use of the 50ppb REE,Y,Sc solution for calibration improved the accuracy somewhat (graph (5)); likewise, applying both corrections was superior to the single step correction, especially for scandium (graph (8)). 5% accuracy can be achieved for the light and middle rare earths in this fashion.

It should be noted that the curves of graph (6) are irregular with respect to mass. This would seem to undermine the premise of equation (1) that the matrix effect is a linear function of mass.

Graph (11) evaluates the use of a well characterised standard reference material, in this case BCR-1, for calibration instead of a made-up solution. It can be seen that for nearly all elements this offers an advantage in accuracy of a few percent. It appears that the Re, In matrix correction is still worthwhile; using both drift and matrix correction and then using an SRM for calibration, better than 5% accuracy is achieved for most elements. This could offer a quick technique for real time data reduction.

A-2.5 Conclusions and recommended procedure

1. To offset the effects of excessive drift, drift monitors should be run in pairs after each six or so unknowns. The instrument can be retuned between pairs of drift monitors
2. Because the calibration is essentially linear, it is sufficient to use a single standard and the origin for calibration, i.e. every drift monitor at the start of a block is also the calibration standard.
3. A single step correction using equation (1) is sufficient for real time data processing, but for optimum accuracy, the two step procedure should be used since the drift correction is not linear with mass.
4. It is doubtful that the Re-In method of matrix correction can yield better than 5% accuracy, or 10% for the heavy REE, because the matrix correction is also not linear with mass.
5. For better accuracy, it may be necessary to run a series of matrix-matched SRMs along with geological materials. The data could then be drift and matrix corrected according to equations (3) and (1) and plots of the sort presented here made to determine the final correction factors, element by element.

Ref	BIR-1	SDC-1	JG-3	SCo-1	ACE	NIMG	JG-1a	JG-2	BCR-1	BHVO	JB-2	BEN
Sc	44	17	8.9	10.8	0.11	1	6.3	2.5	32.6	31.8	54	22
Cr	382	64	23.6	68	3.4	12	18.6	7.6	16	289	27.4	360
Co	51.4	17.9	11.4	10.5	0.2	4	5.7	4.3	37	45	39.8	61
Ni	166	38	13	27	1.5	8	6.4	2.1	13	121	14.2	267
Rb	1	127	66	112	152	320	180	297	47.2	11	6.2	47
Sr	108	183	372	174	3	3	185	16	330	403	178	1370
Y	16	40	17.2	26	184	143	31.6	88.2	38	27.6	26	30
Zr	22	290	137	160	780	300	121	101	190	179	52	265
Nb	2	18	5.6	11	110	53	12	15	14	19	0.8	100
Ba	7.7	630	453	570	55	120	458	67	681	139	208	1025
La	0.88	42.00	20.70	29.50	59.00	109.00	21.80	20.10	24.90	15.80	2.40	82.00
Ce	2.50	93.00	40.10	62.00	154.0	195.00	45.20	49.50	53.70	39.00	6.50	152.0
Pr	0.42	10.32	4.70	6.60	21.00	20.04	5.28	6.00	6.80	5.52	1.20	17.80
Nd	2.50	40.00	16.80	26.00	92.00	72.00	21.00	25.80	28.80	25.20	6.50	70.00
Sm	1.08	8.20	3.40	5.30	24.20	15.80	4.80	7.70	6.59	6.20	2.30	12.00
Eu	0.54	1.71	0.91	1.19	2.00	0.35	0.72	0.09	1.95	2.06	0.85	3.60
Gd	1.90	7.20	2.90	4.60	26.00	14.00	3.80	7.10	6.68	6.40	3.30	9.50
Tb	0.35	1.18	0.46	0.70	4.56	2.49	0.66		1.05	0.96	0.62	1.30
Dy	2.40	6.70	2.60	4.20	29.00	17.00	4.20	11.50	6.34	5.20	3.85	6.40
Ho	0.58	1.46		0.88	6.35	4.07	0.88		1.31	0.99	0.83	1.10
Er	1.80	4.10		2.50	17.70	12.65	2.40		3.63	2.40	2.40	2.50
Tm	0.27	0.61		0.36	2.60	2.00	0.39		0.53	0.33	0.37	0.32
Yb	1.70	4.00	1.90	2.27	17.40	14.20	2.70	7.30	3.38	2.02	2.50	1.80
Lu	0.26	0.61	0.27	0.34	2.45	2.26	0.44	1.20	0.51	0.29	0.40	0.24
Ta	0.062	1.21		0.92	6.4		1.7	1.9	0.81	1.23	0.2	5.5
Pb	3.2	25	12.3	3.1	39	40	27	32.8	13.6	2.6	5.4	4
Th	0.27	12.1	8	9.7	18.5	51	12.1	29.7	5.98	1.08	0.33	11
U	0.025	3.14	2	3	4.6	15	4.7	12.5	1.75	0.42	0.16	2.4

Table A-4: Reference values used (ppm). (Govindaraju, K., 1989, Geostandards newsletter, 13.).

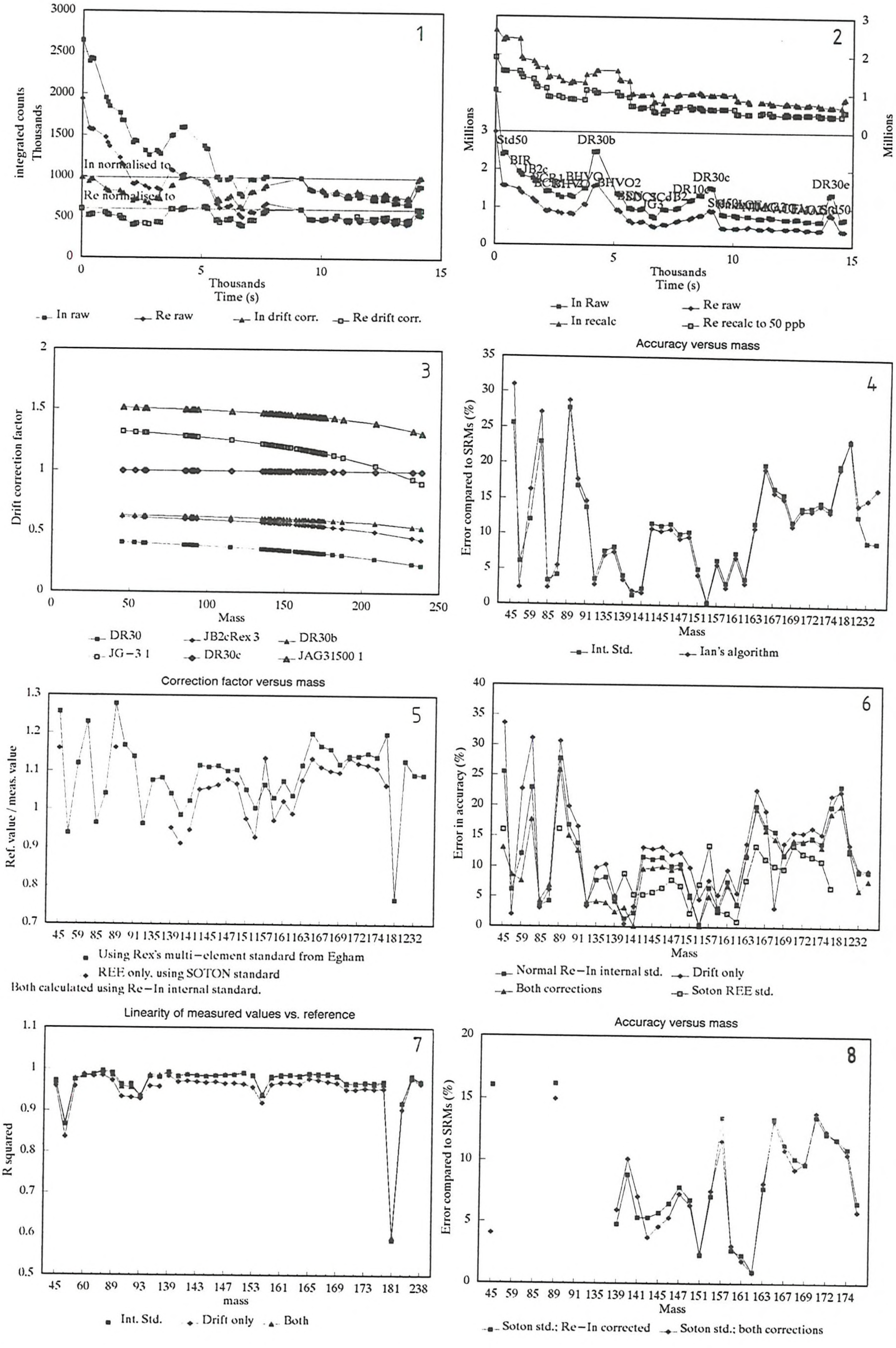

Figure A-9: 1: Raw counts for In and Re before and after drift correction. 2: DR10, DR20 and DR30 standards normalised as if they contained 50ppb Re, In. Bottom traces, rawdata; top traces, corrected. See text for details. 3: Drift correction v. mass for various samples. The run is normalised to DR30c. 4: Comparison between correction using equation (1)(int std) and (2)("Ian's algorithm"); the difference is not critical for most elements. 5: Calibration using multi-element standard DR30 compared with REE only standard Std50. 6&7: One-step correction compared with drift correction alone and both corrections. 8: Accuracy as a function of correction method and mass for Std50.

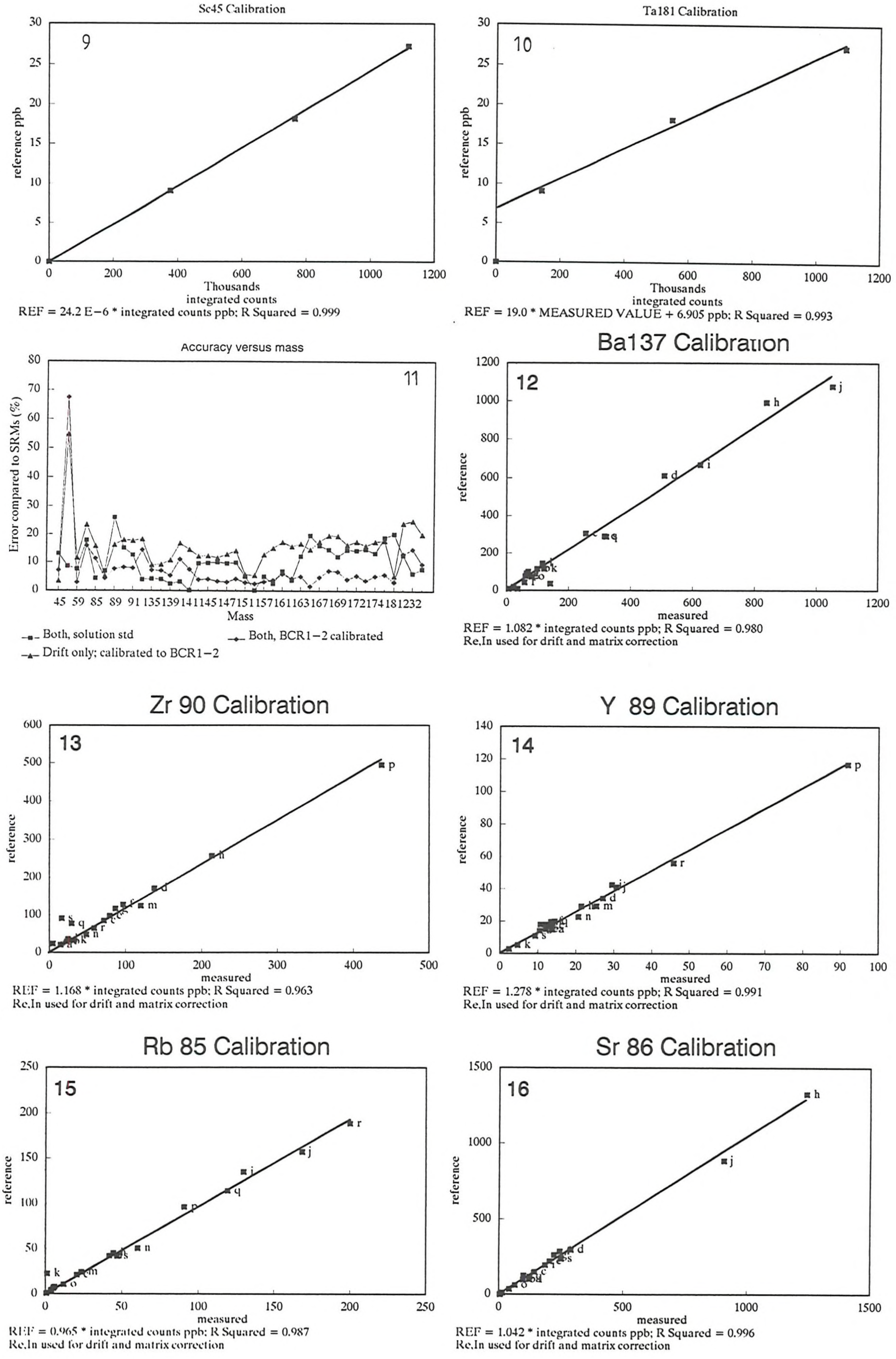

Figure A-10: 9: Typical calibration line using DR10 - DR30 and the origin. 10: Ta was the only element to have a non-zero intercept. See text for details. 11: Effect of using an SRM (BCR-1) for calibration instead of a solution standard. 5% accuracy is easily achieved for most REE. 12-16: Best fit regression lines for measured ppb v. reference value in ppb (expressed at the run dilution factor). Slope is a measure of accuracy; R^2 is a measure of linearity. Letters refer to different SRMs (see text).

Ce140 Calibration

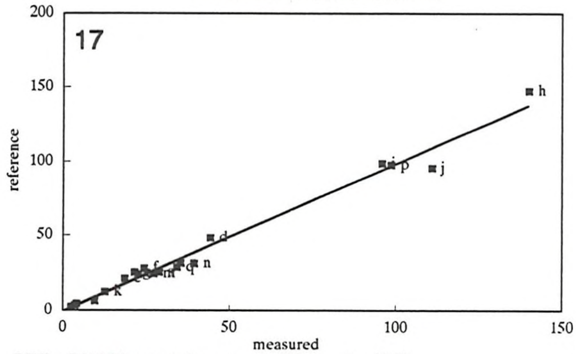

REF = 0.986 * integrated counts ppb; R Squared = 0.983
Re.In used for drift and matrix correction

Sm147 Calibration

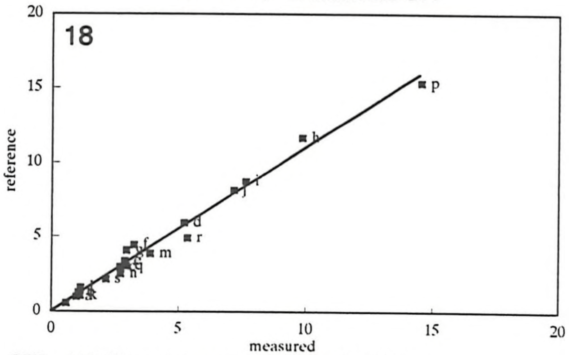

REF = 1.101 * integrated counts ppb; R Squared = 0.984
Re.In used for drift and matrix correction

Eu151 Calibration

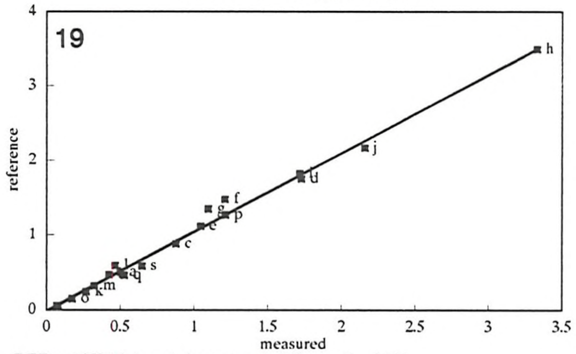

REF = 1.053 * integrated counts ppb; R Squared = 0.991
Re.In used for drift and matrix correction

Gd157 Calibration

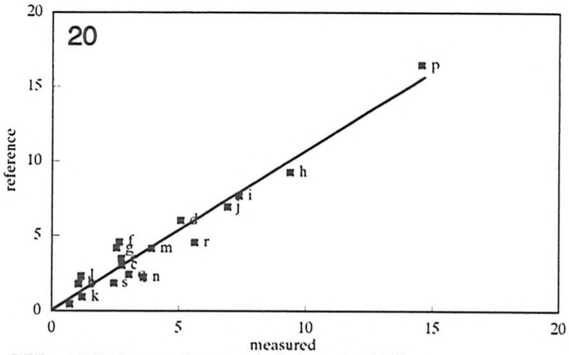

REF = 1.065 * integrated counts ppb; R Squared = 0.937
Re.In used for drift and matrix correction

Yb173 Calibration

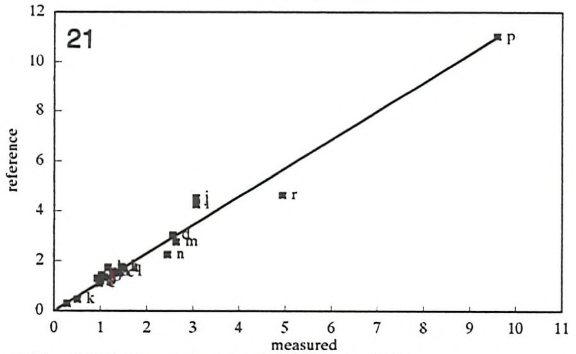

REF = 1.148 * integrated counts ppb; R Squared = 0.968
Re.In used for drift and matrix correction

Pb208 Calibration

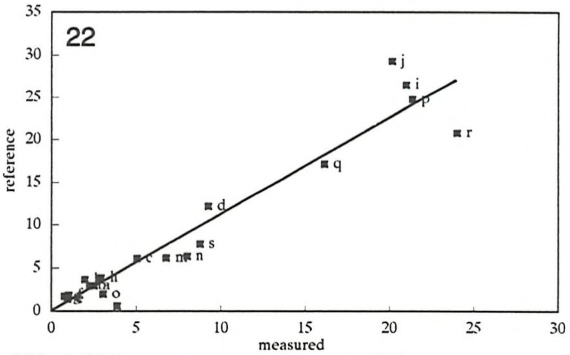

REF = 1.128 * integrated counts ppb; R Squared = 0.920
Re.In used for drift and matrix correction

Th232 Calibration

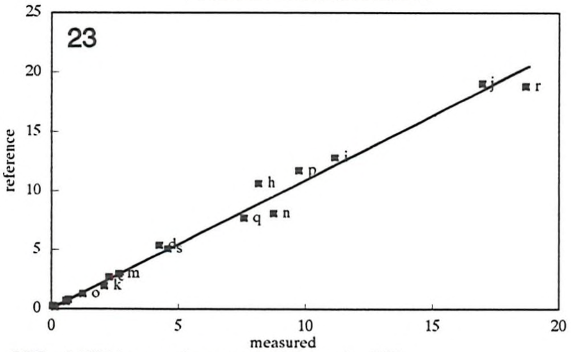

REF = 1.092 * integrated counts ppb; R Squared = 0.984
Re.In used for drift and matrix correction

U 238 Calibration

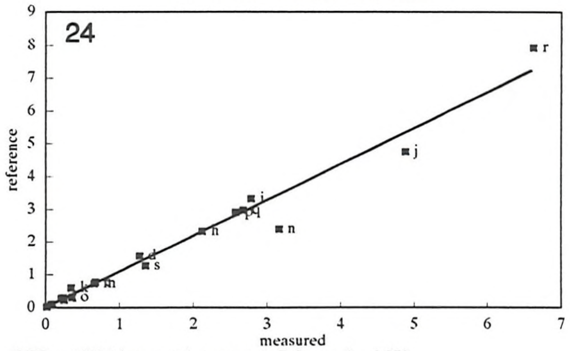

REF = 1.092 * integrated counts ppb; R Squared = 0.970
Re.In used for drift and matrix correction

Figure A-11: 17-24: Further best-fit measured v. reference lines for selected elements. For details see Fig. A-10

A3: Analytical methods used in this study

The geochemical data were acquired in two main intervals. The section at Valleleor (A0 - A29) was sampled in April 1991. Mineral separations, whole-rock and heavy mineral analyses were performed over the next six months. The section at Santa Maria (F20 - F37), the cone-in-cone material (e.g., F51) and the base of the Calymene formation to the west of Navas de Estena (F40 - F64) were sampled in October 1992.

Major and trace elements were determined for all the samples by XRF. Fused discs were prepared for major element analysis and pressed powder discs for trace elements. The procedures used are described by Croudace and Williams-Thorpe (1988).

Rare earth elements for the 1991 sampling and for the basal Calymene (F40 - F64) were determined by ICP-MS using a Plasmaquad PQ2 at the NERC facility, RHBNC, University of London at Egham. The technique is described by Jarvis (1988). To prepare the solutions, 0.5 g of powder was digested using three cycles of 10 ml HF/$HClO_4$, each time evaporating to incipient dryness at 180°C; the residue was taken up in dilute nitric acid. Heavy mineral concentrates were treated the same way, starting with 50mg of material and using 4 ml of acid mix. To monitor accuracy, reference material SCo-1 was included in the whole - rock runs (figure A-12). A drift monitor was used to correct for instrumental drift, but no matrix correction was made. Accuracy is estimated at 10% for the light REE, and possibly worse for the heavies. The heavy mineral fractions consisted predominantly of monazite, and approximate to the solution "free from matrix

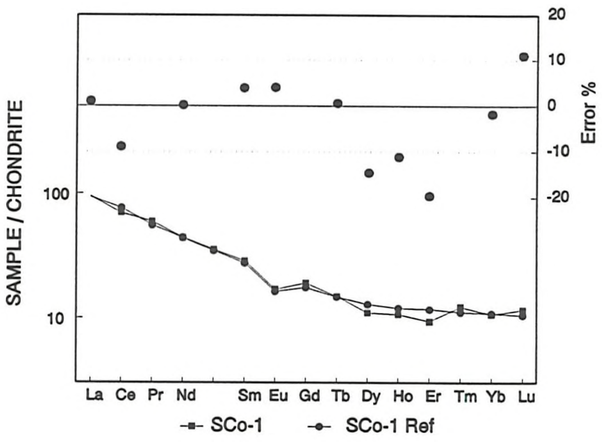

Figure A-12: Standard shale SCO-1, run in Feb. 1992, compared with recommended reference values (Govindaraju, 1984).

elements " used by Hirata et al. (1988). In this case the matrix correction is very small, and so the accuracy is estimated to be better than 5% for the REE.

The October 1992 material was run on the Plasmaquad PQ2+ machine at Southampton. Sample dissolution was by a single cycle of HF/HClO$_4$ in a teflon bomb at 150°C, followed by 5 ml of 6N HCl. This resulted in complete dissolution and an adequately low blank. An aliqout of this solution was evaporated to dryness, taken up in 2N HNO$_3$, and diluted as appropriate with the inclusion of 50 ppb Re and In as internal standards (see above). Reference materials SDC-1, BCR-1, JB-2 and JG-3 were included in the runs (figure A-13). The procedure of drift correction, matrix correction, and normalisation using the SRMs was applied as discussed above. The heavy mineral concentrates were drift and matrix corrected only. Dilution factors were $\approx 2.5*10^3$ and $5*10^6$ for whole rocks and heavy minerals, respectively (this was possible because detection limits were better than 1 ppt for the heavy REE). Accuracy is difficult to assess because the reference materials are not sufficiently well characterised (e.g., the reference values often have uneven chondrite-normalised patterns); however, it is estimated at around 5% for all the REE.

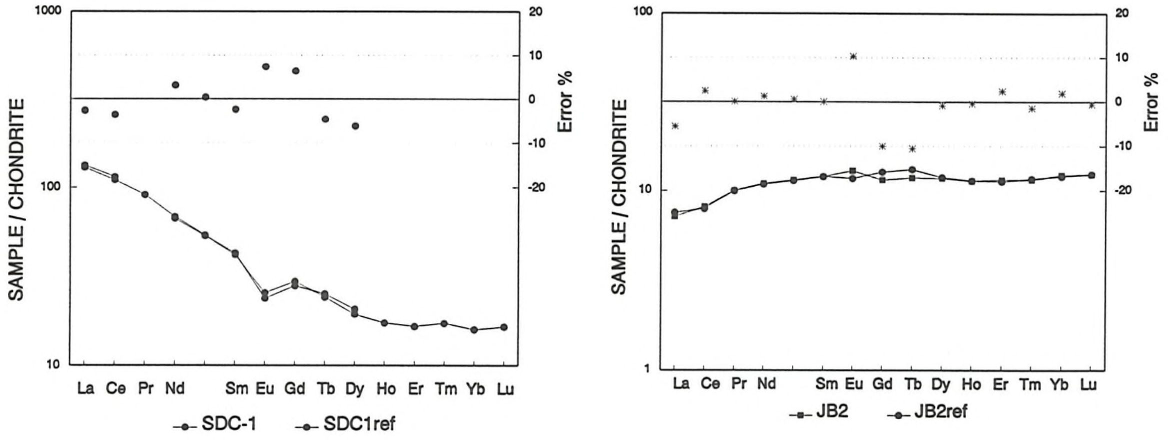

Figure A-13: Reference materials SDC-1 and JB-2 compared with the reference values from Govindaraju (1984). For SDC-1, only recommended values are given.

Organic carbon was determined using a Carlo Erba EA 1108 elemental analyzer as described by Wilkinson (1991). Samples are run before and after treatment with dilute HCl to remove any carbonate ions. Carbonate can then be calculated from the difference between the two values. In the material studied, carbonate was always below detection limit (≈0.1%) and so the acidified samples were taken to represent total organic carbon directly. Sulphur was analysed at the same time, but was below the detection limit of ≈0.3%, despite the frequent occurrence of fine framboidal pyrite in the sediment.

A number of polished thin sections, some containing in-situ monazites, were prepared for petrological and microanalytical study. Microprobe traverses were made using a JEOL JSM - 6400 scanning electron microscope fitted with a JEOL energy dispersive spectrometer and a Tracor series 2 image analysis system. X-ray mapping techniques are discussed earlier in this appendix.

Appendix B: Geochemical Data

Table B-1: Electron microprobe data

The aim of this study was to compare silicate inclusions in monazites and the corresponding phases in the host shales. The work was performed at the department of Earth Sciences, University of Cambridge, using a Cameca SX50 instrument. Operating conditions were 15 kV accelerating voltage, using an EDs detector. Polished thin sections were selected which contained *in situ* monazites. Analysis points were selected from back-scattered electron images, and the instrument was then run in automated mode, collecting 40 or 50 analyses from a typical thin section.

Table entries

The major element oxides are in weight percent. Ce_2O_3 (inferred) is calculated by assuming all the phosphorus in an analysis, which results from a component of monazite in analyses of fine grained silicate inclusions, is contained in cerium phosphate. It is used to calculate the corrected "Total including REEP (Rare Earth Element Phosphate)".

"Type" refers to the approximate position of the analysis: the core of a concretion (c), the rim (r), intermediate between the two (i) or the host shale matrix (m).

Mineral I.D. is based on the following parameters:

Quartz: SiO_2 / Al_2O_3 > 20
Illite: (FeO + MgO) < 7% and Al(IV) < 1.85 and (Na + K) < 1.85
Muscovite: (FeO + MgO) < 7% and Al(IV) > 1.85 and (Na + K) > 1.85
Chlorite: SiO_2 < 30% and (FeO + MgO) > 30%
Biotite: (FeO + MgO) > 25% and Al(IV) > 2.0 and 1.6 < (Na + K) < 2.1

The weight percent data are recalculated to 28 oxygens per formula for chlorites, and 22 for everything else. Water content is estimated by assuming sixteen (OH) per formula for chlorites, and four for everything else except quartz. Corrected totals are listed including the inferred water content and with the inferred rare earth content as well.

Tetrahedral aluminium is calculated as 8 - Si.

All iron is as FeO.

LABEL	TYPE	P_2O_5	Ce_2O_3 (inf)	min I.D.		SiO_2	TiO_2	Al_2O_3	FeO	MgO	CaO	Na_2O	K_2O	H_2O (inf)	Total	with H_2O	with REEP	n Oxygens		Si	Al(IV)	Al	Fe	Mg	Ca	Na	K	OH		cation total
A27	i	1.28	2.96	?		58.1	0.00	19.39	0.25	0.12	0.13	0.63	4.41	4.16	83.04	87.26	91.50	22		8.39	0.00	3.11	0.03	0.02	0.02	0.18	0.81	4.00		3.17
A34	i	0.86	1.98	?		58.7	0.00	8.17	14.3	2.13	0.03	0.00	0.08	3.99	83.35	87.46	90.29	22		8.84	0.00	1.37	1.80	0.48	0.01	0.00	0.02	4.00		3.65
A35	m	0.13	0.30	Illite		60.1	0.06	35.09	0.48	0.28	0.34	3.19	4.06	5.07	103.63	108.7	109.1	22		7.12	0.88	3.74	0.05	0.05	0.04	0.73	0.61	4.00		3.84
A36	r	0.68	1.56	?		63.2	0.06	23.57	0.52	0.23	0.11	1.15	4.87	4.67	93.77	98.44	100.6	22		8.14	0.00	3.37	0.06	0.04	0.01	0.29	0.80	4.00		3.47
A39	r	0.05	0.12	?		66.7	0.15	25.65	0.22	0.05	0.00	0.73	6.25	4.95	99.70	104.7	104.8	22		8.09	0.00	3.46	0.02	0.01	0.00	0.17	0.97	4.00		3.49
A40	r	0.55	0.38	?		93.0	0.12	0.00	0.03	0.00	0.00	0.08	0.00	5.07	92.90	98.37	99.30	22		11.0	0.00	0.00	0.00	0.00	0.00	0.02	0.00	4.00		0.00
A41	r	0.23	18.14	Qz		92.5	0.04	2.67	0.00	0.00	0.00	0.07	0.61	0.00	95.79	95.93	114.3	22		10.7	0.00	0.34	0.00	0.00	0.00	0.02	0.09	0.00		0.32
A42	r	1.17	3.48	chl		22.2	0.00	20.91	26.8	6.36	0.14	0.15	0.42	9.59	77.11	86.73	91.38	28		5.57	2.43	3.39	5.62	2.37	0.04	0.07	0.13	16.0		11.39
A43	r	0.37	0.14	Qz		90.2	0.01	4.04	0.11	0.00	0.05	0.16	0.81	0.00	95.36	95.40	95.91	22		10.5	0.00	0.53	0.01	0.00	0.01	0.04	0.12	0.00		0.53
A45	r	0.31	1.29	chl		27.0	0.00	24.43	25.0	5.89	0.27	0.20	0.49	10.7	83.39	94.15	95.74	28		6.04	1.96	4.11	4.68	1.96	0.07	0.09	0.14	16.0		10.75
A46	r	1.06	1.56	?		92.8	0.05	0.00	0.15	0.00	0.00	0.16	0.00	5.07	93.00	98.23	100.8	22		10.9	0.00	0.00	0.01	0.00	0.00	0.04	0.00	4.00		0.01
A47	r	2.00	0.30	?		84.7	0.00	0.00	0.29	0.00	0.00	0.03	0.02	4.62	84.71	89.69	92.00	22		11.0	0.00	0.00	0.03	0.00	0.00	0.01	0.00	4.00		0.02
A48	r	0.60	0.84	Qz		89.1	0.00	1.71	2.13	0.44	0.08	0.05	0.01	0.00	93.52	93.55	94.99	22		10.6	0.00	0.23	0.21	0.08	0.01	0.01	0.00	0.00		0.52
A49	r	0.66	4.63	?		90.2	0.00	0.00	0.08	0.00	0.02	0.00	0.00	4.89	89.55	95.27	100.5	22		11.0	0.00	0.00	0.01	0.00	0.00	0.00	0.00	4.00		0.00
A50	r	0.92	2.12	Illite		45.6	0.00	34.95	0.53	0.41	0.09	2.32	6.07	4.28	89.95	94.26	97.31	22		6.40	1.60	3.86	0.06	0.09	0.01	0.63	1.09	4.00		4.01
A54	r	0.67	2.45	chl		23.6	0.00	21.85	24.5	6.31	0.15	0.07	0.82	9.80	77.29	87.24	90.36	28		5.80	2.20	3.76	5.03	2.31	0.04	0.03	0.26	16.0		11.09
A55	r	0.29	0.78	chl		27.7	0.12	23.77	25.6	6.63	0.14	0.04	0.28	10.8	84.30	95.18	96.25	28		6.11	1.89	3.95	4.72	2.18	0.03	0.02	0.08	16.0		10.85
A60	r	0.78	1.53	chl		25.8	0.00	22.62	25.2	6.40	0.24	0.50	0.44	10.3	81.28	91.67	93.98	28		5.98	2.02	3.80	4.87	2.21	0.06	0.22	0.13	16.0		10.87
A62	r	0.34	1.27	Qz		98.7	0.00	0.00	0.13	0.00	0.00	0.06	0.00	0.00	98.38	98.95	100.5	22		11.0	0.00	0.00	0.01	0.00	0.00	0.01	0.00	0.00		0.00
A63	m	0.16	0.38	Illite		50.0	0.09	35.43	1.28	0.45	0.07	2.24	5.04	4.54	94.65	99.19	99.73	22		6.61	1.39	3.82	0.14	0.09	0.01	0.57	0.85	4.00		4.05
A64	c	0.65	0.66	Qz		98.0	0.00	0.00	0.00	0.00	0.00	0.01	0.00	0.00	97.42	98.02	99.34	22		11.0	0.00	0.00	0.00	0.00	0.00	0.00	0.00	0.00		0.00
A65	c	0.29	0.70	?		94.3	0.00	0.00	0.00	0.00	0.01	0.00	0.00	5.11	93.60	99.43	100.4	22		11.0	0.00	0.00	0.00	0.00	0.00	0.00	0.00	4.00		0.00
A70	c	0.30	8.50	Qz		98.8	0.00	0.12	0.00	0.00	0.00	0.12	0.00	0.00	99.04	99.13	107.9	22		10.9	0.00	0.02	0.00	0.00	0.00	0.03	0.00	0.00		0.00
A75	i	1.51	9.83	Qz		91.0	0.00	0.65	0.60	0.13	0.00	0.02	0.07	0.00	92.51	92.52	103.8	22		10.8	0.00	0.09	0.06	0.02	0.00	0.01	0.01	0.00		0.17
A79	i	1.44	27.87	Qz		71.2	0.12	5.93	0.11	0.00	0.00	0.38	1.51	4.20	79.23	83.44	112.7	22		10.1	0.00	0.94	0.01	0.00	0.00	0.11	0.28	4.00		0.95
A80	i	0.30	0.75	Qz		96.9	0.07	0.15	0.03	0.00	0.00	0.00	0.11	0.00	96.80	97.27	98.32	22		11.0	0.00	0.02	0.00	0.00	0.00	0.00	0.02	0.00		0.00
A81	i	1.78	17.37	?		70.3	0.00	0.00	0.24	0.00	0.01	0.00	0.00	3.83	70.18	74.39	93.55	22		11.0	0.00	0.00	0.03	0.00	0.00	0.00	0.00	4.00		0.00
A92	r	1.16	2.68	Illite		55.8	0.00	25.65	4.10	0.96	0.00	0.52	5.12	4.45	92.15	96.65	100.5	22		7.53	0.47	3.39	0.46	0.19	0.00	0.14	0.88	4.00		4.04
A93	r	0.71	6.49	Qz		82.9	0.00	1.83	3.63	0.31	0.00	0.09	0.06	0.00	88.79	88.88	96.07	22		10.5	0.00	0.26	0.39	0.06	0.00	0.02	0.01	0.00		0.71
A95	r	0.06	0.14	Illite		49.0	0.27	36.54	0.53	0.35	0.00	0.77	8.49	4.55	96.02	100.5	100.7	22		6.48	1.52	3.85	0.06	0.07	0.00	0.20	1.43	4.00		3.97
A96	r	0.14	0.32	Illite		60.1	2.67	28.60	1.49	0.83	0.28	1.37	5.78	4.90	101.14	106.0	106.5	22		7.36	0.64	3.25	0.15	0.15	0.04	0.32	0.90	4.00		3.55
A97	r	1.17	2.70	?		31.0	0.38	26.05	22.9	5.96	0.16	0.48	1.13	3.70	88.14	91.83	95.70	22		5.04	2.96	1.74	3.11	1.44	0.03	0.15	0.23	4.00		6.30
A99	r	0.29	7.84	Qz		91.9	0.06	5.73	0.02	0.00	0.09	0.00	0.05	5.28	97.73	103.2	111.3	22		10.4	0.00	0.72	0.00	0.00	0.01	0.00	0.01	4.00		0.71
b1	m	0.00	0.00	Illite		46.5	0.14	38.03	0.62	0.24	0.03	1.38	6.86	4.46	93.89	98.35	98.35	22		6.27	1.73	3.96	0.07	0.05	0.00	0.36	1.18	4.00		4.08
b2	m	0.13	0.31	chl		23.2	0.08	24.65	30.7	7.81	0.09	0.27	0.07	10.7	87.00	97.76	98.19	28		5.18	2.82	3.30	5.74	2.60	0.02	0.12	0.02	16.0		11.64
b3	m	0.11	0.25	chl		23.7	0.05	25.10	29.7	8.08	0.08	0.13	0.06	10.8	86.97	97.82	98.17	28		5.25	2.75	3.43	5.49	2.66	0.02	0.05	0.02	16.0		11.59

LABEL	TYPE	P_2O_5	Ce_2O_3 (inf)	min I.D.		SiO_2	TiO_2	Al_2O_3	FeO	MgO	CaO	Na_2O	K_2O	H_2O (inf)	Total	with H_2O	with REEP	n Oxygens		Si	Al(IV)	Al	Fe	Mg	Ca	Na	K	OH		cation total
b4	m	0.09	0.21	chl		22.4	0.07	23.37	30.7	7.06	0.05	0.18	0.15	10.3	84.08	94.41	94.72	28		5.20	2.80	3.25	5.98	2.44	0.01	0.08	0.04	16.0		11.67
b5	m	0.06	0.15	chl		25.1	0.00	26.57	30.1	7.82	0.07	0.18	0.06	11.3	90.00	101.3	101.5	28		5.35	2.65	3.63	5.35	2.47	0.02	0.08	0.02	16.0		11.45
b6	m	0.01	0.03	Illite		45.4	0.08	37.36	0.50	0.04	0.02	1.07	7.56	4.36	92.07	96.43	96.48	22		6.26	1.74	3.99	0.06	0.01	0.00	0.29	1.33	4.00		4.05
b7	m	0.00	0.00	Illite		47.1	0.08	38.24	0.59	0.17	0.00	1.01	7.82	4.50	95.08	99.58	99.58	22		6.29	1.71	3.96	0.07	0.03	0.00	0.26	1.33	4.00		4.06
b8	m	0.11	0.26	chl		23.6	0.05	24.95	30.5	7.70	0.06	0.00	0.14	10.8	87.06	97.88	98.25	28		5.25	2.75	3.41	5.67	2.55	0.01	0.00	0.04	16.0		11.62
b9	m	0.20	0.46	chl		23.6	0.08	22.94	27.3	6.18	0.11	0.40	0.47	10.1	81.17	91.33	92.00	28		5.58	2.42	3.61	5.41	2.18	0.03	0.18	0.14	16.0		11.19
b10	m	0.07	0.15	Illite		48.2	0.16	35.72	0.91	0.13	0.97	2.50	3.81	4.45	92.44	96.89	97.11	22		6.50	1.50	3.86	0.10	0.03	0.14	0.65	0.66	4.00		3.99
b11	m	0.00	0.00	Illite		45.0	0.25	36.06	1.05	0.46	0.00	1.02	7.69	4.32	91.62	95.94	95.94	22		6.27	1.73	3.85	0.12	0.09	0.00	0.27	1.36	4.00		4.07
b12	m	0.03	0.06	chl		22.8	0.07	25.12	31.4	7.93	0.00	0.01	0.10	10.7	87.51	98.30	98.39	28		5.08	2.92	3.30	5.85	2.63	0.00	0.00	0.03	16.0		11.77
b13	m	0.00	0.00	Illite		45.0	0.48	34.92	4.20	0.93	0.69	2.16	3.99	4.34	92.38	96.72	96.72	22		6.22	1.78	3.58	0.49	0.19	0.10	0.58	0.70	4.00		4.26
b14	m	0.10	0.23	Illite		45.7	0.49	34.99	4.48	0.86	0.64	2.00	3.70	4.38	92.92	97.30	97.64	22		6.27	1.73	3.60	0.51	0.18	0.09	0.53	0.65	4.00		4.29
b15	m	0.12	0.28	chl		23.7	0.01	23.64	30.3	6.56	0.11	0.15	0.31	10.5	84.88	95.39	95.79	28		5.42	2.58	3.43	5.80	2.24	0.03	0.07	0.09	16.0		11.47
b16	m	0.00	0.00	chl		25.1	0.00	25.30	29.8	7.66	0.04	0.12	0.10	11.0	88.17	99.23	99.23	28		5.45	2.55	3.56	5.41	2.48	0.01	0.05	0.03	16.0		11.44
b17	m	0.13	0.29	Illite		49.3	1.19	33.93	1.05	0.35	0.23	2.79	4.14	4.48	93.05	97.53	97.95	22		6.61	1.39	3.68	0.12	0.07	0.03	0.73	0.71	4.00		3.86
c1	r	0.12	0.27	Illite		53.2	0.08	33.33	1.25	0.45	0.17	1.83	6.27	4.64	96.66	101.2	101.6	22		6.90	1.10	3.70	0.14	0.09	0.02	0.46	1.03	4.00		3.92
c2	r	1.32	3.05	?		35.3	0.00	24.36	18.9	4.18	0.20	0.49	1.08	3.68	84.60	88.28	92.65	22		5.77	2.23	2.19	2.58	1.02	0.04	0.16	0.23	4.00		5.79
c3	r	0.16	0.37	Illite		46.0	0.09	37.01	0.26	0.08	0.00	0.87	8.90	4.39	93.27	97.66	98.19	22		6.30	1.70	3.93	0.03	0.02	0.00	0.23	1.55	4.00		3.98
c4	r	0.09	0.22	Illite		44.5	0.89	34.49	0.88	0.34	0.05	1.17	8.14	4.24	90.50	94.75	95.05	22		6.30	1.70	3.72	0.10	0.07	0.01	0.32	1.47	4.00		3.90
c5	r	0.48	1.11	?		51.3	1.15	19.80	9.72	2.68	0.13	0.71	1.98	4.13	87.47	91.61	93.19	22		7.45	0.55	2.64	1.18	0.58	0.02	0.20	0.37	4.00		4.40
c6	r	0.71	1.65	chl		29.3	0.00	21.34	24.4	5.61	0.12	0.09	0.19	10.5	81.13	91.71	94.07	28		6.66	1.34	4.04	4.63	1.90	0.03	0.04	0.06	16.0		10.57
c7	r	0.80	1.85	?		35.6	2.51	25.02	15.0	3.79	0.08	0.71	3.01	3.76	85.83	89.58	92.23	22		5.69	2.31	2.14	2.02	0.90	0.01	0.22	0.61	4.00		5.05
c8	l	0.46	1.07	Illite		48.0	0.21	32.22	0.49	0.17	0.02	0.93	7.44	4.27	89.58	93.85	95.39	22		6.75	1.25	3.79	0.06	0.04	0.00	0.25	1.33	4.00		3.89
c12	r	1.05	2.42	Illite		45.0	0.00	35.00	1.47	0.26	0.00	0.97	8.07	4.26	90.82	95.08	98.55	22		6.34	1.66	3.83	0.17	0.05	0.00	0.27	1.45	4.00		4.06
c13	r	2.76	6.38	?		29.9	0.00	23.88	22.2	5.45	0.09	0.60	0.54	3.48	82.78	86.26	95.40	22		5.17	2.83	1.75	3.21	1.40	0.02	0.20	0.12	4.00		6.36
c14	r	1.28	2.95	?		62.0	1.20	20.39	1.40	0.47	0.11	1.12	3.56	4.51	90.25	94.76	98.98	22		8.26	0.00	3.02	0.16	0.09	0.02	0.29	0.60	4.00		3.27
c16	c	0.00	0.00	Illite		45.9	0.08	36.84	0.53	0.08	0.00	0.91	7.58	4.36	91.95	96.31	96.31	22		6.33	1.67	3.97	0.06	0.02	0.00	0.24	1.33	4.00		4.05
c23	c	0.90	2.08	Illite		43.1	0.08	31.51	0.79	0.45	0.02	0.69	7.29	3.97	84.00	87.98	90.96	22		6.52	1.48	3.81	0.10	0.10	0.00	0.20	1.40	4.00		4.01
c26	i	0.28	0.65	Illite		45.9	0.66	32.41	2.32	0.81	0.04	0.95	6.68	4.23	89.77	94.00	94.93	22		6.50	1.50	3.61	0.27	0.17	0.01	0.26	1.21	4.00		4.06
c27	r	0.30	0.70	chl		29.7	0.25	26.16	25.4	6.48	0.14	0.08	0.78	11.5	89.06	100.6	101.6	28		6.16	1.84	4.19	4.41	2.00	0.03	0.03	0.21	16.0		10.60
c28	r	2.84	6.57	?		33.0	0.00	26.45	11.9	2.90	0.30	1.68	1.43	3.47	77.73	81.20	90.61	22		5.70	2.30	2.79	1.73	0.75	0.06	0.56	0.32	4.00		5.26
c29	r	0.95	2.20	?		39.1	0.00	19.98	20.4	4.53	0.13	0.34	0.69	3.72	85.21	88.93	92.08	22		6.31	1.69	1.90	2.76	1.09	0.02	0.11	0.14	4.00		5.75
c30	m	0.26	0.60	?		32.6	0.06	23.67	24.0	5.51	0.19	0.25	0.69	3.66	87.13	90.79	91.64	22		5.36	2.64	1.68	3.30	1.35	0.03	0.08	0.14	4.00		6.32
c31	m	0.12	0.28	?		35.2	0.19	26.12	23.7	5.63	0.14	0.45	1.15	3.92	92.57	96.50	96.90	22		5.38	2.62	1.83	3.03	1.28	0.02	0.13	0.22	4.00		6.15
c32	m	0.19	0.45	?		30.7	0.05	25.63	23.2	5.92	0.26	0.27	0.96	3.65	87.04	90.68	91.33	22		5.05	2.95	1.75	3.20	1.45	0.05	0.08	0.20	4.00		6.40
c33	m	0.07	0.17	chl		24.5	0.02	25.82	30.8	7.53	0.05	0.19	0.09	11.1	89.06	100.1	100.4	28		5.30	2.70	3.52	5.58	2.43	0.01	0.08	0.02	16.0		11.52
c34	m	0.15	0.35	Illite		57.2	0.48	30.31	2.19	0.75	0.15	1.44	4.34	4.72	96.89	101.6	102.1	22		7.27	0.73	3.56	0.23	0.14	0.02	0.36	0.70	4.00		3.94

LABEL	TYPE	P_2O_5	Ce_2O_3 (inf)	min I.D.		SiO_2	TiO_2	Al_2O_3	FeO	MgO	CaO	Na_2O	K_2O	H_2O (inf)	Total	with H_2O	with REEP	n Oxygens		Si	Al(IV)	Al	Fe	Mg	Ca	Na	K	OH		cation total
c35	m	0.00	0.00	Illite		59.9	0.17	25.77	1.73	0.41	0.13	1.66	4.24	4.63	94.09	98.72	98.72	22		7.77	0.23	3.49	0.19	0.08	0.02	0.42	0.70	4.00		3.76
c36	m	0.00	0.00	Illite		45.8	0.13	37.20	0.53	0.18	0.07	1.22	5.96	4.35	91.09	95.45	95.45	22		6.31	1.69	4.02	0.06	0.04	0.01	0.33	1.05	4.00		4.11
G4	c	0.78	1.81	Qz		94.9	0.00	0.02	0.12	0.00	0.00	0.00	0.04	0.00	95.14	95.14	97.74	22		10.9	0.00	0.00	0.01	0.00	0.00	0.00	0.01	0.00		0.01
G5	c	1.45	3.35	Qz		77.9	0.00	0.45	3.63	0.16	0.05	0.14	0.00	0.00	82.38	82.38	87.17	22		10.7	0.00	0.07	0.42	0.03	0.01	0.04	0.00	0.00		0.52
G6	i	0.46	1.05	?		71.9	0.01	5.26	10.5	1.49	0.00	0.00	0.05	4.46	89.25	93.71	95.22	22		9.66	0.00	0.79	1.19	0.30	0.00	0.00	0.01	4.00		2.27
G8	i	4.77	11.03	chl		14.2	0.00	15.06	24.7	5.19	0.12	0.28	0.07	7.07	59.69	66.76	82.56	28		4.82	3.18	2.51	7.04	2.63	0.04	0.19	0.03	16.0		12.18
G10	r	0.43	1.00	chl		23.3	6.41	23.15	27.8	7.67	0.03	0.30	0.18	11.1	88.93	100.0	101.5	28		5.03	2.97	2.57	5.00	2.46	0.01	0.13	0.05	16.0		10.03
G11	m	0.21	0.49	?		51.5	3.24	22.25	7.97	2.17	0.17	0.64	3.20	4.30	91.16	95.47	96.17	22		7.18	0.82	2.63	0.93	0.45	0.03	0.17	0.57	4.00		4.02
G12	i	2.43	5.63	chl		21.6	0.00	23.44	27.1	7.07	0.02	0.00	0.26	9.93	79.59	89.52	97.58	28		5.22	2.78	3.53	5.50	2.55	0.01	0.00	0.08	16.0		11.58
G14	l	3.01	6.96	chl		26.1	0.00	19.49	24.4	6.28	0.08	0.00	0.08	9.83	76.46	86.29	96.27	28		6.38	1.62	3.67	4.98	2.29	0.02	0.00	0.02	16.0		10.94
G16	r	1.75	4.04	chl		26.3	0.00	21.28	24.6	6.28	0.06	0.12	0.70	10.1	79.38	89.56	95.35	28		6.21	1.79	3.79	4.85	2.21	0.02	0.06	0.21	16.0		10.85
G17	r	0.50	1.16	chl		21.9	0.00	22.65	28.7	7.12	0.00	0.16	0.20	9.99	80.82	90.81	92.47	28		5.26	2.74	3.32	5.78	2.55	0.00	0.08	0.06	16.0		11.64
G18	r	1.31	3.04	Qz		90.9	0.00	0.60	0.18	0.00	0.00	0.00	0.16	0.00	91.84	91.84	96.19	22		10.9	0.00	0.08	0.02	0.00	0.00	0.00	0.02	0.00		0.10
G20	c	0.26	0.59	?		33.6	0.00	32.19	18.5	4.57	0.23	0.62	2.44	3.98	92.30	96.28	97.13	22		5.08	2.92	2.49	2.34	1.03	0.04	0.18	0.47	4.00		5.85
G22	c	3.18	7.35	chl		19.5	0.00	20.89	27.2	7.15	0.04	0.04	0.10	9.22	75.02	84.24	94.76	28		5.08	2.92	3.14	5.94	2.77	0.01	0.02	0.03	16.0		11.85
G33	m	0.00	0.00	chl		27.2	0.17	26.69	27.0	7.16	0.07	0.10	0.85	11.4	89.38	100.8	100.8	28		5.73	2.27	3.96	4.75	2.24	0.02	0.04	0.23	16.0		10.95
G34	m	0.00	0.00	chl		23.5	0.08	24.45	30.6	8.04	0.03	0.31	0.23	10.8	87.39	98.21	98.21	28		5.23	2.77	3.27	5.69	2.66	0.01	0.14	0.07	16.0		11.61
G35	m	0.00	0.00	Illite		46.1	0.47	33.88	2.14	0.95	0.00	0.48	8.83	4.33	92.91	97.25	97.25	22		6.39	1.61	3.61	0.25	0.20	0.00	0.13	1.56	4.00		4.06
G36	m	0.03	0.08	?		30.4	0.13	29.54	23.4	5.91	0.14	0.61	1.41	3.83	91.65	95.49	95.60	22		4.77	3.23	1.92	3.07	1.38	0.02	0.19	0.28	4.00		6.37
G37	m	0.00	0.00	Illite		46.9	0.29	35.91	1.35	0.69	0.23	1.03	7.72	4.43	94.15	98.58	98.58	22		6.35	1.65	3.76	0.15	0.14	0.03	0.27	1.33	4.00		4.05
G38	m	0.03	0.07	chl		24.9	0.04	24.96	30.2	7.68	0.07	0.10	0.18	11.0	88.24	99.27	99.37	28		5.43	2.57	3.47	5.51	2.49	0.02	0.04	0.05	16.0		11.47
G39	m	0.00	0.00	chl		24.0	0.03	25.92	29.6	7.66	0.17	0.25	0.10	10.9	87.81	98.79	98.79	28		5.25	2.75	3.56	5.42	2.50	0.04	0.11	0.03	16.0		11.48
H41	r	1.74	4.01	chl		22.9	0.00	24.27	28.6	7.99	0.03	0.25	0.36	10.5	84.49	95.01	100.7	28		5.23	2.77	3.39	5.47	2.72	0.01	0.11	0.11	16.0		11.57
H43	r	0.32	0.75	chl		23.8	0.00	24.28	30.3	8.00	0.06	0.27	0.18	10.8	86.97	97.77	98.84	28		5.31	2.69	3.31	5.63	2.65	0.01	0.12	0.05	16.0		11.59
H45	r	0.18	0.41	Illite		46.3	0.03	37.11	0.14	0.11	0.00	0.64	8.17	4.39	92.59	96.97	97.56	22		6.34	1.66	3.99	0.02	0.02	0.00	0.17	1.42	4.00		4.03
H47	r	1.32	3.05	chl		23.3	0.00	23.62	29.7	7.57	0.12	0.05	0.08	10.5	84.55	95.05	99.41	28		5.34	2.66	3.34	5.68	2.58	0.03	0.02	0.02	16.0		11.61
H48	r	0.50	1.15	?		40.4	0.00	20.60	24.8	6.24	0.07	0.07	0.19	3.97	92.52	96.49	98.14	22		6.11	1.89	1.57	3.14	1.40	0.01	0.02	0.04	4.00		6.12
H49	r	2.12	4.91	chl		24.5	0.00	24.25	24.0	6.63	0.01	0.30	0.65	10.3	80.41	90.71	97.75	28		5.71	2.29	3.99	4.69	2.30	0.00	0.14	0.19	16.0		10.98
H50	r	0.72	1.67	chl		25.0	0.02	25.37	29.0	7.65	0.00	0.25	0.25	11.0	87.62	98.64	101.0	28		5.45	2.55	3.60	5.30	2.48	0.00	0.11	0.07	16.0		11.38
H51	i	0.14	0.33	Illite		50.7	0.26	32.70	0.86	0.30	0.00	0.75	7.77	4.45	93.37	97.82	98.29	22		6.83	1.17	3.74	0.10	0.06	0.00	0.20	1.34	4.00		3.90
H52	i	1.14	2.64	chl		20.5	0.00	21.21	29.6	6.70	0.03	0.07	0.08	9.55	78.31	87.86	91.64	28		5.16	2.84	3.09	6.23	2.51	0.01	0.03	0.03	16.0		11.84
H53	i	0.74	1.71	chl		22.7	0.00	22.96	29.4	8.16	0.07	0.29	0.03	10.3	83.72	94.09	96.55	28		5.27	2.73	3.18	5.69	2.81	0.02	0.13	0.01	16.0		11.69
H54	i	1.21	2.80	Qz		92.2	0.00	0.01	0.60	0.00	0.00	0.00	0.00	0.00	92.88	92.88	96.89	22		10.9	0.00	0.00	0.06	0.00	0.00	0.00	0.00	0.00		0.06
H55	c	0.00	0.01	Qz		100.	0.04	0.00	0.06	0.00	0.00	0.12	0.00	0.00	101.03	101.0	101.0	22		10.9	0.00	0.00	0.01	0.00	0.00	0.03	0.00	0.00		0.01
H57	r	0.25	0.59	chl		22.2	0.06	24.13	30.9	6.93	0.06	0.09	0.22	10.4	84.64	95.03	95.88	28		5.13	2.87	3.33	5.97	2.39	0.01	0.04	0.07	16.0		11.68
H59	r	4.11	9.49	chl		21.8	0.00	22.40	25.4	6.59	0.04	0.20	0.31	9.66	76.88	86.54	100.1	28		5.44	2.56	3.63	5.29	2.44	0.01	0.10	0.10	16.0		11.36

LABEL	TYPE	P_2O_5	Ce_2O_3 (inf)	min I.D.		SiO_2	TiO_2	Al_2O_3	FeO	MgO	CaO	Na_2O	K_2O	H_2O (inf)	Total	with H_2O	with REEP	n Oxygens		Si	Al(IV)	Al	Fe	Mg	Ca	Na	K	OH		cation total
H60	r	4.43	10.24	chl		13.3	0.00	13.38	24.0	3.81	0.02	0.00	0.09	6.42	54.67	61.09	75.76	28		4.99	3.01	2.56	7.52	2.12	0.01	0.00	0.04	16.0		12.20
H62	c	2.34	5.42	Illite		42.3	0.35	32.63	1.08	0.58	0.00	0.89	7.67	4.02	85.56	89.58	97.34	22		6.33	1.67	3.75	0.14	0.13	0.00	0.26	1.46	4.00		4.02
H63	c	0.64	1.48	chl		22.6	0.00	23.27	28.9	7.32	0.07	0.00	0.12	10.2	82.38	92.62	94.73	28		5.31	2.69	3.39	5.67	2.56	0.02	0.00	0.04	16.0		11.61
H64	c	0.52	1.21	chl		23.5	0.02	23.81	29.6	7.43	0.00	0.14	0.28	10.5	84.89	95.44	97.17	28		5.35	2.65	3.38	5.65	2.52	0.00	0.06	0.08	16.0		11.55
H65	c	0.22	0.50	Qz		98.0	0.00	0.00	0.06	0.00	0.00	0.01	0.00	0.00	98.12	98.12	98.84	22		11.0	0.00	0.00	0.01	0.00	0.00	0.00	0.00	0.00		0.01
H66	c	0.10	0.22	Illite		47.3	0.21	32.01	1.47	1.14	0.00	0.51	8.39	4.29	91.12	95.41	95.73	22		6.63	1.37	3.61	0.17	0.24	0.00	0.14	1.50	4.00		4.02
H68	c	1.34	3.09	?		30.6	0.04	24.32	26.2	6.55	0.07	0.30	0.62	3.66	88.76	92.42	96.85	22		5.01	2.99	1.44	3.59	1.60	0.01	0.10	0.13	4.00		6.64
H70	i	1.04	2.42	chl		21.0	0.01	20.45	27.0	5.83	0.04	0.16	0.30	9.26	74.92	84.18	87.64	28		5.46	2.54	3.36	5.86	2.25	0.01	0.08	0.10	16.0		11.48
H71	i	0.16	0.36	chl		24.7	0.02	24.71	29.1	7.97	0.00	0.32	0.34	10.9	87.29	98.23	98.74	28		5.43	2.57	3.47	5.36	2.61	0.00	0.13	0.10	16.0		11.43
H72	i	0.38	0.88	?		30.3	0.11	27.38	23.8	5.45	0.00	0.59	1.72	3.72	89.45	93.17	94.43	22		4.90	3.10	1.82	3.22	1.31	0.00	0.18	0.35	4.00		6.34
H73	i	0.35	0.80	Qz		99.3	0.00	0.00	0.13	0.00	0.00	0.00	0.00	0.00	99.45	99.45	100.6	22		10.9	0.00	0.00	0.01	0.00	0.00	0.00	0.00	0.00		0.01
H74	i	0.34	0.79	chl		24.4	0.01	24.02	28.7	7.28	0.04	0.11	0.54	10.6	85.23	95.89	97.02	28		5.50	2.50	3.52	5.42	2.44	0.01	0.05	0.15	16.0		11.38
H75	i	0.37	0.86	Qz		101.	0.02	0.00	0.06	0.00	0.00	0.00	0.00	0.00	101.63	101.6	102.8	22		11.0	0.00	0.00	0.01	0.00	0.00	0.00	0.00	0.00		0.01
H77	r	0.70	1.62	Qz		97.8	0.00	0.00	0.09	0.00	0.00	0.00	0.00	0.00	97.97	97.97	100.2	22		11.0	0.00	0.00	0.01	0.00	0.00	0.00	0.00	0.00		0.01
H78	r	0.15	0.35	?		43.1	0.00	17.99	24.6	5.25	0.03	0.06	0.04	3.95	91.17	95.12	95.63	22		6.55	1.45	1.59	3.13	1.19	0.00	0.02	0.01	4.00		5.91
H79	r	0.17	0.40	Qz		99.9	0.00	0.00	0.00	0.00	0.00	0.08	0.00	0.00	100.05	100.0	100.6	22		11.0	0.00	0.00	0.00	0.00	0.00	0.02	0.00	0.00		0.00
H80	r	0.58	1.34	chl		22.1	0.00	23.75	29.9	8.15	0.00	0.12	0.06	10.4	84.21	94.61	96.54	28		5.12	2.88	3.22	5.78	2.80	0.00	0.05	0.02	16.0		11.80
H82	r	0.29	0.67	chl		24.1	0.00	23.47	28.6	7.54	0.02	0.04	0.76	10.5	84.61	95.17	96.13	28		5.49	2.51	3.43	5.44	2.55	0.01	0.02	0.22	16.0		11.42
H83	r	4.20	9.71	chl		22.1	0.00	22.74	25.6	6.64	0.05	0.21	0.29	9.77	77.65	87.42	101.3	28		5.43	2.57	3.65	5.26	2.43	0.01	0.10	0.09	16.0		11.35
H84	r	0.12	0.29	chl		23.7	0.25	24.13	30.2	7.77	0.05	0.02	0.08	10.7	86.34	97.07	97.48	28		5.32	2.68	3.32	5.66	2.59	0.01	0.01	0.02	16.0		11.57
H85	r	0.48	1.12	chl		23.1	0.07	23.99	29.5	7.08	0.04	0.15	0.23	10.4	84.24	94.70	96.31	28		5.32	2.68	3.44	5.66	2.42	0.01	0.07	0.07	16.0		11.52
H86	i	0.00	0.00	chl		22.7	0.10	24.08	31.6	7.68	0.01	0.23	0.01	10.6	86.52	97.15	97.15	28		5.14	2.86	3.19	5.98	2.58	0.00	0.10	0.00	16.0		11.75
H87	r	0.94	2.18	chl		23.6	0.00	23.38	25.4	5.71	0.05	0.21	1.11	10.0	79.59	89.63	92.74	28		5.65	2.35	3.88	5.09	2.03	0.01	0.10	0.34	16.0		11.00
H88	m	0.08	0.19	chl		27.1	0.46	23.75	27.4	7.41	0.01	0.16	0.62	11.0	86.98	98.05	98.32	28		5.89	2.11	3.62	4.96	2.39	0.00	0.07	0.17	16.0		10.97
H89	m	0.09	0.22	Illite		54.5	0.20	33.28	1.23	0.23	0.10	1.27	6.73	4.69	97.61	102.3	102.6	22		6.98	1.02	3.72	0.13	0.04	0.01	0.31	1.10	4.00		3.89
H90	m	0.16	0.37	chl		23.1	0.05	24.44	30.8	7.81	0.04	0.04	0.10	10.7	86.48	97.18	97.72	28		5.20	2.80	3.30	5.78	2.61	0.01	0.02	0.03	16.0		11.70
H91	m	0.03	0.07	chl		25.7	0.25	27.14	30.3	8.11	0.09	0.13	0.42	11.5	92.18	103.7	103.8	28		5.33	2.67	3.60	5.26	2.51	0.02	0.05	0.11	16.0		11.36
H92	m	0.00	0.00	?		65.4	0.19	22.44	0.55	0.19	0.02	1.30	4.45	4.73	94.62	99.35	99.35	22		8.30	0.00	3.17	0.06	0.04	0.00	0.32	0.72	4.00		3.26
H93	m	0.24	0.56	?		65.8	0.17	22.46	0.90	0.49	0.09	0.95	4.58	4.77	95.46	100.2	101.0	22		8.28	0.00	3.15	0.09	0.09	0.01	0.23	0.74	4.00		3.33
H94	m	0.00	0.00	?		43.3	0.20	31.12	8.71	2.52	0.04	0.89	4.77	4.20	91.57	95.77	95.77	22		6.19	1.81	3.14	1.04	0.54	0.01	0.25	0.87	4.00		4.72
D2	m	0.11	0.25	chl		28.0	0.11	27.94	27.0	7.01	0.11	0.51	1.31	11.7	92.06	103.8	104.1	28		5.71	2.29	4.05	4.62	2.13	0.02	0.20	0.34	16.0		10.79
D3	m	0.17	0.39	?		70.1	0.27	17.76	2.31	0.42	0.03	1.21	2.51	4.79	94.64	99.43	99.99	22		8.78	0.00	2.48	0.24	0.08	0.00	0.29	0.40	4.00		2.80
D4	m	0.12	0.29	chl		24.4	0.09	26.81	28.2	6.78	0.08	0.45	0.53	11.0	87.42	98.42	98.83	28		5.34	2.66	3.84	5.15	2.21	0.02	0.19	0.15	16.0		11.19
D5	m	0.27	0.63	Illite		45.7	1.56	32.53	5.51	1.24	0.15	2.04	5.79	4.38	94.57	98.94	99.84	22		6.27	1.73	3.24	0.63	0.25	0.02	0.54	1.01	4.00		4.12
D6	m	0.16	0.36	?		75.4	0.27	15.62	0.63	0.21	0.03	0.36	3.45	4.93	95.98	100.9	101.4	22		9.18	0.00	2.12	0.06	0.04	0.00	0.09	0.54	4.00		2.22
D7	m	0.22	0.51	Illite		55.8	0.94	26.10	2.74	0.75	0.11	1.53	4.17	4.48	92.20	96.69	97.42	22		7.48	0.52	3.36	0.31	0.15	0.02	0.40	0.71	4.00		3.82

LABEL	TYPE	P_2O_5	Ce_2O_3 (inf)	min I.D.		SiO_2	TiO_2	Al_2O_3	FeO	MgO	CaO	Na_2O	K_2O	H_2O (inf)	Total	with H_2O	with REEP	n Oxygens		Si	Al(IV)	Al	Fe	Mg	Ca	Na	K	OH		cation total
D8	m	0.43	0.99	chl		24.2	0.68	24.86	29.1	7.20	0.05	0.15	0.42	10.8	86.77	97.62	99.04	28		5.37	2.63	3.49	5.38	2.37	0.01	0.06	0.12	16.0		11.24
D9	m	0.00	0.00	Illite		46.5	0.03	37.38	0.29	0.00	0.00	0.80	8.41	4.41	93.30	97.83	97.83	22		6.33	1.67	3.99	0.03	0.00	0.00	0.21	1.46	4.00		4.00
E54	m	0.22	0.50	?		50.9	0.76	27.58	8.76	2.01	0.37	1.51	3.45	4.46	95.39	99.85	100.5	22		6.86	1.14	2.99	0.99	0.40	0.05	0.39	0.59	4.00		4.38
E?	m	0.27	0.62	?		51.1	0.75	27.96	8.94	1.91	0.37	1.40	3.49	4.49	96.01	100.5	101.3	22		6.85	1.15	3.01	1.00	0.38	0.05	0.36	0.60	4.00		4.39
E55	m	0.08	0.18	?		37.1	0.38	28.63	17.4	4.58	0.08	0.41	4.63	4.02	93.25	97.27	97.54	22		5.54	2.46	2.29	2.18	1.02	0.01	0.12	0.88	4.00		5.49
E56	m	0.08	0.18	Illite		57.3	3.95	26.36	0.78	0.19	0.33	1.83	3.58	4.64	94.37	99.01	99.26	22		7.42	0.58	3.22	0.08	0.04	0.05	0.46	0.59	4.00		3.34
E57	m	0.51	1.18	?		39.9	0.13	22.35	18.1	3.44	0.11	0.74	1.50	3.81	86.34	90.15	91.84	22		6.31	1.69	2.23	2.39	0.81	0.02	0.23	0.30	4.00		5.42
E58	m	0.00	0.00	Illite		56.2	0.09	35.98	0.86	0.30	0.49	2.51	4.59	4.90	101.03	105.9	105.9	22		6.88	1.12	3.79	0.09	0.06	0.06	0.60	0.72	4.00		3.93
E59	r	0.00	0.00	?		46.1	0.05	37.21	1.15	0.26	0.00	0.10	10.9	4.44	95.89	100.3	100.3	22		6.23	1.77	3.82	0.13	0.05	0.00	0.03	1.89	4.00		4.01
E60	r	0.96	2.22	chl		23.6	0.00	25.38	29.7	7.50	0.07	0.25	0.09	10.8	86.71	97.53	100.7	28		5.25	2.75	3.52	5.53	2.48	0.02	0.11	0.02	16.0		11.53
E61	r	1.34	3.10	?		41.5	1.77	26.51	4.28	1.69	0.01	0.32	9.75	3.89	85.85	89.74	94.18	22		6.41	1.59	2.96	0.55	0.39	0.00	0.10	1.92	4.00		3.90
E62	r	1.68	3.87	chl		21.8	0.00	22.94	27.2	7.16	0.12	0.21	0.27	9.93	79.72	89.65	95.20	28		5.27	2.73	3.44	5.50	2.58	0.03	0.10	0.08	16.0		11.52
E63	r	0.36	0.83	chl		23.3	0.06	24.99	30.6	7.76	0.09	0.15	0.09	10.8	87.20	98.01	99.21	28		5.19	2.81	3.37	5.70	2.57	0.02	0.06	0.03	16.0		11.63
E69	c	1.76	4.07	?		40.3	0.74	29.31	1.96	0.49	0.12	1.32	7.55	3.80	81.87	85.67	91.50	22		6.37	1.63	3.52	0.26	0.11	0.02	0.40	1.52	4.00		3.90
E70	r	0.16	0.37	?		44.2	0.65	35.07	3.89	0.68	0.14	1.05	8.30	4.33	94.04	98.37	98.91	22		6.13	1.87	3.54	0.45	0.14	0.02	0.28	1.47	4.00		4.13
E71	i	0.12	0.28	?		48.4	0.50	31.03	2.77	1.71	0.00	0.38	10.3	4.40	95.19	99.59	99.99	22		6.61	1.39	3.32	0.32	0.35	0.00	0.10	1.79	4.00		3.98
E72	i	2.00	4.63	Qz		90.2	0.00	0.00	0.13	0.00	0.04	0.11	0.03	0.00	90.56	90.56	97.18	22		10.9	0.00	0.00	0.01	0.00	0.00	0.03	0.00	0.00		0.01
E74	r	1.62	3.76	chl		21.4	0.00	23.04	29.5	7.15	0.04	0.08	0.06	10.0	81.32	91.34	96.72	28		5.14	2.86	3.28	5.91	2.55	0.01	0.04	0.02	16.0		11.75
E75	r	2.27	5.24	chl		20.7	0.00	22.41	27.6	6.75	0.03	0.00	0.13	9.62	77.76	87.39	94.89	28		5.18	2.82	3.40	5.77	2.51	0.01	0.00	0.04	16.0		11.68
E76	r	0.46	1.06	Qz		97.9	0.00	0.00	0.10	0.00	0.01	0.00	0.00	0.00	98.10	98.10	99.63	22		10.9	0.00	0.00	0.01	0.00	0.00	0.00	0.00	0.00		0.01
E78	m	0.19	0.45	chl		26.4	0.06	24.40	28.1	9.22	0.18	0.08	0.11	11.2	88.69	99.95	100.5	28		5.64	2.36	3.42	5.02	2.93	0.04	0.03	0.03	16.0		11.38
E80	m	0.00	0.00	chl		28.9	0.07	24.05	29.0	7.99	0.03	0.01	0.06	11.5	90.14	101.6	101.6	28		6.03	1.97	3.61	5.05	2.48	0.01	0.01	0.02	16.0		11.14
E81	m	0.09	0.21	chl		24.7	0.01	25.81	29.7	8.23	0.09	0.29	0.16	11.1	88.99	100.1	100.4	28		5.32	2.68	3.50	5.35	2.64	0.02	0.12	0.04	16.0		11.49
E82	m	0.16	0.37	Qz		100.	0.05	0.52	0.49	0.00	0.00	0.00	0.09	0.00	101.45	101.4	101.9	22		10.9	0.00	0.06	0.04	0.00	0.00	0.00	0.01	0.00		0.11
E83	m	0.37	0.85	?		50.9	0.11	27.15	7.27	1.45	0.29	2.09	2.64	4.36	91.97	96.33	97.55	22		7.02	0.98	3.19	0.84	0.30	0.04	0.56	0.46	4.00		4.32
F1	c	1.24	2.86	chl		23.0	0.00	24.72	29.7	7.50	0.06	0.00	0.11	10.5	85.16	95.75	99.85	28		5.23	2.77	3.46	5.63	2.53	0.02	0.00	0.03	16.0		11.62
F2	i	0.14	0.31	chl		24.1	0.02	25.43	30.2	8.14	0.08	0.22	0.11	11.0	88.40	99.43	99.88	28		5.26	2.74	3.42	5.51	2.64	0.02	0.09	0.03	16.0		11.57
F3	i	1.70	3.93	chl		18.5	0.02	18.70	26.9	6.18	0.11	0.25	0.06	8.62	70.83	79.44	85.08	28		5.17	2.83	2.97	6.27	2.57	0.03	0.13	0.02	16.0		11.81
F6	r	0.13	0.29	chl		30.6	0.00	29.42	26.1	6.95	0.04	0.63	0.92	12.3	94.77	107.1	107.5	28		5.96	2.04	4.33	4.26	2.02	0.01	0.24	0.23	16.0		10.61
F7	c	2.91	6.74	chl		27.4	0.00	26.65	22.9	5.41	0.13	0.75	1.05	10.9	84.41	95.40	105.0	28		5.99	2.01	4.47	4.20	1.76	0.03	0.32	0.29	16.0		10.43
F8	c	1.75	4.04	?		35.4	0.14	26.38	13.9	3.03	0.13	0.23	5.87	3.69	85.12	88.81	94.59	22		5.76	2.24	2.53	1.89	0.73	0.02	0.07	1.22	4.00		5.16
F10	i	0.35	0.81	chl		25.4	0.23	26.30	29.0	8.18	0.16	0.50	0.27	11.3	90.11	101.4	102.6	28		5.38	2.62	3.57	5.13	2.58	0.04	0.20	0.07	16.0		11.28
F11	i	0.13	0.30	?		75.3	0.10	17.59	0.62	0.06	0.02	0.42	3.93	5.01	98.02	103.0	103.4	22		9.02	0.00	2.35	0.06	0.01	0.00	0.10	0.60	4.00		2.42
F12	i	0.68	1.57	chl		24.6	0.00	24.78	26.8	7.73	0.13	0.47	0.20	10.7	84.79	95.53	97.79	28		5.50	2.50	3.66	5.02	2.58	0.03	0.20	0.06	16.0		11.26
F13	r	0.98	2.27	chl		20.3	0.01	21.65	28.1	7.63	0.06	0.23	0.13	9.62	78.26	87.88	91.13	28		5.08	2.92	3.10	5.88	2.84	0.02	0.11	0.04	16.0		11.81
F14	r	0.28	0.66	chl		27.9	0.00	23.48	28.6	7.60	0.03	0.14	0.07	11.1	87.90	99.09	100.0	28		5.99	2.01	3.59	5.14	2.43	0.01	0.06	0.02	16.0		11.16

LABEL	TYPE	P_2O_5	Ce_2O_3 (inf)	min I.D.		SiO_2	TiO_2	Al_2O_3	FeO	MgO	CaO	Na_2O	K_2O	H_2O (inf)	Total	with H_2O	with REEP	n Oxygens		Si	Al(IV)	Al	Fe	Mg	Ca	Na	K	OH		cation total
F16	c	2.11	4.88	chl		23.8	0.01	23.58	25.9	6.13	0.11	0.19	0.44	10.1	80.28	90.43	97.42	28		5.63	2.37	3.83	5.14	2.16	0.03	0.09	0.13	16.0		11.13
F18	m	0.04	0.10	?		63.6	0.11	15.40	15.4	3.84	0.03	0.12	0.65	4.70	99.25	103.9	104.1	22		8.12	0.00	2.19	1.65	0.73	0.00	0.03	0.11	4.00		4.57
F19	m	0.11	0.25	Illite		55.5	0.24	35.49	0.53	0.36	0.54	3.30	3.47	4.84	99.43	104.2	104.6	22		6.88	1.12	3.77	0.05	0.07	0.07	0.79	0.55	4.00		3.89
F20	m	0.86	1.98	Illite		40.0	0.56	32.08	2.40	0.90	0.12	1.15	6.23	3.90	83.49	87.39	90.22	22		6.16	1.84	3.65	0.31	0.21	0.02	0.34	1.22	4.00		4.16
F21	m	0.46	1.06	chl		25.9	0.30	27.53	27.9	7.08	0.07	0.25	0.23	11.3	89.32	100.7	102.2	28		5.48	2.52	3.94	4.92	2.23	0.02	0.10	0.06	16.0		11.10
F22	r	0.19	0.44	Illite		47.2	0.20	34.28	1.30	1.09	0.04	0.74	8.81	4.39	93.70	98.10	98.73	22		6.45	1.55	3.66	0.15	0.22	0.01	0.20	1.53	4.00		4.03
F23	r	0.33	0.75	chl		25.7	0.10	24.00	29.1	7.40	0.03	0.06	0.30	10.9	86.72	97.64	98.71	28		5.66	2.34	3.53	5.35	2.43	0.01	0.03	0.08	16.0		11.31
F24	i	0.38	0.87	?		65.5	0.08	25.29	0.09	0.12	0.01	0.44	6.65	4.86	98.18	103.0	104.2	22		8.08	0.00	3.47	0.01	0.02	0.00	0.11	1.05	4.00		3.51
F25	i	0.93	2.15	Illite		45.7	0.14	36.49	0.28	0.29	0.03	1.13	8.14	4.35	92.26	96.62	99.70	22		6.31	1.69	3.90	0.03	0.06	0.00	0.30	1.43	4.00		3.99
F27	c	1.99	4.60	chl		26.1	0.07	24.49	24.8	6.87	0.36	1.21	0.32	10.8	84.34	95.15	101.7	28		5.81	2.19	3.86	4.62	2.28	0.09	0.52	0.09	16.0		10.75
F28	c	1.16	2.68	chl		18.7	0.26	18.92	27.9	5.90	0.17	0.59	0.17	8.78	72.64	81.42	85.26	28		5.12	2.88	2.88	6.38	2.40	0.05	0.31	0.06	16.0		11.66
F29	r	0.03	0.06	Illite		46.0	0.13	37.17	0.22	0.34	0.03	1.35	8.27	4.41	93.54	97.95	98.04	22		6.27	1.73	3.90	0.03	0.07	0.00	0.36	1.44	4.00		3.99
F31	r	0.40	0.94	chl		23.1	0.09	23.48	29.6	7.08	0.04	0.15	0.07	10.3	83.66	94.04	95.38	28		5.34	2.66	3.38	5.73	2.44	0.01	0.07	0.02	16.0		11.55
F34	r	0.00	0.00	Illite		45.6	0.16	36.68	0.68	0.42	0.14	0.95	8.74	4.38	93.36	97.74	97.74	22		6.25	1.75	3.85	0.08	0.09	0.02	0.25	1.53	4.00		4.01
F35	i	1.79	4.15	Qz		88.9	0.00	0.00	0.03	0.00	0.04	0.04	0.00	0.00	89.06	89.06	95.00	22		10.9	0.00	0.00	0.00	0.00	0.01	0.01	0.00	0.00		0.00
F38	m	0.03	0.07	chl		30.9	0.38	28.65	27.9	7.52	0.15	0.53	0.40	12.5	96.57	109.0	109.1	28		5.94	2.06	4.06	4.49	2.15	0.03	0.20	0.10	16.0		10.71
F39	m	0.12	0.27	chl		27.2	0.12	25.28	28.3	8.08	0.04	0.00	0.26	11.3	89.33	100.7	101.1	28		5.74	2.26	3.68	4.99	2.54	0.01	0.00	0.07	16.0		11.21
F40	m	0.02	0.05	chl		24.2	0.09	23.53	30.4	8.05	0.02	0.18	0.00	10.7	86.61	97.38	97.46	28		5.41	2.59	3.25	5.67	2.68	0.01	0.08	0.00	16.0		11.60
F41	m	0.01	0.03	Illite		48.9	0.34	33.39	2.51	0.90	0.35	1.78	6.33	4.46	94.51	98.97	99.00	22		6.58	1.42	3.57	0.28	0.18	0.05	0.46	1.09	4.00		4.03

Table B-2: Major element geochemistry

Weight %	m. above base	Monazite (ppm)	SiO_2	TiO_2	Al_2O_3	Fe_2O_3	MnO	MgO	CaO	Na_2O	K_2O	P_2O_5	LOI (%)	Sum
Valleleor														
A0	5	684	56.4	1.11	25.75	10.00	0.05	2.10	0.05	0.51	4.53	0.10	5.29	100.68
A1	31	467	54.0	1.02	26.39	10.74	0.09	2.39	0.57	0.71	4.23	0.54	5.25	100.75
A2	41	353	51.7	0.97	26.11	13.58	0.12	2.90	0.26	0.65	3.74	0.34	5.57	100.37
A3	51	374	54.0	0.99	25.66	12.57	0.11	2.68	0.14	0.69	3.82	0.23	5.21	100.93
A4	62.5	268	52.0	0.97	25.67	14.24	0.14	3.08	0.36	0.65	3.35	0.41	5.55	100.88
A5	74	217	51.7	1.07	26.10	14.28	0.14	3.09	0.12	0.80	3.07	0.26	6.13	100.64
A6	83.5	298	52.4	1.06	26.09	13.79	0.12	3.08	0.25	0.89	2.93	0.31	5.98	100.99
A7	95	280	55.5	1.11	26.34	9.40	0.08	2.13	0.21	1.10	3.33	0.16	5.67	99.43
A8	109	479	56.2	1.11	27.11	8.66	0.07	2.02	0.22	1.22	3.52	0.15	5.59	100.29
A9	123	300	55.5	1.05	26.15	10.00	0.08	2.31	0.24	1.07	3.22	0.15	5.54	99.78
A10	137	158	55.4	1.07	26.65	9.59	0.08	2.28	0.23	1.08	3.31	0.11	5.67	99.88
A11	151	169	48.2	0.92	24.77	19.00	0.21	4.31	0.20	0.59	2.07	0.30	6.21	100.58
A12	161.5	193	47.8	0.89	24.89	17.79	0.17	3.88	1.51	0.65	2.09	1.23	6.21	100.99
A13	171	123	42.4	0.86	26.26	22.16	0.21	4.76	0.99	0.55	1.85	0.86	6.59	100.98
A14	180.5	56	49.2	0.98	26.12	16.87	0.16	3.47	0.31	0.73	2.66	0.26	6.08	100.77
A15	188.5	168	47.8	1.01	27.13	16.87	0.15	3.58	0.32	0.73	2.69	0.30	6.19	100.67
A16	198	73	44.8	0.94	26.01	20.82	0.19	4.29	0.68	0.61	1.90	0.68	6.38	100.99
A17	208	211	47.3	1.04	27.23	17.58	0.16	3.67	0.24	0.84	2.45	0.23	6.16	100.76
A18	217.5	189	47.4	1.04	27.89	16.75	0.15	3.50	0.33	0.91	2.62	0.31	6.26	100.95
A19	231.5	104	47.8	0.98	25.54	17.15	0.14	3.71	1.36	0.75	2.24	1.22	6.19	100.98
A20	251	146	55.1	1.07	26.24	9.79	0.07	2.34	0.66	1.08	3.12	0.56	5.43	100.08
A22	276.5	133	63.1	0.79	19.27	11.91	0.08	2.68	0.14	0.62	1.70	0.12	4.56	100.50
A23	309.5	288	56.0	1.19	28.05	8.34	0.05	1.83	0.24	1.31	3.44	0.19	5.73	100.73
A24	341.5	145	54.7	1.00	25.92	12.25	0.09	2.66	0.21	0.99	2.85	0.20	5.95	100.92
A25	366.5	154	52.8	1.09	26.31	13.57	0.10	3.04	0.25	1.01	2.55	0.20	5.93	100.92
A26	390.5	86	49.0	1.11	27.61	15.40	0.11	3.44	0.25	0.95	2.67	0.27	6.16	100.84
A27	416	65	48.6	1.08	27.18	16.57	0.12	3.63	0.24	0.88	2.43	0.24	6.34	100.98
A28	437	115	56.4	1.00	23.38	13.21	0.10	2.93	0.25	0.81	2.30	0.30	5.31	100.77
A29	458	76	52.9	1.21	27.16	12.21	0.09	2.88	0.23	1.09	2.89	0.24	6.00	100.99
Others														
B1		340	55.2	1.12	26.76	9.56	0.08	2.19	0.11	1.15	3.53	0.18	5.38	99.95
B2			57.5	1.21	27.90	6.23	0.05	1.56	0.11	1.34	4.32	0.09	4.82	100.38
B3		549	56.6	1.14	27.90	7.33	0.06	1.62	0.05	0.72	5.32	0.10	5.21	100.85
B4		200	51.1	1.06	25.65	13.85	0.12	2.95	1.46	0.95	2.67	1.14	5.38	100.98
B5			34.9	0.33	7.66	9.18	0.02	1.09	25.18	0.07	0.98	19.84	3.55	99.27
B6		50	57.7	1.05	25.60	8.33	0.05	2.44	0.08	0.20	5.34	0.09	4.91	100.92
B7		1	66.0	1.37	19.75	6.06	0.03	1.54	0.12	0.28	4.38	0.20	3.71	99.76
B8		3	64.6	1.14	21.48	6.25	0.03	1.78	0.03	0.32	4.68	0.11	3.82	100.48
B9		395	59.0	1.30	24.74	7.22	0.04	1.76	0.07	0.49	5.05	0.12	4.55	99.88
C2		185	56.5	1.22	27.66	8.20	0.06	1.93	0.16	1.32	3.48	0.16	6.28	100.76
C4		46	58.7	1.26	25.21	9.42	0.04	1.59	0.16	1.19	3.18	0.18	5.9	100.93
C5		41	61.7	1.24	24.27	7.29	0.05	1.78	0.11	1.16	3.21	0.13	5.61	100.94
C6		218	64.6	1.51	27.17	0.79	0.00	0.34	0.27	1.85	3.99	0.07	5.34	100.65
C7		220	55.9	1.19	26.37	10.19	0.08	2.46	0.16	1.17	3.10	0.17	6.18	100.88

	Monazite	SiO_2	TiO_2	Al_2O_3	Fe_2O_3	MnO	MgO	CaO	Na_2O	K_2O	P_2O_5	LOI	TOTAL
Santa Maria													
F20	513	54.4	1.2	25.0	6.78	0.00	0.26	0.15	1.56	3.33	0.10	5.88	98.7
F21	692	54.4	1.2	25.2	7.37	0.01	0.22	0.11	1.52	3.32	0.11	5.60	99.1
F22	462	51.4	1.1	25.2	8.74	0.06	2.12	0.14	1.33	3.19	0.15	5.80	99.3
F23	187	54.2	1.2	24.3	6.59	0.04	1.62	0.18	1.58	3.37	0.15	5.45	98.6
F24	168	55.0	1.2	23.4	7.63	0.05	1.76	0.12	1.37	3.11	0.14	5.37	99.1
F25	350	55.4	1.3	24.1	6.10	0.04	1.39	0.14	1.39	3.34	0.21	5.36	98.7
F26	350	55.8	1.2	24.8	4.77	0.02	1.14	0.16	1.54	3.59	0.16	5.63	98.8
F27	13	57.6	1.1	20.8	8.16	0.05	1.79	0.09	1.42	2.91	0.13	5.63	99.7
F28	93	52.8	1.2	25.4	7.91	0.05	1.83	0.13	1.47	3.24	0.15	5.63	99.8
F29	67	50.0	1.0	23.2	12.04	0.07	2.34	0.11	1.13	2.56	0.20	7.12	99.8
F30	427	55.9	1.4	25.7	3.73	0.02	0.83	0.16	1.72	3.69	0.17	5.75	99.0
F31	15	59.1	1.2	21.4	6.36	0.04	1.43	0.12	1.19	3.07	0.16	5.09	99.1
F32	185	53.3	1.2	24.6	6.46	0.04	1.64	0.15	1.61	3.28	0.15	5.44	97.9
F33	93	55.5	1.3	24.0	5.87	0.03	1.29	0.19	1.56	3.32	0.20	5.58	98.8
F34	100	54.2	1.2	23.9	7.38	0.06	1.81	0.18	1.31	3.34	0.14	5.29	98.8
F35	152	51.1	1.1	24.4	9.19	0.07	1.96	0.23	1.32	3.13	0.18	5.99	98.6
F36	191	50.2	1.2	25.5	9.34	0.08	2.16	0.22	1.41	3.15	0.16	5.82	99.2
F37	166	54.9	1.2	23.1	8.25	0.07	1.87	0.13	1.21	3.11	0.16	5.07	99.1

Notes.

Monazite abundance is in ppm monazite in the 250-500 μm fraction . For details see chapter 2.

Major elements determined by X-ray fluorescence, using ignited powders (Valleleor data, and B1..C7) and air-dried powders (Santa Maria data).

Table B-3: Trace element data

ppm	Corg	Rb	Sr	Y	Zr	Nb	Th	U	Pb	Zn	Ni	Ga	Cr	V	Ba	As	Mo	Sn	Bi	W	Cu
A0	0.43	180	131	36	126	20	19	2	34	127	45	31	112	157	818	4	1	3	0		
A1	0.41	180	154	46	104	20	20	4	38	134	58	32	120	166	743	2	0	2	0		
A2	0.42	160	139	37	101	19	19	4	49	162	66	33	117	166	657	3	1	1	0		
A3	0.41	159	134	33	104	19	19	3	29	152	61	33	116	161	629	3	0	2	0		
A4	0.50	143	132	37	99	18	19	4	32	168	68	34	121	158	580	6	1	1	0		
A5	0.68	133	141	37	120	20	19	3	32	170	70	33	124	158	575	6	1	1	0		
A6	0.64	130	158	40	119	19	21	5	39	166	67	34	115	171	525	0	0	5	0		
A7	0.54	154	196	34	125	20	20	4	31	113	49	33	123	171	612	1	0	3	0		
A8	0.42	159	203	35	119	21	22	2	28	106	46	34	128	177	614	5	0	3	0		
A9	0.40	149	182	34	120	20	19	3	30	120	52	35	119	166	581	3	1	4	0		
A10	0.42	154	182	34	113	21	20	4	29	120	52	34	123	168	579	0	1	2	0		
A11	0.51	92	99	33	110	17	16	3	19	241	94	34	96	151	370	7	1	2	0		
A12	0.57	95	126	46	94	16	17	3	45	225	86	35	104	161	366	6	1	0	0		
A13	0.54	81	100	48	91	16	15	4	33	261	100	35	98	159	321	0	1	4	0		
A14	0.43	121	128	33	104	18	18	4	40	212	85	34	108	163	440	2	0	2	0		
A15	0.49	122	134	36	103	19	19	3	27	209	88	36	115	168	447	5	1	4	0		
A16	0.50	86	120	41	99	17	17	5	36	235	93	36	111	175	348	7	1	4	0		
A17	0.38	111	146	34	107	20	20	5	58	203	85	36	125	182	394	11	0	4	0		
A18	0.36	123	152	38	106	19	21	3	23	186	80	38	119	180	427	5	1	3	0		
A19	0.45	105	134	52	111	18	17	4	42	215	87	35	103	178	392	24	1	3	0		
A20	0.40	150	175	53	121	20	20	2	37	132	56	33	119	170	519	8	0	3	0		
A22	0.22	83	114	30	82	16	12	3	224	162	51	27	89	130	309	1	0	0	0		
A23	0.42	167	196	39	125	22	22	3	29	112	46	36	129	179	567	5	1	2	0		
A24	0.46	133	151	43	114	18	17	3	42	168	63	33	103	160	484	0	1	1	0		
A25	0.42	121	165	37	119	20	19	2	31	169	67	35	116	175	428	10	2	1	0		
A26	0.39	124	157	44	134	21	21	5	46	200	81	38	119	179	434	14	1	0	0		
A27	0.40	115	148	40	122	19	21	5	43	210	91	37	120	174	404	11	2	5	0		

ppm	Corg	Rb	Sr	Y	Zr	Nb	Th	U	Pb	Zn	Ni	Ga	Cr	V	Ba	As	Mo	Sn	Bi	W	Cu
A28	0.34	107	232	38	130	19	16	5	83	175	64	32	102	147	418	9	0	3	0		
A29	0.54	137	224	41	158	22	20	5	45	166	67	34	120	179	589	7	1	2	0		
B1	0.68	164	229	39	128	21	21	4	32	115	50	34	124	176	696	1	1	2	0		
B2	0.34	199	235	42	139	23	20	4	28	80	38	35	133	183	789	6	0	3	0		
B3	0.40	225	174	41	107	21	20	2	14	93	38	34	132	173	940	2	0	0	0		
B4	0.40	125	146	46	117	20	20	4	30	166	67	34	117	167	436	8	1	1	0		
B5	1.21	42	2511	139	81	8	7	19	29	72	32	10	24	56	474	19	0	0	0		
B6	0.50	218	94	35	145	20	19	3	9	84	47	31	107	153	1190	0	0	1	0		
B7	0.26	160	67	53	613	25	23	5	8	73	24	27	91	137	697	1	0	5	0		
B8	0.18	176	69	42	249	21	16	4	10	82	33	28	89	129	740	0	0	1	0		
B9	0.33	198	102	37	257	23	21	3	9	94	38	32	117	161	851	0	0	1	0		
C2	1.20	164	179	37	129	22	24	5	28	100	43	34	132	177	541	7	0	1	0		
C4	0.86	153	153	37	175	22	21	5	46	90	37	34	119	171	531	25	1	1	0		
C5	0.95	150	151	36	179	22	18	4	30	94	33	32	106	151	536	13	0	1	0		
C6	1.10	193	237	43	191	26	20	4	37	7	3	34	109	181	690	13	1	3	0		
C7	1.06	148	167	38	135	22	24	3	28	124	54	32	128	168	508	10	1	2	0		
F20		168	208	36	137	23	24	3	20	18	14	34	135	170	586	0		5	0	24	8
F21		171	195	42	146	23	23	3	27	18	21	34	131	160	596	0		6	0	16	8
F22		163	173	38	128	22	25	4	24	135	61	35	137	177	534	0		5	1	15	18
F23		172	185	44	151	24	26	4	30	85	43	35	138	179	599	9		5	1	11	23
F24		158	169	43	149	23	23	3	35	95	45	35	128	177	546	8		3	0	14	21
F25		170	193	41	145	24	24	3	32	69	38	36	137	181	582	8		7	1	18	17
F26		186	200	39	137	24	26	5	28	56	31	36	137	169	614	13		4	0	11	11
F27		143	126	35	171	22	18	1	25	104	39	32	112	141	497	12		3	0	22	12
F28		162	185	39	141	22	23	3	37	101	44	34	128	166	562	10		6	0	17	14
F29		128	159	35	143	19	19	4	49	157	59	31	108	156	435	21		4	1	12	30

ppm	**Corg**	**Rb**	**Sr**	**Y**	**Zr**	**Nb**	**Th**	**U**	**Pb**	**Zn**	**Ni**	**Ga**	**Cr**	**V**	**Ba**	**As**	**Mo**	**Sn**	**Bi**	**W**	**Cu**
F30		183	215	42	157	24	24	3	27	34	23	38	135	200	620	18		5	0	8	12
F31		147	144	37	187	21	20	3	23	77	30	32	141	144	523	14		2	0	17	12
F32		167	179	44	161	23	22	2	25	99	41	34	132	188	582	6		1	0	14	9
F33		166	188	39	160	23	24	3	28	58	35	36	131	169	555	13		6	2	9	17
F34		168	154	40	173	23	23	3	22	98	42	35	122	166	550	8		3	1	15	16
F35		160	171	37	135	21	21	2	30	114	50	32	146	170	526	2		2	1	12	22
F36		159	179	40	130	22	24	2	32	127	54	35	133	179	512	0		5	0	7	19
F37		158	144	38	164	22	24	4	26	106	45	34	132	160	523	10		4	0	15	17

Table B-4: REE data for all areas except Santa Maria

ppm	Y	La	Ce	Pr	Nd	Sm	Eu	Gd	Tb	Dy	Ho	Er	Tm	Yb	Lu
A0	30.89	65.80	127.90	15.48	55.65	11.91	2.69	11.07	1.53	7.40	1.47	3.45	0.65	3.48	0.60
A0d	21.64	61.82	121.67	14.66	53.90	11.38	2.49	10.10	1.28	5.93	1.07	2.78	0.57	2.84	0.47
A1	35.73	41.82	86.6	10.91	40.7	9.785	2.251	10.63	1.46	8.346	1.577	3.938	0.6725	3.879	0.579
A1b	23.92	31.11	64.46	8.26	31.41	7.53	1.76	7.54	1.13	6.28	1.19	3.10	0.48	2.84	0.44
A2b	23.23	25.94	51.04	6.33	23.93	5.58	1.36	6.23	0.98	5.89	1.19	3.22	0.50	3.06	0.46
A3b	20.31	40.02	77.36	9.06	31.32	6.51	1.40	6.17	0.92	5.14	1.02	2.64	0.45	2.61	0.41
A4d	26.41	55.22	105.33	12.20	42.67	8.89	1.96	8.62	1.22	6.29	1.25	3.07	0.53	3.06	0.46
A5d	27.11	43.38	93.21	11.07	39.36	7.8835	1.7525	8.087	1.217	6.192	1.381	3.252	0.5439	3.2825	0.5106
A5b	23.56	41.81	83.39	9.64	34.81	7.18	1.65	7.07	1.10	6.00	1.21	3.03	0.52	2.93	0.48
A6	30.98	57.86	113.63	13.19	46.87	9.64	2.16	9.14	1.39	7.40	1.47	3.54	0.59	3.64	0.56
A6 Lts	27.20	23.85	38.62	4.15	15.60	3.48	0.99	4.47	0.83	5.62	1.14	3.15	0.60	2.97	0.41
A7b	24.77	56.88	106.73	12.43	43.27	8.65	1.85	7.61	1.15	6.34	1.25	3.10	0.52	3.21	0.50
A7d	22.70	74.77	144.37	16.05	54.52	10.11	2.11	8.35	1.15	5.33	1.16	2.64	0.48	2.90	0.49
A8	31.24	86.63	182.05	22.05	78.78	15.54	3.09	11.74	1.52	7.21	1.48	3.52	0.62	3.77	0.64
A8b	25.11	60.33	121.27	14.14	50.02	9.89	2.09	8.19	1.18	6.04	1.25	2.91	0.52	3.04	0.51
A9b	25.68	53.10	101.10	11.21	38.50	7.29	1.64	7.02	1.10	6.06	1.24	3.16	0.53	3.25	0.52
A9d	26.11	69.88	136.80	15.67	53.57	10.10	2.05	8.11	1.14	5.50	1.17	2.78	0.47	2.96	0.50
A10b	25.84	39.12	70.09	7.91	27.14	5.44	1.31	5.96	1.07	5.91	1.26	3.22	0.54	3.21	0.52
A11	20.90	35.23	66.24	7.49	27.41	5.86	1.31	5.78	0.94	4.92	0.99	2.39	0.43	2.38	0.41
A11b	24.20	29.99	55.16	6.24	22.32	5.05	1.18	5.68	1.05	6.10	1.25	3.09	0.52	3.01	0.46
A12	35.74	56.16	118.50	14.65	55.35	12.71	2.84	12.33	1.74	8.67	1.61	3.84	0.59	3.52	0.53
A13d	26.83	40.16	81.26	9.61	35.86	8.40	1.99	8.77	1.38	6.71	1.29	3.05	0.57	2.70	0.46
A14b	25.39	47.41	89.19	10.29	35.05	6.73	1.49	6.60	1.05	5.90	1.20	3.04	0.52	3.09	0.47
A14d	17.95	39.52	75.60	8.66	29.33	5.64	1.25	5.22	0.85	4.32	0.83	2.09	0.35	2.28	0.36
A15b	26.46	49.48	93.80	11.16	38.41	7.59	1.68	7.25	1.10	6.20	1.24	3.22	0.50	3.07	0.47
91A15	26.56	40.35	72.80	8.16	29.70	5.57	1.26	5.60	0.93	5.66	1.10	3.11	0.48	2.92	0.39
A16	31.57	43.01	87.00	10.71	38.72	8.88	2.01	8.97	1.32	7.12	1.41	3.52	0.53	3.27	0.49
A16d	22.78	36.20	74.26	8.99	33.11	7.82	1.71	7.75	1.11	5.63	1.06	2.75	0.44	2.58	0.39
A17b	24.96	45.77	87.18	10.42	35.49	7.05	1.50	6.66	1.01	5.91	1.18	3.10	0.50	3.05	0.48
A18	20.77	52.60	115.55	11.95	40.75	7.88	1.81	7.30	1.08	5.61	1.12	2.59	0.42	2.53	0.41
A19	39.07	43.84	93.73	11.16	41.27	10.01	2.51	11.12	1.67	8.89	1.76	4.11	0.60	3.52	0.52
91A19	38.87	44.33	91.55	10.28	41.74	8.89	2.27	9.61	1.36	7.80	1.38	3.61	0.56	3.00	0.39
A20b	37.76	49.91	105.09	12.45	46.80	10.84	2.68	11.55	1.74	9.44	1.87	4.46	0.67	3.87	0.59
A22	11.75	35.63	81.23	10.56	40.75	9.56	1.69	6.65	0.76	3.20	0.61	1.46	0.26	1.52	0.26
A23	28.12	75.68	154.10	18.44	66.09	12.97	2.59	10.56	1.37	6.98	1.37	3.47	0.54	3.42	0.54
A24	25.81	54.96	116.45	14.10	53.54	11.28	2.34	8.97	1.20	5.63	1.16	2.76	0.51	2.76	0.45
91A24	28.12	44.99	90.04	10.55	41.71	8.12	1.75	7.27	1.04	5.59	1.05	2.85	0.42	2.73	0.38
A25	21.32	47.57	92.67	10.68	37.50	7.30	1.58	6.53	0.96	5.12	1.05	2.59	0.44	2.61	0.41
A25D	17.97	48.23	95.05	11.09	38.70	7.67	1.62	6.50	0.91	4.91	0.93	2.20	0.37	2.42	0.39
A25A	20.05	40.65	86.90	10.40	39.02	8.85	2.01	8.27	1.14	5.72	1.09	2.62	0.41	2.60	0.41
A25Ad	18.05	35.93	79.77	9.79	35.96	8.39	1.89	7.81	1.09	5.39	1.02	2.48	0.39	2.51	0.39
A26	23.51	44.41	88.85	10.85	38.75	8.13	1.80	7.72	1.18	6.62	1.25	3.18	0.52	3.18	0.52
A26d	19.87	45.77	91.50	10.90	37.91	7.62	1.67	7.35	0.99	5.94	1.21	2.59	0.42	2.68	0.40
A27	19.29	32.17	66.97	8.15	28.99	6.02	1.34	6.11	1.04	5.68	1.18	2.91	0.51	3.06	0.47
A27d	18.11	45.97	94.80	11.11	39.47	7.88	1.64	6.79	1.02	4.90	0.93	2.38	0.39	2.52	0.39
A28	22.03	52.95	126.88	16.21	60.43	12.97	2.78	11.24	1.29	6.41	1.11	2.63	0.37	2.38	0.35
A29	18.68	45.59	104.68	12.71	44.29	8.75	1.96	8.01	1.01	5.27	0.97	2.44	0.38	2.46	0.41
B1b	25.65	52.33	112.10	13.58	47.10	9.34	2.03	8.34	1.13	6.47	1.32	3.34	0.52	3.27	0.52
B2b	33.20	67.86	146.43	18.15	60.79	11.71	2.60	10.45	1.49	8.15	1.66	4.17	0.64	3.84	0.61

ppm	**Y**	**La**	**Ce**	**Pr**	**Nd**	**Sm**	**Eu**	**Gd**	**Tb**	**Dy**	**Ho**	**Er**	**Tm**	**Yb**	**Lu**
91B2	33.05	77.64	149.93	17.23	65.88	12.21	2.70	10.02	1.33	7.42	1.42	3.88	0.59	3.53	0.48
B3b	31.60	46.44	75.86	11.15	37.60	7.93	1.92	8.28	1.26	7.22	1.53	3.93	0.64	3.94	0.64
B4b	36.62	45.17	80.44	10.88	37.30	8.91	2.21	9.61	1.48	8.26	1.65	4.09	0.61	3.69	0.58
B5	99.62	24.87	72.11	10.75	47.52	16.46	38.42	24.56	3.69	20.69	4.27	10.96	1.77	10.21	1.55
B5b	96.62	23.52	67.18	9.81	43.50	15.12	34.41	22.48	3.27	18.72	3.87	9.72	1.57	9.43	1.39
B6d	14.33	40.30	79.91	9.83	35.53	6.80	1.66	5.61	0.70	3.84	0.79	2.24	0.41	2.70	0.41
B7d	15.33	59.64	122.30	14.48	52.18	9.95	1.82	8.01	1.04	4.34	0.82	2.11	0.42	2.48	0.43
B8b	28.12	46.06	89.68	10.90	41.17	8.72	1.97	7.86	1.10	6.24	1.30	3.52	0.60	3.82	0.57
B9	13.84	50.01	101.75	12.34	45.75	8.78	1.98	6.50	0.78	4.08	0.74	1.97	0.40	2.33	0.42
B9b	24.85	52.66	105.27	12.66	46.58	8.98	1.95	7.68	1.05	5.73	1.24	3.21	0.60	3.59	0.56
c2b	25.64	62.1	120.5	14.34	51.88	10.97	2.19	8.182	1.195	6.50	1.321	3.49	0.6512	3.68	0.5731
c4b	27.03	53.77	105.8	12.55	46.00	9.82	2.14	9.036	1.244	7.27	1.38	3.90	0.6605	3.94	0.6121
c5b	25.97	51.39	101.1	12.03	42.85	8.75	1.85	7.416	1.143	5.99	1.255	3.36	0.5908	3.70	0.5757
c6	20.45	47.17	93.77	10.99	38.88	7.58	1.81	6.331	0.9911	5.12	1.104	2.92	0.5495	3.06	0.4968
c7	19.07	61.93	122.1	14.07	50.81	9.70	2.05	8.132	1.036	5.38	1.085	2.71	0.482	3.03	0.4778
b8h	30	4477	9671	1100	3645	559	83	202	33	70	36	1	23	0	33
a0h	1949	88585	171054	18745	65620	9664	1757	5576	459	1348	126	175	14	38	0
a1h	2568	93601	192599	21446	76596	12266	2181	7082	583	1631	148	191	13	39	4
a2h	1392	54761	117875	13166	47291	7638	1369	4616	393	1092	96	124	10	28	3
a3h	1976	68484	152907	17885	64712	10878	1907	6468	548	1508	134	173	12	36	3
a4h	2150	70928	161731	19215	71178	12110	2102	7042	593	1633	143	184	14	46	4
a5h	318	12713	29292	3389	12409	2131	375	1256	110	307	30	41			
a6h	2407	81724	190635	23239	88104	15879	2738	8996	735	1931	168	214	14	50	4
a7h	2463	78574	185102	22559	85980	15883	2737	9059	749	1962	168	215	16	48	5
a8h	2775	80741	191634	24309	93678	17711	3027	9958	811	2112	180	229	16	52	4
a9h	2288	63299	153238	19100	73593	13980	2394	7913	634	1670	144	180	12	44	4
a10h	2313	65400	166989	21305	83419	16100	2756	9077	746	1879	167	214			
a11h	1295	23159	60663	7531	29518	5606	992	3243	275	665	73	88			
a12h	2095	56529	146271	18456	72831	13952	2345	7783	625	1593	141	175	13	40	6
a13h	346	9546	26933	3585	14458	2861	484	1602	130	316	29	38	4	10	
a14h	46	912	2377	320	1289	263	45	155	17	52	8	18			
a15h	381	9888	25980	3453	13882	2754	460	1550	127	315	28	39	4	13	
a16h	1590	44777	117102	15274	61843	12458	2060	7128	569	1414	139	177			
a17h	2831	56281	154168	20903	86978	17855	2917	9888	772	1929	166	217	16	53	5
a18h	2433	56994	158295	20886	86609	17888	2943	9910	783	1949	166	223	16	50	5
a19h		262	686	92	373	79	14	47	4	12	2	4	1	4	1
a20h	1365	30022	91775	12381	53362	11549	1849	6379	493	1205	103	129	11	33	5
a22h	1538	28440	96070	14247	65174	15436	2399	8174	608	1416	117	152	10	37	5
a23h	2541	46742	157635	22609	103558	24359	3916	13078	934	2268	183	229	16	58	5
a24h	71	1329	3755	516	2207	475	79	255	19	48	4	6	1	2.5	0.3
a25h	1915	46083	131194	17539	74165	16113	2592	8768	688	1668	147	181			
a26h	919	17855	55517	7728	33634	7548	1244	4064	311	743	61	84	6	22	
a27h	375	9438	27894	3944	16682	3707	603	2037	153	381	33	42			
a28h	891	20504	60783	8221	34782	7584	1273	4168	315	778	66	85	6	24	3
a29h	298	5554	16423	2261	9615	2103	345	1208	90	229	21	29			
b1h	2147	79258	167827	20506	69988	12071	2113	6952	526	1330	145	151	30	35	25
b3h	1455	64394	123743	14725	49200	8289	1456	4829	357	869	96	88	22	0	16
b4h	486	15285	34314	4052	14319	2544	448	1544	126	320	38	11	20	21	19
b6h	1517	51490	122274	16918	58352	11355	2157	5899	510	1123	189	33	158	0	62
b7h	0	53	685	0	81	0	0	0	30	0	27	1	23	0	14

ppm	Y	La	Ce	Pr	Nd	Sm	Eu	Gd	Tb	Dy	Ho	Er	Tm	Yb	Lu
b9h	1588	62371	133930	15958	56828	8765	1530	4818	343	988	125	112	23	0	18
c2h	252	7118	18045	2242	8137	1535	263	776	90	180	21	1	18	0	18
c4h	25	493	1316	165	637	148	19	29	16	25	30	1	27	0	24
c5h	44	1336	3522	433	1715	309	41	225	30	49	23	1	12	0	11
c6h	1921	47063	123812	16258	60282	11497	2049	6425	518	1378	140	135	33	56	20
c7h	2180	53646	137925	17905	65929	12716	2089	6861	539	1387	136	151	38	50	33
monave	2484	90792	200132	24576	92325	15792	2787	9163	749	1999	175	230	17	58	5
F40(a)	11.73	25.29		6.41	24.77	4.38	0.90	3.66	0.48	1.97	0.39	0.97		1.17	0.19
F40(s)	9.33	13.15		3.33	13.37	2.65	0.60	2.87	0.44	1.72	0.31	0.57		0.61	0.08
F41(a)	15.48	33.02		9.02	36.18	6.63	1.35	5.30	0.65	3.15	0.68	1.84		2.20	0.36
F41(s)	5.00	8.78		2.14	8.52	1.48	0.37	1.68	0.24	0.54	0.11	0.12		0.33	0.03
F42	14.96	26.59		6.77	26.17	4.37	0.83	3.86	0.57	2.67	0.54	1.34		1.47	0.22
F43	12.62	50.12		15.33	64.61	11.46	2.06	7.03	0.77	3.23	0.50	1.23		1.27	0.19
F44(a)	18.83	41.65		13.13	56.56	10.70	1.85	7.04	0.94	4.55	0.84	2.29		2.51	0.38
F44(s)	9.52	20.03		5.38	22.45	4.27	0.60	3.18	0.40	1.50	0.27	0.61		0.75	0.11
F45(a)	20.25	34.25		8.83	33.70	6.08	1.34	5.44	0.77	4.08	0.81	2.24		2.26	0.34
F45(s)	13.54	21.45		5.36	21.89	4.57	0.95	4.52	0.63	2.84	0.51	1.22		1.19	0.17
RW(a)	24.15	44.17		11.81	46.36	8.98	1.76	7.20	0.93	4.72	0.90	2.62		2.99	0.51
RW(s)	21.22	29.94		7.75	30.42	5.77	1.18	5.27	0.75	3.86	0.77	2.24		2.67	0.46
F61(a)	19.25	29.96		7.21	28.67	5.24	1.15	4.77	0.71	3.78	0.76	2.02		2.02	0.30
F61(a)2	14.33	45.30		12.12	48.48	8.31	1.65	5.60	0.69	2.99	0.56	1.30		1.41	0.21
F61(s)	12.98	24.98		5.96	24.01	4.63	0.87	3.88	0.54	2.37	0.41	1.05		1.21	0.18
F62	19.17	32.18		7.43	28.44	5.34	1.18	4.95	0.75	4.17	0.79	2.03		2.02	0.29
F63(a)	14.56	33.63		8.04	30.79	5.26	0.99	4.28	0.56	2.64	0.52	1.41		1.65	0.26
F63(s)	20.19	45.41		11.84	46.01	8.85	1.36	6.82	0.93	4.29	0.72	1.78		1.69	0.26
F64	8.71	31.10		7.61	28.98	5.11	0.69	3.80	0.48	1.70	0.29	0.55		0.78	0.12

Notes. Suffix b indicates sample digestion by sodium peroxide sinter. No suffix or suffix d indicates acid digestion. 91 prefix indicates an initial batch of samples run in 1991, prepared by acid digestion. Lower case with h suffix indicates heavy mineral separate. For the "F" series, suffixes (a) and (s) denote neighbouring shale and sandstone lithologies, respectively. Cerium data were lost because of signal saturation. RW(a) and RW(s) are BRGM sample RW1045 from Rwanda.

Table B-5: REE data for Santa Maria section

ppm	Y	La	Ce	Pr	Nd	Sm	Eu	Gd	Tb	Dy	Ho	Er	Tm	Yb	Lu
f20	28	57	109	12.0	43	7.5	1.8	7.2	1.0	5.9	1.1	3.2	0.46	3.03	0.46
f21	32	58	123	13.9	52	10.2	2.2	9.1	1.2	6.7	1.3	3.6	0.52	3.32	0.51
f22	28	47	100	11.1	40	7.3	1.7	6.8	1.0	5.9	1.1	3.2	0.45	2.99	0.44
F23	31	55	116	13.4	49	9.4	2.1	8.8	1.3	7.4	1.4	3.9	0.56	3.63	0.54
F24	27	54	121	14.4	54	10.5	2.3	9.0	1.2	6.7	1.2	3.4	0.48	3.12	0.47
f25	28	57	119	13.3	50	9.8	2.2	8.9	1.2	6.5	1.2	3.3	0.48	3.04	0.47
F26	29	50	93	10.5	38	6.8	1.6	6.8	1.1	6.4	1.2	3.6	0.52	3.39	0.53
F27	25	56	112	12.8	48	8.8	1.9	8.0	1.1	6.0	1.1	3.2	0.45	2.93	0.45
F28	33	77	158	18.8	71	13.5	2.9	11.6	1.5	7.9	1.4	4.0	0.57	3.74	0.56
F29	29	56	127	15.1	58	12.2	2.7	11.5	1.5	7.6	1.3	3.5	0.49	3.13	0.49
F30	30	69	137	16.0	60	11.0	2.5	9.7	1.3	7.4	1.4	3.8	0.56	3.63	0.56
F31	30	59	118	13.5	50	9.2	2.0	8.4	1.2	6.7	1.3	3.6	0.52	3.38	0.52
f32	34	54	118	13.4	48	9.0	2.2	8.9	1.3	7.9	1.5	4.2	0.60	3.68	0.54
f33	32	59	117	12.8	45	7.8	1.9	8.1	1.2	6.9	1.3	3.7	0.54	3.45	0.53
f34	33	57	119	13.6	49	8.7	2.0	8.5	1.2	6.9	1.3	3.7	0.54	3.45	0.52
f35	30	85	198	22.9	82	14.3	3.0	11.2	1.4	7.2	1.3	3.5	0.49	3.14	0.48
f36	34	65	139	15.8	56	9.8	2.2	8.7	1.3	7.2	1.4	3.8	0.55	3.40	0.51
f37	30	61	131	15.0	55	10.6	2.2	9.1	1.2	6.3	1.2	3.3	0.47	3.08	0.46

Table B-6: Statistical model data

	S-M	Vl	All		F1	F2	F3	F4	F5	F6	F7	F8	F9	F10
Const	199.6	217.4	213.2											
Y	-21.51	-4.37	-3.77		0.00	0.12	-0.02	-0.01	-0.02	0.07	-0.02	-0.02	-0.07	0.01
La	0.29	7.30	4.82		-0.06	-0.02	0.19	0.05	-0.14	-0.10	0.13	0.09	-0.04	-0.09
Ce	0.81	4.68	-0.26		-0.05	-0.05	0.20	0.04	-0.11	-0.08	0.05	0.08	-0.02	-0.03
Pr	1.77	4.77	0.19		-0.04	-0.05	0.19	0.02	-0.03	-0.09	0.05	0.04	0.01	-0.04
Nd	1.91	3.70	0.55		-0.02	-0.04	0.18	0.01	0.01	-0.07	0.02	0.00	0.03	-0.06
Sm	1.60	5.28	6.33		0.00	-0.03	0.16	0.00	0.05	-0.08	-0.05	-0.04	0.04	-0.02
Eu	4.47	4.98	5.90		0.02	-0.01	0.13	-0.02	0.04	-0.07	-0.08	-0.06	0.01	0.04
Gd	-0.46	4.68	6.14		0.02	0.01	0.11	-0.02	0.06	-0.08	-0.08	-0.06	0.02	0.05
Tb	-1.97	-0.11	3.39		0.01	0.07	0.05	-0.01	0.03	-0.01	-0.06	-0.08	-0.01	0.02
Dy	-2.39	-4.04	-5.81		0.00	0.11	-0.02	-0.01	0.02	0.02	-0.02	0.06	0.02	0.08
Ho	-5.94	-5.57	-5.47		0.00	0.13	-0.04	-0.01	-0.05	0.07	0.01	0.04	-0.03	0.07
Er	-7.08	-5.84	-9.98		0.01	0.16	-0.07	0.01	0.04	0.07	0.02	0.03	0.01	0.00
Tm	-8.67	3.20	4.77		-0.01	0.17	-0.03	-0.01	0.01	-0.02	0.18	-0.11	0.02	-0.10
Yb	-9.03	-4.91	-4.66		-0.02	0.19	-0.05	0.02	0.07	0.05	0.18	0.03	0.04	-0.12
Lu	-3.96	-0.60	2.33		-0.02	0.19	-0.03	0.03	0.06	0.00	0.25	-0.09	0.04	-0.13
SiO_2	-8.21	-2.41	-0.04		0.08	0.00	-0.02	-0.10	-0.03	0.16	0.00	0.00	-0.02	0.02
TiO_2	-8.58	-0.17	-8.81		0.02	0.02	0.01	0.05	0.02	-0.04	0.19	-0.08	0.03	0.18
Al_2O_3	13.72	9.37	17.62		-0.01	0.00	0.03	0.25	0.02	-0.12	-0.07	-0.11	0.06	-0.10
Fe_2O_3	-4.65	-0.18	-0.76		-0.10	-0.01	0.03	0.03	0.02	-0.15	0.08	0.04	0.01	0.02
MnO	-17.30	-4.01	-3.33		-0.11	0.00	0.01	0.02	-0.04	-0.07	0.08	0.20	0.08	-0.07
MgO	-13.48	-6.07	-5.81		-0.10	0.00	0.01	0.01	0.02	-0.08	0.10	0.01	0.02	0.02
CaO	2.25	-5.25	2.87		0.04	0.00	-0.01	0.07	0.04	0.12	-0.45	-0.10	0.05	-0.03
Na_2O	16.64	-35.35	-20.91		-0.02	0.03	-0.04	0.06	-0.05	0.53	-0.08	-0.01	0.04	-0.16
K_2O	6.48	38.68	42.15		0.14	-0.03	0.00	0.02	0.02	-0.36	-0.09	-0.01	0.00	0.08
P_2O_5	-3.74	0.70	6.35		0.04	-0.01	-0.01	0.06	0.04	0.00	-0.39	-0.03	0.06	0.05
As	-0.30	1.28	-14.33		0.01	-0.03	-0.02	0.00	-0.22	-0.22	0.06	0.14	-0.07	0.83
Sn	-4.13	1.70	31.42		0.04	-0.01	-0.01	-0.05	-0.05	0.02	-0.04	-0.09	-0.98	0.10
Rb	9.26	27.98	26.57		0.14	-0.02	-0.01	0.04	0.02	-0.20	-0.13	-0.02	0.01	0.03
Sr	23.31	-26.50	-11.32		0.04	-0.02	-0.02	-0.02	0.10	0.40	-0.11	0.02	-0.03	-0.05
Zr	-25.56	-16.68	-26.95		-0.01	0.05	-0.01	-0.08	0.09	0.08	0.37	-0.14	0.07	0.26
Nb	-0.14	0.75	-6.15		0.03	0.04	-0.01	0.06	0.10	-0.03	0.18	-0.04	0.10	0.07
Th	4.06	11.96	10.14		0.04	-0.01	0.01	0.19	0.05	-0.13	-0.08	0.11	-0.01	-0.01
U	-1.93	-7.75	10.48		-0.02	0.06	-0.03	0.09	0.64	-0.06	0.05	-0.08	0.06	-0.31
Pb	7.82	-11.14	-5.33		0.03	0.00	0.00	-0.07	0.45	0.04	-0.02	-0.05	0.01	-0.04
Zn	-10.63	-4.88	-6.89		-0.10	0.00	0.03	0.00	0.05	-0.11	0.13	-0.02	0.07	0.04
Ni	-10.21	-4.55	-4.51		-0.10	0.00	0.01	0.04	0.03	-0.11	0.09	0.02	0.03	0.06
Ga	7.34	-11.43	-8.56		-0.10	-0.01	0.03	0.20	-0.07	0.05	-0.02	-0.02	0.09	-0.04
Cr	5.59	13.19	3.18		0.04	-0.02	-0.01	0.18	0.04	-0.12	-0.11	0.18	0.07	-0.03
V	17.18	-3.36	-2.30		0.01	0.00	-0.02	0.22	0.00	0.01	-0.18	0.00	-0.11	0.12
Ba	10.60	34.91	40.41		0.15	-0.01	-0.01	0.00	0.07	-0.32	-0.06	-0.06	0.00	0.07

Table B-6: Statistical results. F1 to F10 are coefficients of the first ten principal components of the Valleleor geochemical data. The first three columns are monazite predictive functions derived from linear regression modelling. "Vl" is based on Valleleor dataset, "S-M" on Santa Maria dataset, and "All" on both datasets.

References

Akers, W.T., Grove, M., Harrison, T.M. and Ryerson, F.J., 1993, The instability of rhabdophane and its unimportance in monazite paragenesis: Chem. Geol., 110, 169-176.

Awwiller, D.N., 1993, Illite/smectite formation and potassium mass transfer during burial diagenesis of mudrocks: a study from the Texas Gulf Coast Paleocene-Eocene: J. Sed. Pet, 63, 501-512.

Bailey, S.W., Brindley, G.W., Kodama, H. and Martin, R.T., 1982, Report of the Clay Minerals Society Nomenclature Committee for 1980-1981. Nomenclature for regular interstratifications: Clays clay min. 30, 76-78.

Bailey, S.W., 1980, Structures of layer silicates: *in:* Brindley, G.W. and Brown, G., eds., Crystal structures of clay minerals and their X-ray identification, Min. Soc., London.

Balashov, Yu.A. and Girin, Yu.P., 1969, On the reserve of mobile REE in sedimentary rocks: Geochem. International 6, 649-659.

Baldwin, B., and Butler, C.O., 1985, Compaction curves: Am. Assoc. Pet. Geol. Bull. 69, 622-626.

Barker, C.E. and Pawlewicz, M.J., 1986, The correlation of vitrinite reflectance with maximum temperature in humic organic matter: *in*: Buntebarth, G. and Stegena, L, *eds*, Lecture notes in Earth Sciences 5, Palaeogeothermics. Springer-Verlag, Berlin.

Bau, M., 1991, Rare earth element mobility during hydrothermal and metamorphic fluid-rock interaction and the significance of the oxidation state of europium: Chem. Geol. 93, 219-230.

Bau, M., 1993, Effects of syn- and post-depositional processes on the rare earth element distribution in Precambrian iron-formations: Eur. J. Mineral., 5, 257-267.

Bennett, R.H., Bryant, W.R. and Keller, G.H., 1981, Clay fabric of selected submarine sediments: fundamental properties and models: J. Sed. Pet., 51, 217-232.

Boles, J.R. and Franks, S.G., 1979, Clay diagenesis in Wilcox sandstones of Southwest Texas: implications of smectite diagenesis on sandstone cementation: J.Sed.Pet. 49, 55-70.

Brenchley, P.J., Romano, M. and Gutierrez Marco, J.C., 1986, Proximal and distal hummocky cross - stratification facies on a wide Ordovician shelf in Iberia: Can. Soc. Petrol. Geol. Mem. 11, 241-255.

Burnotte, E., Pirard, E. and Michel, G., Genesis of grey monazites: evidence from the paleozoic of Belgium: Economic Geology, 84, 1417-1429.

Chenery, S. and Cook, J., 1993, Determination of REE in single mineral grains by laser ablation microprobe inductively coupled plasma mass spectrometry - preliminary study: Journal of analytical atomic spectrometry, 8,299-303.

Coleman, M.L., 1985, Geochemistry of diagenetic non - silicate minerals: kinetic considerations: PTRS A315, 39-56.

Cooper, D.C., Basham, I.R., and Smith, T.K., 1983, On the occurrence of an unusual form of monazite in panned stream sediments in Wales: Geological Journal 18, 121-127.

Croudace, I.W., and Williams - Thorpe, O., 1988, A low dilution, wavelength - dispersive X - ray fluorescence procedure for the analysis of archaeological rock artefacts: Archaeometry, 30, 227-236.

Curtis, C.D., Coleman, M.L., and Love, L.G., 1986, Pore water evolution during sediment burial from isotopic and mineral chemistry of calcite, dolomite and siderite concretions: GCA 50, 2321-2334.

Curtis, C.D., 1985, Clay mineral precipitation and transformation during burial diagenesis: PTRS A315, 91-105.

Curtis, C.D., Hughes, C.R., Whiteman, J.A. and Whittle, C.K., 1985, Compositional variation within some sedimentary chlorites and some comments on their origin: Min. Mag. 49, 375-386.

Demaison, G.J. and Moore, G.T., 1980, Anoxic environments and oil source bed genesis: AAPG Bull., 64, 1179-1209.

Donnot, M., Guigues, J., Lulzac, Y., Magnien, A., Parfenoff, A. and Picot, P., 1973, Un nouveau type de gisement d'europium: la monazite grise à europium en nodules dans les schistes paléozoïques de Bretagne: Min. Deposita, 8, 7-18.

Elderfield, H., 1988, The oceanic geochemistry of the rare earth elements: PTRS A325, 105-126.

Franks, P.C., 1969a, Nature, origin and significance of cone-in-cone structures in the Kiowa formation (early Cretaceous), North-Central Kansas, J.Sed.Pet 39,1438-1454.

Franks, P.C., 1969b, Synaeresis features and genesis of siderite concretions, Kiowa formation (early Cretaceous), north-central Kansas: J.Sed.Pet., 39, 799-803

Gilman, R.A. and Metzger, W.J., 1967, Cone-in-cone concretions from western New York, J.Sed.Pet 37,87-95.

Gomez, M., 1991, Investigacion de monacitas grises en la reservs monacita (Ciudad Real - Toledo y Badajoz): Unpublished internal report, Minas de Almaden y Arrayanes, 13400 Almaden, Spain.

Govindaraju, K., 1989, Geostandards newsletter, 13.

Grauch, R.I., REE in metamorphic rocks, *in:* Lipin, B.R. and McKay, G.A., eds.,1989, Geochemistry and mineralogy of REE: Min. Soc. Am. Reviews in Mineralogy 21.

Hayes, J.B., 1970, Polytypism of chlorite in sedimentary rocks: Clays and clay mins., 18, 285-306.

Hillier, S.J. and Marshall, J.E.A., 1988, A rapid technique to make polished thin sections of sedimentary organic matter concentrates: J.Sed.Pet.58, 754-755.

Hirata, T., Shimizu, H., Agaki, T., Sawatari, H. and Masuda, A, 1988, Precise determination of rare earth elements in geological standard rocks by inductively coupled plasma source mass spectrometry: Anal. Sci. 4, 637-643.

Hower, J., Eslinger, E.V., Hower, M.E. and Perry, E.A., 1976, Mechanism of burial metamorphism of argillaceous sediment: 1. Mineralogical and chemical evidence: GSA Bull., 87, 725-737.

Huebschman, R.P., 1973, Correlation of fine carbonaceous bands across a Precambrian stagnant basin: J.Sed. Pet 43, 688-699.

Israilev, L.M. and Solovleva, N.A., 1975, Accessory authigenic monazite in the Upper Palaeozoic deposits of northern Verkhoyan'e: Lithology and mineral resources, 9,624-628.

I.T.G.E., 1989, Mapa Geologico de España, escala 1:50,000, Hoja 710 "Retuerta del Bullaque": Instituto Tecnológico GeoMinero de España, Madrid.

Jackson, M.L., 1975, Soil chemical analysis - advanced course (2nd edition): published by the author, Madison, Wis. 53705

Jarvis, I. and Pearce, T., 1993, High resolution chemostratigraphy of quaternary distal turbidites: a case study of new methods for the correlation of barren strata: Unpublished conference abstract, Dating and correlating biostratigraphically barren strata, May 1993, Geological Society, London.

Jarvis, K.E. and Williams, J.G., 1993, Laser ablation inductively coupled plasma mass spectrometry (LA-ICP-MS): a rapid technique for the direct, quantitative determination of major, trace and rare-earth elements in geological samples: Chem. Geol., 106, 251-262.

Jarvis, K.E., 1988, Inductively Coupled Plasma Mass Spectrometry: A new technique for the rapid or ultra - trace level determination of the REE in geological materials: Chem. Geol. 68, 31-39.

Kisch, H.J., 1987, Correlation between indicators of very low-grade metamorphism, *in*: Frey, M. (ed), Low temperature metamorphism, Blackie and Sons, London.

Kübler, B., 1967, La cristallinité de l'illite et les zones tout à fait supérieures du métamorphisme: in Etages tectoniques, Colloque de Neuchâtel 1966, A la Baconnière, Neuchâtel, Switzerland, 105-121.

Lacomme, A. and Fontan, F., 1971, Sur la présence de monazite dans les Pyrénées: C.R. Ac. Sci. Paris, D272, 1193-1194.

Lacomme, A., Hottin, A.M. and Laval, M., 1993, La monazite grise du massif de l'Arize (Pyrénées françaises): BRGM report R 37041, Orléans, France.

Laval, M., Hottin, A.M., Salpeteur, I., Lacomme,A. and Jézéquel, P., 1993, La monazite grise du Rwanda et des Pyrénées françaises: BRGM report R 36698, Orléans, France.

Lee, J.H. and Byrne, R.H., 1992, Examination of comparative REE behaviour using linear free - energy relationships: GCA 56, 1127-1137.

Limbourg, Y., 1986, Découverte de monazite grise en nodules dans l'Eodévonien du synclinorium de Neufchâteau (Belgique): Bulletin de la societé belge de Géologie, 95, 281-285.

Mariano, A.N., 1989, Economic Geology of rare earth minerals, *in*: Lipin, B.R. and McKay, G.A., (eds.) Geochemistry and mineralogy of REE: Min. Soc. Am. Reviews in Mineralogy 21.

Mason, B. and Moore. C.B., 1982, Principles of geochemistry: 4th edition, Wiley, New York.

Masuda, A., Nakamura, N. and Tanaka, T., 1973, Fine structures of mutually normalized rare earth patterns of chondrites: GCA 37, 239-248.

McKie, D., 1962, Goyazite and florencite from two African carbonatites: Min. Mag. 33, 280-297.

McLennan, S.M.,1989, Rare earth elements in sedimentary rocks: influence of provenance and sedimentary processes, in: Lipin, B.R. and McKay, G.A., eds., Geochemistry and mineralogy of REE: Min. Soc. Am. Reviews in Mineralogy 21.

Milodowski, A.E. and Zalasiewicz, J.A., 1991b, The origin and sedimentary, diagenetic and metamorphic evolution of chlorite - mica stacks in Llandovery sediments of central Wales, UK: Geol. Mag. 128, 263-278.

Milodowski, A.E. and Zalasiewicz, J.A., 1991, Redistribution of REE during diagenesis of turbidite / hemipelagite mudrock sequences of Llandovery age from central Wales, *in* Morton, A.C., Todd, S.P., and Haughton, P.D.W., eds., Developments in sedimentary provenance studies: Geol. Soc. London Spec. Pub. 57, 103-132.

Mineyev, D.A., 1968, Mean compositions of the lanthanides in minerals, Geochemiya Translations, 1968 (supplement to Geochem. Internat. vol. 5),354-366.

Murphy, D.W.A., 1993, The rare earths - from flints to phosphors and beyond (abstract): *in* Rare Earth Minerals: Chemistry, origin and ore deposits, conference abstracts volume, Mineralogical Society, London, April 1993.

Nonnon, M., 1984, Découverte de monazite grise en nodules et de l'or alluvionaire dans le massif de la Croix-Scaille: Bulletin de la societé belge de Géologie, 93, 307-314.

Nonnon, M., 1989, Une nouvelle occurrence de monazite grise en Belgique: Bulletin de la societé belge de Géologie, 98, 73-76.

Ortega, E., (ed.), 1993, Assessment of alluvial deposits related to stratabound Eu-rich monazite mineralization: a major future source for specific rare earths used in new technology: EEC contract no. MA2A-CT91-0049, Final Report, European Commission, Brussels.

Pouit, G., and Laval, M., 1990, Monazite grise: guides de prospection d'apres une analyse bibliographique: report R31733, BRGM,Orléans.

Pye, K., Dickson, J.A.D., Sciavon, N., Coleman, M.L. and Cox, M., 1990, formation of siderite - Mg - calcite - iron sulphide concretions in intertidal marsh and sandflat sediments, north Norfolk, England: Sedimentology 37, 325-343.

Rabano, I., 1989, Trilobites del Ordovícico Medio del sector meridional de la zona centro - ibérica española. Parte 1: Yacimientos, bioestratigrafía y aspectos paleobiogeográficos: Boletin Geológico y Minero 100, 3-35.

Raiswell, R., 1987, Non- steady state microbial diagenesis and the origin of concretions and nodular limestones, *in* Marshall, J.D., ed., 1987, Diagenesis of sedimentary sequences: Geol. Soc. London Spec. Pub. 36, 41-54.

Read, D., Cooper, D.C. and McArthur, J.M., 1987, The composition and distribution of nodular monazite in the Lower Paleozoic rocks of Great Britain: Min. Mag. 51, 271-280.

Read D., 1983, Rare earth element behaviour during subaerial weathering: Unpublished Ph.D. thesis, University of London.

Roaldset, E., 1975, REE distributions in some Precambrian rocks and their phyllosilicates, Numedal, Norway: GCA 39, 455-469.

Rosenblum, S. and Mosier, E.L., 1983, Mineralogy and occurrence of europium - rich dark monazite: USGS Prof. Paper 1181, 67pp.

Saupé, F., Dunoyer de Segonzac, G. and Teichmüller, M., 1977, Etude de métamorphisme régional dans la zone d'Almaden (province de Ciudad Real, Espagne) par la cristallinité de l'illite et par le pouvoir réflecteur de la matière organique: Science Terre (Nancy) 21, 251-269.

Sellwood, B.W., 1986, Shallow marine carbonate environments: *in* Reading, H.G., (ed.), Sedimentary environments and facies, Blackwell, Oxford.

Serdyuchenko, D.P. and Kochetkov, O.S., 1974, Metasedimentary monazite in Riphean schists of the Timans: Dok. Acad. Sci. USSR, Earth Science section.

Smith, R.D.A., 1987, Early diagenetic phosphate cements in a turbidite basin, *in* Marshall, J.D., ed., 1987, Diagenesis of sedimentary sequences: Geol. Soc. London Spec. Pub. 36, 141-156.

Środoń, J., 1980, Precise identification of illite/smectite interstratifications by X-ray powder diffraction: Clays and clay mins., 28, 401-411.

Środoń, J., 1984, X-ray powder identification of illitic minerals: Clays and clay mins., 32, 337-349.

Suggate, R.P., 1982, Low-rank sequences and scales of organic metamorphism: J. Petrol. Geol., 4, 377-392.

Tarr, W.A., 1932, Cone-in-cone, in Twenhofel (ed.), Treatise on sedimentation, William and Williams, Baltimore, 716-733.

Teichmuller, M, 1987, Organic material and very low-grade metamorphism, *in*: Frey, M. (ed), Low temperature metamorphism, Blackie and Sons, London.

Tellier, K.E., Hluchy, M.M., Walker, J.R. and Reynolds, R.C., 1988, Application of high gradient magnetic separation (HGMS) to structural and compositional studies of clay mineral mixtures: J. Sed. Pet., 58, 761-763.

Todd, J.E., 1903, Concretions and their geological effects: Bull. Geol. Soc. Am., 14, 353-360.

Tricker, P.M., Marshall, J.E.A. and Badman, T.D., 1992, Chitinozoan reflectance: a Lower Paleozoic thermal maturuty indicator: Marine and Petroleum geol., 9, 302-307.

Van Wambeke, L., 1971, Hinsdalite and corkite: indicator minerals in Central Africa: Mineral. Deposita, 6, 130-132.

Velde, B., 1985, Clay minerals: Developments in sedimentology no. 40, Elsevier, 427pp.

Walker, J.R., 1993, Chlorite polytype geothermometry: Clays clay min. 41, 260-267.

White, W.M. and Patchett, P.J., 1984, Hf-Nd-Sr and incompatible element abundances in island arcs: implications for magma origins and crust-mantle evolution: EPSL 67, 167-185.

Wilkinson, J.J., 1991, Volatile production during contact metamorphism: The role of organic matter in pelites: J.Geol. Soc. 148, 731-736.

Wilkinson, L., 1990, SYSTAT: The system for statistics: SYSTAT,Inc., Evanston, IL.

Williams, J.G. and Jarvis, K.E., 1993, Preliminary assessment of Laser ablation inductively coupled plasma mass spectrometry for quantitative multi-element determination in silicates: J.A.A.S., 8, 25-34.

Wood, S.A., 1990a, The aqueous geochemistry of the REE and Yttrium. 1. Review of the available low - temperature data for inorganic complexes and the inorganic REE speciation of natural waters: Chem. Geol. 82, 159-186.

Wood, S.A., 1990b, The aqueous geochemistry of the REE and Yttrium. 2.Theoretical predictions of speciation in hydrothermal solutions to 350°C at saturation water vapour pressure: Chem. Geol,88, 99-125.

Wybrecht, E., Duplay, J., Piqué, A. and Weber, F., 1985, Mineralogical and chemical evolution of whitew micas and chlorites, from diagenesis to low-grade netamorphism; data from various size fractions of greywackes (Middle Cambrian, Morocco): Min. Mag. 49, 401-411.

Zemel, V.K., 1936, Analyses of monazites from gold placers of Aldan and SO Yenesei: Zhurnal Prikladnoi Khimii, 9, 1969-1971.